Charles University

Faculty of Sciences

Programme of study: Geology

Dissertation thesis



Ondřej Krýza

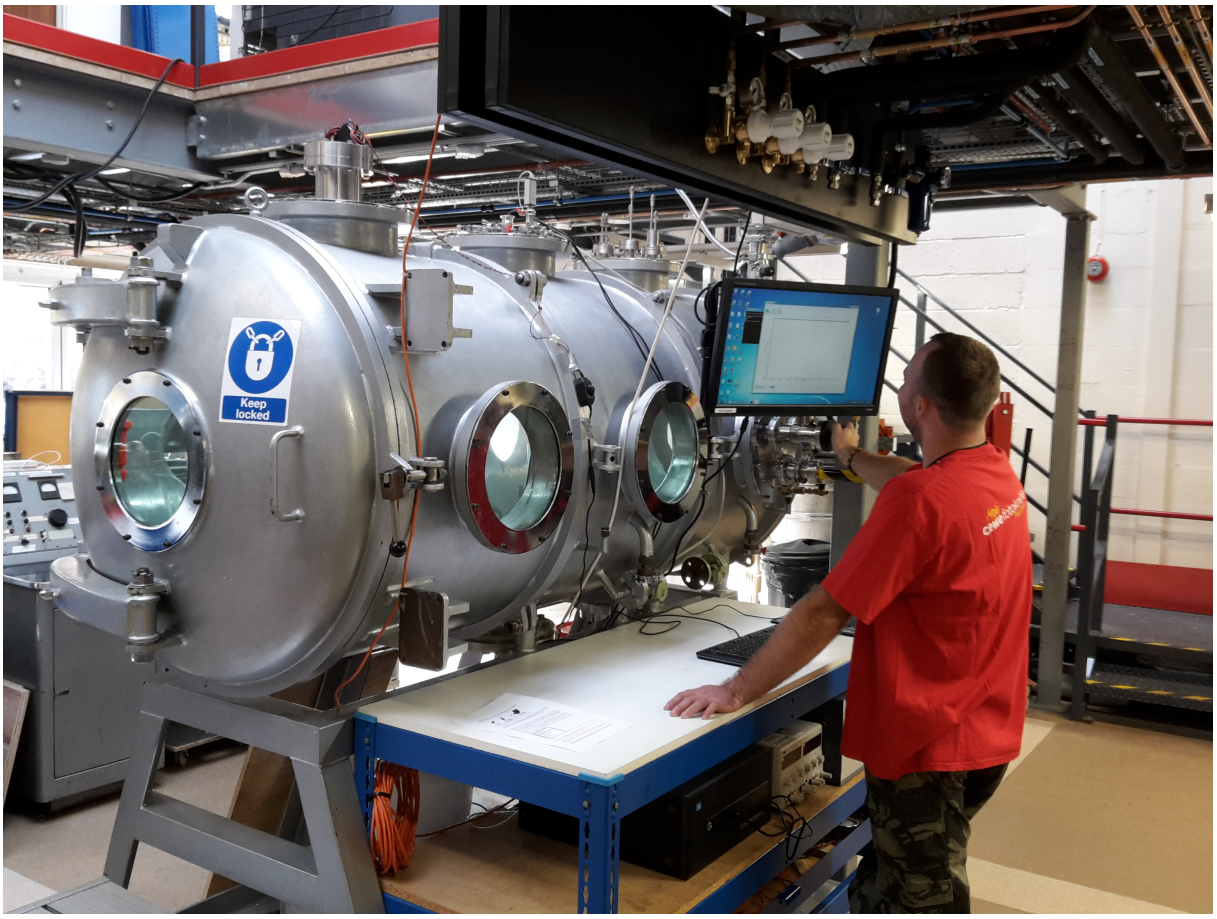
Analogue and numerical simulations of the geodynamical systems - insights from the models of the Earth collision tectonics and Martian mudflows

Analogové a numerické simulace geodynamických systémů - poznatky z modelů kolizní tektoniky na Zemi a bahenních proudů na Marsu

Institute of Petrology & Structural Geology

Supervisor: doc. Mgr. Ondrej Lexa, Ph.D.
Consultant: Mgr. Prokop Závada, Ph.D

Prague, 2020



Large Mars Vacuum Chamber in the Hypervelocity Impact Facility at the Open University in Milton Keynes

This thesis represents an effort of many people that were involved to individual research projects as well as a people that contributed by discussions, technical help and moral support.
At the first place I would like to thank to my supervisor Ondrej Lexa who led me during my studies and who was always open to new ideas and discussion. Many thanks belong to Prokop Závada for all the help with the manuscripts and for fruitful cooperation on many interesting topics related to analogue modelling. Great thanks to Karel Schulmann for many interesting talks about oroclinal buckling and for help with related manuscript.
During the studies I was invited to participate on many interesting topics mainly related to modelling in geosciences and planetology. In this place I would like to thank to Petr Brož who showed me a beauties of the Mars research. Likewise, I would like to thank to Petra Maierová who consecrate me to the numerical model of the Bohemian Massif evolution and helped me with the model used in Chapter IV. Big thanks to Václav Špilar and Steve Collett for careful reading, commenting and grammar corrections of this thesis.
Also many thanks belongs to all remaining co-authors which participated on individual manuscripts and who are not mentioned namely here. As well, I appreciate all the work of the reviewers and editors and I would like to thank them for many relevant comments and ideas associated with the first versions of manuscripts.
It should be noted that significant part of this thesis would not be realized without work in the analogue modelling laboratories (at the Géosciences Rennes - University of Rennes 1, Geophysical Institute of Czech Academy of Sciences and at the Open University in Milton Keynes). This thesis was also realized with significant support from research grant projects (GAČR: 19-27682X, GAČR: 17-17540S, 16-17457S, UNCE/SCI/006, EPN2020-RI: 654208).
I am glad that I found so warm atmosphere and many good friends at both institutions where I spent the best years of my life. Thanks to my friends and colleagues from the Institute of Petrology and Structure Geology and from the Geophysical Institute of the CAS. Especially, I would like to gratefully thank to Drahomíra Seemannová for all the support and help with administrative background.
Hana Smejkalová and Sabina Sládková deserve great appreciation for huge portion of patience during all the years of my studies.
Last but not least is my family that I would like to warmly thank. This thesis will be dedicated to them.

Prohlašuji, že jsem závěrečnou práci vypracoval samostatně, a že jsem uvedl všechny použité informační zdroje a literaturu. Tato práce ani její podstatná část nebyla předložena k získání jiného nebo obdobného druhu vysokoškolské kvalifikace. Výsledky teze jsou produktem mé vlastní práce nebo práce ve výzkumném týmu.

V Praze dne 17.1. 2020 .....

I declare that this thesis is a result of my own work and that I have cited all the resources and literature. Neither this thesis nor its substantial part has been submitted to fulfill requirements for any other academic degree. The results of the thesis are my own work or the product of collaboration with other members of the research teams.

In Prague, 17.1. 2020 .....

Abstract

Analogue and numerical modelling in geosciences is an excellent tool for studying complex spatio-temporal relationships in mass and energy transfer. Recent developments and advances in plate tectonics and planetology require a combination of both approaches to simulate processes that cannot be studied directly in-situ. Advanced physical models are complemented by deformation analysis which is based on image velocimetry and photogrammetry, while numerical simulations utilize both modern and traditional methods to solve corresponding equations in complex domains.

This work compiles several models that are focused on deformation analysis associated with material and heat transfer in large accretionary systems. The second subject of the thesis represent the investigation of the formation and propagation of large mudflows in martian atmospheric conditions.

In the first part of the work we present a general overview of the problems of analogue and numerical modelling including scaling theory, governing equations, individual methods and history. In the second part of the thesis we deal with laboratory and numerical simulations of collision-indentation tectonics associated with the emergence of large accretionary systems on Earth. The last part of the thesis is devoted to experiments designed for the study of the formation and development of mudflows, which arise as a result of supposed cryovolcanic activity on the surface of Mars.

The first models involves oroclinal buckling of an accretionary belt and continental ribbon in the post-subduction stage related to the indentation of a cratonic system at an orthogonal direction. The results of the individual experiments showed a complex flow of the material of the lower crust and the upper mantle in the axial plane of both progressively buckled interlimb areas. This ductile flow is associated with the deformation response of the upper crust and with the emergence of large pop-up and pop-down domains, local faults and shear zones. The correlation of the results from the surface deformation analysis and from the deformation analysis of the orthogonal sections of the model confirms the significant exhumation of the continental and oceanic mantle in the proximal hinge area. This exhumation is correlated with the existence of a significant gravimetric anomaly in the Hangai region of the Tuva-Mongol orocline which is located within the CAOB (Central Asian Orogenic Belt).

The second series of experiments is focused on the study of the melt amount and migration style effect on the dynamics of detachment folding in the pre-indentative part of crustal domain. This thermally dependent model produces a series of folds over a thin layer of the melt that migrates along the shortening direction and is simultaneously sucked into the inter-limb zones of the resulting fold-dome structures. A method for quantifying the divergence of the PIV based velocity field in the target sub-regions of the model domain was developed to balance the inflow and outflow of this material. The correlation of the time evolution of the divergence and the amount of the melt in the individual folds internal structures revealed the polyphase

development of each fold. The systematic change in the height of the folds and the modal melt content of the individual locked folds is proportional to the rate of inflow of the melt into their cores. Overpressure of the melt in locked folds leads to its extrusion back into the source layer, where it can be further transferred along the shortening direction and support further detachment folding.

Since these models are produced in an unscaled gravitational field, potential diapiric exhumation of the lower crust is also the subject of discussion. The model of the Rayleigh-Taylor instability was used with tested variation of rheological, geometric and thermal properties. The model simulates the evolution of a large-scale lithosphere segment, related to late orogeny which is characterized by a massively thickened crustal domain, during the post-collision stage. Analysis of the selected simulations showed that the crustal-scale diapirism is typical for collisional and post-collisonal systems, that are characterized by a distinctly weak and hot lower felsic crust with developed density perturbations at the border with the overlying mafic crust. The rate of diapiric exhumation depends on the convergence rate of the indenter as well as on the amplitude/wavelength of the density perturbation and specially on the density contrast of the crustal material. The rheological parameters are controlled by time-variations of the heat redistribution from the mantle into the crust and by thermal productivity of the felsic lower crust. Diapirism and folding are involved in dependence on the slowing of the convergence and on distance of the perturbation from the indenter.

The last part of the thesis presents physical modeling of the mudflows propagating in atmospheric conditions at the surface of Mars. The series of more than sixty experiments was designed to study mudflow on both cold and hot surfaces made of granular unconsolidated material (sand) or solid consolidated material (plastic plate). The effect of the subsoil inclination on the distribution and shape of mudflows was also tested.

Experiments, conducted on pre-cooled sand, revealed significant geomorphological similarity between mudflows produced at reduced atmospheric pressure and Pahoehoe lava flows at the Earth's surface atmospheric pressure. The emergence of mudflows reflects several development stages, including initial surface flow, mud degassing / freezing, and flow in closed channels with a progressive propagation at the head of the stream. The mud propagation through an enclosed channel and progressive development of the lobes in the stream foreland is similar to the development of pillow lavas on Earth.

Experiments conducted on a warm sand substrate revealed a different process of transporting mud material that combines 'classical flows' and 'levitation' of mud above a warm surface, depending on the distance from the source area.

Keywords

Analogue modelling, Numerical modelling, Orocline, Detachment folding, PIV analysis, DEM models, Diapirism, Mudflows, Mars

Abstrakt

Analogové a numerické modelování v geovědách představuje vynikající nástroj ke studiu složitých časoprostorových vztahů při transferu hmoty a energie. Současný rozvoj a pokrok na poli deskové tektoniky a planetologie vyžaduje kombinaci obou přístupů pro simulaci procesů, které nelze studovat přímo in situ. Pokročilé fyzické modely jsou doplňovány deformační analýzou vycházející z obrazové velocimetrie a fotogrammetrie zatímco numerické simulace využívají moderních i tradičních metod pro řešení příslušných rovnic ve složitých doménách.

Předkládaná práce kompletuje několik typů modelů, které jsou zaměřeny jednak na deformační analýzu spojenou s transferem materiálu a tepla v akrečních systémech, tak i na simulaci vzniku a vývoje rozsáhlých bahenních proudů v atmosférických podmínkách Marsu.

V první části práce uvádíme obecný přehled problematiky analogového a numerického modelování včetně škálovacích vztahů, řídících rovnic, jednotlivých metod a historie. Ve druhé části práce se zabýváme laboratorními i numerickými simulacemi kolizní-indentační tektoniky spojené se vznikem velkých akrečních systémů na Zemi. Poslední část práce je věnována experimentům navrženým pro studium vzniku a vývoje bahenních proudů, které vznikají v důsledku předpokládané kryovulkanické činnosti na povrchu Marsu.

První série modelů zahrnuje oroklinální ohyb akrečního pásu a kontinentálního žebra v post-subdukční etapě, který je způsobený indentací kratonického systému v ortogonálním směru. Výsledky experimentů prokázaly komplexní tok materiálu spodní kůry a svrchního pláště v osní rovině obou vznikajících zámkových oblastí, který je spojen s deformační odezvou svrchní kůry a vznikem rozsáhlých násunovo-poklesových domén i střižných zón. Kinematika, dynamika a geometrie těchto svrchno-korových deformačních struktur byla analyzována pomocí fotogrammetrických metod (DEM) a obrazové rychlostní analýzy (PIV). Korelace povrchové deformační analýzy a deformační analýzy ortogonálních řezů modelu potvrzuje významnou exhumaci kontinentálního i oceánského pláště v proximální zámkové oblasti. Tento efekt je korelován s existencí významné gravimetrické anomálie v Hangaiském regionu Tuva-Mongolské orokliny situované v rámci CAOB (Central Asian Orogenic Belt).

Druhá série experimentů je zaměřena na studium vlivu migrace a množství taveniny na dynamiku vrás odlepení v před-indentační korové doméně. Tento termálně závislý model produkuje sérii vrás nad tenkou vrstvou taveniny, která migruje podél směru zkracování a je souběžně nasávána do meziramenních zón vznikajících vrásovo-dómových struktur. Pro bilanci vtoku a výtoku tohoto materiálu byla vyvinuta metoda využívající kvantifikaci divergence rychlostního pole produkovaného PIV analýzou v cílových podoblastech modelové domény. Korelace časové změny divergence a množství taveniny v jednotlivých vrásách odhalila polyfázový vývoj každé vrásy. Systematická změna ve výšce vrás a modálním obsahu taveniny v jednotlivých uzamčených vrásách je úměrná rychlosti vtoku taveniny do jejich jader. Přetlakování taveniny v uzamčených vrásách vede k jejímu vytlačení zpět do zdrojové vrstvy, kde

může být dále přenesena ve směru zkracování a usnadnit tak další odlepené vrásnění.

Neboť tyto modely jsou produkovány v neškálovaném gravitačním poli, byla rovněž diskutována potenciální diapirická exhumace spodnokorového materiálu. Byl použit model Rayleigh-Taylorovy nestability s variací reologických, geometrických a termálních vlastností spodní kůry pozdně orogení a ztluštěné litosférické domény. Analýza vybraných simulací ukázala, že korový diapirismus je charakteristický pro kolizní systémy, které jsou typické výrazně 'měkkou' a teplou spodní felzickou kůrou s výrazně vyvinutou hustotní perturbací na hranici s nadložní mafickou kůrou. Tvar diapirismu je ovlivněn viskozitním kontrastem korových vrstev a rychlostí konvergence. Rychlost diapirické exhumace závisí na rychlosti konvergence indentoru, amplitudě a vlnové délce hustotní perturbace a hustotním kontrastu materiálu spodní kůry. Reologické parametry jsou řízené časově proměnlivou distribucí tepla z pláště a tepelnou produktivitou felzické spodní kůry. Diapirismus a vrásnění se zastupují v závislosti na zpomalování konvergence a vzdálenosti od indentoru.

Poslední část práce prezentuje fyzické modelování bahenních proudů v atmosférických podmínkách Marsu. Série více než šedesáti experimentů byla navržena pro studium toku bahna po chladném i horkém povrchu tvořeném granulárním nezpevněným materiálem (písek) nebo pevném konsolidovaném materiálu (plastická deska). Rovněž byl testován vliv úklonu podloží na distribuci a tvar bahenních proudů. Všechny experimenty probíhaly při tlaku 7 mbar s různými rychlostmi extruze bahna. Pro studium topografických charakteristik jednotlivých proudů byla použita metoda rekonstrukce DEM na základě pořízených fotografií povrchu modelu.

Série experimentů probíhajících na podchlazeném písku prokázala významnou geomorfologickou podobnost mezi bahenními proudy ve sníženém atmosférickém tlaku a lávovými proudy typu Pahoehoe v pozemském povrchovém tlaku. Vznik bahenního proudu reflektuje několik vývojových stádií, které zahrnují počáteční povrchový tok, odplyňování/mrznutí bahna a tok v uzavřených kanálech s progresivní propagací v čele proudu. Proces propagace z uzavřeného kanálu je podobný výlevům polštářových bazických láv na Zemi.

Experimenty probíhající na teplém pískovém podkladu odhalily odlišný proces transportu bahenního materiálu, který kombinuje 'klasický proud' a 'levitaci' bahna nad teplým povrchem v závislosti na vzdálenosti od zdrojové oblasti.

Klíčová slova

Analogové modelování, numerické modelování, oroklina, vrásy odlepení, PIV analýza, DEM modely, diapirismus, bahenní proudy, Mars

List of related papers and authors contribution

This thesis is a monography combined with one published paper, two manuscripts under review and one manuscript before submitting. The candidate is the first author on two of them and contributed as second author to two others.

Krýza, O., Závada, P., & Lexa, O. (2019). Advanced strain and mass transfer analysis in crustal-scale oroclinal buckling and detachment folding analogue models. *Tectonophysics*, **764**, 88-109.

- Article is related to Chapter 3. Candidate was responsible for all modelling, programming of all procedures, PIV and DEM calculations, data processing and analysis. Candidate prepared all figures and original text body except paragraph related to scaling of detachment folding model. The careful reading and modifications of text were made by co-authors.
  (Authors contribution: 70%)

Krýza, O., Lexa, O., Schulmann, K., Guy, A., Gapais, D., Cosgrove, J. & Xiao, W. Oroclinal buckling and associated lithospheric-scale material flow - insights from physical modelling: implication for Mongolian orocline. In prep.

- Article is related to Chapter 2. Candidate designed and conducted all models. Candidate is responsible for PIV and DEM calculations, data processing and analysis. Candidate prepared most of the figures and main text body which was improved with co-authors.

Brož, P., Krýza, O., Wilson, L., Conway, S.J., Hauber E., Mazzini A., Raack, J., Patel, M.R., Balme, M.R. & Sylvest, M.E. (2019) Lava-like mud flows on Mars. *Nature Geoscience*, In review

- Article is related to Chapter 5. Candidate contribution was co-designing of the methodology, model setup and data analysis. Candidate calculated all DEM models.
  (Authors contribution: 40%)

Brož, P., Krýza, O., Conway, S.J., Mueller, N.T., Hauber E., Mazzini A., Raack, J., Patel, M.R., Balme, M.R. & Sylvest, M.E. (2019) Mud Flow Levitation on Mars: Insights from Laboratory Simulations. *Earth and Planetary Sciences Letters*, In review

- Article is related to Chapter 6. Candidate contribution was co-designing of the methodology, model setup and data analysis. Candidate calculated all DEM models.
  (Authors contribution: 40%)

I certify that the above descriptions are accurate and representing the involvement of the candidate in the aforementioned research articles.

Signed:

Doc. Mgr. Ondrej Lexa, PhD.

Project supervisor

Contents

I Introduction to geodynamical modelling **1**

1 Analogue and numerical simulations **3**

1.1 Introduction . . . 3
1.2 Brief history and advances in analogue modelling . . . 5
1.3 Scaling of the analogue models . . . 7
1.3.1 Materials and rheology . . . 8
1.3.2 Scaling of a linear and non-linear rheology and flow properties 11
1.3.3 Artificial gravitational field . . . 14
1.4 Recent analogue models of a large-scale mantle/lithosphere dynamics 16
1.5 Brief history and advances in the numerical geodynamic modelling . . 16
1.6 Numerical solution and governing equations . . . 18
1.6.1 Continuity equation . . . 19
1.6.2 Momentum equation . . . 19
1.6.3 Heat transfer equation . . . 20
1.6.4 Numerical methods . . . 21
1.7 Objectives of the research part of the thesis . . . 26
1.8 References . . . 28

II Mass and heat transfer in the accretionary systems **43**

2 Oroclinal buckling and associated lithospheric-scale material flow **45**

2.1 Abstract . . . 45
2.2 Introduction . . . 46
2.2.1 Geodynamic setting of Mongolian orocline . . . 48
2.3 Model setup . . . 51
2.3.1 Model geometry . . . 51
2.3.2 Model materials . . . 51
2.3.3 Model scaling . . . 53
2.3.4 Experimental procedure . . . 54
2.3.5 Model sectioning . . . 55
2.3.6 Surface topography analysis . . . 56

2.4 Results . . . 57
2.4.1 Finite geometry of modeled domain . . . 57
2.4.2 Sections perpendicular to the shortening direction (i.e. parallel to the axial plane of the orocline) . . . 57
2.4.3 Sections parallel to the shortening direction (i.e. perpendicular to the orocline axial plane) . . . 59
2.4.4 Incremental evolution . . . 59
2.4.5 Evolution of model surface deformation . . . 61
2.5 Discussion . . . 64
2.5.1 Model limitations . . . 64
2.5.2 Rheological interfaces and associated model dynamics . . . 65
2.5.3 Mantle and crustal fluxes related to oroclinal buckling . . . 66
2.5.4 Why the O→C and C→O hinges have opposite inclinations? . . . 68
2.5.5 Is the deformation driven by top or bottom fluxes? . . . 69
2.5.6 Implications for geodynamic concepts of curved orogenic belts 69
2.6 Conclusions . . . 72
2.7 Appendix . . . 73
2.7.1 The first generation of experiments . . . 73
2.7.2 Interlimb areas of the orocline . . . 73
2.7.3 Velocity components and displacement differences . . . 75
2.7.4 General 3D flow . . . 75
2.7.5 Mantle exhumation and Bouguer anomalies in Hangai zone . . . 77
2.8 Acknowledgments . . . 80
2.9 References . . . 80

3 Advanced strain and mass transfer analysis in crustal-scale oroclinal buckling and detachment folding analogue models 89
3.1 Abstract . . . 89
3.2 Introduction . . . 90
3.3 Models of oroclinal buckling . . . 92
3.3.1 Model background and setup . . . 92
3.3.2 Model materials . . . 93
3.3.3 Experimental procedure and model development . . . 93
3.3.4 Application of the PIV method for oroclinal buckling models . 95
3.3.5 Derived model parameters . . . 96

3.3.6 Correlation of the calculated parameters with deformation features . . . 97
3.4 Models of detachment folding . . . 99
3.4.1 Model background and setup . . . 99
3.4.2 Model materials and scaling . . . 100
3.4.3 Experimental procedure and model development . . . 104
3.4.4 Improvement of colour variability for PIV analysis . . . 105
3.4.5 The PIV calculations and testing of accuracy . . . 105
3.4.6 Derived model parameters . . . 107
3.5 Divergence and the volumetric flow on local scale in the detachment fold experiments . . . 109
3.5.1 Divergence in a static window . . . 109
3.5.2 Adaptive subgrids . . . 112
3.5.3 Divergence in adaptive subgrids and mass balance . . . 113
3.6 Discussion . . . 116
3.6.1 Interpretation and significance of the calculated parameters in the oroclinal buckling models . . . 116
3.6.2 Interpretation and significance of the calculated parameters in models of the detachment folding . . . 118
3.6.3 Melt flow and mass balance in the sequence of detachment folds 120
3.6.4 Application of modelling results to accretionary orogens with partially molten lower crust . . . 121
3.7 Conclusions . . . 122
3.8 Appendix . . . 123
3.8.1 Accuracy of the calculated displacement field . . . 123
3.8.2 Subgrid calculations and Marker in Cell method . . . 125
3.8.3 Testing of the PIV resultant displacement field . . . 125
3.8.4 Rheometry of the analogue materials used in Part II and Part III 126
3.9 Acknowledgements . . . 136
3.9.1 Funding . . . 136
3.9.2 Author Contributions Statement . . . 136
3.10 References . . . 136

4 Numerical modelling of crustal-scale Rayleigh-Taylor instabilities 143
4.1 Introduction . . . 143
4.2 Model setup . . . 144
4.2.1 Governing equations . . . 146
4.2.2 Boundary conditions . . . 151
4.2.3 Initial conditions . . . 151
4.2.4 Numerical implementation . . . 152
4.3 Results . . . 152
4.3.1 The output model parameters . . . 153
4.3.2 Initial thermal field and geotherm . . . 155
4.3.3 Evolutionary stages and the main simulation differences . . . 155
4.3.4 The velocity field and strain(-rate) in the model domain . . . 162
4.4 Discussion . . . 166
4.4.1 The effect of the heating on diapiric extrusion . . . 167
4.4.2 The density contrast of the lower crust . . . 168
4.4.3 The role of the perturbation shape for diapiric exhumation rate 169
4.4.4 Diapiric or detachment folding? . . . 170
4.5 Conclusions . . . 172
4.6 References . . . 173

III Mud flows under the Martian conditions 179

5 Lava-like mud flows on Mars 181
5.1 Abstract . . . 181
5.2 Introduction . . . 181
5.3 Model setup and experimental procedure . . . 182
5.3.1 DEM calculation . . . 185
5.4 Results and discussion . . . 185
5.5 Conclusions . . . 190
5.6 Appendix . . . 192
5.6.1 Cooling and freezing of mud when the external pressure is less than the saturation vapour pressure of the water. . . . 192
5.7 Acknowledgements . . . 195
5.8 Author contribution . . . 195

5.9 Data availability . . . 196
5.10 References . . . 196

6 Mud Flow Levitation on Mars: Insights from Laboratory Simulations 201
6.1 Abstract . . . 201
6.2 Introduction . . . 201
6.3 Methods . . . 204
6.3.1 Experimental setup . . . 204
6.3.2 Modeling of Mars surface temperatures . . . 205
6.4 Observations . . . 207
6.5 Discussion . . . 212
6.5.1 Application to Mars . . . 212
6.5.2 Temperature drop within the mud and substrate . . . 215
6.5.3 Scaling to Mars and experimental limitations . . . 218
6.6 Conclusions . . . 220
6.7 Acknowledgements . . . 220
6.8 References . . . 221

IV Concluding summary 227

7 General conclusions 229
7.1 Conclusions of the Part II . . . 229
7.2 Conclusions of the Part III . . . 231
7.3 Afterword . . . 232

"Kryten, you have a real gift. You make things that are really, really complicated sound really, really complicated."

— A.J. Rimmer

Part I

Introduction to geodynamical modelling

1 Analogue and numerical simulations

1.1 Introduction

Analogue and numerical modelling represent powerful tools in many fields including the physical sciences, natural sciences, engineering and others. Both approaches represent also an increasingly well established technique in geosciences. The employment of the analogue techniques in this branch is historically older but, as well as numerical modelling, is currently used to simulate a wide range of problems.

While analogue modelling employs mainly the principles of dynamic and kinematic similarity between the laboratory experiment and real natural situations (e.g Hubbert, 1937; Ramberg, 1981; Weijermars and Schmeling, 1986; Brun, 2002; Cagnard et al., 2006; Bajolet et al., 2012; Pastor-Galán et al., 2012; Bajolet et al., 2013; Strak and Schellart, 2014; Bajolet et al., 2015; Kettermann et al., 2016; Brune et al., 2017), numerical modelling involves algorithm based solutions to a discretized equation system, which describes the dynamics of the studied system, and physical properties of the materials (e.g. Podladchikov et al., 1993; Burg and Ford, 1997; Beaumont et al., 2001; Gerya et al., 2002; Beaumont et al., 2004; Duretz et al., 2011a; Tackley, 2012; Tackley et al., 2013; Gerya et al., 2015; Menant et al., 2016)(Fig. 1). In many current studies, both approaches to modelling are even combined and mutualy compared, given that an analogue model is simplified – marked by limited geometric or physical properties, and the numerical approach is first tested against the simplified analogue model and then further developed to involve the complex geometry, rheology, or a time scale of a given geodynamic process (e.g. Buiter et al., 2016; Schreurs et al., 2016; Warsitzka et al., 2017; Menant et al., 2016; Brune et al., 2017; Zwaan and Schreurs, 2017).

The output of the numerical modelling approach is a serie of a discrete model data, either in the form of point values (pressure, temperature, density, viscosity, etc) or fields (velocity, strain(-rate), potential energy, volume changes, integral or average values of temperature, pressure, etc.).

The analysis of analogue models is generally more complex than analysis of numerical models, since it is usually not possible to obtain all of the physical parameter data at selected points of the model domain. Thus, finite model state has been historically studied in orthogonal section views or topographical views of the model surface, while the inner dynamics and structures were roughly reconstructed from only a few cross-sections and time frames. In addition, quantification of the deformation typically required manual calculations of the strain from changes of the angles and distances between the material marker lines (e.g. square grids at the model surface). However, with the development of digital imaging equipment and the growing potential of computing, nowadays, it is possible to accurately calculate the velocity and strain fields using the PIV (Particle Image Velocimetry) or DPIV (Digital Particle Image Velocimetry) methods in a documented areas of the model (e.g.

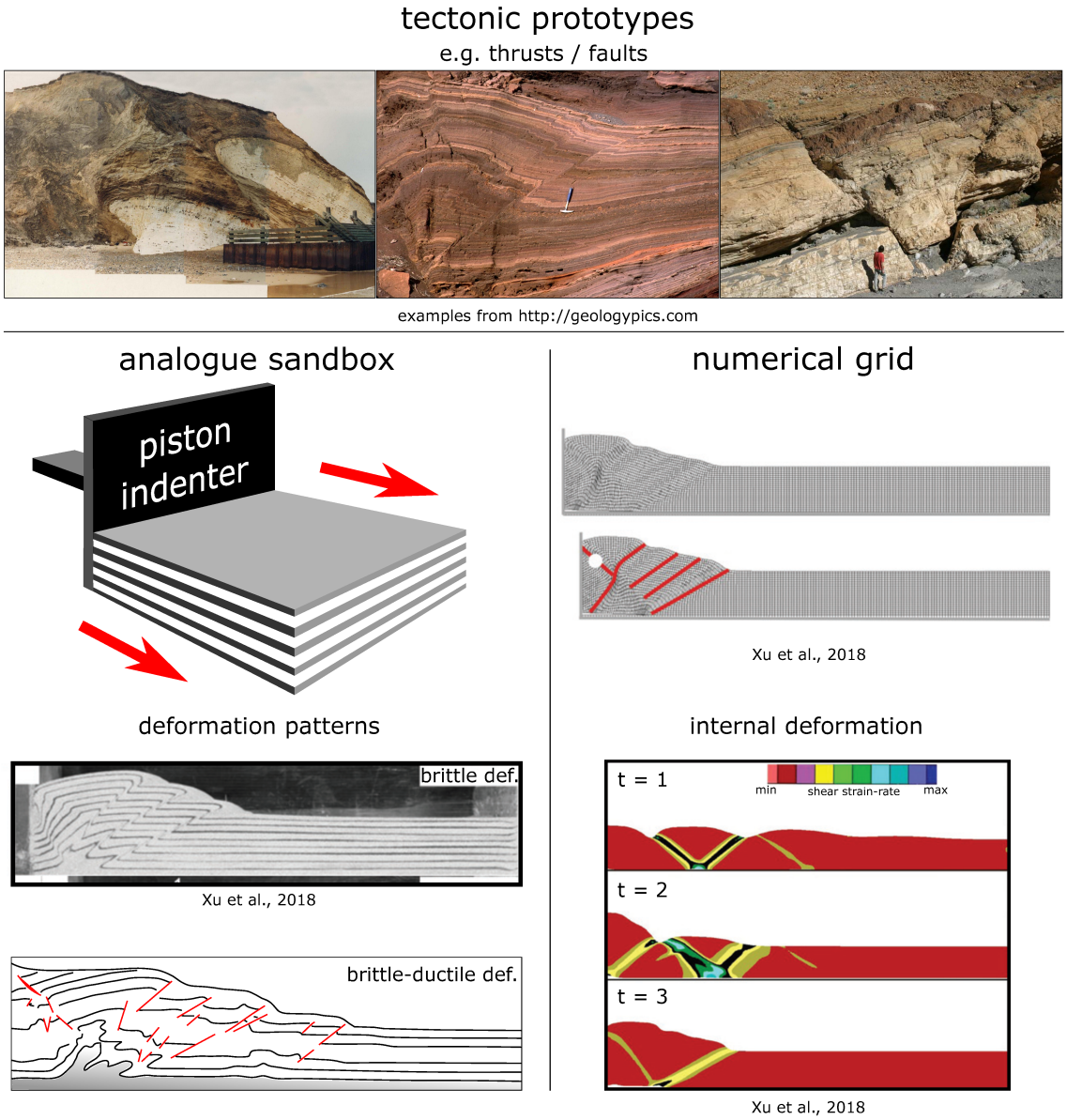


Fig. 1: Examples of analogue and numerical modelling results in geology. The model domain is prepared with respect to the natural situation (e.g. thrusting, faulting, shearing, folding etc.) and employing the analogue materials (in the case of physical models) or implemented by physical equations, coded in a computer software platform. In the analogue sandbox, the prepared model domain is progressively physically deformed while in the numerical grid domain, all deformation features are derived from the calculated velocity field according to a prescribed and discretized differential equations. Examples and comparison of both approaches are presented e.g. by Xu et al. (2018).

Strak and Schellart, 2014; Boutelier, 2016). The topography or the internal structure of the model can be also reconstructed using the photogrammetric methods (e.g. Galland et al., 2016), or X-ray tomography (e.g. Colletta et al., 1991; Pastor-Galán et al., 2012; Graveleau et al., 2012; Adam et al., 2013).

The brief introductory part summarizes the historical development of both modeling approaches, together with their philosophy, principles, applications and future potential.

1.2 Brief history and advances in analogue modelling

The history of analogue modeling is older than the numerical approach and dates back to the early 19th century. One of the first modellers in geosciences was James Hall, who was interested in fold systems (that he produced in a simple compression apparatus by compressing layers of clay), lava flows, or layered sequences and their geometric relationship with granitic bodies (Hall, 1812; Hall, 1805 and Hall 1815). These early works of James Hall are described in detail by Giorgio Ranalli (Ranalli, 2001). The studies of modelling of geological structures that followed in the rest of the century were mainly focused to the study of the fractures, faults, thrusts or folds (e.g. Favre, 1878a, Favre, 1878b, Daubre, 1879, Schardt, 1884, Cadell, 1889, Willis, 1893). Since the beginning of the 20th century, the range of problems addressed by this technique greatly expanded. and comprised the local deformation events associated with brittle and ductile tectonics and regional geodynamic processes including, for example, large-scale folding (e.g. Mead, 1920; Ramberg, 1964), thrusting and normal faulting (e.g. Hubbert, 1951), salt tectonics or formation of diapiric structures (e.g. Escher and Kuenen, 1929; Parker and McDowell, 1955; Berner et al., 1972), fracturing (e.g. Cloos, 1955), orogenesis (e.g. Kuenen, 1936), mantle flow (e.g. Griggs, 1939), boudinage and plutonism (e.g. Ramberg, 1955; Ramberg, 1970) and development of mantle plumes (e.g. Whitehead and Luther, 1975). Proto-subduction (e.g. Kuenen, 1936) has also been studied in the pre-plate tectonics era, and since the 1960s, more and more extensive regional models associated with divergent interfaces and rifting (e.g. Benes and Davy, 1996; Corti et al., 2003) have been also involved in an increasing number of studies. Another group of studies investigated the strain development during transform and transcurrent motion along discrete interfaces (e.g. Dauteuil and Mart, 1998), advanced models of convergent zones (including collision and indentation tectonics) (e.q. Tapponnier et al., 1982, Davy and Cobbold, 1988) and subduction of the lithosphere (e.q. Jacoby, 1973).

A more detailed list of the works and a review related to the analogue modelling over the past century was compiled by Schellart and Strak (2016) or Koyi (1997). Various examples of the application of analogue modelling to geodynamic problems are shown in (Fig. 2).

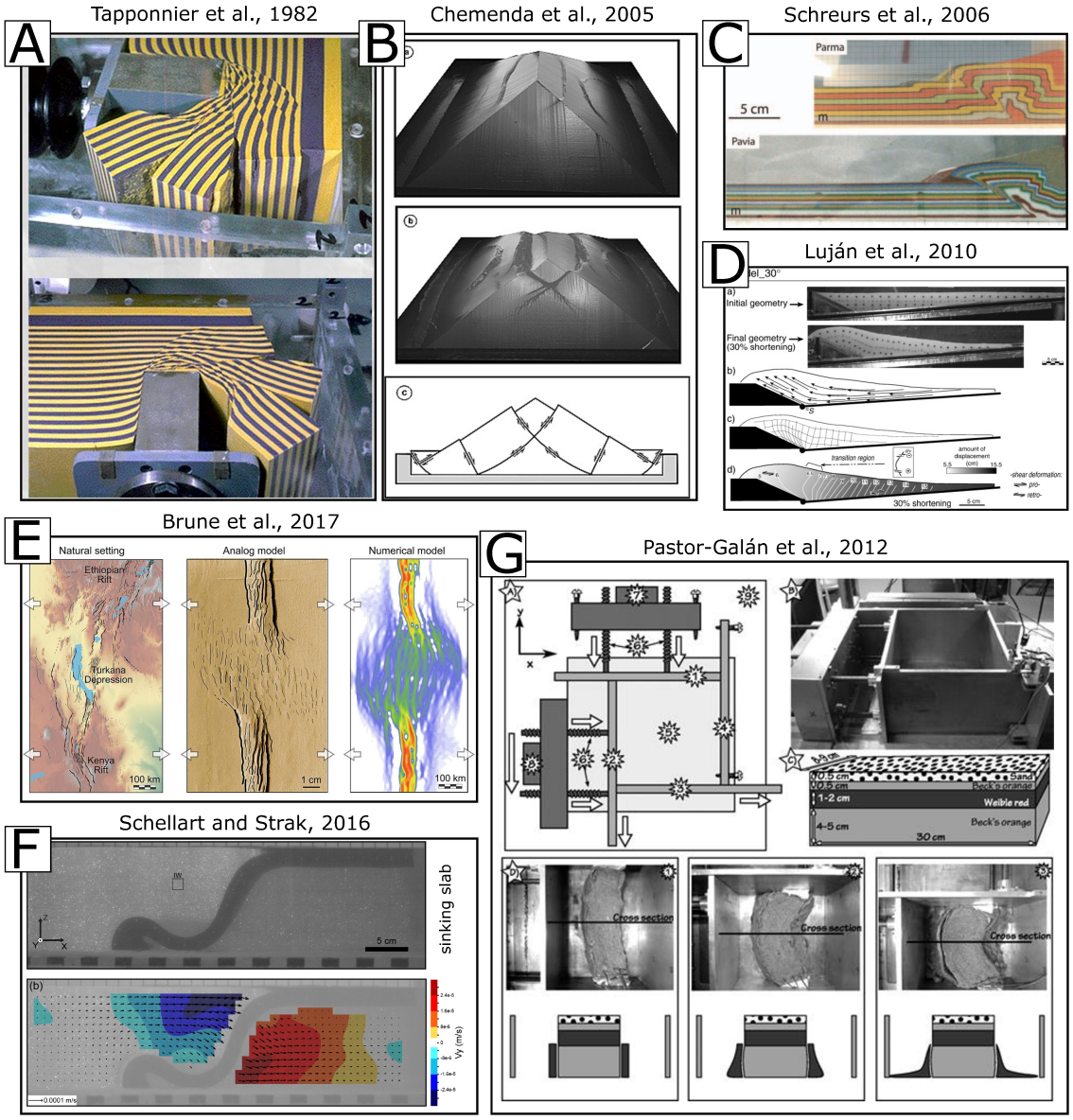


Fig. 2: Examples of analogue modelling of various geodynamical problems. From upper-left corner: (A) the indentation of the Indian plate in to the Euro-Asian plate (Tapponier et al., 1982); (B) deeply seated landslides under artificial gravitational acceleration (Chemenda et al., 2005); (C) the development of brittle thrust wedges (Schreurs et al., 2006); (D) the study of flow trajectories in viscous orogenic wedges (Luján et al., 2010); (E) centrifuge modeling of rifting in a lithosphere with inherited extension structures (Brune et al., 2017); (F) models of slab subduction and associated asthenospheric flow (Schellart and Strak, 2016) and (G) modelling of oroclinal buckling (Pastor-Galán et al., 2012).

1.3 Scaling of the analogue models

In 1937, M. K. Hubbert introduced a theory describing the principle of scaling analogue models with respect to a corresponding natural pattern - "prototype" (Hubbert, 1937). The geometric, kinematic and dynamic similarity between the model and the prototype is judged based on the analysis of acting forces, principal stresses, strains and rheological properties (elastic, viscous, plastic and brittle deformations or their combinations), for the model and prototype, respectively.

For geometric similarity, it must be true that the individual angles between surfaces in the deformed body of the prototype and the model are similar, while for the lengths, only the proportionality is necessary (e.g. Koyi, 1997). Relations between the length of the model and length of the prototype is:

$$\frac{l_n^m}{l_n^p}, \quad for \quad (n = 1, 2, 3..), \tag{1.1}$$

where l^m and l^p are the length of the model line or natural body line, respectively. For each n this ratio has to be identical and equality of angles between the lines must be guaranteed:

$$\alpha_n^p = \alpha_n^m, \quad \text{for} \quad (1, 2, 3..). \tag{1.2}$$

Another important scaling factor is the kinematic similarity, which is conditioned by geometric similarity and is proportional to the dimension of time (duration) required for development of the model and prototype, respectively. The time and relative linear velocities in the model, can then be determined by the following relationships (e.g. Hubbert, 1937 or Schellart and Strak, 2016):

$$\frac{t_n^m}{t_n^p}, \quad \text{for} \quad (1, 2, 3..), \tag{1.3}$$

$$v_p = v_m \frac{l^p t^m}{l^m t^p}. \tag{1.4}$$

Again, the ratio between model and prototype must be attained for all times n for these expressions.

Dynamic similarity is based on both geometric and kinematic similarity between the model and natural prototype. Here, the proportionality between forces acting on any point of the model and the real environment are considered. These forces are F_g (gravitational force), F_v (viscous force), F_p (tensile or compressive force), F_f

(frictional force) and possibly others (F_n). As in the previous case of geometric and kinematic similarity, have to be true that:

$$\frac{F_g^m}{F_g^p} = \frac{F_v^m}{F_v^p} = \frac{F_p^m}{F_p^p} = \frac{F_f^m}{F_f^p} = \frac{F_n^m}{F_n^p}, \tag{1.5}$$

wherein further (based on Cauchy equation of motion (Acheson, 1990) and Stokes' law (Stokes, 1851)) the following applies:

$$\frac{F^m}{F^p} = \frac{\rho^m (l^m)^3}{\rho^p (l^p)^3} = \frac{\Delta\rho^m (l^m)^3}{\Delta\rho^p (l^p)^3} \tag{1.6}$$

Here ρ is the density and for Earth's conditions is $g^m = g^p$.

1.3.1 Materials and rheology

A great variety of analogue materials can be used for analogue modelling, depending on the desired rheological properties (Fig. 3; Fig. 4) and the geometry of the prototype. Among the most widely used materials employed for tectonic analogue models of the upper crust and its brittle deformation are quartz sand (Fontainebleau sand) (Li, et al., 2013), glass microspheres (Schellart and Strak, 2016) or feldspar powder (Agostini et al, 2009). The scaling for the upper crustal strength is based on Byerlee's law (Byerlee, 1978), and for differential stress it can be expressed from the difference of maximum and minimum principal stress (Ranalli, 2000, Cagnard et al., 2006):

$$\sigma_1 - \sigma_3 = \frac{[2\mu\rho g z(1-\lambda) + 2S]}{[(\mu^2+1)^{1/2} - \mu]}, \tag{1.7}$$

where μ is the friction coefficient, ρ is the density, g is the gravitational acceleration, z is the thickness of the layer which is affected by brittle deformation, λ is the pore fluid factor and S is the cohesion factor of the used analogue material (specifically negligible for Fontainebleau sand).

The ductile deformation of the lower lithosphere includes several different subclasses of rheological models (Fig. 3), depending on the type of used material. These models combine elastic (transition to brittle deformation of the upper crust), plastic and viscous behavior of the material (Fig. 4) and are a prerequisite for a complex flow and deformation in the Earth's lithosphere. In the models that are associated with multi-layered domains (e.g. the upper and lower crust or salt and sedimentary cover - e.g. Brun, 2002; Brun and Fort, 2004) silicone putties are usually used for

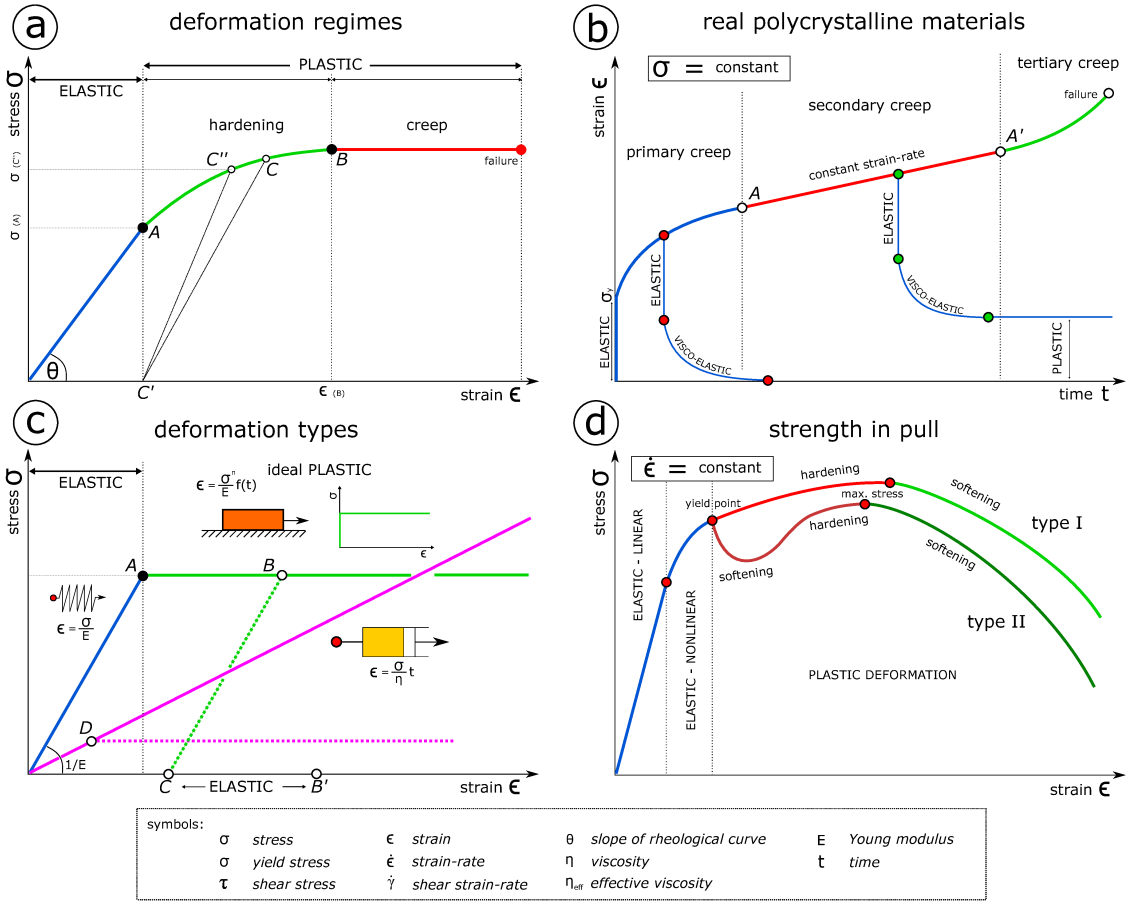


Fig. 3: Rheological relations and deformation regimes. Diagram (a) displays strain-stress relationship for polycrystalline rocks. The three elementary mechanical behavior regimes are characterized by elasto-visco-plastic deformation. A corresponds to the yield stress and change between elastic and plastic deformation, B-C segment represents hardened material after decreasing and repeatedly increasing of the stress (C→C'→C" hysteresis), and C represents the initiation of the creep when material is deformed under constant pressure. Slope of the elastic curve segment θ is related with $1/E$ (inverse Young's modulus). Diagram (b) displays a strain evolution in polycrystalline materials under constant applied stress. Diagram (c) represents the general overview of the basic rheological models for elastic, plastic and viscous deformation. Diagram (d) represents the strain-stress evolution of the materials in pull regime under the constant strain-rate where type I and type II curves differ in the rapid decreasing of the strength typically for different types of a crystalline/polycrystalline material. Diagrams (a-c) are modified after http://www.geosci.usyd.edu.au/users/prey/Teaching/ACSGT/Module1/Mod1LectPract/ and diagram (d) is modified after https://physics.mff.cuni.cz/kfpp/skripta/kurz_fyziky_pro_DS/.

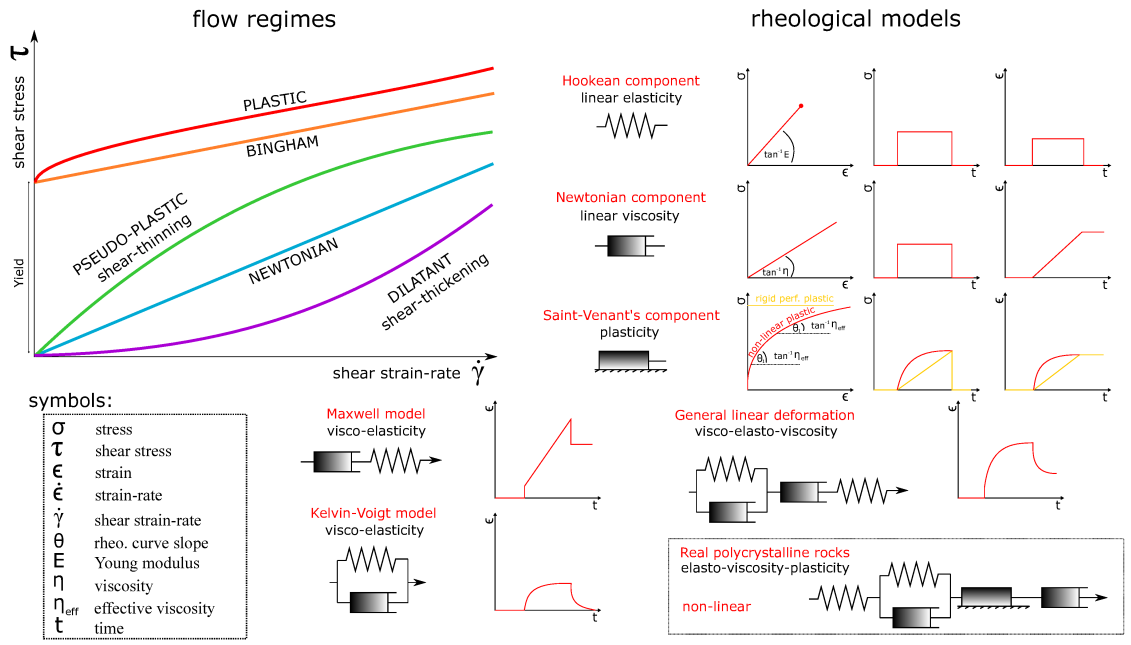


Fig. 4: Rheological models and flow regimes. The figure shows an overview of the general flow regimes in the shear-strain/stress diagram and the basic rheological models with basic interconnection to approximating the real rock behavior (strain-stress-time diagrams are modified after http://psgt.earth.lsa.umich.edu/PDF/2017/10_Lithosphere_2017.pdf).

ductile lower crust (Cagnard et al., 2006) and correspond to linear viscous Newtonian rheology. Ductile deformation (e.g. visco-plastic flow) of the more complex non-linear / power-law Non-Newtonian materials in the crust or mantle, can be alternatively simulated by plasticine (Pastor-Galán et al., 2012) or other materials undergoing the plastic (optionally viscous) deformation such as paraffine (Rossetti et al., 1999) or gelatine (visco-elasto-plastic deformation) (Kavanagh et al., 2013). Multi-layer models (that include e.g. the upper mantle and multilayered crust (e.g. Cagnard et al., 2006; Bajolet et al., 2015)) typically employ the same analogue material, only modified to match a specific density or viscosity for each successive layer. Thus, the correct scaling with respect to the prototype can still be justified, inspite of the fact that the linear and nonlinear rheology may not be appropriately scalable when used simultaneously in a single model. Different types of glucose syrups, glycerol solutions, heavy liquids etc are used for asthenosphere simulation (e.g. Mériaux et al., 2016, 2015; Schellart and Strak, 2016; Bajolet et al., 2015; Corti, 2012; Corti et al., 2003).

An overview of the relationships describing the visco-elasto-plastic deformation (including the viscous deformation and creep mechanisms, ductile flow or brittle deformation) can be found in Krýza (2013) or in Becker and Kaus, 2016; Ismail-Zadeh and Tackley (2010); Gerya (2009)

1.3.2 Scaling of a linear and non-linear rheology and flow properties

There are generally two approaches for scaling, depending on the rheological properties of employed analogue materials and dynamic properties of the flow. At geological time-scale and distances, the mechanism of viscous flow can be described by the creep relationship (e.g. Twiss and Moores, 2007):

$$\dot{\varepsilon} = A\sigma^n \exp\left(-\frac{E_A}{RT}\right), \tag{1.8}$$

where $\dot{\varepsilon}$ is the strain-rate, σ^n is the differential stress, E_A is the activation energy for creep, R is the Boltzman (gas) constant, T is the temperature and A is a material constant. Thus, linearly dependent strain (flux) can be scaled (e.q. Diffusion creep, Nabarro-Herring creep, Coble creep, where $n \sim 1$; Gerya, 2010) as well as non-linearly dependent strain (e.q. Dislocation creep, where $n > 1$).

To preserve the kinematic and dynamic similarity between the model and the prototype (see relations 1.3 - 1.6), it is necessary to match the parameters (dimensionless numbers) that control the equation of motion (Weijermars and Schmeling, 1986; Gerya, 2010) or derived equation of dynamics (Brun, 2002).

The equation of motion for a viscous medium (see subclass Navier-Stokes equations (e.q. Krýza, 2013)) can be expressed as follows (Weijermars and Schmeling, 1986):

$$\rho_0 \left(\frac{\partial v}{\partial t} + v \cdot \nabla v\right) = -\nabla p + \frac{\partial \tau_{ij}}{\partial x_j} + \rho g n_z, \tag{1.9}$$

where ρ is the density, v is the velocity, t is the time, p is the pressure, τ_{ij} is the shear stress, g is the gravitational acceleration and n_z is the unit vector along vertical direction. The driving parameters of the equation are following (Weijermars and Schmeling, 1986; Ramberg, 1981):

$$Re = \frac{vl\rho_0}{\eta}, \tag{1.10}$$

$$Sm = \frac{gl\rho_0}{\Delta p}, \tag{1.11}$$

$$St = \frac{l\Delta p}{\eta v}, \tag{1.12}$$

$$Rm = \frac{gl^2\rho_0}{\eta v}, \tag{1.13}$$

where $v, l, \rho, \eta, g, \Delta p$ are the velocity, length, density, viscosity, gravitational acceleration and pressure difference (Re: Reynolds number; Sm: Schmoluchowski number; St: Stokes number; Rm: Ramberg number). It can be shown that it is true that $Rm = S_t \cdot S_m$ and at the same time Re is extremely small for geological flows ($< 10-20$; Weijermars and Schmeling, 1986). Individual numbers can be interpreted as the following ratios: Re (inertia/viscous force), Sm (gravity/pressure gradient force), St (pressure gradient force/viscous force), Rm (gravity/viscous force).

So that the equation (1.9) becomes dimensionless and dimensionless variables can be used to characterize the relationship between the model and the prototype (linear rheology):

$$\begin{aligned}
\rho &= \rho'\rho_0, \\
r &= r'l, \\
t &= \frac{t'\eta_0}{\rho_0 gl}, \\
v &= \frac{v'\rho_0 gl^2}{\eta_0}, \\
\dot{e}_{ij} &= \frac{\dot{e}'_{ij}\rho_0 gl}{\eta_0}, \\
\tau_{ij} &= \tau'_{ij}\rho_0 gl, \\
p &= p'\rho_0 gl, \\
\nabla &= \nabla'/l, \\
\frac{\partial}{\partial t} &= \frac{\partial}{\partial t'}\frac{\rho_0 gl}{\eta_0},
\end{aligned} \tag{1.14}$$

where the scaling factor is marked by an apostrophe and scaling parameters are (l, ρ_0, η_0, g). These parameters express the dimensionless variables that can be substituted into the equation 1.9, which will change to:

$$\frac{gl^3\rho_0^2}{\eta_0^2}\left(\frac{\partial v'}{\partial t'} + v' \cdot \nabla' v'\right) = -\nabla' p' + \frac{\partial \tau'_{ij}}{\partial x'_j} + \rho' n_z, \tag{1.15}$$

where the scaling parameters are expressed on the left, while the right side shows dimensionless scaling factors. Since $Rm = St \cdot Sm$ and $Rm \cdot Re = gl^3\rho_0^2/\eta_0^2$ (or

$(Rm \cdot Re) \cdot L = R)$, it is possible to neglect the left side of equation (1.15) for $Re << 1$ and neglect the inertia forces (e.g. Buiter et al., 2016). Expression of dimensionless variables in the case of non-Newtonian viscous flow is following (eqs. 1.14 are the same as for the Newtonian flow):

$$\begin{aligned} t &= \frac{t'}{2^{n_0} A_0 l (lg\rho_0)^{n_0}}, \\ v &= v' 2^{n_0} A_0 l (lg\rho_0)^{n_0}, \\ \dot{e}_{ij} &= \dot{e}'_{ij} 2^{n_0} A_0 (lg\rho_0)^{n_0}, \\ \frac{\partial}{\partial t} &= \frac{\partial}{\partial t'} 2^{n_0} A_0 (lg\rho_0)^{n_0}, \end{aligned} \tag{1.16}$$

where A and n represent the material constant (empirically determined; e.g. by Carter, 1976; Kirby, 1983; Ranalli, 1997) and power of the non-linear behavior.

Based on the above relationships, the model can be directly scaled with respect to the real natural situation (prototype). The following relationships are given for both linear and non-linear viscous flow (Weijermars and Schmeling, 1986):

Linear

$$\begin{aligned} \rho_N &= \frac{\rho_{0N}}{\rho_{0M}} \rho_M, \\ r_N &= \frac{l_N}{l_M} r_M, \\ t_N &= \frac{\eta_{0N}}{\eta_{0M}} \left(\frac{\rho_{0M} g_M l_M}{\rho_{0N} g_N l_N} \right) t_M, \\ v_N &= \frac{\eta_{0M}}{\eta_{0N}} \left(\frac{\rho_{0N} g_N l_N^2}{\rho_{0M} g_M l_M^2} \right) t_M, \\ \dot{\gamma}_N &= \frac{\eta_{0M}}{\eta_{0N}} \left(\frac{\rho_{0N} g_N l_N}{\rho_{0M} g_M l_M} \right) \dot{\gamma}_M, \\ \tau_N &= \frac{\rho_{0N} g_N l_N}{\rho_{0M} g_M l_M} \tau_M, \\ p_N &= \frac{\rho_{0N} g_N l_N}{\rho_{0M} g_M l_M} p_M, \end{aligned} \tag{1.17a}$$

Non-linear

$$
\begin{aligned}
t_N &= \frac{A_{0M}}{A_{0N}} \left(\frac{\rho_{0M} g_M l_M}{\rho_{0N} g_N l_N} \right)^{n_{0M}} t_M, \\
v_N &= \frac{A_{0N}}{A_{0M}} \left(\frac{\rho_{0M} g_M l_M}{\rho_{0N} g_N l_N} \right)^{n_{0M}} \frac{l_N}{l_M} v_M, \\
\dot{\gamma}_N &= \frac{A_{0N}}{A_{0M}} \left(\frac{\rho_{0N} g_N l_N}{\rho_{0M} g_M l_M} \right)^{n_{0M}} \dot{\gamma}_M,
\end{aligned}
\tag{1.17b}
$$

where $\gamma = 2\dot{\varepsilon}$ is the engineering strain-rate.

The scaling laws, including local variations of scaling relationships in inhomogeneous media, are described in detail by Weijermars and Schmeling (1986). The scaling relationships for dynamic similarity between the model and prototype with conservation of the equation of dynamics was also analyzed by Brun (2002). The thermal scaling relationships in analogue models were developed by Katz et al. (2005), Rossetti et al (1999) or Cobbold and Jackson (1992).

1.3.3 Artificial gravitational field

In models, where the effect of gravity on a material flow is crucial, the gravitational acceleration must be scaled. Such models are typical, for example, for gravitational inversion of the Earth's crustal materials (e.g. Dixon and Summers, 1983; Acocella et al., 2000; Godin et al., 2011; Harris et al., 2012; Nikkilä et al., 2015; Faisal and Dixon, 2015) or mantle dynamics (Tentler, 2003; Connolly et al, 2009) in the form of diapirism or mantle plumes (Fig. 5a). The rheological properties of analogue materials, that are scaled for crustal-scale analogue models, are discussed e.g. by Waffle et al. (2016). Also, extensional tectonics modelling can be provided by simulated and scaled gravitational acceleration (e.g. Brune et al., 2017; Agostini et al., 2009, etc.) which is usually generated by a centrifuge (Fig. 5b). Another type of models allow to apply an artificial gravitational field applied to compressional apparatus used in centrifuge and to produce thrust faults or folds in combination with gravitational inversion (Liu and Dixon, 1990; Liu and Dixon, 1991; Dixon and Liu, 1992).

The magnitude of gravitational acceleration itself can be expressed as the relationship between the angular velocity ω, rotations per minute x and radial distance R between the element of the model domain and the rotational axis of the centrifuge:

$$
g_M = \omega^2 \cdot R \left(\frac{2\pi x}{60} \right)^2 R \quad [m/s]. \tag{1.18}
$$

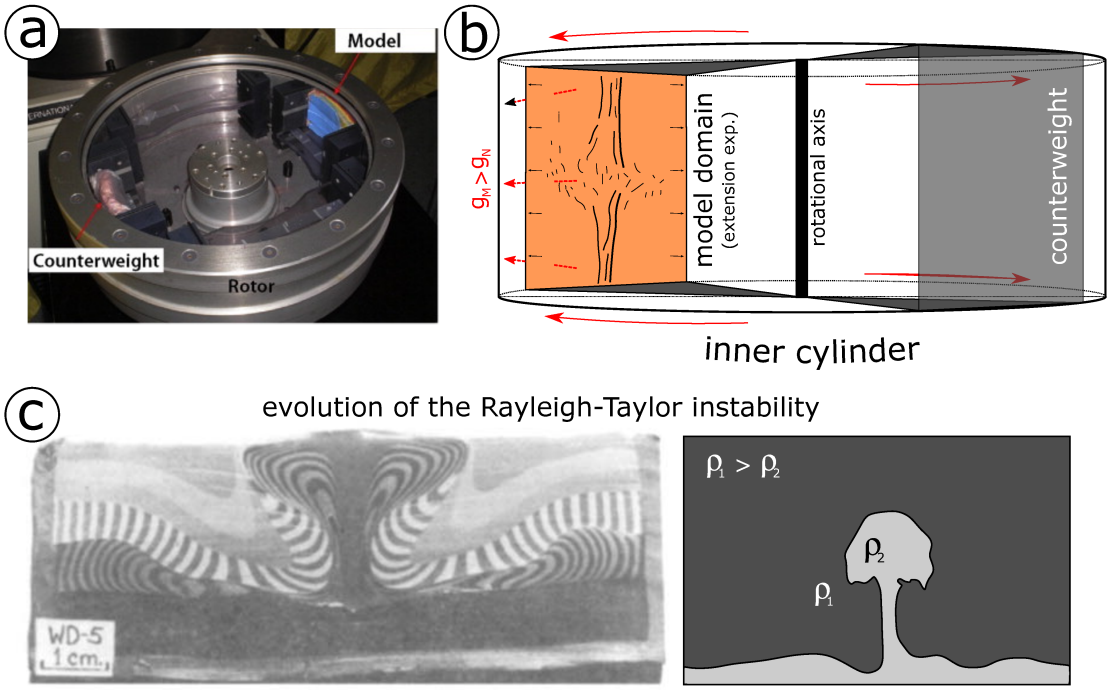


Fig. 5: Centrifuge modelling. Figure (a) displays the centrifuge device which is used for the geodynamical analogue modelling (taken from Harris et al., 2012). Schematic diagram(b) represents the principle of the centrifuge and simulation of the artificial gravitational field in the model domain (g_M). Example of the modelling with simulation of the Rayleigh-Taylor instability and gravitational inversion of the Earth's crust in the form of crustal-scale diapirs (*photo of the model is taken from Koyi (1997) according to experiments of Dixon (1974)*).

In this case, it should be noted that the Coriolis forces, which are insignificant in the case of solid-state flow of natural rock, also arise (Weijermars and Schmeling, 1986), however, they will play a significant role only for the low-viscosity models. Coriolis force damping effect of viscous forces is expressed by Taylor number (from equation of motion):

$$T_\alpha = \left(\frac{2\omega l^2 p_0}{\eta_0} \right)^2 . \tag{1.19}$$

For any solid-state flow in geological conditions, it is true that $Re << 1$ and $T_\alpha << 1$ (Weijermars and Schmeling, 1986). The second way to simulate greater gravity, for example in slope motion models (Nolesini et al., 2013),development of accretionary wedges (Luján et al., 2010; Graveleau et al., 2012) or salt bodies (e.g. Weijermars et al., 1993), may be scaled for the inclination of a plane, on which the model is placed. In this case, the hydrostatic pressure value will be $h_M \cdot \rho_M \cdot g$ and the force F_g will be expressed for the inclination $\alpha_M > \alpha_N$. However, this way is not

suitable for simulation of a material gravitational inversion such as e.g. formation and evolution of the Rayleigh-Taylor instabilities (Fig. 5c).

1.4 Recent analogue models of a large-scale mantle/lithosphere dynamics

During the last two decades, the technique and concepts of analogue models have advanced considerably allowing for simulation of more complex geodynamic processes. These models include both small scale processes (e.g. thrusting (Maillot and Koyi, 2006; Dotare et al., 2016), faulting (Mansfield and Cartwright; Corti et al., 2005), strike-slips (Rosas et al., 2015), water/magma/mud (channel-)flow (e.g. Mathieu et al., 2008; Mukherjee et al., 2012), pore fluid flow (Mourgues and Cobbold, 2016), erosion/sedimentation (Le Guerroué and Cobbold, 2006; Malavieille, 2010) etc.) and large-scale deformation of the lithosphere or mantle flow (e.g. subduction/rifting (Guillaume et al., 2009; Luth et al., 2010; Brune et al., 2017), salt diapirism (Warsitzka et al., 2013), mantle dynamics (Pysklywec and Cruden, 2004) and volcanic/magmatic processes (Martí et al., 2008; Gottsmann and Martí, 2011; Kavanagh et al., 2013)).

With the progressive development of photogrammetric methods and velocimetry (PIV), from the beginning of the 21st century, it is also possible to better quantify volume and surface changes and to obtain a deformation parameters based on $2D/3D$ velocity field (e.g. Adam et al., 2005). The implementation of these methods extends not only the possibility of deformation evaluation in the model domains, but also provides for higher scaling accuracy with respect to natural prototypes. For this reason, the application of the photogrammetry and the PIV is an integral part of this work.

1.5 Brief history and advances in the numerical geodynamic modelling

The beginning of approximate numerical methods in the broader sense can be dated back to the pre-Euclidean period. Simple methods for numerical solutions have also been widely used in ancient China and India. Compared to the ancient world, which was more concerned with the geometrical aspects of mathematics, the Asian-world scientists-philosophers dealt with algorithmization of calculations and the development of simple iterative numerical methods (e.g. Folta, 1988; Benzi, 2018 - online source).

During the modern history (from the 17th century), the ground for a more rigorous concept of numerical methods was gradually prepared as the infinitesimal mathematics developed. In connection with this period, we can mention a number of significant mathematicians who worked in the field of mathematical analysis

and contributed to the foundations of modern numerical analysis (Newton, Euler, Lagrange, Gauss, Jacobi, Chebyschev, etc.). These mathematicians were in most cases natural scientists, and the application of mathematics was therefore offered in a number of disciplines, especially the physical ones (e.g. astronomy, hydrodynamics or engineering related problems). One of the first problems solved is an example of Isaac Newton's work: searching for a curved line of a parabolic type that can pass through a given number of points (polynomial of the nth order) mentioned in Book III, Lemma V (Newton, 1687).

Later, at the beginning of the 20$^{\text{th}}$ century, there were already specialized publications dealing with the specific development of a numerical solution of a number of scientific and technical problems (e.g. Whittaker and Robinson, 1924; Cassinis, 1928 or Longley, 1932). During this period, computers or handhelds were still not available for complex calculations and each computation is provided by hand calculations, slide rulers, desk calculators, electro-mechanical and other analogue devices (history can be found in Goldstine, 2012). The first computerized calculations were performed roughly between the 1930s and 1950s (Goldstine, 1980).

Modern numerical analysis was based on the concept of the Finite Difference Method (FDM) (Richardson, 1911; Courant and Lewy, 1928) developed during the 1960's -70's years, and contemporaneous with the development of the theory of plate tectonics. This revolution in geosciences was accompanied by definition of a range of new geodynamic problems (e.g. subduction models, models of the thermal and chemical mantle convection, a gravitational inversion of the crust etc.). The second major method which has been developed since the 1940's is the Finite Element Method (FEM) (e.g. Courant, 1943). This method is particularly suitable for the solution of partial differential equations in geometrically complex numerical domains. Development of this method marks the period of 1950 - 1970 and soon became another very important approach, widely used in geodynamics (from modelling of processes in the Earth's core, through the mantle and lithosphere dynamics to sedimentary processes).

From the beginning of the 70's until the end of the 1980, the most significant works representing the FDM and FEM calculations are following (list modified after Gerya, 2009):

- **1970:** *First 2D numerical models of subduction* (Minear and Toksoz, 1970). Purely thermal subduction model with prescribed corresponding velocity field (downgoing slab inclined at 45°).

- **1971:** *First 2D mantle thermal convection models* (Torrance and Turcotte, 1971). Possible implications for mantle convection with temperature-dependent viscosity for continental drift. Thermomechanical models based on the stream function formulation for the mechanical part were explored.

- **1972, 1978:** *First 2D numerical (FEM) models of salt dome dynamics* (Berner et al., 1972; Woidt, 1978). Until that moment, the geodynamic analogue modelling and analytical solutions were employed to investigate crustal diapirism only. Paper by Woidt (1978) discussed inconsistency of the numerical approach used by Berner et al. (1972).

- **1977-1980:** *First 2D mantle thermo-chemical convection modelling* (Keondzhyan and Monin, 1977, 1980). A binary stratified medium used to study the effects of compositional layering on mantle convection.

- **1978:** *First numerical models of continental collision* (Daignieres et al., 1978; Bird, 1978). Mechanical models exploring the finite-element approach.

- **1985-1986:** *First 3D spherical mantle convection models* (Baumgardner, 1985; Machetel et al., 1986). This first 3D models were spherical and not Cartesian.

- **1988:** *First 3D Cartesian mantle convection models* (Cserepes et al., 1988; Houseman, 1988).

With increasing computational potential, numerical modelling is nowadays a common part of complex geodynamic studies with wide application in plate tectonics. Key recent numerical models in the area of mantle and lithosphere dynamics and convergent tectonics will be discussed in appropriate chapters and sections.

1.6 Numerical solution and governing equations

The principle of a numerical approach is to solve an ordinary differential equation (ODE) or a partial differential equation (PDE) at discrete spatial distances or time steps. Thus, the solution is not a continuous analytical function, but a discrete function with a specific value at a particular space-time point, sharply separated from the surrounding space without an infinitesimal transition to the next point value. This approach is appropriate for very complex domains of interest where the key equations are addressed for 2D / 3D space with multiple boundary conditions and environmental properties (complex rheological models, complex heat transfer between subdomains, etc.) - as well as for equations whose analytical solution is nontrivial or is not possible to find it in reasonable time. In geoscience (geodynamic modelling), mainly the three governing equations are important: 1. Continuity equation (mass conservation); 2. Equations of motion (conservation of momentum); 3. Heat transfer equation (energy conservation).

1.6.1 Continuity equation

The continuity equation expresses the preservation of a quantity in a particular space-time element or volume. The basic derivation uses the divergence theorem (Gauss theorem):

$$\oint_{\Omega} \mathbf{A} \cdot \mathrm{d}\mathbf{S} = \int_{V} (\nabla \cdot \mathbf{A}) \mathrm{d}V, \tag{1.20}$$

where Ω is an enclosed surface which surrounds the volume V and which is oriented by the exterior normal vector $\mathrm{d}\mathbf{S} = \mathbf{n}\mathrm{d}S$ ($\mathbf{n}$ is the unit vector of the external normal vector), $\mathbf{A}$ is the vector field and ∇ is the nabla operator. The relation 1.20 expresses equality between the vector flux ($\mathbf{A}$) over the closed area and the volumetric integral of the vector $\mathbf{A}$ divergence (the flow across the boundary is equal to the sum of resources and sinks). This relationship can be used for scalar, vector and tensor quantities.

The continuity equation itself (derivation is possible to find e.g. in Krýza (2013)) then can be expressed in the Euler formulation (the point in the reference frame is fixed against the mobile environment) or in Lagrange formulation (the point of the mobile environment moves relative to the static reference frame). Both formulations of the continuity equation can be expressed (e.g. for density) as follows (e.g. Gerya, 2010):

Eulerian

$$\frac{\partial \rho}{\partial t} + \nabla \cdot (\rho \vec{v}) = 0, \tag{1.21}$$

Lagrangian

$$\frac{D\rho}{Dt} + \rho \nabla \cdot \vec{v} = 0, \tag{1.22}$$

where ρ is the density, $\vec{v}$ is the velocity and $\frac{D\rho}{Dt}$ is the material (Lagrange) derivative.

1.6.2 Momentum equation

The momentum conservation expresses the balance between the external and internal forces acting on a medium or body (continuum) in the gravitational field given by g. The effect and imbalance of these forces leads to the continuum deformation which can be described, for example, by Navier-Stokes equations for compressible or incompressible fluids. These equations are derived from the momentum equation by

the relationship between the total stress (σ_{ij}) and deviatoric stress (σ'_{ij}) (e.g. Gerya, 2010; derivation is also possible to find in Ismail-Zadeh and Tackley (2010) or Krýza (2013)). The conservation of angular momentum itself can be expressed as follows (Lagrangian form):

$$\frac{\partial \sigma_{ij}}{\partial x_j} + \rho g_i = \rho \frac{D v_i}{D t}. \tag{1.23}$$

Then the Navier-Stokes equations can be expressed from Cauchy momentum equation which contains the deviatoric stress tensor and pressure gradient:

$$\frac{\partial \sigma'_{ij}}{\partial x_j} - \frac{\partial P}{\partial x_i} + \rho g_i = \rho \frac{D v_i}{D t}, \tag{1.24}$$

where P is the pressure (for the hydrostatic pressure is: $P = 1/3(xx + yy + zz)$). The Navier-Stokes momentum equation is then expressed as follows (convective formulation for compressible fluid):

$$\rho \frac{D\vec{v}}{Dt} = -\nabla \bar{p} + \mu \nabla^2 \vec{v} + \frac{1}{3}\mu \nabla(\nabla \cdot \vec{v}) + \rho g, \tag{1.25}$$

where ρ is the density of the fluid, μ is the fluid viscosity, $\vec{v}$ is the velocity and g is the gravitational acceleration.

1.6.3 Heat transfer equation

Another crucial equation is the heat transfer equation describing systems that include all known heat transfer mechanisms in the geological environment (advection, convection, conduction, radiation). In the integral form of the equation, it expresses the law of conservation of energy or the rate of change of energy E in the fixed volume of mass V. This change is equal to the sum of the work at the S boundary, the work produced by the external force F in a certain volume V, minus the heat which is transported internally by thermal conduction and convection, plus other heat sources (e.g. radiogenic heating, latent heat etc.). The equation can be written as follows (Ismail-Zadeh and Tackley, 2010):

$$\frac{\partial}{\partial t}\int_V \rho E \mathrm{d}\tau = \int_S v_i \sigma_{ij} \mathrm{d}S_j + \int_V \rho v_i F_i \mathrm{d}\tau - \int_S k \frac{\partial T}{\partial x_j} \mathrm{d}S_j - \int_S \rho E v_j \mathrm{d}S_j + \int_V \rho H \mathrm{d}\tau, \tag{1.26}$$

where t is the time, v is the velocity, T is the temperature, k is the conduction coefficient and H represents a heat sources (rate of the heat production, respectively).

The equation 1.26 can also be expressed in a differential form (Gerya, 2010) including the source terms H:

$$\rho C_P \frac{DT}{Dt} = -\frac{\partial q_i}{\partial x_i} + \sigma'_{ij} : \dot{\varepsilon}'_{ij} + T\alpha \frac{DP}{Dt} + H_L + H_r \tag{1.27}$$

where C_P is the heat capacity under the constant pressure, q is the heat flux (Fourier law), σ' is the deviatoric part of the stress tensor, $\dot{\varepsilon}'$ is the deviatoric part of the strain-rate tensor, P is the pressure and : is the double dot product symbol. The members on the right side of the equation represent (from the left) thermal conduction and heat sources such as: shear heating, adiabatic heating, latent heating (H_L) and radioactive heat production (H_r).

In addition to the conservation laws outlined above, other relationships relevant to a particular model situation, such as the isostatic compensation, erosion, sedimentation, phase transitions, chemical reactions, tidal effects or complex rheological models, play an important role (these model specifications were already described in Krýza (2013) and will not be described in detail in this thesis).

1.6.4 Numerical methods

In recent numerical mathematics, a large number of computational methods is available for a numerical solution of various types of partial differential equations. After designing the mathematical model which describe the specific area of interest, it is necessary to choose the most appropriate computational procedure. This method takes into account the geometry of the studied domain (and development of the convenient numerical grid) as well as optimized calculation of specific governing equations for current problem (Fig. 6).

Several different classes of numerical methods were developed, such as the Finite Difference Method (FDM)(e.g. Gerya, 2009; Grossmann et al., 2007), the Finite Element Method (FEM)(e.g. Becker and Kaus, 2016; Ismail-Zadeh and Tackley, 2010; Logan, 2011), the Finite Volume Method (FVM)(e.g. Ismail-Zadeh and Tackley, 2010; LeVeque, 2002; Eymard et al., 2000), spectral methods (e.g. Ismail-Zadeh and Tackley, 2010; Canuto et al., 2006), the Distinct Element Method (DEM)(e.g. Radjaï and Dubois, 2011; Munjiza, 2004), The Lattice Boltzmann Methods (LBM)(e.g. Mora and Yuen, 2017; Aharonov and Rothman, 1993) or the Numerical Manifold Method (NMM)(e.g. Wu and Wong, 2011; Ma et al., 2010). A short overview including applications and main advantages of these methods will be presented below.

FDM

The Finite Difference Method is one of the oldest numerical methods using a rectangular Eulerian grid. This approach using finite difference as direct approximation

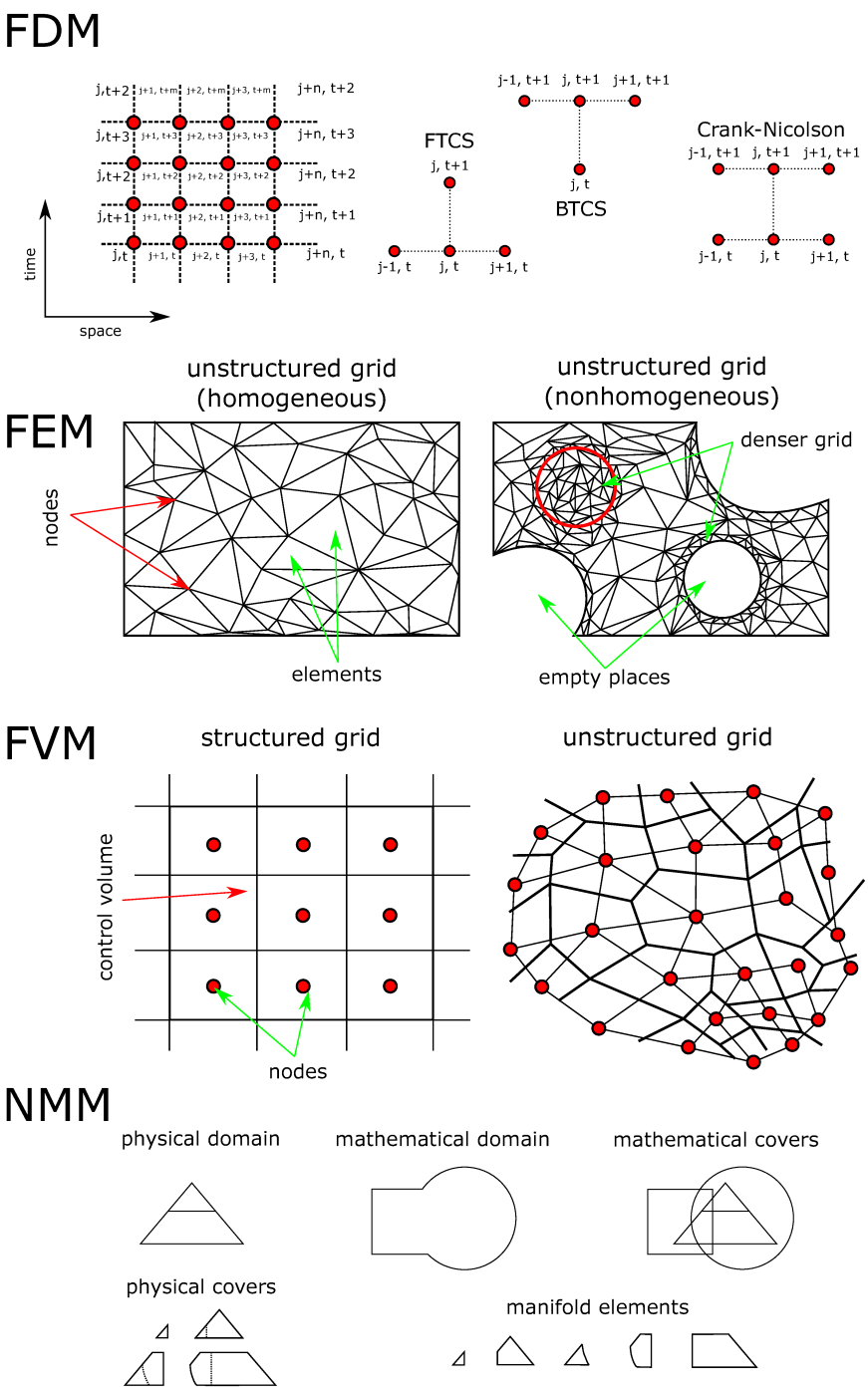


Fig. 6: Examples of the numerical grids for selected numerical methods. *The FVM grid scheme is modified after Ismail-Zadeh and Tackley (2010). The NMM domains and components are redrawn from Ma et al. (2010).*

and discretization of the differential equation. Each grid node then represents one finite difference member (respective derivative) from the series of the other differences that cover the whole model domain in a current time-step (Fig. 6). Discretization of the equation and the substitution of the derivatives by finite differences leads to the recurrent Euler scheme where a substituted system of algebraic equations is solved (Euler, 1768).

Generally, three basic calculation concepts are defined for algorithmization and determination of the finite differences (Fig. 6): 1. The explicit scheme - FTCS (Forward-Time Central-Space); 2. The implicit scheme - BTCS (Backward-Time Central-Space); 3. Crank-Nicolson scheme (combination of FTCS and BTCS schemes). The FTCS scheme represents the approach where the difference at the certain time t_n and second-order central space difference is used for calculation of the differences in t_{n-1} while BTCS scheme analogously using backward difference (i.e. the central space and time differences are expressed at t_{n-1} from differences at time t_n). For the FTCS scheme, the numerical stability (expressed by number of the numerical errors) is smaller than for BTCS scheme which is always numerically stable (BTCS scheme does not require any pre-condition for stability) and convergent. Numerical errors are proportional to the size of the time-step (linear over the time-step for the BTCS) and quadratically proportional to the space-step in both approaches. The Crank-Nicolson scheme is also always stable and convergent and both, time and space steps, are quadratic (Recktenwald, 2004).

FEM

The Finite Element Method represents one of the most common methods for solution of partial differential equations in wide spectra of computational applications. In contrast to the FEM, this method is not aimed to direct approximation of the system of the PDE. The core of the method is to convert the equation solution to the variational problem and to integrate the PDE in the whole model domain. The geometrically complex domain (Fig. 6) is divided into system of sub-domains (the finite elements) and solution of the PDE is substituted and approximated by polynomial function (contributed weight function) on each element. The set of these functions smoothly cover whole model domain and kind of their interlink determines the appropriate degree of local smoothness over the entire domain. The individual functions from each element then contribute to the variational integral. The resultant set of algebraic equations giving the approximate finite solution (in contrast to infinitesimal partial differential equation) as similar as in the FDM. In contrast to the FDM the discretization leads to approximate solution which is known in the form of polynomial functions and not set of isolated points.

For solutions where the advection transport of the material plays a key role, the Particle-In-Cell method is often employed together with the FEM (e.g. Wang et al., 2015). A similar approach is covered by implementation of the Marker-In-Cell method for FDM (e.g. Gerya and Yuen, 2003; Duretz et al., 2011b) where several

factors are achieved by this technique, such as: 1. conservation of the stresses under conditions involving sharply discontinuous viscosity distribution; 2. heat and chemical composition conservation (non-linear transport coefficients, sharply variable conductivity or thermal gradients, etc); 3. Conservation of the scalar quantities with multiscale properties - e.g. thermal properties (thermal field), pressure properties, density in flows with strong advection (Gerya and Yuen, 2003).

FVM

The Finite Volume Method, which is also commonly used in geodynamic modelling, is similar to the FEM. The principle of the method is similar as in the case of the FEM but rather then elements, weight functions and variational integral, multiple control sub-volumes (Fig. 6) are used for discretization of the current equation. This equation is then integrated over each control volume where the volume integrals are converted to the surface integrals by using the divergence theorem (Gauss-Ostrogradsky Theorem)(e.g. Katz, 1979). Discretized equation then compare and equates the fluxes through control volumes respective to sources and sinks (divergence theorem) inside the current control volume. The solution of a discretized equation follows some of the standard methods for direct or iterative solution of the system of algebraic equations. This method can be easily used for unstructured grids as well as for regular Eulerian grids and thus the FVM combines advantages of both previously described methods (FDM and FEM).

Spectral methods

A principle of the spectral methods is similar to the FEM and FDM. However, in contrast to the FEM, FDM and FVM, the spectral methods using variables that are expanded as a sum of orthogonal global basis functions that are typically polynomial or trigonometric (nonzero basis functions through whole volume than in discrete element). The advantage of this method is that the convergence of the calculations is faster than for the above mentioned methods (spatial methods). High mathematical accuracy can be achieved for various spectra of models with simplified and smooth material and geometrical properties. This is provided by global prescription of the representative basis functions (that are local for spatial methods). These basis functions are typically different along prime directions - horizontal (azimuthal) and vertical (radial) - with respect to the differences in boundary conditions (e.g. periodicity of the side space boundary condition). As the basis functions can be easily used spherical harmonics and methods then became to be suitable for calculations of the problems defined in spherical geometry. The main disadvantage of this method is that for geometrically complicated domains, where sharp interfaces between material properties are implemented (sharp gradients are involved), the accuracy can rapidly decrease (Ismail-Zadeh and Tackley, 2010).

DEM

The Distinct Element Methods (or Discrete Element Methods) are characterized by using a large amount of discrete small particles that interact and simulate the effect of flow motion. The family of these methods is often used for geometrically complex model domains. However, rather than for complex rheological properties (combination of creeps and thermal flows) of the studied systems, the method is used to study granular flows and rock mechanics with more or less uniform composition. The advantage is that the method is well-designed to study brittle deformation (as development and propagation of joints, tears, faults, thrusts etc.) which is more difficult to approximate in the above mentioned methods. The starting point for implementation of the mentioned factors represents a combination of the DEM with the FEM (combined finite-discrete element method)(e.g. Lewis et al., 2005 or Gethin et al., 2006). The main disadvantage is that the method strongly depends on the amount of used particles and computational power (complex flows need to be simulated on computer clusters). Another disadvantage represents the complicated simulation of complex heat transfer in complicated domains where Lattice Boltzmann Method promises a more suitable approach.

LBM

The Lattice Boltzmann Method represents a relatively new technique for numerical simulations in computational fluid mechanics and geosciences. The principle of the method is to use a discrete mesh of fictitious particles that interact in sequential alternation of collision and streaming steps. Methods using a lattice Boltzmann equation apply discrete-velocity Boltzmann equations where the number of particles is decreased and the particles are confined by nodes of a lattice. The calculations of fluid density evolutions in current time and space coordinates produces multiple density components that are equal to the number of lattice vectors that are connected to each lattice point (Bao and Meskas, 2011).

The advantage of the method is that it is suitable for complex boundaries, geometries and porous media (and multiphase flows). Also the method is well designed to solve flow coupled with heat transfer and chemical reactions and can be effectively run on parallel architectures (parallel computing for large simulations). The main disadvantage and limitations are unduly small time steps for very small flows and potential errors related to artificial compressibility when the incompressible Navier-Stokes equations are solved (Bao and Meskas, 2011).

NMM

The Numerical Manifold Method is a relatively newly developed technique with applications mainly in modelling of strongly discontinuous features such as joints, faults, cracks etc (Zhang et al., 2010; Zhang et al., 1999; Ma et al., 2010).

Unlike FEM, where the model domain is divided into a set of elements (Fig. 6)(with a fixed number of nodes and vertices) and polynomial functions are used to establish unknown variables in an unknown field (by interpolation points and sets of algebraic equations), the approach of the NMM is based on physical and mathematical covers of the model domain with implementation of numerical manifolds. The method defines the physical domain (where an aimed physical problem is defined), mathematical domain (union of a finite number of patches - with potential to partly or totally overlap to each other - dividing the physical domain), mathematical cover (defined patches), physical covers (intersections of mathematical covers and physical domain) and manifold elements (defined as regions shared by several physical covers). The weight functions are formulated using an individual manifolds covering physical domain. Derivation of a weak form of governing equations then using the principle of virtual work and NMN interpolations are defined for each manifold. The discretized equations using element matrices that are assembled to form the system matrices based on the physical cover manifold topology. Similarly as in the FEM, the integration scheme uses individual elements. The manifolds represent general polygons (generalized shape of elements) that can be partitioned into variations of several triangles (depending on shape complexity) and integration scheme follows specific formulations using differential geometry relations. Generally, the FEM represents a special case of the FEM (Ma et al., 2010).

The overview of the numerical modelling components such as development of a Mathematical model, setting of the coordinate system, selection of a discretization method, numerical grid or convergence, stability and consistency criteria is described by Ismail-Zadeh and Tackley (2010).

The convergent and collisional tectonics represents complicated component of Earth dynamics which is associated with complex heat and material transfer. The regional scale models of the last decade revealed how various parameters (such as rheology, plate convergence rate, dip of subduction, geometry etc.) can affect specific heat and material distribution, phase processes, stress and deformation localization and P-T-t-d conditions (e.g. Podladchikov et al., 1993; Burg and Ford, 1997; Beaumont et al., 2001; Gerya et al., 2002; Beaumont et al., 2004; Duretz et al., 2011a; Tackley, 2012; Tackley et al., 2013; Gerya et al., 2015; Menant et al., 2016). Other models that are relevant for chapter IV of this study are presented in discussion sections.

1.7 Objectives of the research part of the thesis

Many of recent geodynamic research topics, where analogue modelling represents a native investigative component, is also combined with numerical modelling techniques. Similarly, in this work we combine both approaches. The core of the thesis is to study inner endogenic geodynamical processes as well as an exogenic

dynamical processes at the surface of Earth and Mars. The two following chapters are aimed at the development and investigation of two analogue models representing oroclinal buckling and detachment folding. In chapter IV we present a numerical model of the crustal-scale Rayleigh-Taylor instability evolution (using FEM) while the chapters V and VI, are focused on simulations and studying of the Martian cryovolcanic mudflows (using analogue modelling, numerical approach combined with analytical calculations).

The second chapter of the thesis discusses the modelling and investigation of complex material flow and deformation in large accretionary systems associated with the development of large arcuate orogens such as the Tuva-Mongol orocline (e.g. Xiao et al., 2018, 2015), Cantabrian orocline (e.g. Li et al., 2018), Kazachstania orocline (e.g. Del Greco et al., 2016), etc.

The third chapter of the thesis is focused on the application of velocimetry and photogrammetry methods to advanced analogue indentation experiments (including detachment folding and oroclinal buckling). Here we find methods how to use the determined strain-related parameters and quantified material flux between specific model subdomains. In detachment folding experiments (e.g. Lehmann et al., 2017), we investigated the mechanism of melt ascent and injection along axial planes of developed folds. The model is aimed at describing complex dynamics of folding with dependence on time-space coordinates in a folded system.

In the fourth chapter of the thesis presents a numerical model where we study the effect of the Rayleigh-Taylor instability to crustal inversion and discuss the role of these instabilities in dynamics of indentation systems. The model is based on modelling approach used for development of orogenic root in Bohemian Massif during Brunia indentation (Maierová et al., 2014, 2012).

The fifth and sixth chapters are aimed at the investigation of mud behavior under Martian atmospheric conditions. The studied mudflows are related to cryovolcanic activity on Mars surface (e.g. Wilson and Mouginis-Mark, 2014). The analogue experiments are set to simulate pressure conditions at the Mars surface while gravity effects are discussed.

The major goals and questions of the thesis are:

- What is the mechanical interplay between oceanic and continental lithosphere during oroclinal buckling. How a general material transfer during this event is interlinked with deformation distribution/character and how this affects the global and local dynamics of these systems.
- What is the role of anatectic lower crust redistribution during indentation episode and regional-scale folding of the crust?

- How the rheological gradients and presence of light felsic lower crust affects the dynamics of collision systems? What is the role of Rayleigh-Taylor instability in the systems with various convergence rate?
- Do mudflows exist on the Mars surface? What is the dynamics of these cryovolcanism-based (potential) flows and which similarities they have with mud or lava flows that are developed on Earth?

1.8 References

Acheson, D. J. (1990). Elementary Fluid Dynamics. Oxford University Press. p. 205. ISBN 0-19-859679-0.

Acocella, V., Cifelli, F., and Funiciello, R. (2000). Analogue models of collapse calderas and resurgent domes. Journal of Volcanology and Geothermal Research, 104(1-4), 81-96.

Adam, J., Urai, J. L., Wieneke, B., Oncken, O., Pfeiffer, K., Kukowski, N., Lohrmann, J., Hoth, S., van der Zee, W. and Schmatz, J. (2005). Shear localisation and strain distribution during tectonic faulting—New insights from granular-flow experiments and high-resolution optical image correlation techniques. Journal of Structural Geology, 27(2), 283-301.

Adam, J., Klinkmüller, M., Schreurs, G., and Wieneke, B. (2013). Quantitative 3D strain analysis in analogue experiments simulating tectonic deformation: Integration of X-ray computed tomography and digital volume correlation techniques. Journal of Structural Geology, 55, 127-149.

Agostini, A., Corti, G., Zeoli, A., and Mulugeta, G. (2009). Evolution, pattern, and partitioning of deformation during oblique continental rifting: Inferences from lithospheric-scale centrifuge models. Geochemistry, Geophysics, Geosystems, 10(11).

Aharonov, E., and Rothman, D. H. (1993). Non-Newtonian flow (through porous media): A lattice-Boltzmann method. Geophysical Research Letters, 20(8), 679-682.

Bajolet, F., Galeano, J., Funiciello, F., Moroni, M., Negredo, A. M., and Faccenna, C. (2012). Continental delamination: Insights from laboratory models. Geochemistry, Geophysics, Geosystems, 13(2).

Bajolet, F., Replumaz, A., and Lainé, R. (2013). Orocline and syntaxes formation during subduction and collision. Tectonics, 32(5), 1529-1546.

Bajolet, F., Chardon, D., Martinod, J., Gapais, D., and Kermarrec, J. J. (2015).

Synconvergence flow inside and at the margin of orogenic plateaus: Lithospheric-scale experimental approach. Journal of Geophysical Research: Solid Earth, 120(9), 6634-6657.

Bao, Y. B., and Meskas, J. (2011). Lattice Boltzmann method for fluid simulations. Department of Mathematics, Courant Institute of Mathematical Sciences, New York University, 44.

Baumgardner, J. R. (1985) Three-dimensional treatment of convective flow in the Earth's mantle. Journal of Statistical Physics, 39, 501–11.

Beaumont, C., Jamieson, R. A., Nguyen, M. H., and Lee, B. (2001). Himalayan tectonics explained by extrusion of a low-viscosity crustal channel coupled to focused surface denudation. Nature, 414(6865), 738.

Beaumont, C., Jamieson, R. A., Nguyen, M. H., and Medvedev, S. (2004). Crustal channel flows: 1. Numerical models with applications to the tectonics of the Himalayan-Tibetan orogen. Journal of Geophysical Research: Solid Earth, 109(B6).

Becker, T. W., and Kaus, B. J. (2016). Numerical Modeling of Earth Systems. An introduction to computational methods with focus on solid Earth applications of continuum mechanics. University of Southern California, Los Angeles. Lecture notes (224 pages), available online at http://www-udc. ig. utexas. edu/external/becker/Geodynamics557. pdf, accessed, 9, 2017.

Benes, V., and Davy, P. (1996). Modes of continental lithospheric extension: experimental verification of strain localization processes. Tectonophysics, 254(1-2), 69-87.

Berner, H., Ramberg, H., and Stephansson, O. (1972). Diapirism theory and experiment. Tectonophysics, 15(3), 197-218.

Bird, P. (1978) Finite elements modeling of lithosphere deformation: The Zagros collision orogeny, Tectonophysics, 50, 307–36.

Boutelier, D. (2016). TecPIV—A MATLAB-based application for PIV-analysis of experimental tectonics. Computers and Geosciences, 89, 186-199.

Brun, J. P. (2002). Deformation of the continental lithosphere: Insights from brittle-ductile models. Geological Society, London, Special Publications, 200(1), 355-370.

Brun, J. P., and Fort, X. (2004). Compressional salt tectonics (Angolan margin). Tectonophysics, 382(3-4), 129-150.

Brune, S., Corti, G., and Ranalli, G. (2017). Controls of inherited lithospheric heterogeneity on rift linkage: Numerical and analog models of interaction between the Kenyan and Ethiopian rifts across the Turkana depression. Tectonics, 36(9), 1767-1786.

Burg, J. P., and Ford, M. (1997). Orogeny through time: an overview. Geological Society, London, Special Publications, 121(1), 1-17.

Buiter, S. J., Schreurs, G., Albertz, M., Gerya, T. V., Kaus, B., Landry, W., ... and Maillot, B. (2016). Benchmarking numerical models of brittle thrust wedges. Journal of structural geology, 92, 140-177.

Byerlee, J. (1978). Friction of rocks. In Rock friction and earthquake prediction (pp. 615-626). Birkhäuser, Basel.

Cadell, H. M. (1889) Experimental researches in mountain building Tans. R. Soc. Edinburgh, 1, pp. 339-343

Canuto, C., Hussaini, M. Y., Quarteroni, A., and Zang, T. A. (2006). Spectral methods. Springer-Verlag, Berlin.

Carter, N. L. (1976). Steady state flow of rocks. Reviews of Geophysics, 14(3), 301-360.

Cassinis G. (1928): Calcoli numerici grafici e meccanici. Mariotti – Pacini, Pisa.

Chemenda, A., Bouissou, S., and Bachmann, D. (2005). Three-dimensional physical modeling of deep-seated landslides: New technique and first results. Journal of Geophysical Research: Earth Surface, 110(F4).

Cloos, E. (1955). Experimental analysis of fracture patterns. Geological Society of America Bulletin, 66(3), 241-256.

Cobbold, P. R., and Jackson, M. P. A. (1992). Gum rosin (colophony): a suitable material for thermomechanical modelling of the lithosphere. Tectonophysics, 210(3-4), 255-271.

Colletta, B., Letouzey, J., Pinedo, R., Ballard, J. F., and Balé, P. (1991). Computerized X-ray tomography analysis of sandbox models: Examples of thin-skinned thrust systems. Geology, 19(11), 1063-1067.

Connolly, J. A., Schmidt, M. W., Solferino, G., and Bagdassarov, N. (2009). Permeability of asthenospheric mantle and melt extraction rates at mid-ocean ridges.

Nature, 462(7270), 209.

Corti, G. (2012). Evolution and characteristics of continental rifting: Analog modeling-inspired view and comparison with examples from the East African Rift System. Tectonophysics, 522, 1-33.

Corti, G., Moratti, G., and Sani, F. (2005). Relations between surface faulting and granite intrusions in analogue models of strike-slip deformation. Journal of Structural Geology, 27(9), 1547-1562.

Corti, G., Bonini, M., Conticelli, S., Innocenti, F., Manetti, P., and Sokoutis, D. (2003). Analogue modelling of continental extension: a review focused on the relations between the patterns of deformation and the presence of magma. Earth-Science Reviews, 63(3-4), 169-247.

Courant, R., Friedrichs, K. O., and Lewy, H. (1928) Über die partiellen Differenzengleichungen der mathematischen Physik, Mathematische Annalen 100, pp. 32

Courant, R. (1943). Variational methods for the solution of problems of equilibrium and vibrations. Verlag nicht ermittelbar.

Cserepes, L., Rabinowicz, M. and Rosemberg-Borot, C. (1988) Three-dimensional infinite Prandtl number convection in one and two layers and implications for the Earth's gravity field. Journal of Geophysical Research, 93, 12009–25.

Daignieres, M., Fremond, M. and Friaa, A. (1978) Modele de type Norton-Hoff généralisé pour l'étude des déformations lithosphériques (exemple: la collision Himalayenne), Comptes Reudus Hebdomadaires des Séances de l'Academie de Sciences, 268B, 371–74.

Daubre, A. (Dunod) (1879) Etudes synthétiques de géologie expérimentale, pt 1, Paris

Dauteuil, O., and Mart, Y. (1998). Analogue modeling of faulting pattern, ductile deformation, and vertical motion in strike-slip fault zones. Tectonics, 17(2), 303-310.

Davy, P., and Cobbold, P. R. (1988). Indentation tectonics in nature and experiment. 1. Experiments scaled for gravity. Bull. Geol. Inst. Univ. Uppsala, 14, 129-141.

Del Greco, K., Johnston, S. T., Gutiérrez-Alonso, G., Shaw, J., and Lozano, J. F. (2016). Interference folding and orocline implications: A structural study of the Ponga Unit, Cantabrian orocline, northern Spain. Lithosphere, 8(6), 757-768.

Dixon, J. M. (1974). A new method of determining finite strain in models of geological structures. Tectonophysics, 24(1-2), 99-114.

Dixon, J. M., and Summers, J. M. (1983). Patterns of total and incremental strain in subsiding troughs: experimental centrifuged. models of inter-diapir synclines. Canadian Journal of Earth Sciences, 20(12), 1843-1861.

Dixon, J. M., and Liu, S. (1992). Centrifuge modelling of the propagation of thrust faults. In Thrust tectonics (pp. 53-69). Springer, Dordrecht.

Dotare, T., Yamada, Y., Adam, J., Hori, T., and Sakaguchi, H. (2016). Initiation of a thrust fault revealed by analog experiments. Tectonophysics, 684, 148-156.

Duretz, T., Gerya, T. V., and May, D. A. (2011a). Numerical modelling of spontaneous slab breakoff and subsequent topographic response. Tectonophysics, 502(1-2), 244-256.

Duretz, T., May, D. A., Gerya, T. V., and Tackley, P. J. (2011b). Discretization errors and free surface stabilization in the finite difference and marker-in-cell method for applied geodynamics: A numerical study. Geochemistry, Geophysics, Geosystems, 12(7).

Escher, B. G., and Kuenen, P. H. (1928). Experiments in connection with salt domes. Leidse Geologische Mededelingen, 3(1), 151-182.

Euler, L. (1768). Institutiones Calculi Integralis, Vol. 1. Petersburg: Académie del Science (in French).

Eymard, R., Gallouët, T., and Herbin, R. (2000). Finite volume methods. Handbook of numerical analysis, 7, 713-1018.

Faisal, S., and Dixon, J. M. (2015). Physical analog (centrifuge) model investigation of contrasting structural styles in the Salt Range and Potwar Plateau, northern Pakistan. Journal of Structural Geology, 77, 277-292.

Favre, A. (1878a) Expériences sur les effets des refoulements ou écrasements latéraux en géologie Comptes Rendus Hebdomadaires des Séances de l'Académie des Sciences, pp. 1092-1095

Favre, A. (1878b) Expériences sur les effets des refoulements ou écrasements latéraux en géologie La Nature. Archives des sciences physiques et naturelles, 246 (1878), pp. 278-283

Folta, J. (1988). Some remarks on the history of Numerical Analysis especially in the area of Prague. Llull: Revista de la Sociedad Española de Historia de las Ciencias y de las Técnicas, 11(21), 217-234.

Galland, O., Bertelsen, H. S., Guldstrand, F., Girod, L., Johannessen, R. F., Bjugger, F., Burchardt, S. and Mair, K. (2016). Application of open-source photogrammetric software MicMac for monitoring surface deformation in laboratory models. Journal of Geophysical Research: Solid Earth, 121(4), 2852-2872.

Gerya, T. V., Stöckhert, B., and Perchuk, A. L. (2002). Exhumation of high-pressure metamorphic rocks in a subduction channel: A numerical simulation. Tectonics, 21(6), 6-1.

Gerya, T. (2009). Introduction to numerical geodynamic modelling. Cambridge University Press.

Gerya, T. V., and Yuen, D. A. (2003). Characteristics-based marker-in-cell method with conservative finite-differences schemes for modeling geological flows with strongly variable transport properties. Physics of the Earth and Planetary Interiors, 140(4), 293-318.

Gerya, T. V., Stern, R. J., Baes, M., Sobolev, S. V., and Whattam, S. A. (2015). Plate tectonics on the Earth triggered by plume-induced subduction initiation. Nature, 527(7577), 221.

Gethin, D. T., Yang, X. S., and Lewis, R. W. (2006). A two dimensional combined discrete and finite element scheme for simulating the flow and compaction of systems comprising irregular particulates. Computer methods in applied mechanics and engineering, 195(41-43), 5552-5565.

Godin, L., Yakymchuk, C., and Harris, L. B. (2011). Himalayan hinterland-verging superstructure folds related to foreland-directed infrastructure ductile flow: insights from centrifuge analogue modelling. Journal of Structural Geology, 33(3), 329-342.

Goldstine, H. H. (1980). The computer from Pascal to von Neumann. Princeton University Press.

Goldstine, H. H. (2012). A History of Numerical Analysis from the 16th through the 19th Century (Vol. 2). Springer Science and Business Media.

Gottsmann, J., and Martí, J. (Eds.). (2011). Caldera volcanism: analysis, modelling and response (Vol. 10). Elsevier.

Guillaume, B., Martinod, J., and Espurt, N. (2009). Variations of slab dip and overriding plate tectonics during subduction: Insights from analogue modelling. Tectonophysics, 463(1-4), 167-174.

Graveleau, F., Malavieille, J., and Dominguez, S. (2012). Experimental modelling of orogenic wedges: A review. Tectonophysics, 538, 1-66.

Griggs, D. T. (1939). A theory of mountain-building. American Journal of Science, 237(9), 611-650.

Grossmann, C., Roos, H. G., and Stynes, M. (2007). Numerical treatment of partial differential equations (Vol. 154). Berlin: Springer.

Hall Sir, J., 1805. Experiments on whinstone and lava. Trans. R. Soc. Edin. 5, 43–75.

Hall Sir, J., 1812. Account of a series of experiments, shewing the effects of compression in modifying the action of heat. Trans. R. Soc. Edin. 6, 71–185.

Hall Sir, J., 1815. On the vertical position and convolution of certain strata, and their relation with granite. Trans R. Soc. Edin. 7, 79–108.

Harris, L. B., Yakymchuk, C., and Godin, L. (2012). Implications of centrifuge simulations of channel flow for opening out or destruction of folds. Tectonophysics, 526, 67-87.

Houseman, G. (1988) The dependence of convection planform on mode of heating. Nature, 332, 346–9.

Hubbert, M. K. (1951) Mechanical basis for certain familiar geologic structures. Geol. Soc. Am. Bull., 62, pp. 355-372

Hubbert, M.K., 1937. Theory of scale models as applied to the study of geologic structures. Bull. Geol. Soc. Am. 48, 1459–1520.

Ismail-Zadeh, A., and Tackley, P. (2010). Computational methods for geodynamics. Cambridge University Press.

Jacoby, W. R. (1973). Model experiment of plate movements. Nature Physical Science, 242(122), 130.

Kavanagh, J. L., Menand, T., and Daniels, K. A. (2013). Gelatine as a crustal analogue: Determining elastic properties for modelling magmatic intrusions. Tectono-

physics, 582, 101-111.

Katz, V. J. (1979). The history of Stokes' theorem. Mathematics Magazine, 52(3), 146-156.

Katz, R. F., Ragnarsson, R., and Bodenschatz, E. (2005). Tectonic microplates in a wax model of sea-floor spreading. New Journal of Physics, 7(1), 37.

Keondzhyan, V. P. and Monin, A. S. (1977) Continental drift and large-scale wandering of the Earth's pole. Izvestiya Physics of the Solid Earth, 13, 760–72.

Keondzhyan, V. P. and Monin, A. S. (1980) Compositional convection in the Earth's Mantle. Dokladi Akademii Nauk SSSR, 253, 78–81.

Kettermann, M., von Hagke, C., van Gent, H. W., Grützner, C., and Urai, J. L. (2016). Dilatant normal faulting in jointed cohesive rocks: a physical model study.

Kirby, S. H. (1983). Rheology of the lithosphere. Reviews of Geophysics, 21(6), 1458-1487.

Koyi, H. (1997). Analogue modelling: from a qualitative to a quantitative technique—a historical outline. Journal of Petroleum Geology, 20(2), 223-238.

Krýza, O. (2013) Application of the multivariate statistical methods for the analysis of the 2D thermo-mechanical numerical models of diapirism. Diploma thesis. Charles University, Prague.

Kuenen, P. H. (1936). The negative isostatic anomalies in the East Indies (with experiments). Leid. Geol. Med., 8, 169-214.

Le Guerroué, E., and Cobbold, P. R. (2006). Influence of erosion and sedimentation on strike-slip fault systems: insights from analogue models. Journal of Structural Geology, 28(3), 421-430.

Lehmann, J., Schulmann, K., Lexa, O., Závada, P., Štípská, P., Hasalová, P., ... and Corsini, M. (2017). Detachment folding of partially molten crust in accretionary orogens: A new magma-enhanced vertical mass and heat transfer mechanism. Lithosphere, 9(6), 889-909.

LeVeque, R. J. (2002). Finite volume methods for hyperbolic problems (Vol. 31). Cambridge university press.

Lewis, R. W., Gethin, D. T., Yang, X. S., and Rowe, R. C. (2005). A combined

finite-discrete element method for simulating pharmaceutical powder tableting. International journal for numerical methods in engineering, 62(7), 853-869.

Li, Z., Escoffier, S., and Kotronis, P. (2013). Using centrifuge tests data to identify the dynamic soil properties: Application to Fontainebleau sand. Soil Dynamics and Earthquake Engineering, 52, 77-87.

Li, P., Sun, M., Rosenbaum, G., Yuan, C., Safonova, I., Cai, K., ... and Zhang, Y. (2018). Geometry, kinematics and tectonic models of the Kazakhstan Orocline, Central Asian Orogenic Belt. Journal of Asian Earth Sciences, 153, 42-56.

Liu, S. and Dixon, J. M. (1990). Centrifuge modelling of thrust faulting: strain partitioning and sequence of thrusting in duplex structures. Geological Society, London, Special Publications, 54(1), 431-444.

Liu, S. and Dixon, J. M. (1991). Centrifuge modelling of thrust faulting: structural variation along strike in fold-thrust belts. Tectonophysics, 188(1-2), 39-62.

Longley, W. R. (1932). JB Scarborough, Numerical Mathematical Analysis. Bulletin of the American Mathematical Society, 38(5), 331-332.

Logan, D. L. (2011). A first course in the finite element method. Cengage Learning.

Luján, M., Rossetti, F., Storti, F., Ranalli, G., and Socquet, A. (2010). Flow trajectories in analogue viscous orogenic wedges: Insights on natural orogens. Tectonophysics, 484(1-4), 119-126.

Luth, S., Willingshofer, E., Sokoutis, D., and Cloetingh, S. (2010). Analogue modelling of continental collision: influence of plate coupling on mantle lithosphere subduction, crustal deformation and surface topography. Tectonophysics, 484(1-4), 87-102.

Ma, G., An, X., and He, L. (2010). The numerical manifold method: a review. International Journal of Computational Methods, 7(01), 1-32.

Machetel, P., Rabinowicz, M. and Bernardet, P. (1986) Three-dimensional convection in spherical shells. Geophysical and Astrophysical Fluid Dynamics, 37, 57–84.

Maierova, P., Lexa, O., Schulmann, K., and Štípská, P. (2014). Contrasting tectonometamorphic evolution of orogenic lower crust in the Bohemian Massif: a numerical model. Gondwana Research, 25(2), 509-521.

Maierová, P., Čadek, O., Lexa, O., and Schulmann, K. (2012). A numerical model of

exhumation of the orogenic lower crust in the Bohemian Massif during the Variscan orogeny. Studia Geophysica et Geodaetica, 56(2), 595-619.

Maillot, B., and Koyi, H. (2006). Thrust dip and thrust refraction in fault-bend folds: analogue models and theoretical predictions. Journal of Structural Geology, 28(1), 36-49.

Malavieille, J. (2010). Impact of erosion, sedimentation, and structural heritage on the structure and kinematics of orogenic wedges: Analog models and case studies. Gsa Today, 20(1), 4-10.

Mansfield, C., and Cartwright, J. (2001). Fault growth by linkage: observations and implications from analogue models. Journal of Structural Geology, 23(5), 745-763.

Martí, J., Geyer, A., Folch, A., and Gottsmann, J. (2008). A review on collapse caldera modelling. Developments in Volcanology, 10, 233-283.

Mathieu, L., De Vries, B. V. W., Holohan, E. P., and Troll, V. R. (2008). Dykes, cups, saucers and sills: Analogue experiments on magma intrusion into brittle rocks. Earth and Planetary Science Letters, 271(1-4), 1-13.

Mead, W. J. (1920) Notes on the mechanics of geologic structures J. Geol., 28, pp. 505-523

Menant, A., Sternai, P., Jolivet, L., Guillou-Frottier, L., and Gerya, T. (2016). 3D numerical modeling of mantle flow, crustal dynamics and magma genesis associated with slab roll-back and tearing: The eastern Mediterranean case. Earth and Planetary Science Letters, 442, 93-107.

Mériaux, C. A., Mériaux, A. S., Schellart, W. P., Duarte, J. C., Duarte, S. S., and Chen, Z. (2016). Mantle plumes in the vicinity of subduction zones. Earth and Planetary Science Letters, 454, 166-177.

Mériaux, C. A., Duarte, J. C., Duarte, S. S., Schellart, W. P., Chen, Z., Rosas, F., ... and Terrinha, P. (2015). Capture of the Canary mantle plume material by the Gibraltar arc mantle wedge during slab rollback. Geophysical Journal International, 201(3), 1717-1721.

Minear, J. W., and Toksöz, M. N. (1970). Thermal regime of a downgoing slab and new global tectonics. Journal of Geophysical Research, 75(8), 1397-1419.

Mora, P., and Yuen, D. A. (2017). Simulation of plume dynamics by the Lattice Boltzmann Method. Geophysical Journal International, 210(3), 1932-1937.

Mourgues, R., and Cobbold, P. R. (2006). Thrust wedges and fluid overpressures: Sandbox models involving pore fluids. Journal of Geophysical Research: Solid Earth, 111(B5).

Mukherjee, S., Koyi, H. A., and Talbot, C. J. (2012). Implications of channel flow analogue models for extrusion of the Higher Himalayan Shear Zone with special reference to the out-of-sequence thrusting. International Journal of Earth Sciences, 101(1), 253-272.

Munjiza, A. A. (2004). The combined finite-discrete element method. John Wiley and Sons.

Newton, I. (1687). Philosophiae Naturalis Principia Mathematica.

Nikkilä, K., Korja, A., Koyi, H., and Eklund, O. (2015). Analog modeling of one-way gravitational spreading of hot orogens–A case study from the Svecofennian orogen, Fennoscandian Shield. Precambrian Research, 268, 135-152.

Nolesini, T., Di Traglia, F., Del Ventisette, C., Moretti, S., and Casagli, N. (2013). Deformations and slope instability on Stromboli volcano: Integration of GBInSAR data and analog modeling. Geomorphology, 180, 242-254.

Parker, T. J., and McDowell, A. N. (1955). Model studies of salt-dome tectonics. AAPG Bulletin, 39(12), 2384-2470.

Pastor-Galán D., Gutiérrez-Alonso G., Zulauf G. and Zanella F. (2012) Analogue modeling of lithospheric-scale orocline buckling: Constraints on the evolution of the Iberian-Armorican Arc. Geological Society of America Bulletin, 124, 1293-1309.

Podladchikov, Y., Talbot, C., and Poliakov, A. N. B. (1993). Numerical models of complex diapirs. Tectonophysics, 228(3-4), 189-198.

Pysklywec, R. N., and Cruden, A. R. (2004). Coupled crust-mantle dynamics and intraplate tectonics: Two-dimensional numerical and three-dimensional analogue modeling. Geochemistry, Geophysics, Geosystems, 5(10).

Radjaï, F., and Dubois, F. (2011). Discrete-element modeling of granular materials (pp. 425-p). Wiley-Iste.

Ramberg, H. (1981). Gravity, deformation, and the earth's crust: In theory, experiments, and geological application. Academic press.

Ramberg, H. (1970). Model studies in relation to intrusion of plutonic bodies,

in: Newall, G., Rast, N. (Eds.), Mechanism of igneous intrusion, 2 ed, pp. 261–286

Ramberg, H. (1964). Selective buckling of composite layers with contrasted rheological properties, a theory for simultaneous formation of several orders of folds. Tectonophysics, 1(4), 307-341.

Ramberg, H. (1955). Natural and experimental boudinage and pinch-and-swell structures. The Journal of Geology, 63(6), 512-526.

Ranalli, G. (2001). Experimental tectonics: from Sir James Hall to the present. Journal of Geodynamics, 32(1-2), 65-76.

Ranalli, G. (2000). Rheology of the crust and its role in tectonic reactivation. Journal of geodynamics, 30(1-2), 3-15.

Ranalli, G. (1997). Rheology of the lithosphere in space and time. Geological Society, London, Special Publications, 121(1), 19-37.

Recktenwald, G. W. (2004). Finite-difference approximations to the heat equation. Mechanical Engineering, 10, 1-27.

Richardson, L. F. (1911). IX. The approximate arithmetical solution by finite differences of physical problems involving differential equations, with an application to the stresses in a masonry dam. Philosophical Transactions of the Royal Society of London. Series A, Containing Papers of a Mathematical or Physical Character, 210(459-470), 307-357.

Rosas, F. M., Duarte, J. C., Schellart, W. P., Tomás, R., Grigorova, V., and Terrinha, P. (2015). Analogue modelling of different angle thrust-wrench fault interference in a brittle medium. Journal of Structural Geology, 74, 81-104.

Rossetti, F., Ranalli, G., and Faccenna, C. (1999). Rheological properties of paraffin as an analogue material for viscous crustal deformation. Journal of Structural Geology, 21(4), 413-417.

Schellart, W. P., and Strak, V. (2016). A review of analogue modelling of geodynamic processes: Approaches, scaling, materials and quantification, with an application to subduction experiments. Journal of Geodynamics, 100, 7-32.

Schreurs, G., Buiter, S. J., Boutelier, D., Corti, G., Costa, E., Cruden, A. R., ... and Lohrmann, J. (2006). Analogue benchmarks of shortening and extension experiments. Special Publication-Geological Society of London, 253, 1.

Schreurs, G., Buiter, S. J., Boutelier, J., Burberry, C., Callot, J. P., Cavozzi, C., ... and Cruz, L. (2016). Benchmarking analogue models of brittle thrust wedges. Journal of structural geology, 92, 116-139.

Stokes, G. G. (1851). "On the effect of internal friction of fluids on the motion of pendulums". Transactions of the Cambridge Philosophical Society. 9, part ii: 8–106.

Strak, V., and Schellart, W. P. (2014). Evolution of 3-D subduction-induced mantle flow around lateral slab edges in analogue models of free subduction analysed by stereoscopic particle image velocimetry technique. Earth and Planetary Science Letters, 403, 368-379.

Tackley, P. J., Ammann, M., Brodholt, J. P., Dobson, D. P., and Valencia, D. (2013). Mantle dynamics in super-Earths: Post-perovskite rheology and self-regulation of viscosity. Icarus, 225(1), 50-61.

Tackley, P. J. (2012). Dynamics and evolution of the deep mantle resulting from thermal, chemical, phase and melting effects. Earth-Science Reviews, 110(1-4), 1-25.

Tapponnier, P., Peltzer, G., Le Dain, A. Y., Armijo, R., and Cobbold, P. (1982). Propagating extrusion tectonics in Asia: New insights from simple experiments with plasticine. Geology, 10(12), 611-616.

Tentler, T. (2003). Analogue modeling of overlapping spreading centers: insights into their propagation and coalescence. Tectonophysics, 376(1-2), 99-115.

Torrance, K. E. and Turcotte, D. L. (1971) Thermal convection with large viscosity variations. Journal of Fluid Mechanics, 47, 113–25.

Twiss, R. J., and Moores, E. M. (2007). Structural geology (2nd ed., 736 p). New York: W. H. Freeman and Company

Waffle, L., Godin, L., Harris, L. B., and Kontopoulou, M. (2016). Rheological and physical characteristics of crustal-scaled materials for centrifuge analogue modelling. Journal of Structural Geology, 86, 181-199.

Wang, H., Agrusta, R., and van Hunen, J. (2015). Advantages of a conservative velocity interpolation (CVI) scheme for particle-in-cell methods with application in geodynamic modeling. Geochemistry, Geophysics, Geosystems, 16(6), 2015-2023.

Warsitzka, M., Kley, J., and Kukowski, N. (2013). Salt diapirism driven by differential loading—Some insights from analogue modelling. Tectonophysics, 591, 83-97.

Warsitzka, M., Kukowski, N., and Kley, J. (2017, April). Kinematics and dynamics of salt movement driven by sub-salt normal faulting and supra-salt sediment accumulation-combined analogue experiments and analytical calculations. In EGU General Assembly Conference Abstracts (Vol. 19, p. 9213).

Weijermars, R., and Schmeling, H. (1986). Scaling of Newtonian and non-Newtonian fluid dynamics without inertia for quantitative modelling of rock flow due to gravity (including the concept of rheological similarity). Physics of the Earth and Planetary Interiors, 43(4), 316-330.

Weijermars, R. M. P. A., Jackson, M. T., and Vendeville, B. (1993). Rheological and tectonic modeling of salt provinces. Tectonophysics, 217(1-2), 143-174.

Whitehead Jr, J. A., and Luther, D. S. (1975). Dynamics of laboratory diapir and plume models. Journal of Geophysical Research, 80(5), 705-717.

Whittaker, E. T., and Robinson, G. (1924). The calculus of observations: a treatise on numerical mathematics. The calculus of observations.

Willis, B. (1893) Part 2; The Mechanics of Appalachian Structure United States Geological Survey Annual Report 13 (1893), pp. 211-281 (Part 2)

Wilson, L., and Mouginis-Mark, P. J. (2014). Dynamics of a fluid flow on Mars: Lava or mud?. Icarus, 233, 268-280.

Woidt, W. D. (1978) Finite-element calculations applied to salt dome analysis. Tectonophysics, 50 (2–3), 369–86.

Wu, Z., and Wong, L. N. Y. (2012). Frictional crack initiation and propagation analysis using the numerical manifold method. Computers and Geotechnics, 39, 38-53.

Xiao, W., Windley, B. F., Han, C., Liu, W., Wan, B., Zhang, J. E., ... and Song, D. (2018). Late Paleozoic to early Triassic multiple roll-back and oroclinal bending of the Mongolia collage in Central Asia. Earth-Science Reviews, 186, 94-128.

Xiao, W., Windley, B. F., Sun, S., Li, J., Huang, B., Han, C., ... and Chen, H. (2015). A tale of amalgamation of three Permo-Triassic collage systems in Central Asia: oroclines, sutures, and terminal accretion. Annual review of earth and planetary sciences, 43, 477-507.

Xu, Q., Zhao, Y., Hou, T., Wang, J., Zhao, X., Liu, J., and Wang, D. (2018). The evolution of folds-thrust wedges: Mathematical simulation based on finite difference method. Journal of Intelligent and Fuzzy Systems, 34(2), 1071-1081.

Zhang, G. X., Sugiura, Y., and Saito, K. (1999). Application of manifold method to jointed dam foundation. In Proc. Third Int. Conf. Analysis of Discontinuous Deformation (ICADD-3) (pp. 211-220).

Zhang, H. H., Li, L. X., An, X. M., and Ma, G. W. (2010). Numerical analysis of 2-D crack propagation problems using the numerical manifold method. Engineering analysis with boundary elements, 34(1), 41-50.

Zwaan, F., and Schreurs, G. (2017). How oblique extension and structural inheritance influence rift segment interaction: Insights from 4D analog models. Interpretation, 5(1), SD119-SD138.

Internet sources

http://geologypics.com/geological-item/brittle-structures-photos/ (11.2.2019)

https://physics.mff.cuni.cz/kfpp/skripta/kurz_fyziky_pro_DS/display.php/kontinuum/2 (12.2.2019)

http://psgt.earth.lsa.umich.edu/PDF/2017/10_Lithosphere_2017.pdf (12.2.2019)

http://www.geosci.usyd.edu.au/users/prey/Teaching/ACSGT/Module1/Mod1LectPract/Sld025.htm (20.2.2019)

Benzi, M. http://www.mathcs.emory.edu/~benzi/andhttp://history.siam.org/5C/pdf/nahist_Benzi.pdf (28.12. 2018)

List of abbreviations

2D - two dimensional
3D - three dimensional
DEM - Discrete/distinct Element Method
FDM - Finite Difference Method
FEM - Finite Element Method
FVM - Finite Volume Method
LBM - Lattice Boltzmann Method
NMM - Numerical Manifold Method
ODE - ordinary differential equation
PDE - partial differential equation
SM - spectral method

Part II

Mass and heat transfer in the accretionary systems

2 Oroclinal buckling and associated lithospheric-scale material flow

Ondřej Krýza, Ondrej Lexa, Karel Schulmann, Alexandra Guy, Denis Gapais, John Cosgrove and Wenjio Xiao

2.1 Abstract

We present a new analogue model of oroclinal buckling which is based on recent advances in our understanding of the giant Mongolian orocline in central Asia. The model simulates an amplification of a preexisting, gently folded, accretionary system represented by oceanic crust relaminated by felsic material separated from the oceanic lithosphere by a continental ribbon above a subduction zone. Consequently, in the analogue model we established two neighboring subdomains that represent continental and oceanic domains separated by a steep elastic "subduction" interface. The orthogonal shortening of the model domain, which is parallel to the pseudo-linear interface between these subdomains, produces two different deformation patterns in the orocline amplified interlimb areas. We used a standard modeling techniques to investigate both, flow of a ductile lithosphere and brittle deformation of an upper crust that are associated with orocline development. The modelling results show that: (1) two types of regional-scale folds develop, including the steeply plunging orocline and upright folds with horizontal hinges, (2) the overall deformation distribution shows significant thickening/thinning and exhumation of lower ductile layers with variations in dependence on the distance from the piston, (3) the finite geometry of the lithosphere is strongly contrasting in both oceanic and continental orocline hinge sectors, (4) the geometry of orocline is non-cylindrical with increasing plunge of the fold axis from upper crust towards deeper lithospheric layers. The model results are used to explain geophysically constrained deep crustal structure and surface deformation pattern of the Mongolia orocline.

Keywords: Analogue modelling, Tuva-Mongol orocline, oroclinal buckling, indentation

Highlights:

- Oroclinal buckling model of vertical belt separating horizontally stratified domains
- Early buckling stage shows characteristic of indentation tectonics
- Orocline amplification causes large scale vortex flow around inflection line

2.2 Introduction

The three-dimensional character of orogenic systems has long been recognized and studied by a range of authors (e.g. Şengör, 1993). However, commonly, the geodynamic evolution of orogenic systems has been presented perpendicular to the orogenic belt using two-dimensional cross-sections, as this is the plane in which most of material transfers occur. Similarly, most existing numerical models of continental collision and/or oceanic subduction are two-dimensional. Even if these models are very successful in simulating the main features of orogenic processes, they are no substitute for the fully scaled, 3D modeling required to examine the role of the systems mechanical anisotropy and material flow which also occurs along the strike of the belt. 3D numerical modeling of such systems is considerably sophisticated, difficult for programming and time-consuming (Gerya and Stöckhert, 2006; Gerya, 2014; Maierová et al., 2012, 2014 and 2018). It was therefore decided to study the behavior of these systems under laboratory conditions via analogue modeling.

The simulation of the oroclinal buckling of orogenic systems requires a 3D approach because the material flows both laterally and vertically during deformation (Pastor-Galán et al., 2012). Oroclinal bending affects linear orogenic systems located between oceanic lower plate and oceanic or continental upper plate either by passive oroclinal bending (e.g. Menant et al., 2016; Rosenbaum and Lister, 2004; Rosenbaum, 2012) or active oroclinal bending and buckling (Edel et al., 2014; Lehmann et al., 2010; Rosenbaum, 2014; Weil et al., 2001). The passive bending mode is uniquely controlled by the geometry of the subducting plate such as curvatures produced by variations in rollback velocity (Fig. 7a). In contrast, active oroclinal bending is controlled by horizontal indentation perpendicular to the subduction/accretionary orogen (e.g. the entry of an oceanic plateau or a continental block into a subduction zone) or high localized friction producing elevated and localized interplate coupling between the subducting plate and forearc region (Boutelier et al., 2014). In contrast, oroclinal buckling results from buckling instability during the orogen-parallel shortening of a linear orogenic belt (Fig. 7a and b) between two continental blocks (Lehmann et al., 2010; Edel et al., 2014). Recent analogue modeling of Boutelier et al., (2019) showed that the oroclinal buckling occurs during pull of continental ribbon by subduction and simultaneous extension forming a back-arc domain. In their model, both passive bending and buckling modes enhance each other occur simultaneously, which is the preferred model of Xiao et al. (2018) to explain deformation pattern of the central Asian oroclines.

Oroclinal buckling tectonics, the topic of this study, can be considered as a specific type of indentation tectonics accompanied by lateral movements of oroclinal hinges perpendicular to the movements of continental blocks. The whole process of oroclinal buckling depends on a number of factors including: the lateral surface curvature of the accretionary belt, variations in geometry and thickness of the upper and lower plate, variations in rheology and thermal state of both interacting plates and the evolution of the lithosphere after slab break-off (e.g. Menant et al., 2016). In

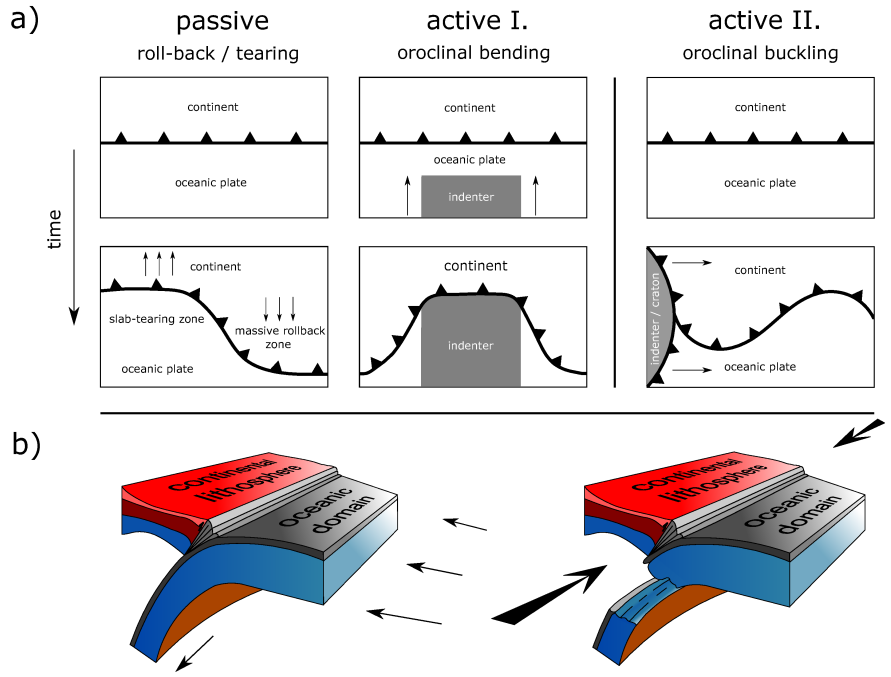


Fig. 7: Illustration of the mechanisms responsible for oroclinal arcuating. Three different basic styles of arcuating (passive/active) of the orogens are shown in (a). Passive arcuating is related to laterally asymmetrical progressive subduction where asymmetrical roll-back is developed by one-side tearing of the sinking slab. The first class active arcuating (bending) is produced by indentation tectonics where a microcontinent is embedded into a continental block while the indentation tectonics forms a gently curved contact line. The second class active arcuating (buckling) is a product of lateral accretion of a lithospheric block (e.g. cratonic part) that leads to amplification of a pre-developed accretionary complex. The assumption for the oroclinal buckling (active II) is a slab break-off of the originally subducted slab as is illustrated in (b).

particular, the rheological behavior of the system can be influenced by perturbation of the thermal structure of the lithosphere associated with the elevation of lithospheric mantle, partial melting of the lower crust and the possible presence of felsic lower crustal material at the bottom of a continental domain (e.g. Maierová et al., 2018).

Convergent analogue models are characterized by ductile flow of the lower crust, regional folding and the formation of a range of brittle structures in the upper crust as a consequence of mechanical coupling between ductile and brittle layers (Brun, 2002). These processes are linked with the dynamic evolution of topography due to differential burial and uplift of the brittle upper crust related to vertical movements of deeper ductile crust forming the so-called pop-down structures (Cagnard et al., 2006). These topographical patterns are significantly more complex than those developed during lower crustal channel flow typical for continental collision tectonics (Beaumont et al., 2004, 2006; Duretz et al., 2011; Luján et al., 2010).

We examine the above mentioned complexities of boundary conditions and

dynamically evolving interactions between the lower crust, mantle and upper brittle crust by means of analogue modelling in which we study the mechanism of oroclinal buckling by the folding of a vertical elastic beam confined by a horizontally stratified viscous medium. This approach is in contrast to existing analogue models where a buckled domain is represented by a single unit with free boundaries (Gutiérrez-Alonso et al., 2012; Pastor-Galán et al., 2012). Here we examine the shortening of a vertically layered lithospheric segment (e.g. Brun, 2002) immersed in low viscosity material without direct contact with immobile boundaries (Fig. 8, Fig. 9). In the set of experiments performed, we combine different horizontal stratification of silicon layers of variable viscosity for specific subdomains representing a relic of the oceanic lithosphere on one side and continental domain on the opposite side (Fig. 8, Fig. 9b). These subdomains are separated from each other by a steep subduction/accretionary complex. Such model geometry was set up to fit the geological evolution of the Central Asian Orogenic Belt (CAOB) – in particular the Mongolian oroclinal system (Yakubchuk, 2005). Its evolution is interpreted as a result of the oroclinal buckling of the subduction-accretionary belt after cessation of E-W subduction beneath the Mongolian continental ribbons followed by orthogonal, belt-parallel, N-S shortening of the whole zone in between the North China and Siberian cratonic jaws (Edel et al., 2014; Lehmann et al., 2010).

In this paper we focus on analogue experiments of oroclinal buckling of linear accretionary orogens developed after cessation of oceanic subduction, the formation of an accretionary wedge and Andean type thickening. During subsequent along-strike convergence, the accretionary system is deformed to produce a half-wavelength fold due to one-sided continental indentation or a full wavelength fold due to shortening of the system between continental jaws. The deformation of the domain is governed by the amplification of the orocline which has a sub-vertical axis and the formation of one or two hinge zones that indent the surrounding lithosphere. Lateral movement of fold hinges perpendicular to the shortening direction affects the surface structural patterns, regional topography and the complex 3D flow of the ductile crust and lithospheric mantle. The results of modeling are discussed on the basis of geophysically constrained crustal structure and surface deformation pattern of the Mongolian orocline.

2.2.1 Geodynamic setting of Mongolian orocline

The Kazakh and Mongolian oroclines are characterized by long lasting and orthogonal oceanic subduction beneath continental ribbons during the whole Early Paleozoic (Şengör et al., 1993). The architecture of this accretionary system (Fig. 8) is thus formed by a central continental ribbon and wide accretionary system similar to peri-Pacific accretionary systems in Japan or SE Asia. This belt was surrounded from one side by back-arc type oceanic lithosphere and from the other side by an accretionary wedge and subducting oceanic lithosphere from Cambrian to Silurian times (Fig. 8; e.g. Jiang et al., 2017; Wilhem et al., 2012). The evolution of the Mongolian orocline changed in the Devonian when the giant accretionary wedge

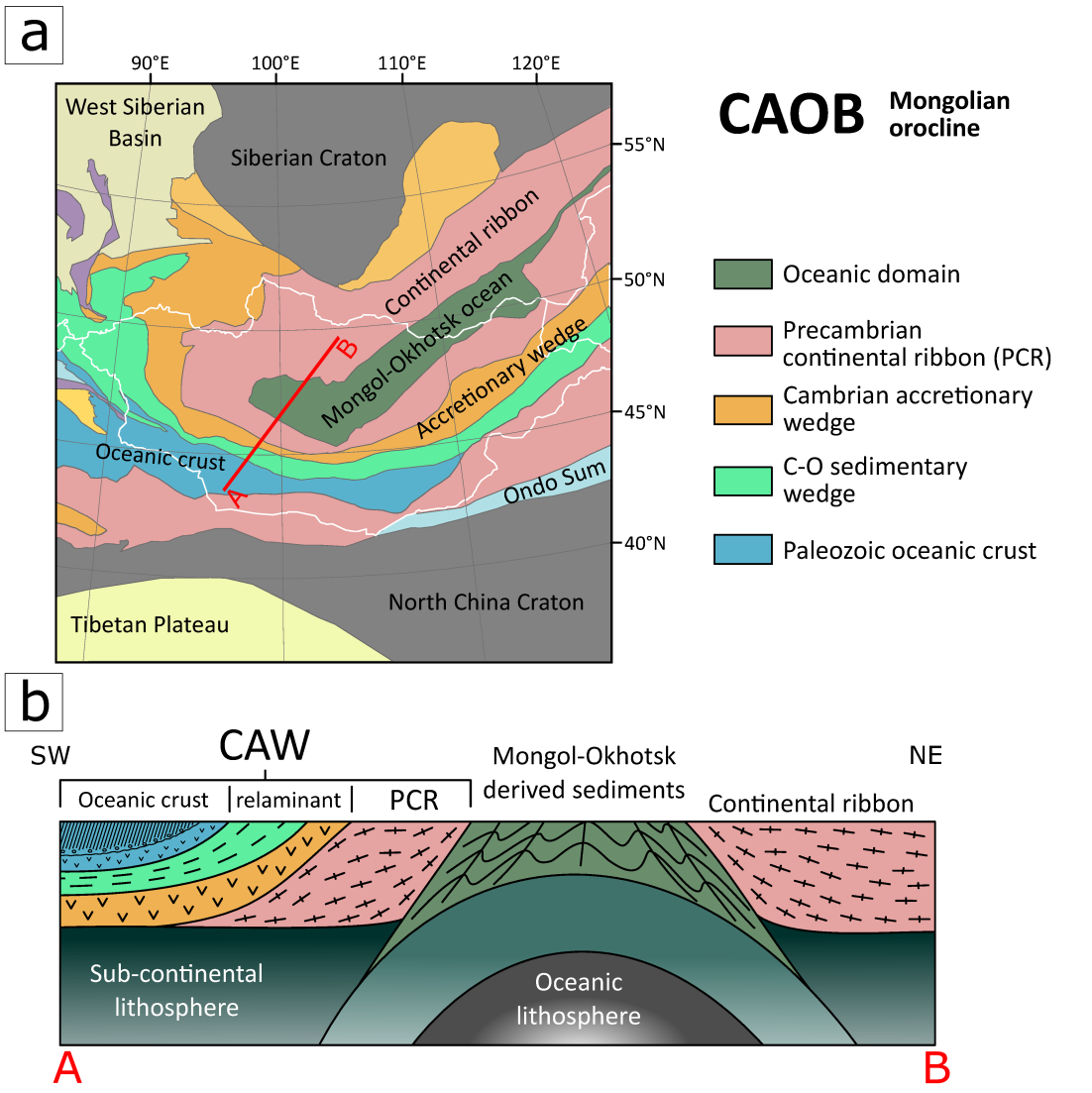


Fig. 8: Geological setting of the Tuva-Mongol orocline in the CAOB. (a) Geological background of modelled domain involving Mongol-Okhotsk oceanic domain, continental ribbon rimmed by the Cambrian accretionary, mainly volcanic, wedge, Cambro-Ordovician sedimentary wedge and Early Palaeozoic oceanic crust to the south. (b) The structure of the continental ribbon-accretionary wedge-hybrid lithosphere (CAW) represented by the relaminated, mostly felsic wedge, material beneath the oceanic crust (Guy et al., 2015; Nguyen et al., 2018) together with northerly continental ribbon. The oceanic domain is represented by the Mongol-Okhotsk oceanic lithosphere.

became molten above rolling back subduction. The wedge sediments were transformed to migmatites and granulites and flowed underneath the hanging wall oceanic plate generating vast gneissic relaminant (Guy et al., 2015). In that way originated a specific lithospheric structure marked by the existence of a continental ribbon, rimmed by an accretionary wedge partially transformed to high grade gneisses (Jiang et al., 2016) and by a hybrid lithosphere formed by an upper oceanic crust in addition to a lower crust formed by high grade gneisses issued from a metamorphosed accretionary wedge and possibly also a magmatic arc (Guy et al., 2015; Nguyen et al., 2018). This crustal segment can be considered as an embryonic and partly cratonized continental crust called here Continental Accretionary Wedge lithosphere (CAW). This specific setup was completed at the Carboniferous, when the whole complex system rotated together with Siberia in a clockwise manner (Cocks and Torsvik, 2007; Xiao et al., 2015; 2018). At the end of rotation, the Mongolian accretionary system was stitched to Siberia in the north, while its largest southern part pointed to the south. The belt was then surrounded by the Mongol Okhotsk Ocean in the east and a large subducting oceanic plate in the west (Fig. 8). It is also likely that the oroclinal bending of the subduction zone and CAW started to bend passively as illustrated by Lehmann et al. (2010) and Xiao et al. (2018).

The principal event modeled in this work is related to the Permo-Jurassic northward advance of the North China Craton (Edel et al., 2014) that resulted in the squeezing of the gently bended CAW between its northern edge and the southern boundary of northerly Siberia (Fig. 8). This stage resulted in massive shortening of the CAW which finally formed an isoclinal buckle fold surrounded by cratonic jaws. The core of the orocline was formed by the suture of the Mongol Okhotsk Ocean surrounded by the highly shortened CAW. The oroclinal buckling is accompanied by the formation of large scale E-W deformation zones similar to axial planar cleavage (Lehmann et al., 2010) and folding of horizontal strata between them. The deformation zones are characterized by narrow gravity anomalies implying important heterogeneous thickening of heavy upper oceanic crust (Guy et al., 2014). The hybrid lithosphere was transformed into a continental one i.e. into crust with intermediate granulitic lower crust, felsic middle crust and strong and brittle upper crust (Guy et al., 2015; Jiang et al., 2016; Nguyen et al., 2018).

It is important to understand how the whole laterally and vertically stratified system behaved during oroclinal buckling. In particular, the most interesting phenomena is the relative role of the buckled strong vertical layer, represented by a basement ribbon with a relic of subducted lithosphere, towards the advancing rigid North China Craton promontory, on vertical and horizontal fluxes of a weak relaminant and an underlying soft mantle. On the other hand, the complex lower crustal-mantle fluxes induced by buckling around a vertical axis and the surface deformation pattern related to upright folding with horizontal axis needs to be studied and understood. It is our plan here, to use analogue modeling and examine the above mentioned tectonic problems using a series of experiments which may lead to a better understanding of oroclinal bending processes which represents the most complex 3D tectonic system

and may help to unravel the mechanical aspects of continental growth in general.

2.3 Model setup

In order to understand the 3D deformation of the complexly stratified CAW, we need to produce a model setup that will resemble the ancient peri-Pacific accretionary system described above before the beginning of oroclinal buckling. The setup thus represents the oceanic lithosphere, continental ribbon with relic of subducted lithosphere and hybrid domain marked by the presence of continental and viscous relaminant beneath the upper rigid oceanic crust.

2.3.1 Model geometry

Eight experiments were conducted to simulate oroclinal buckling of a linear, Pacific-type accretionary belt developed along a continental margin. Experiments were setup to simulate full-wavelength oroclinal buckling of the subduction zone with a vertical mechanical anisotropy, and oceanic (O) and continental (C = CAW) subdomains characterized by horizontal mechanical anisotropy. The modeled continental subdomain was isolated from the sandbox by silicone putty to minimize the negative effect of the boundary conditions represented by the immobile walls of the apparatus and to enable an investigation of material transfer during the shortening of the domain. The initial curvature of the accretionary subdomain controls the full wavelength buckling of vertically oriented anisotropy (Fig. 9a) and allows the complex 3D interactions between oceanic and continental subdomains to be modeled. All experiments were conducted in the same analogue modeling box (lateral, horizontal and vertical dimensions – 43 cm to 43 cm to 20 cm).

2.3.2 Model materials

In both experiments we simulated the large-scale oroclinal buckling process induced by the collision between two continental blocks. The work was inspired by models of Edel et al. (2014), Guy et al. (2014a) and Lehmann et al. (2010) concerning the development of the CAOB generated by the convergence of the North-China (the piston in our models) and the Siberia cratons (the rigid wall in our models).

All rock analogue materials have numerous limitations in mimicking real-world rock rheology. In some experiments it is suitable to use Newtonian silicone putties for approximation of viscous rheology (usually in the lower ductile lithospheric parts), while many advanced experiments (numerical and analogue sandboxes) use combinations of more complex rheologies (for details see Buiter and Schreurs, 2006). For example, the combination of a sand material for approximation of a brittle rheology in the upper lithospheric part - and in some four layer experiments in the

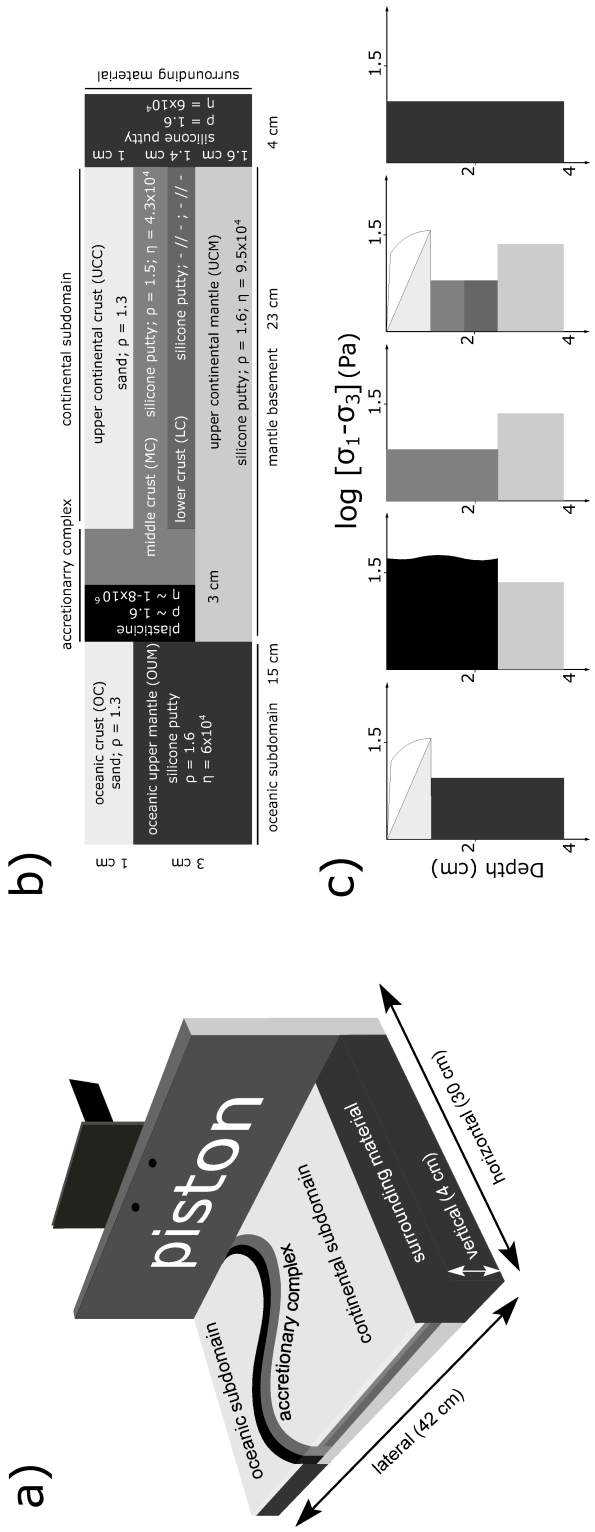


Fig. 9: Model setup of the oroclinal buckling experiments. 3D model view of the model domain with pre-folded orocline is shown in (a). The individual model layers with a specific material properties are illustrated in (b) with corresponding strength profiles in (c).

upper mantle segment (e.g. Brun, 2002) - with silicone putties (e.g. Cagnard et al., 2006) or with plasticine (e.g. Boutelier et al., 2008; Koyi and Mancktelow, 2001) for simulation of ductile flow of the lower crust and ductile mantle, is common. In other experiments, authors have used special types of plasticine for the construction of the whole model domain except for the upper crust or asthenosphere layer (e.g. in the modeling of oroclinal buckling, indentation, regional-scale folding, etc. (Duretz et al., 2011; Pastor-Galán et al., 2012; Tapponier et al., 1982)). Usually standard scaling methods based on the relationship between natural and laboratory conditions are used for the estimation of the model geometry aspects in combination with the applicability of a specific type of materials (e.g. Brun, 2002; Cobbold and Jackson, 1992; Davy and Cobbold, 1988; Davy and Cobbold, 1991; Hubbert, 1937; Ramberg, 1981).

In our experiments we used a combination of Fontainebleau sand (for modeling the brittle behavior of the upper crust – according to Byerlee, 1978), silicone putties (to represent a ductile crust and upper mantle segments) and plasticine (as a driving-layer of the buckling process i.e. an inner boundary condition). The rheological parameters of individual model layers are described in Tab. 1 and shown at Fig. 9b Fig. 9c. The horizontally layered continental subdomain is composed of silicone putty representing high viscosity upper mantle and low viscosity middle and lower crust, overlain by a Fontainebleau sand layer representing the brittle upper crust. This subdomain represents an oceanic upper crust relaminated by arc type lower crust and metasedimentary middle crustal layer of the CAW (Fig. 8). This subdomain is attached to a vertically layered accretionary subdomain composed of low viscosity silicone putty and a plasticine layer, underlain by silicone putty representing a high viscosity upper mantle. The plasticine layer drives the buckling process as displayed in Fig. 9a (for detail information regarding the use of plasticines for analogue models see Schöpfer and Zulauf (2002) or Pastor-Galán et al. (2012). In our experiments, this layer also represents an initial condition (i.e. a wavelength and amplitude are built into the layer prior to the deformation) that acts as an inner boundary condition. This step is not in conflict with model scaling because the aim of this study is to understand the flow of the lower crustal layers, the lithospheric mantle and the deformation of the upper crust associated with the buckling process. In all experiments the oceanic subdomain is composed of horizontal layers of silicone putty representing a high viscosity upper mantle and an oceanic crust overlain by a layer of Fontainebleau sand representing the brittle upper crust. This subdomain represents oceanic lithosphere of the Mongol-Okhotsk Ocean in Fig. 2. It should be noted that we reduced the friction between modeling box walls and the model materials by using petroleum jelly.

2.3.3 Model scaling

We followed the standard scaling techniques for the approximation of the geodynamic processes under laboratory conditions (see relations 1.1 - 1.6). Following

Tab. 1: Scaling model parameters.

		Upper crust	Middle - lower crust	Upper cont. mantle	Accretionary complex	Surrounding mat. / oc. mantle	Driving layer*
Density ρ (g . cm-^{3})	experiment	1.30	1.54	1.60	1.54	1.61	1.60
	nature	2.70	3.10	3.36	3.10	3.36	2.70
	scaling factor	0.481	0.497	0.480	0.497	0.482	0.59
Viscosity η (Pa . s)	experiment	-	4.30×10^4	9.50×10^4	4.30×10^4	6.50×10^4	-
	nature	-	1.13×10^{21}	5.00×10^{21}	1.13×10^{21}	5.00×10^{21}	-
	scaling factor	-	3.805×10^{-17}	1.90×10^{-17}	3.805×10^{-17}	1.20×10^{-17}	-
Material		Fontainebleau sand**	Silicone putty	Silicone putty	Silicone putty	Silicone putty	Plasticine

stable laboratory temperature: 18-21 °C
constant shortening rate

* two components (high viscosity silicone / thin-sheated plasticine)
** angle of internal friction ~30°

the examples of existing analogue experiments of indentation and shortening of lithospheric domains associated with faulting, surface elevation and displacement of the upper crust, the coupling and flow of lower crust, and the lithospheric mantle (e.g. Brun, 2002; Cagnard et al., 2006; Gapais et al., 2009), we set the model length to $30cm$, the model width to $42cm$ and model height to $4cm$ implying a space dimensions scaling factor $L^* = \frac{L_M}{L_N} = 8 \cdot 10^{-7}$. Due to the negligible role of gravitational Rayleigh-Taylor instability in our models, we ran all experiments under normal gravity acceleration implying $G^* = 1$. The scaling factor for densities ($P^* = \frac{\rho_M}{\rho_N}$) is in the range 0.481 and 0.497. For viscosity ($M^* = \frac{\eta_M}{\eta_N}$) the ratio varies from $1.2 \cdot 10^{-17}$ to $3.8 \cdot 10^{-17}$. From these scaling factors it is possible to obtain the factors for stress, time, strain-rate and velocity using the following relationships:

$$\sigma^* = P^* L^* G^*, \tag{2.1}$$

$$T^* = \frac{M^*}{\sigma^*} = t_M / t_N, \tag{2.2}$$

$$\varepsilon^* = \frac{\sigma^*}{M^*}, \tag{2.3}$$

$$V^* = \varepsilon^* \cdot L^*. \tag{2.4}$$

The Ramberg numbers for appropriate model parts are shown in Tab. 2.

2.3.4 Experimental procedure

In our experiments we applied finite strains represented by 25%, 37%, 45% and 50% horizontal shortening parallel to the lateral subdomain interfaces by the piston moving at a constant velocity of 2 cm/hour (Fig. 10). The laboratory temperature

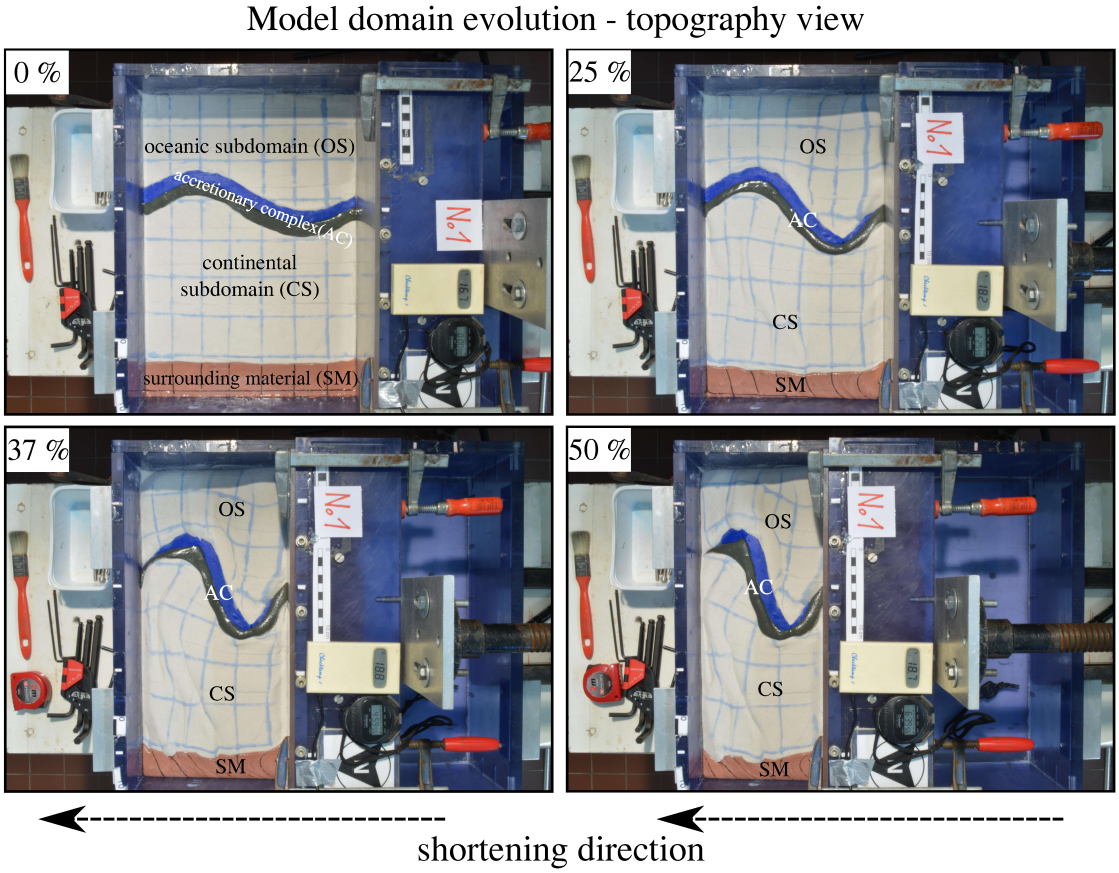


Fig. 10: Topographic view on experiment evolution after 0, 25, 37 and 50% of shortening.

during all experiments was 19 – 20 °C. To achieve different finite strain configurations, each type of experiment started from identical model setups (Fig. 9). All repeated experiments exhibited similar evolutions and verified reproducibility of the modelling. This comparison was performed according to the topography evolution and a visual inspection of model cross-sections. Only a few, negligible differences were noted and these were a result of small variations in the shape and thickness of the plasticine layer.

2.3.5 Model sectioning

An evaluation of the internal structures and mass redistributions was enabled by the sectioning of the deformed model domain along the major directions, i.e. normal to and parallel to the direction of shortening. To prepare these cross-sections, the model has to be frozen to eliminate undesirable deformation of silicon putty under its own weight. To obtain cross sections for different stages of model evolution, a series of identical experiments were carried out each being arrested after different amounts of shortening.

Tab. 2: Model scaling - Ramberg numbers

	model	original	scaling ratio
length (m)	0,03	30000	1,00E-06
time (s)	4500	3,15E+14	1,43E-11

	Upper crust (sand in the experiment)				
	density ($kg \cdot m^{-3}$)	thickness (m)	inter. frict. coef.	coh. Strength (Pa)	Rs
model	1300	0,01	0,6	100	1
nature	2700	1,50E+04	0,6	5,00E+07	7

	Lower crust (silicone in the experiment)					
	density ($kg \cdot m^{-3}$)	thickness (m)	viscosity (Pa·s)	grav.acc. (g) ($m \cdot s^{-2}$)	compr. rate V ($m \cdot s^{-1}$)	Rm
model	1540	0,014	4,30E+04	9,81	5,21E-06	13
nature	3100	1,50E+04	1,13E+21	9,81	6,34E-10	10

	Upper continental mantle (silicone in the experiment)					
	density ($kg \cdot m^{-3}$)	thickness (m)*	viscosity (Pa·s)	grav.acc. (g) ($m \cdot s^{-2}$)	compr. rate V ($m \cdot s^{-1}$)	Rm
model	1600	0,01	4,30E+04	9,81	5,21E-06	7
nature	3360	1,50E+04	1,13E+21	9,81	6,34E-10	10

	Upper oceanic mantle (silicone in the experiment)					
	density ($kg \cdot m^{-3}$)	thickness (m)*	viscosity (Pa·s)	grav.acc. (g) ($m \cdot s^{-2}$)	compr. rate V ($m \cdot s^{-1}$)	Rm
model	1610	0,024	6,50E+04	9,81	5,21E-06	27
nature	3360	3,50E+04	5,00E+21	9,81	6,34E-10	13

	Accretionary complex (silicone in the experiment)					
	density ($kg \cdot m^{-3}$)	thickness (m)	viscosity (Pa·s)	grav.acc. (g) ($m \cdot s^{-2}$)	compr. rate V ($m \cdot s^{-1}$)	Rm
model	1540	0,024	4,30E+04	9,81	5,21E-06	39
nature	3100	3,50E+04	1,13E+21	9,81	6,34E-10	52

* thickness of the thin part of the upper mantle (nature) is proportional to model

2.3.6 Surface topography analysis

Four cameras with different elevations and view angles recorded model surface images every 10 or 5 minutes (determined by the final amount of finite shortening). One camera was situated directly above the experiment – for observing the evolution of the model surface from top view. This was used for 2D velocity fields reconstructions (PIV - particle image velocimetry). The other three cameras were used for the reconstruction of 3D model topography using the Micmac software (e.g. Galland et al., 2016).

For a detail investigation of upper crust deformation and topography evolution the PIVlab software was used (Thielicke and Stamhuis, 2014). This enabled displacement field characteristics, such as velocity magnitude, direction, horizontal components and divergence to be determined. The reconstruction of the velocity

field provided an understanding of the model scale subsurface mass flow as well as the localized velocity gradients in specific parts of the model. The divergence of the velocity field was used to identify zones of localized thickening (negative divergence) or thinning (positive divergence) of the uppermost part of the model. These data were superimposed on the results obtained from the topography reconstruction obtained with the MicMac software to evaluate the mass transfer in a vertical direction.

2.4 Results

2.4.1 Finite geometry of modeled domain

In order to reconstruct lower crustal flow dynamics inside the modeled domain a set of perpendicularly oriented sections were analyzed. Both sections perpendicular and parallel to the shortening direction were obtained from two independent experiments with identical settings (Fig. 11 and Fig. 12).

2.4.2 Sections perpendicular to the shortening direction (i.e. parallel to the axial plane of the orocline)

The sections perpendicular to the shortening direction (referred as sections 1, 2, 3, 4 and 5 in Fig. 11) explore two contrasting domains; on the piston side of the model the fold hinge amplifies towards the continental subdomain (O→C, sections 1 and 2) and in the back stop part of the model the fold hinge amplifies towards the oceanic subdomain (C→O, sections 4 and 5). The inflection part of the fold is examined by section 3. These sections perpendicular to the shortening direction allow the investigation of horizontal and vertical material flows perpendicular to the direction of shortening in the oceanic subdomain (section 1), across the accretionary subdomain area (sections 2, 3, 4) and in the continental subdomain (section 5). Sections 1 and 2 (O→C) show similar pattern characterized by generalized thickening of the ductile part of oceanic and continental lithosphere. The main feature is the shortening of the continental subdomain parallel to the piston boundary resulting in underthrusting of the continental subdomain below the oceanic one. This movement is accompanied by exhumation of the subcontinental mantle beneath the propagating fold hinge and upright folding of the continental crust-mantle interface. Section 3 (across the fold inflection) shows horizontal movements limited to the sub-continental and oceanic mantle lithosphere which is accompanied with minor extrusion of continental mantle beneath the accretionary subdomain. The two sections 4 and 5 (C→O) show considerably thinner ductile part of continental subdomain compared to the O→C sections. This is accompanied with flow of sub-continental mantle lithosphere over the oceanic one in the fold hinge zone.

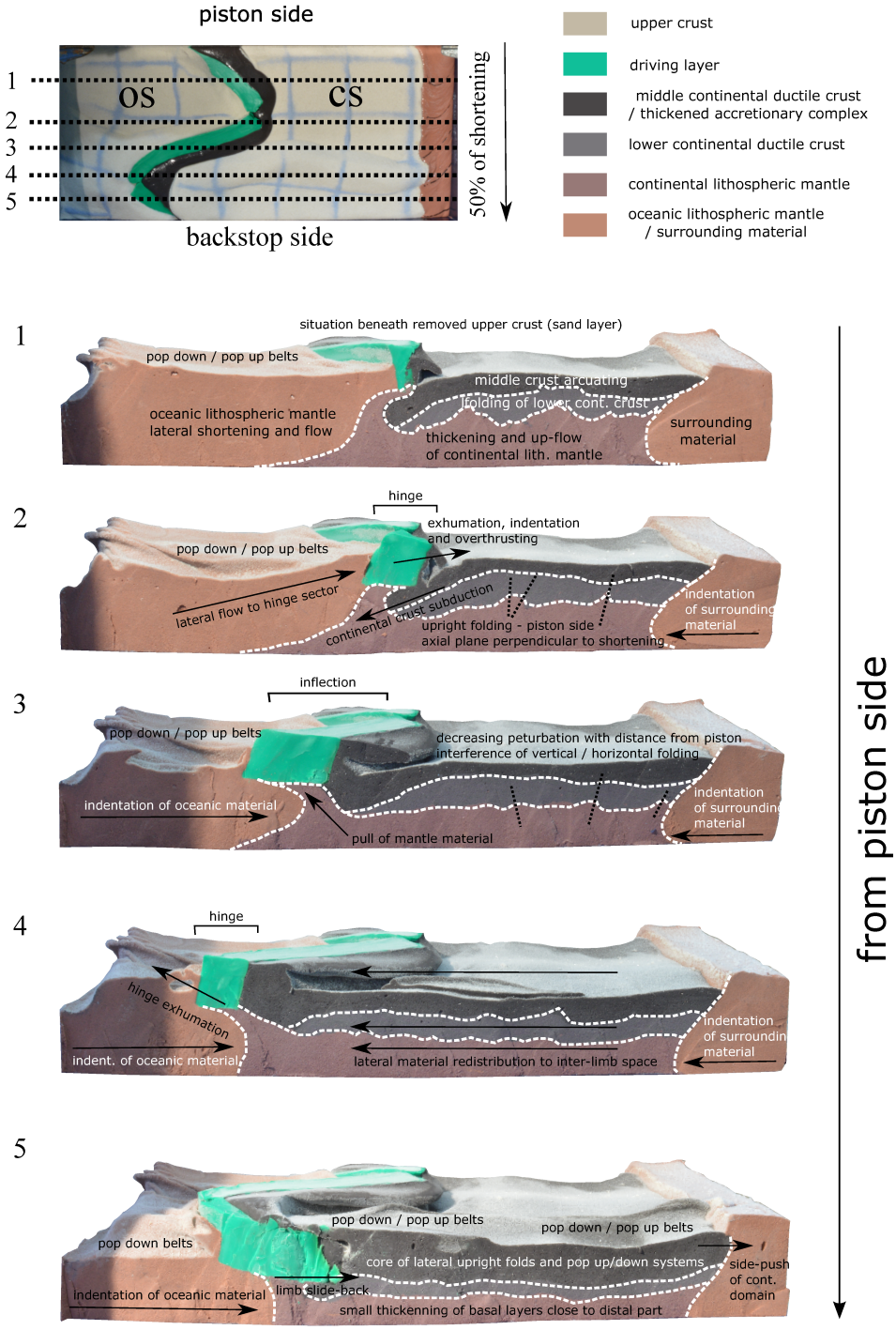


Fig. 11: The sections perpendicular to shortening. The orientation map of individual cross-sections of sliced domain is situated on top of the figure. The cross-sections display major structures and sense of material movement (arrows direction) in different parts of whole domain.

2.4.3 Sections parallel to the shortening direction (i.e. perpendicular to the orocline axial plane)

The sections parallel to the shortening direction (referred to as sections 1, 2, 3, 4, 5 and 6 in Fig. 12) explore the contrasting evolution of oceanic and continental subdomains. The oceanic subdomain (section 1) reveals significant and heterogeneous thickening of the oceanic lithosphere, which is most pronounced close to the piston boundary. This section intercepts the tip of the C→O fold hinge which has been exhumed. Subcontinental mantle has flowed laterally and this now occupies the region beneath the fold hinge. The shortening is accompanied by the deformation of the mantle-crust interface which now exhibits pop-down structures similar to those described by Cagnard et al. (2006). In contrast, the continental subdomain (sections 5 and 6) typically shows pronounced thickening of mantle lithosphere towards the piston accompanied by thickening of ductile crust and thinning of the mantle towards the back stop. The crustal deformation is localized in the axial plane of the hinge area of the C→O fold hinge and is manifested by the formation of pop down structures and cuspate-lobate folding of the crust-mantle interface. Section 4 intercepts the tip of the O→C fold hinge and exhibits overall homogeneous shortening of the whole lithosphere. This is expressed by pop-down structures along the upper-middle crust boundary and by cuspate-lobate upright folding of both the crust-mantle and lower-middle crust interfaces. Section 3 is typified by a contrasting response of the continental and oceanic subdomains. The continental subdomain fold hinge forms an antiformal domal structure formed by middle crust surrounded with marginal synforms and cored by lower crust and mantle associated with cuspate-lobate folding of the crust-mantle interface. The oceanic crust-mantle boundary is characterized by the formation of pop-down structures while the interface between oceanic and continental mantle forms large scale synformal structure. The main feature of section 2 is the influx of the oceanic mantle into the continental subdomain below the amplified crustal antiformal domal structure.

2.4.4 Incremental evolution

The two previous paragraphs described spatial variations in finite deformation pattern corresponding to a bulk shortening of 50%. Here, we make an attempt to understand the evolution of these structures by means of analysis of the incremental deformations. This is achieved by examination of sections across the continental and accretionary subdomains for three repeated identical experiments with different finite shortening 25%, 37% and 45% (Fig. 13). The folded accretionary subdomain (sections A-B) reveals contrasting behavior of the oceanic and continental subdomains. The early shortening (25%) is accommodated mainly by thickening of the oceanic lithosphere. In the second stage (37% shortening) a massive flux of oceanic mantle from the O→C hinge area towards the continental subdomain, can be observed. This flow causes the formation of an antiformal structure with a sub-horizontal

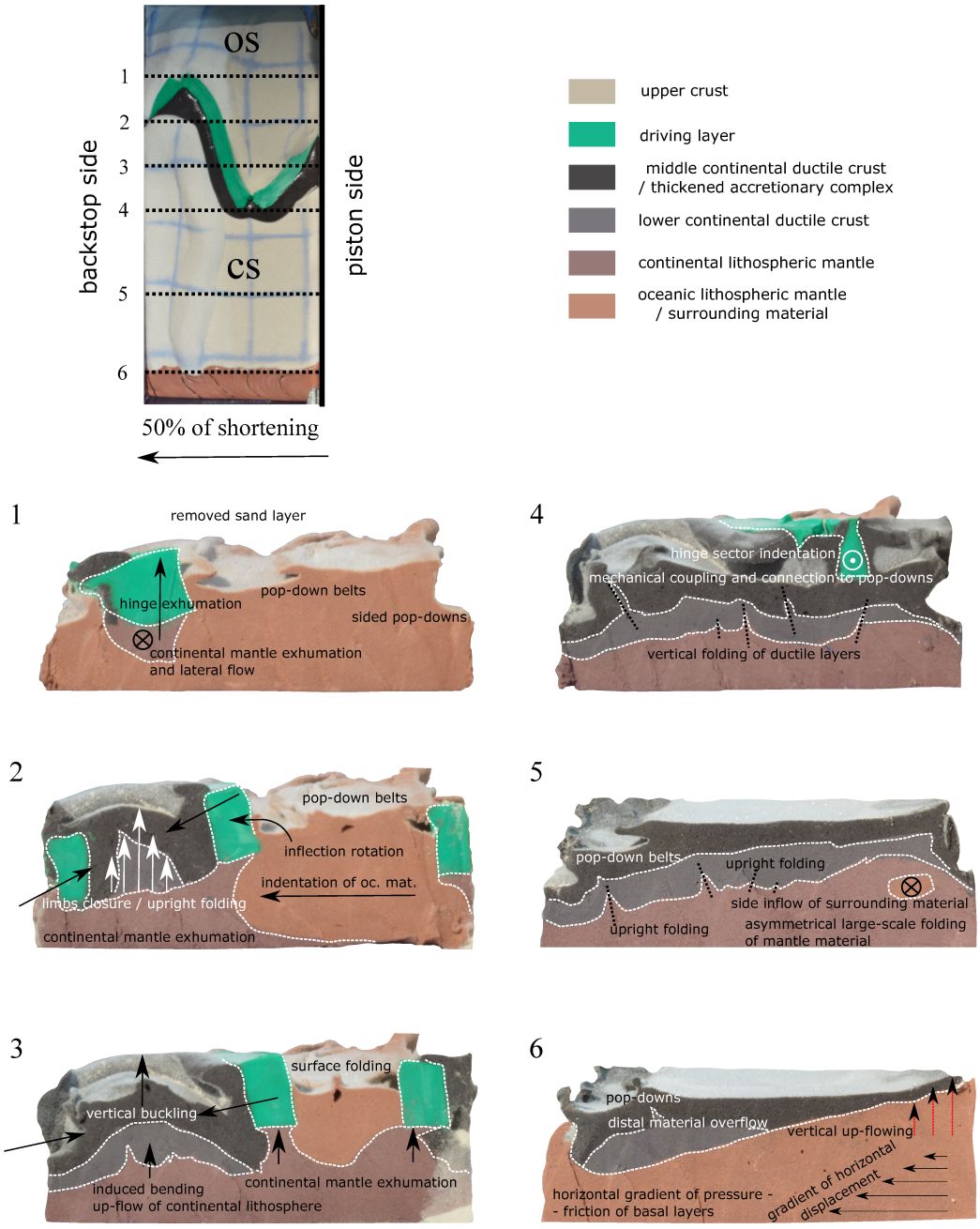


Fig. 12: The sections parallel to shortening. The orientation map of individual sections of sliced domain is situated on a top of figure. The cross-sections display major structures and sense of material movement (arrows direction) in different parts of whole domain.

fold axis in the region of the axial plane of the C→O fold (which has a steeply plunging fold axis. The subsequent stage of deformation (45% shortening) shows an amplification of the antiformal dome structure cored by continental lower crust that has been massively shortened by oceanic mantle lithosphere indentation. Here, the crustal antiformal dome is decoupled from continental mantle due to under thrusting of oceanic lithosphere. The evolution described above is accompanied by the dynamic deformation of the upper crust which is progressively uplifted in the C→O fold domain while in the O→C hinge area forms a synform which evolves into a large-scale pop down structure with ongoing shortening (45%).

The continental subdomain (sections C-D Fig. 13) reveals contrasting behavior of the crust and the lithospheric mantle during progressive shortening. The lithospheric mantle exhibits a classical indentation profile marked by an increase in thickening towards the piston (England and Houseman, 1986). As a consequence, a giant mantle dome structure develops close to the piston with attenuated crust in the apical part of the dome. In contrast, both the upper and lower continental crust thicken as they are traced away from the piston. While the upper crust is thickened as a result of thrusting and buckle folding, the middle and lower crust thickening occurs by homogeneous shortening associated with the development of cuspate-lobate structures at the mantle-lower crust, and lower-middle crust interfaces. Cuspate-lobate instabilities typically develop at boundaries between low viscosity contrast materials, when subjected to layer-parallel compression.

2.4.5 Evolution of model surface deformation

The analysis of the surface (Fig. 14) reflects the deformation of upper crust represented by the sand layer, which is removed before model sectioning. PIV analysis was used to assess the deformation of the uppermost crust during shortening. The deformation of the model surface was analyzed by inspection of the shear strain and velocity field (Fig. 14a) patterns for four shortening stages (3%, 25%, 37% and 45%) and the corresponding divergence of the velocity field (Fig. 14b). The deformation of the surface and corresponding response at depth are shown in a series of interpretative cross-sections for several model runs (Fig. 14c). For detailed analysis of the surface deformation, we refer the reader to follow the technical article aimed to application of the PIV technique for strain-analysis of indentation experiments including oroclinal buckling models (Krýza et al., 2019).

The beginning of the experiment (3% shortening) develops a homogeneous deformation in the continental subdomain (Fig. 14a) which is perturbed in the vicinity of the accretionary domain by the initiation of an active buckling (Fig. 14b). This could be detected by variations in the orientation of the velocity vectors which were observed up to a bulk shortening of 25% followed by a velocity field typical of post-buckle flattening (i.e. parallel velocity vectors). For subsequent increments of shortening (25% and 37%) the surface deformation partitioning can

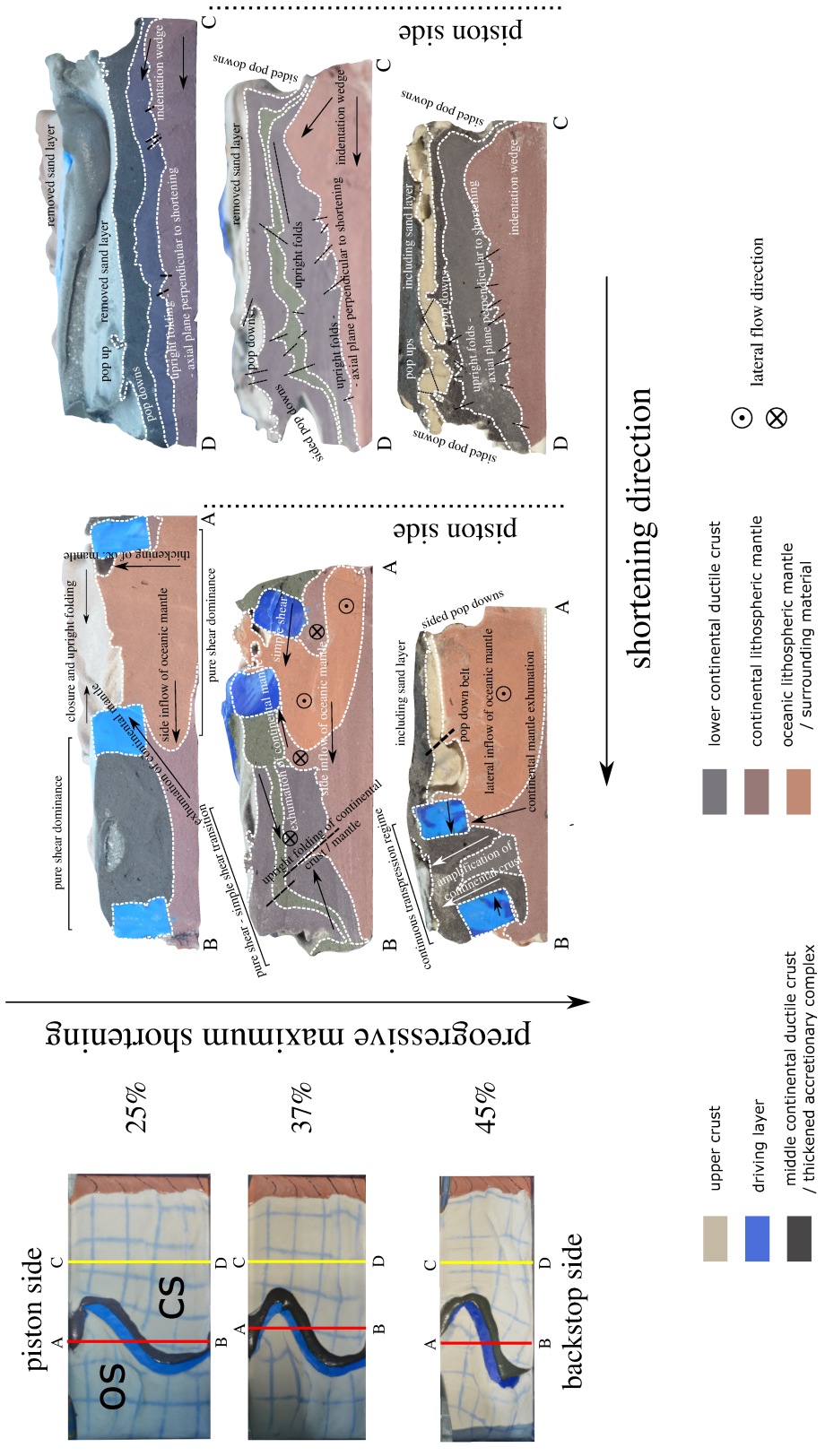


Fig. 13: The incremental evolution of the model domain. Three different stages of the shortening are shown at the left side with two lines for sectioning (red/yellow). The corresponding cross-sections at the right reveal the progressive development of a major deformation features inside the model domain.

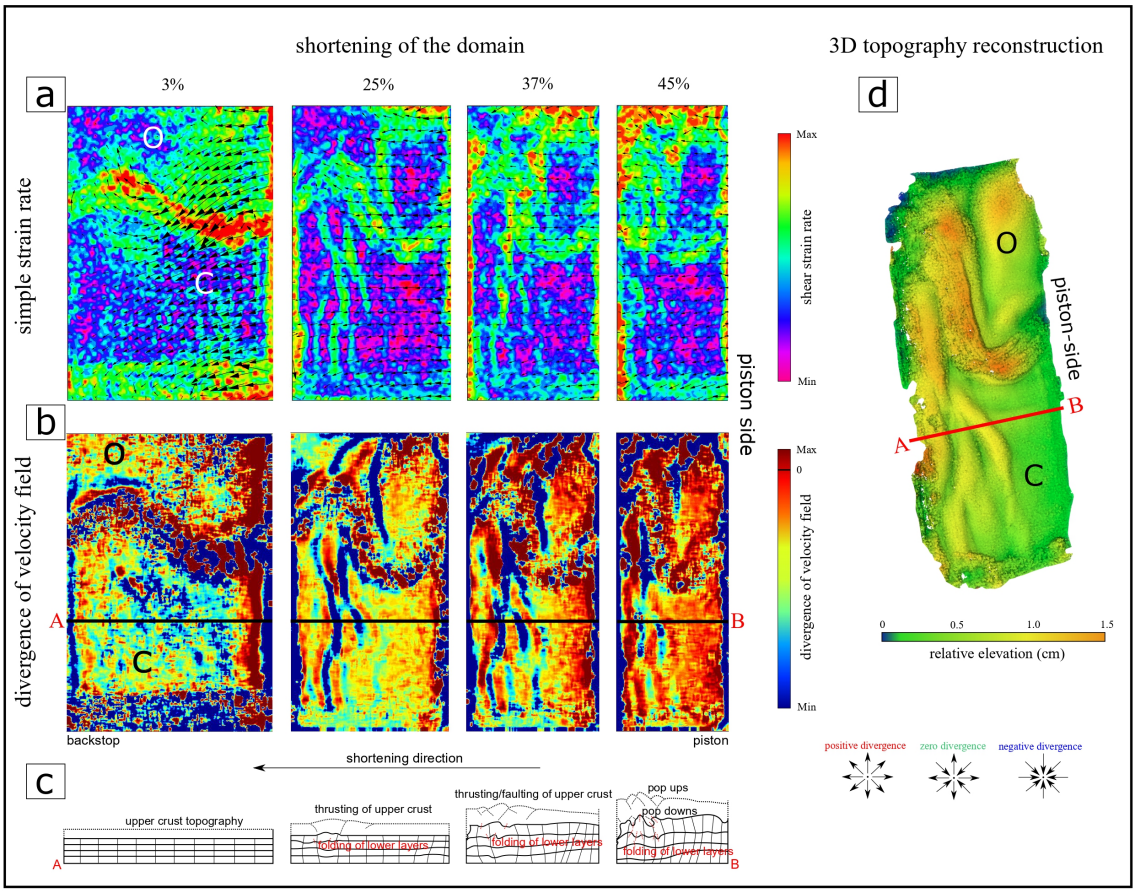


Fig. 14: The model surface analysis. For reconstruction of material transfer at the surface we analyzed the displacement field calculated by PIVlab software. Panel (a) represents a shear strain rate where arrows correspond to the velocity field. The divergence of the velocity field is shown in panel (b) where major anomalies in the field are related to the development of pop ups and synclines (c). The finite topography map is shown in (d). The digital elevation model (DEM) in panel (d) is modified after Krýza et al. (2019).

be observed in both the oceanic and continental subdomains where narrow zones of deformation gradients are developed parallel to fold axial planes (Fig. 14b – blue zones). With ongoing deformation (45% shortening) the domains separate into two areas characterized by different shear strain rate (contours on Fig. 14a); high strain rates in the oceanic domain and low strain rates in the continental domain.

This evolution can be clearly seen in the field of the velocity divergence (Fig. 14b). This shows a noisy pattern for small shortening (3%) reflecting homogeneous deformation. With the development of narrow zones of localized deformation (folding) the velocity field becomes characterized by high frequency negative and positive anomalies which developed preferentially along the axial plane of the C→O fold hinge in the continental subdomain and along the axial plane of the O→C fold in the oceanic domain. These anomalies correspond to the development of thrust related folds which are initial of the pop-up structures (e.g. Brun, 2002) and the narrow

synclines associated with the development of pop-down structures at deeper crustal levels described above (Fig. 14c).

The final topography reconstruction after 50% shortening (Fig. 14d) shows well developed positive topography anomalies along the folded accretionary subdomain and positive narrow linear ranges correspond to thrust related folds. The narrow and low topography anomalies alternate with the above mentioned negative values of divergence and correspond to narrow synclines, while large topography anomalies correspond to positive values of divergence that are associated with the development of the pop-up structures. The wide plateaus of neutral to high topography are developed in both oceanic and continental subdomains close to the piston side.

2.5 Discussion

2.5.1 Model limitations

As with most physical models our experiments are limited by the presence of un-geological boundary conditions which are represented by the fixed walls of the model box. The presence of these boundaries affect the model behavior adjacent to the walls. This can be clearly seen for example on the contour maps of dynamic parameters provided by the PIV calculations and it is possible to distinguish pop-down structures that form as a result of these boundary conditions and which do not relate to structures that might form in nature. However, we argue that the deformation in the inner regions of the model is unaffected by the size of model box and its fixed walls. The planar indentation profile (e.g. England and Houseman, 1986; Tapponier et al., 1982) will be developed in the inner domain of model independently of the box size and model results will not be affected.

The model setup represents an identical geometry to the model domain for all experiments that we analyzed. The subject of this article is not to prepare a parametric study but to bring new insights to mass transfer associated with oroclinal buckling on a lithospheric scale. In future models, we plan to test the effect of different convergent scenarios (e.g. various angle of convergence, shortening rate), and to incorporate an asthenospheric mantle or thermal aspect to the modelling. In the present model we have neglected any initial, pre-buckle, thickening of the model domain and supported orocline amplification by the pre-folding of the accretionary belt (See 0% shortening in Fig. 10). The geometry of pre-folded layers (O→C in the indenter side, C→O in the back-stop side) has been chosen in order to simulate material flow in a specific geological example namely the Mongol orocline after the subduction of the Mongol-Okhotsk oceanic domain (e.g. Lehmann et al., 2010; Edel et al., 2014). This scenario represents only the first part of the model domain (O→C) up to inflection of orocline.

2.5.2 Rheological interfaces and associated model dynamics

The model for oroclinal buckling is composed by a several silicone and sand layers according to the model setup. All interfaces between these layers i.e. inner boundaries represent transitions between domains of various rheological and/or mechanical properties. Here we discuss how general flow and deformation of the model domain is affected by these zones of heterogeneities. In the whole domain, it is possible to distinguish three types of rheological interfaces between the sand (brittle), silicone putty (viscous) and plasticine (plastic) materials: 1. brittle/viscous interface between the upper crust and middle/lower crust in the continental subdomain and between the crust and mantle in the oceanic subdomain; 2. plastic/viscous interfaces between the folded accretionary wedge (vertical subdomain) and both crust and mantle of oceanic and continental subdomains and 3. plastic/brittle interface is only present as the lateral boundary between folded accretionary wedge and oceanic upper crust. In addition, there are transitions between viscous materials of different viscosities reflecting lower crust-mantle transition within the continental and oceanic subdomains. Here we discuss the mechanical role of those interfaces in terms of mechanical coupling and/or decoupling during model evolution.

The major zone of mechanical decoupling is developed along the interface between the brittle upper crust (sand) and viscous middle-lower crust (silicone putty) generally called brittle-ductile transition. It is manifested by contrasting deformation patterns developed within viscous and brittle parts until 40% of shortening. While the viscous part of the model exhibits typical indentation profile in front of the piston, the brittle layer is detached and most of the deformation is localized along the axial plane of C→O fold. During subsequent shortening, this behavior progressively vanishes and both parts of the model exhibit more coupled deformation.

We can distinguish two types of brittle parts of the model according to the types of surrounding interfaces. While brittle part of continental subdomains is exclusively surrounded by viscous materials (except free-slip boundaries with piston and backstop of the model box), the brittle part of oceanic subdomains has different lateral interfaces with both plasticine and model box boundary. Such a configuration is manifested by the contrasting distribution of deformation (Fig. 10 and Fig. 14a,b) during initial shortening (up to 25%). We suggest that this behavior also affects the contrasting distribution of finite deformation within the upper crust of oceanic subdomain in respect to the continental subdomain.

Both plastic/viscous interface and transitions between viscous materials of different viscosities exhibit strong mechanical coupling during experiments and any significant differential motions have not been observed.

2.5.3 Mantle and crustal fluxes related to oroclinal buckling

The analyses of finite strain patterns along the axial plane of an orocline and on sections parallel and orthogonal to the shortening direction together with a study of the incremental evolutions of these sections and surfaces, allow the relationships between deep lithospheric fluxes and surface deformation related to oroclinal buckling to be determined. At the level of the lithospheric mantle, we observe classical indentation profiles in both oceanic and continental subdomains characterized by progressive thickening towards the piston boundary. However, below the folded accretionary domain the deformation pattern is different. Here, the lateral fluxes parallel to the fold axial planes dominate the deformation of both types of mantle lithosphere which are dragged by migrating fold hinges in a vortex manner. In this way the two contrasting mantle lithospheres are laterally juxtaposed where oceanic mantle flows towards the hinge domain of the O→C fold and continental lithosphere flows towards the C→O fold. The less competent oceanic mantle flows more efficiently to the O→C fold hinge area compared to slowly flowing subcontinental mantle. The lack of balance in mantle fluxes has a profound effect on the continental deformation which reacts by efficient flux of continental crust into the C→O fold hinge. These redistributions of mantle and crustal materials are associated with the formation of antiformal fold with horizontal axis in the region of the C→O fold and horizontal synform in the O→C fold domain. These processes are also reflected in the surface where pop-down structures dominate the O→C hinge while the C→O hinge shows the presence of a central antiform surrounded by narrow, marginal synclines (Fig. 15).

The consequence of unbalanced mantle fluxes leads to the development of a region dominated by crustal material in the C→O hinge compared to mantle dominated region in the O→C hinge zones. Mechanically, the C→O hinge is represented by a multilayer system formed by stiff continental mantle at the bottom, overlain by extremely weak lower crustal layer and strong middle and upper crust higher in the column. In contrast, the O→C hinge is formed exclusively by weak oceanic mantle and thin upper crust. Therefore, the integrated strength of the C→O multilayer system (England and Houseman, 1986; England and Houseman, 1989; Thompson et al., 2001) is significantly lower compared to adjacent O→C lithosphere. This difference implies that under horizontal compression the C→O system collapses and shortens preferentially. The deformation is controlled by the presence of a strong substratum overlain by a weak layer which is an ideal condition for detachment of a weak lower crust from the rigid upper mantle and the buckling of the stronger, middle-upper crustal layer. The formation of the detachment antiform in the C→O domain is accompanied by flux of oceanic mantle and the progressive development of material deficit in the OC region close to piston leading to the formation of large scale synform filled by oceanic crust decorated by pop-down structures at the surface.

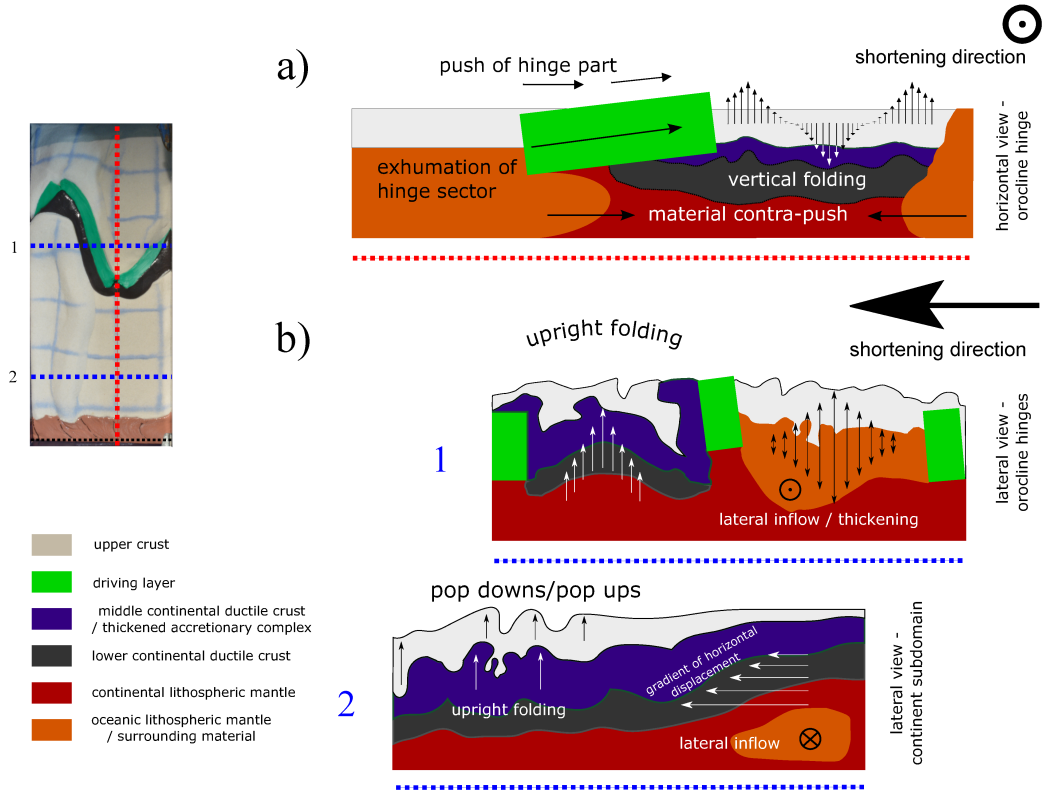


Fig. 15: Schematics of material transfer and key deformation features in the model domain. Section parallel to shortening of direction (a) shows thrusting of orocline hinge, upright folding and side flow of lower lithosphere, while (b) show deformation and material redistribution between both orocline limbs (b1) and asymmetrical folding of basal layers and forming of the pop up/down structures as product of mechanical coupling between ductile lower and brittle upper crust (b2) (*modified after Krýza et al. 2019).*

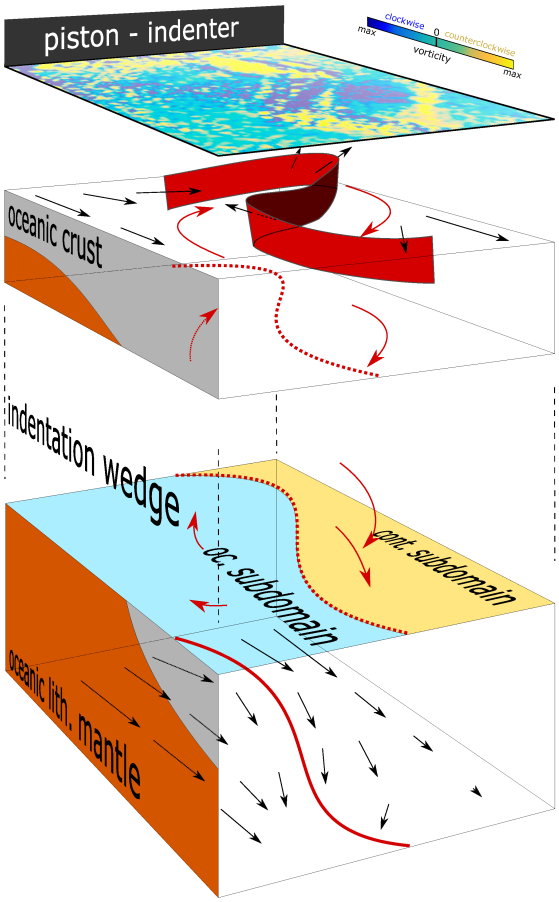


Fig. 16: The blockdiagram of the model inner dynamics. At the top is shown the contour map of the vorticity that reveals a clockwise rotation of the orocline inflection and counterclockwise rotation of the orocline outer limbs. The black arrows correspond to material flow from indenter side to backstop while red arrows show a decreasing vorticity in a material transfer from surface to basement. The red curve represents an interface between oceanic and continental subdomains.

2.5.4 Why the O→C and C→O hinges have opposite inclinations?

Fig. 15a and Fig. 16 show thrusting of oceanic over continental lithosphere in the O→C fold hinge and continental over oceanic in the C→O fold hinge. This requires that the O→C fold hinge plunges towards the oceanic subdomain and that the C→O fold hinge plunges towards the continental subdomain. The inclination angle of fold axes and associated thrusts of the lithospheric segments is governed by difference in vortex velocity between the mantle and upper crust as deduced from the serial sections and the PIV analysis of the surface deformation (Fig. 11, 12, 13, 16). It can be shown that the vortex velocity at the surface is high compared to slower flow of the viscous mantle at depth (Fig. 16). This velocity difference implies a progressive rotation of the fold axes from vertical to less inclined positions and the above described thrusting of mantle lithosphere.

2.5.5 Is the deformation driven by top or bottom fluxes?

Tikoff and Teyssier (2002) discuss the deformation of the lithosphere and argue that it occurs either by the movements of mantle layer (i.e. bottom driven tectonics) or by the rigid crust (i.e. top driven tectonics). In order to determine which of these two models is the more likely, it is necessary to determine which layer is mechanically dominant and controls deformation of the whole system. We have shown that the primary response of the mantle lithosphere with a low mechanical anisotropy is the development of a typical indentation profile (Fig. 12 and Fig. 13 – lateral view; Figure 14a – velocity field) and this has been simulated numerically by England and Houseman (1989). Both crustal sections and surface analysis show that during the early stages of the experiments the mantle governs the bulk lithospheric deformation. However, this behavior changes rapidly after ca. 5-10% shortening i.e. during the maximum amplification of the O→C and C→O folds within crust. The significant crustal flow related to fold amplification affects the mantle flow, so the originally developed indentation profile is modified by lateral redistribution of the continental and oceanic mantle. During this stage, it is the folding of the accretionary belt that governs bulk material fluxes in its vicinity leading to the accumulation of oceanic mantle material in the O→C fold and of continental crustal material in the C→O fold. After ca. 30% shortening the active folding ceases and post-buckle flattening i.e. homogeneous flattening takes over. The deformation becomes partitioning between the O→C and C→O folds because of the different integrated strengths of these two domains. During this stage the lithospheric deformation progressively passes to mechanically coupled behavior.

2.5.6 Implications for geodynamic concepts of curved orogenic belts

Both continental and oceanic lithospheres possess a horizontal stratification characterized by strong upper crust and upper mantle layers. This distribution of rheologically contrasting layers is responsible for typical deformation of the lithosphere such as the formation of thrust and fold belts, continental indentation or “crocodile” type wedging (Burg et al., 1998; Midtkandal et al., 2013). In contrast, oroclines are governed by the presence of vertical strong layer that fold around vertical axis (Pastor-Galán et al., 2012). The primary prerequisite for oroclinal buckling is the existence of a competent and vertical layer surrounded by less competent material. The most common mechanism bringing strong lithosphere into a vertical position is subduction of an oceanic plate as has occurred for example along the western Pacific margin. Here, the vertical subduction and accretionary system separates the back arc region formed by stretched continental crust, marginal basins and arcs from old oceanic lithosphere. These two systems are characterized by horizontal stratification and highly contrasting bulk rheology. There are several examples along the western Pacific margin showing high curvature of a subduction system interpreted as a result

of passive oroclinal bending related to differential subduction retreat (Menant et al., 2016; Rosenbaum and Lister, 2004).

The model presented in this work shows the behavior of such a system when it is compressed parallel to the subduction zone. Such systems are well known from Central Asia, where the giant Paleozoic Kazakh and Mongolian oroclines occur (Şengör et al., 1993; Şengör and Natal'ln, 1996; Yakubchuk, 2005). The well-studied Mongolian orocline is formed by a folded subduction system surrounded by horizontally stratified pericontinental complexes and relaminated oceanic domains called here CAW (e.g. Edel et al., 2014; Lehmann et al., 2010). In this region the C→O and O→C systems exist and their deformation can be explained in the light of model predictions presented above.

The gravity data show large-scale redistribution of the lower crust (Guy et al., 2015) and the development of magmatic provinces spatially related to the orocline geometry (Guy et al., 2014b). In particular, it is a major gravity low in the hinge area of the Mongolian orocline, along its axial plane more or less coinciding with the Permian Hangay and Triassic Khentey alkaline plutonic provinces (Fig. 17a). This alkaline intraplate magmatism was previously interpreted as a result of migration of South Khangai hot spot (e.g. Kovalenko et al., 2004; Yarmolyuk et al., 2007) but may be a proxy of giant elevation of hot lower crust and thermally perturbed mantle in the hinge zone and axial plane of the orocline as predicted by our model. In our model, the elevation of hot mantle (Fig. 11 and 17 – oceanic subdomain fold) might result in its melting and development of massive alkaline magmatic provinces in the region. The presence of hot and low viscosity felsic material at depths that is depicted in the whole accretionary system of southern Mongolia as a source of magmatism (Guy et al., 2014a; 2015; Nguyen et al., 2018) is a necessary requirement to accommodate deformation in both hinge and limb areas of orocline. Petrological and geophysical studies show linear belts of Permian granulites associated with important narrow gravity and magnetic lineaments (Fig. 17b and c) that coincide with extrusions of this exceptionally hot granulitic crust along orocline hinge and limb areas in the Chinese Altai (Li et al., 2004; Broussolle et al., 2018a; 2019). Similarly, E-W trending deformation zones associated to alkaline magmatism coinciding with magnetic lineaments and vertical deformation zones (Seltmann et al., 2011; Guy et al., 2014b) were reported from the study region (Fig. 17c). These recent observations indicate a major mobility of hot felsic relaminant and depleted mantle (source of alkaline magmatism) during Permian times and its redistribution associated with growth of the orocline. All these studies are in agreement with massive mantle and lower crustal fluxes parallel to the axial planes of the orocline and perpendicular to the general shortening direction as shown in this study. These structures can be well seen in Fig. 11 and 12, where narrow vertical cusps can be observed. These lower crustal fluxes resemble those reported in orogen parallel extrusions known from Tibet (Dewey, 1988; Zhang et al., 2004; Zheng et al., 2006) and the Eastern Alps (Ratschbacher et al., 1991a,b). In contrast to these collisional systems that require the existence of a free lateral boundary represented by a retreating subduction zone, in our system the

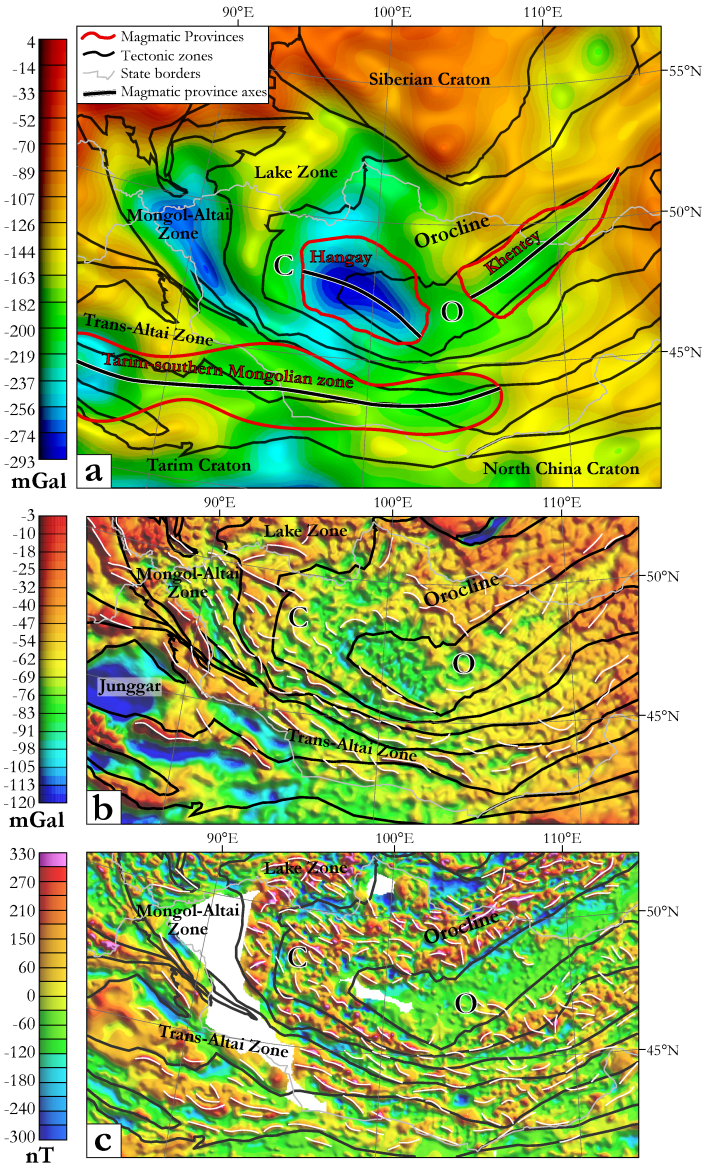


Fig. 17: Geophysical maps used as a likely support of a massive redistribution of the lower crustal material related to the oroclinal bending. (a) Long wavelengths Bouguer gravity anomaly map calculated from EGM08 (Pavlis et al., 2012). The cutoff wavelengths applied is 200 km. The figure shows three major gravity lows related to defined magmatic provinces: the Hangay, Khentey (Yarmolyuk et al., 2013) and Tarim-southern Mongolia magmatic zone (Economos et al., 2012). These alkaline magmatic provinces may result from the melting of elevated mantle and lower crust during oroclinal bend. (b) Isostatic residual gravity anomaly map underlines the distribution of narrow gravity ridges interpreted as zones of intense vertical deformation related to the locking up of oroclinal bend by Guy et al., (2014b). These zones are rooted at 20 km depth (Guy et al., 2015) and may represent proxies of pop down structures modelled in this work. (c) Magnetic anomaly map from EMAG2 (Maus et al., 2009) showing the differences in magnetic signal between low frequency and low amplitude signal in an oceanic domain compared to high frequency and high amplitude signal of continental ribbon domains. Particularly important are narrow magnetic highs related to Permian extrusions of granulite facies material in the Chinese Altai and the shear zones affecting the oceanic crust in Mongolia.

lateral material fluxes are controlled by the active amplification of the oroclinal fold. Finally, a characteristic feature of the Mongolian orocline is a remarkable contrast between a high frequency and amplitude magnetic anomaly signal of the continental ribbons compared to low frequency and amplitude signal of the oceanic domains (Fig. 17c) supporting the main shape of oroclinal bend. Moreover, the development of upright folds with horizontal axes that formed simultaneously with the oroclinal buckling in the continental and oceanic subdomains is observed (Guy et al., 2014a; Lehmann et al., 2010). This folding is best developed in the model surface analysis (Fig. 13). Importantly, the indentation profile expressed in the model may well reflect structural features described recently along the boundary of the Chinese Altai and southerly east Junggar oceanic crust (Jiang et al., 2019; Broussolle et al., 2019).

2.6 Conclusions

This study represents a new approach to the simulation of the mechanical processes related with the building of large oroclinal systems that are associated with lateral compression. It investigates mass transfer at the model surface which is responsible for the deformation of the upper crust and for the development of topography, ductile flows inside the model domain and the mechanical coupling in lithospheric multilayer. The main modelling features can be summarized as follows:

- The lateral shortening of the pre-folded accretionary belt leads to development of two regional-scale types of folds: the steeply plunging orocline and the upright folds which form in the oceanic and continental domains with subhorizontal fold axes.
- Generally, all curvilinear fold developed in the upper crust express geometry of the axial planes of upright folds affecting also deeper lithospheric layers.
- The overall deformation distribution shows significant thickening and exhumation of lower ductile layers at the piston side (results of indentation), accommodated by thickening of the upper crustal material at the back-stop side.
- The overthrusting of oceanic crust along one of the orocline hinges (O→C) and continental crust along the other (C→O) is associated with material vortex flow around the inflection of the orocline. This pattern decays towards deeper lithospheric layers, where the lateral flow of material is negligible.
- Our model suggests that the geometry of the orocline is non-cylindrical with increasing plunge of fold axis from upper crust towards deeper lithospheric layers.
- The redistribution of lower crustal and mantle material related to oroclinal buckling is consistent with some geophysical, namely gravity and magnetic data for the Mongolian orocline. In particular, the model may explain formation of a giant gravity low in the hinge zone of the Mongolian orocline that can

coincide with vertical flux of hot mantle and hot lower crust. In addition, the linear zones of gravity highs associated with vertical zones parallel to orocline axial plane may reflect formation of simulated pop-down structures. Finally, the deformation gradient reported along the southern flank of Mongolian orocline may correspond to indentation profile expressed by our model.

2.7 Appendix

2.7.1 The first generation of experiments

Before we developed the model where a full-wave-length orocline was simulated, the first generation of experiments was performed (Fig. 18). In these models we partly followed the scheme of Pastor-Galán et al. (2012) were the continental ribbon is progressively buckled and developed the architecture of an arcuated orocline with developed orogenic root in the central part of the arc and with large-scale extensional ruptures oriented parallel to the shortening direction. However, in our modelling approach we surrounded the continental ribbon by neutral silicone material (Fig. 18b) and incorporated vertically oriented layers (including driving plastic layer) at the side of the central continental subdomain (Fig. 18a). The model evolution (Fig. 18c) here corresponds more realistically to natural material fluxes which are not separated by discontinuum from surrounding rock materials.

The model domain deformation corresponds to buckling of the driving layer and vertically oriented layers representing an accretionary belt. The axial plane of the developed orocline is characterized by strong hinge indentation through a central continental ribbon (Fig. 18c). Similarly to the second generation of experiments - that are presented above - the significant ascent of the mantle material occur beneath the orocline hinge zone (Fig. 21b). The shear zones with convergence to the hinge zone are partly developed in upper brittle crust in the continental ribbon, however, in comparison to the second generation of experiments, the topography of the models is insignificant.

2.7.2 Interlimb areas of the orocline

The topography of the upper crust in a full-wavelength orocline models (the second generation) is significantly affected by pure-shear deformation between both interlimb sectors (Fig. 19). The deformation of the oceanic domain (O→C) is characterized by less significant vertical extrusion of the oceanic mantle which is compensated for by development of pop-down and pop-up structures. In contrast, the continental domain (C→O) is characterized by buckling of horizontal layers in the interlimb sector and upright folding. The pop-down structures are not fully developed in this region while the pop-ups dominate the topography (Fig. 19 - 45-50% shortening).

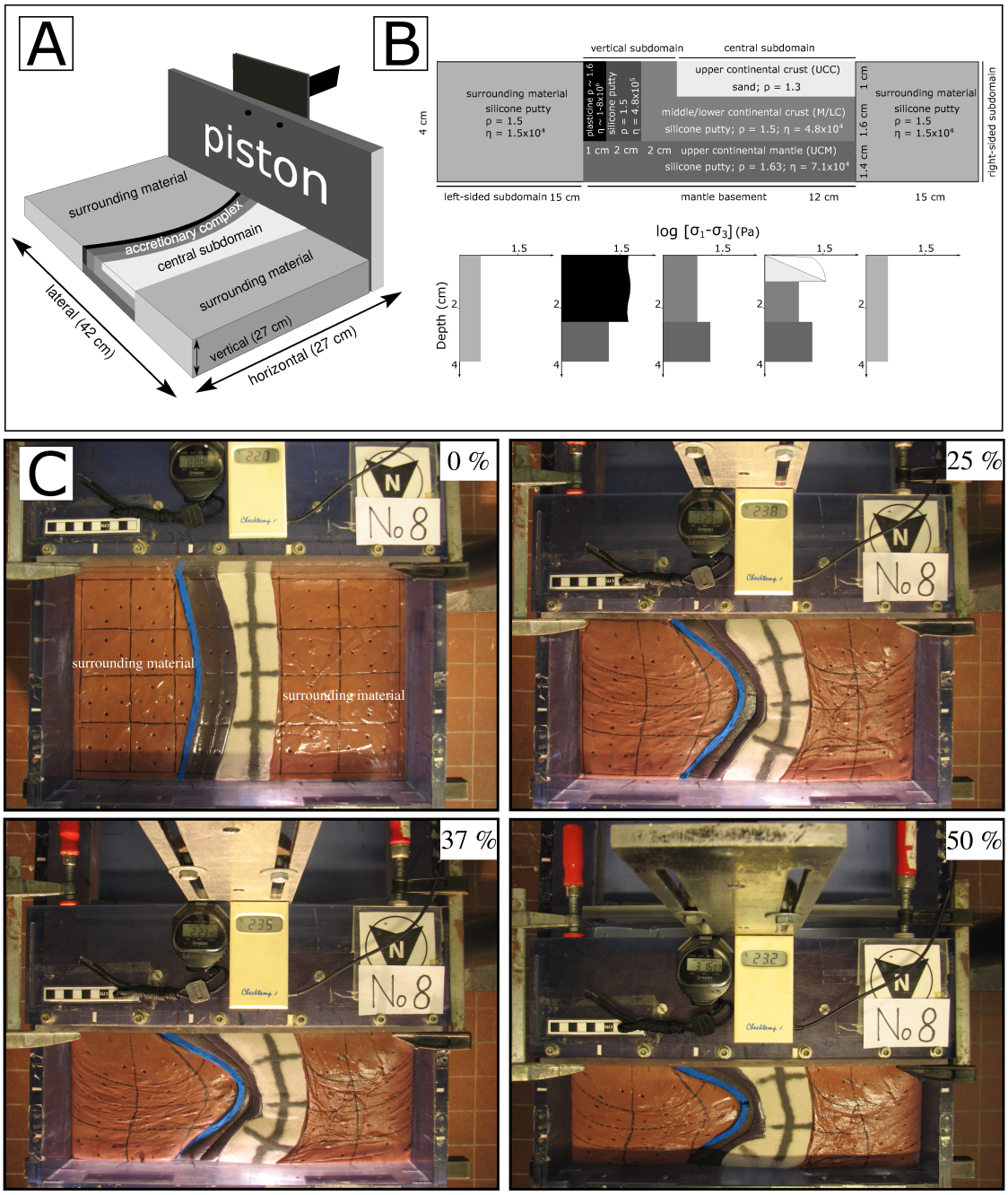


Fig. 18: The first generation of experiments of oroclinal buckling. The geometrical model setup (A) contains half-wave orocline. The model materials with rheological properties and strength profiles are shown at (B). The model evolution with typical buckling of central layers (accretionary complex) is illustrated at (C) for four evolutionary stages.

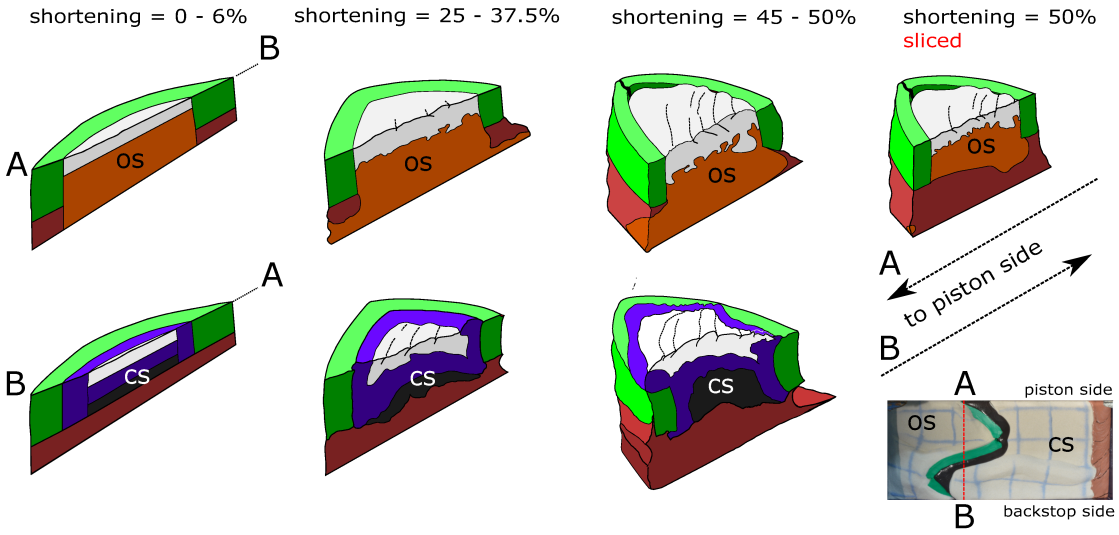


Fig. 19: Evolution of interlimb and hinge orocline sectors for O→C and C→O domains. Both interlimb sectors are reoriented to the same projection direction and orientation respective to piston (indenter) is illustrated by arrows.

2.7.3 Velocity components and displacement differences

The components of displacement and velocity field are shown at Fig. 20. The main deformation lines in the model domain correspond to the gradient in displacement field and as its progressively moved from identer side to back-stop side (Fig. 20a). Both horizontal components of the velocity field show a main direction of the material transfer at the top of the model. The velocity azimuth map shows that the dominant direction of the velocity is in C→O sector during ca 10-20% of shortening while for 0-10% shortening the flow is more significant in O→C sector in the reverse direction.

The horizontal displacement in direction of the domain shortening varies for different model subdomains (Fig. 20b). As the model behaves as a system with the Poiseuille type of channel flow (Fig. 20c) the maximum displacement occurs for central (continental) subdomain while oceanic subdomain has a smaller displacement. This is one of the factors that affect asymmetry of pop-down and pop-up belts distribution in the model domain (Fig. 14).

2.7.4 General 3D flow

The calculations of the real 3D vlocity data were not possible due to absence of the CT (X-ray) tomography device. For this reason we estimated inner material displacement (Fig. 21) from a series of cross-sections (Fig. 11-20) where we analyzed incremental evolution of deformation features. The reconstructed displacement field is supported by a 2D velocity field which was calculated by the PIV (particle image

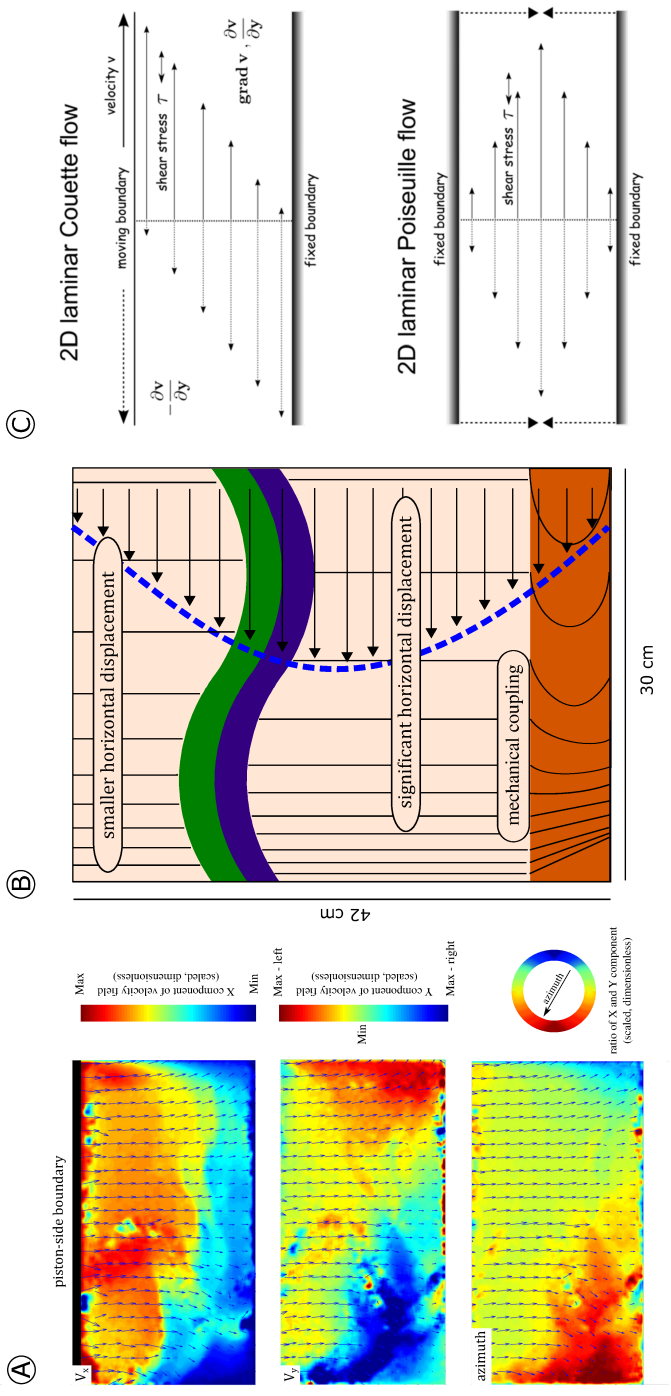


Fig. 20: Velocity components and style of flow in the model domain. (A) representing x and y components of the velocity field and calculated azimuth of material transfer. X component has a highest values distributed close to the indenter while y component has a maximum in both directions, perpendicularly to the indenter. Colorbar for azimuth distinguish left, central and right direction (illustrated by arrow in colored circle). (B) is a map of the main differences in the displacement for all model subdomains. Dashed line denotes Poiseuille type of channel flow while straight black lines and their spacing illustrate differential displacement. (C) shows two basic types of the channel flow in the model domain, Couette flow and Poiseuille flow and their principle.

velocimetry) method. The 3D reconstruction show main directions and estimated magnitudes of the displacement between material elements in a series of the sections that are oriented in perspective view from indenter through inflection plane to the backstop. The individual stars in the 2D velocity field map corresponds to the main deformation features and velocity anomalies (numbers in brackets in further text).

From 1-10% shortening of the model domain is visible rapid amplification of driving layer (1) with indentation of the hinge and inflow of the material which is situated in interlimb sectors (3,4). The significant deformation of the upper crust in the oceanic and continental domain correlates with a sharp gradient in the velocity field (2,6) and maximum velocity is close to the indenter in a central part of the model domain (5). The velocity gradient is progressively moved from indenter to distal parts (8,10) where the main surface deformation will take a place during later evolutionary stages. The mechanical coupling between surrounding material and continental material occurs during this stage (7). Velocity of the material displacement is homogenized in the wide field between these velocity gradients and indenter side (9). In the lower levels of the continental and oceanic domain this displacement is less significant than in top levels due to the presence of the rigid basal plate at the bottom (scheme of displacement follows Couette style of channel flow).

When the model domain is shortened up to 20-25% the localized areas of high velocities and sharp gradients (11,12) became more distributed (15,16) and development of associated structures in the upper crust (pop-up, pop-down structures, strike-slips etc.) is finished. The amplification of hinge areas (14) and rotation of the material around inflection of orocline (13) are also slowed. The indentation of hinges is responsible for vertical gradient in material displacement (Couette flow) and partial mantle pull from lower levels to continental and oceanic subdomains (Fig. 21 - 3D reconstruction panel).

The late evolutionary stage between 37-50% of domain shortening represents dominantly pure shear deformation with no significant development of topography. The small variations in the velocity field are associated with a thrusting in front of hinge areas (14), material rotation around inflection axis (13,17) and small material transfers between continental domain and surrounding material (18,19). The progressive movement of deformation line (velocity gradients) is documented by an indentation profile of surrounding material (Fig. 21 - 3D reconstruction panel). In the piston side, the material is indenting the continental subdomain while in back-stop part the surrounding material is indented by continental material.

2.7.5 Mantle exhumation and Bouguer anomalies in Hangai zone

The model explains to a certain extent the large-scale negative Bouguer anomalies in the Hangai sector of the Tuva-Mongol orocline (Petit et al., 2002) that are probably associated with significant mantle ascent beneath the O→C orocline hinge zone

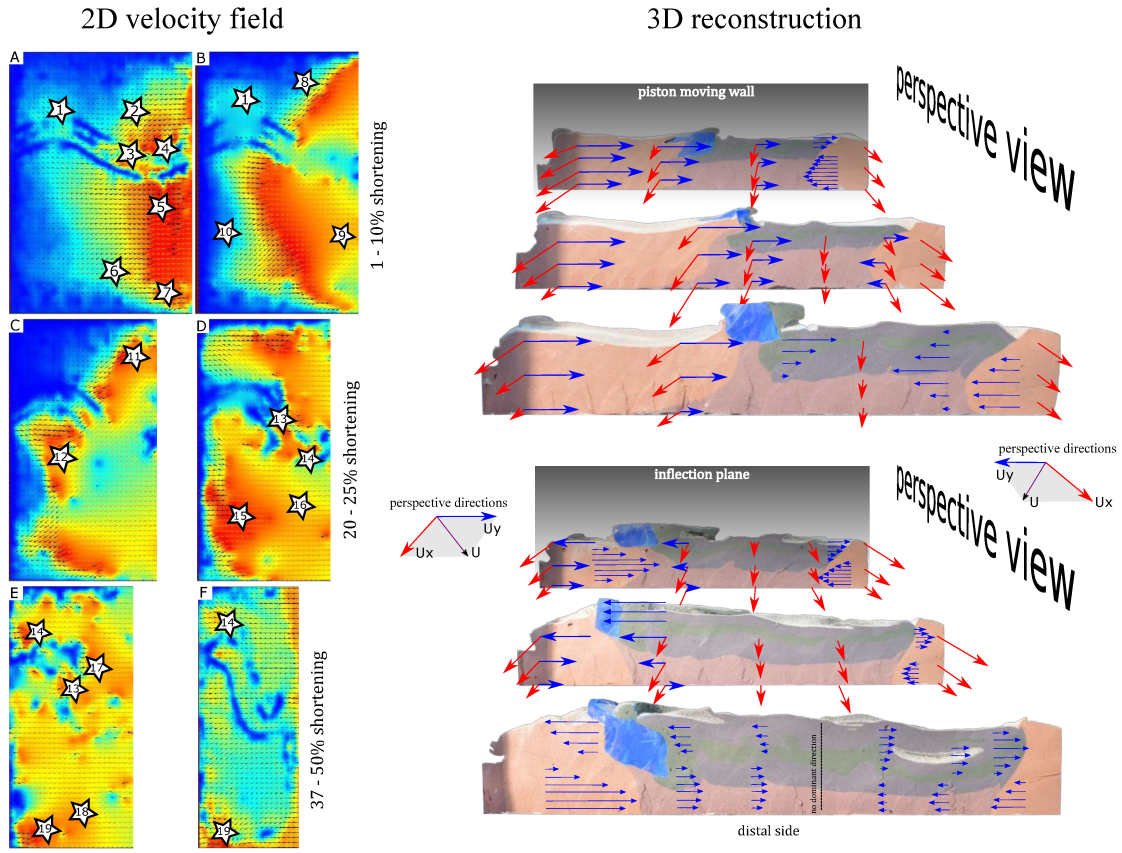


Fig. 21: 2D velocity field was calculated by PIVlab toolbox while 3D reconstruction was derived from sectioned model domain for various finite shortening compared with 2D velocity field. Individual numbers in the small stars represent main flow and deformation features (see text for further explanation). Section in 3D reconstruction are oriented from piston side (upper three sections) through inflection plane to backstop side (lower three sections). All sections and arrows are for illustration of 3D flow oriented in perspective view.

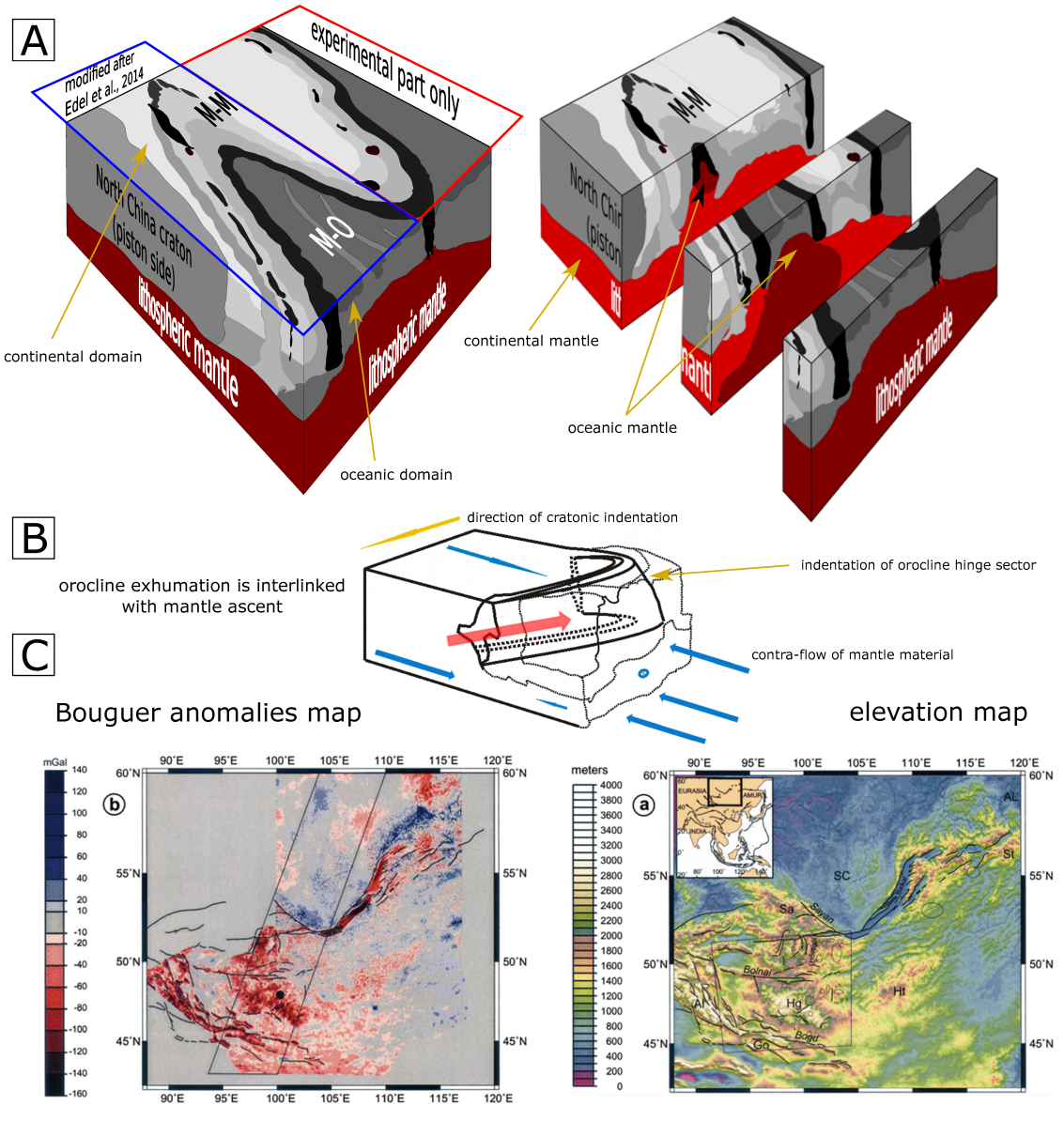


Fig. 22: At the (A) is a block diagram combining the geodynamic model of oroclinal buckling of Tuva-Mogol orocline (Edel et al., 2014) and presented analogue model. The sectioned diagram shows (as previous analysis confirmed) the oceanic mantle ascent during indentation of North-China craton (piston indenter). The mechanics of the ascent of the pushed and pulled mantle is shown at (B). The corresponding sector in Tuva-Mongol orocline is represented by the Hangai dome (C). Diagrams in (C) show residual Bouguer anomaly map and elevation map for Hangai sector (taken from Petit et al., 2002).

(Fig. 22). The block-diagram (Fig. 22a) combines schematics that are modified after Edel et al., 2014 and the presented model. From the sections it is visible how continental and oceanic mantle lithosphere is cambered beneath interlimb zone of arcuated accretionary complex with the most exhumed part situated underneath the hinge sector. This also corresponds to the vertically rotated orocline (Fig. 22b) which is responsible for mantle pull and flow-up. The presence of hot mantle material may be responsible for partial melting of the lower crustal rocks as well as the mantle itself experienced decompression and underwent partial melting. Decreasing regional density of rock material then affects the distribution of light material and negative values of Bouguer anomalies.

2.8 Acknowledgments

This paper was supported by the Czech Science Foundation grant No.: 17-17540S, National Natural Science Foundation of China (41888101), and the Center for Geosphere Dynamics project UNCE/SCI/006. We thank to J. J. Kermarrec for his help in the modeling laboratory at Géosciences Rennes, University of Rennes 1, France. Primary data for: Oroclinal buckling and associated lithospheric-scale material flow - insights from physical modeling: implication for Mongolian orocline" are available on https://dataverse.harvard.edu/dataset.xhtml?persistentId=doi:10.7910/DVN/QNFHDO, Harvard Dataverse

2.9 References

Beaumont, C., Jamieson, R. A., Nguyen, M. H., and Medvedev, S. (2004). Crustal channel flows: 1. Numerical models with applications to the tectonics of the Himalayan-Tibetan orogen. Journal of Geophysical Research: Solid Earth, 109(B6).

Beaumont Ch., Nguyen M. H., Jamieson R. A. and Ellis S. (2006) Crustal flow modes in large hot orogens. Geological Society, London, Special Publications, 268, 91-145.

Boutelier D., Schrank C., Cruden A. (2008) Power-law viscous materials for analogue experiments: New data on the rheology of highly-filled silicone polymers. Journal of Structural Geology, 30, 341-353.

Boutelier D., Oncken O., Cruden A.R. (2014) Trench-parallel shortening in the forearc caused by subduction along a seaward-concave plate boundary: Insights from analogue modelling experiments. Tectonophysics, 611, 192-203.

Boutelier, D., Gagnon, L., Johnston, S., and Cruden, A. (2018). Buckling of orogens: Insights from analogue modelling. Journal of Structural Geology, In Press

(DOI: 10.1016/j.jsg.2018.02.005)

Broussolle, A., M. Sun, K. Schulmann, A. Guy, C. Aguilar, P. Štípská, Y. Jiang, Y. Yu, and W. Xiao (2019), Are the Chinese Altai "terranes" the result of juxtaposition of different crustal levels during Late Devonian and Permian orogenesis?, Gondwana Research, 66, 183-206

Broussolle, A., Aguilar, C., Sun, M., Schulmann, K., Štípská, P., Jiang, Y., Yu, Y., Xiao, W. and Míková, J. (2018). Polycyclic Palaeozoic evolution of accretionary orogenic wedge in the southern Chinese Altai: Evidence from structural relationships and U–Pb geochronology. Lithos, 314, 400-424.

Brun J.-P. (2002) Deformation of the continental lithosphere: Insights from brittle-ductile models. Geological Society, London, Special Publications, 200, 355-370.

Buiter S. J. H. and Schreurs G. (eds) (2006) Analogue and Numerical Modeling of Crustal-Scale Processes. Geological Society, London, Special Publications, 253.

Burg, J.P., Nievergelt, P., Oberli, F., Seward, D., Davy, P., Maurin, J.C., Diao, Z. and Meier, M. (1998) The Namche Barwa syntaxis: evidence for exhumation related to compressional crustal folding. Journal of Asian Earth Sciences, 16(2-3), pp.239-252.

Byerlee J. (1978) Friction of rocks. Pure and Applied Geophysics, 116, 615-626.

Cagnard F., Brun J.-P., Gapais D. (2006) Modes of thickening of analogue weak lithospheres. Tectonophysics, 421, 145–160.

Cobbold, P.R. and Jackson M.P.A. (1992) Gum rosin (colophony): A suitable material for thermomechanical modeling of the lithosphere. Tectonophysics, 210, 255–271.

Cocks, L. R. M., and Torsvik, T. H. (2007). Siberia, the wandering northern terrane, and its changing geography through the Palaeozoic. Earth-Science Reviews, 82(1-2), 29-74.

Davy P. and Cobbold P. R. (1988) Indentation tectonics in nature and experiment. 1. Experiments scaled for gravity. Bulletin of the Geological Institutions of Uppsala, 14, 129-141.

Davy, P. and Cobbold, P. R. (1991) Experiments on shortening of a 4-layer model of the continental lithosphere. Tectonophysics, 188, 1–25.

Dewey, J. F., Shackleton, R. M., Chengfa, C., and Yiyin, S. (1988). The tec-

tonic evolution of the Tibetan Plateau. Phil. Trans. R. Soc. Lond. A, 327(1594), 379-413.

Duretz, T., Kaus, B. J. P., Schulmann, K., Gapais, D., and Kermarrec, J. J. (2011). Indentation as an extrusion mechanism of lower crustal rocks: Insight from analogue and numerical modeling, application to the Eastern Bohemian Massif. Lithos, 124(1), 158-168.

Edel J.-B., Schulmann K., Hanžl P., Lexa O. (2014) Palaeomagnetic and structural constraints on 90° anticlockwise rotation in SW Mongolia during the Permo-Triassic: implications for Altaid oroclinal bending. Journal of Asian Earth Sciences, 94, 157–171.

England, P., and Houseman, G. (1986). Finite strain calculations of continental deformation: 2. Comparison with the India-Asia collision zone. Journal of Geophysical Research: Solid Earth, 91(B3), 3664-3676.

England, P., and Houseman, G. (1989). Extension during continental convergence, with application to the Tibetan Plateau. Journal of Geophysical Research: Solid Earth, 94(B12), 17561-17579.

Gaggero, L., Marroni, M., Pandolfi, L., and Buzzi, L. (2009). Modeling of oceanic lithosphere obduction: constraints from the metamorphic sole of Mirdita ophiolites (Northern Albania). Ofioliti, 34(1), 17-42.

Galland, O., Bertelsen, H. S., Guldstrand, F., Girod, L., Johannessen, R. F., Bjugger, F., ... and Mair, K. (2016). Application of open-source photogrammetric software MicMac for monitoring surface deformation in laboratory models. Journal of Geophysical Research: Solid Earth, 121(4), 2852-2872.

Gerya, T., and Stöckhert, B. (2006). Two-dimensional numerical modeling of tectonic and metamorphic histories at active continental margins. International Journal of Earth Sciences, 95(2), 250-274.

Gerya, T. (2014). Precambrian geodynamics: concepts and models. Gondwana Research, 25(2), 442-463.

Gutiérrez-Alonso, G., Johnston, S. T., Weil, A. B., Pastor-Galán, D., and Fernández-Suárez, J. (2012). Buckling an orogen: The Cantabrian Orocline. GSA Today, 22(7), 4-9.

Guy A., Schulmann K., Clauer N., Hasalová P., Seltmann R., Armstrong R., Lexa O., Benedicto A. (2014) Late Paleozoic–Mesozoic tectonic evolution of the Trans-Altai

and South Gobi Zones in southern Mongolia based on structural and geochronological data. Gondwana Research, 25, 309–337.

Guy, A., Schulmann, K., Munschy, M., Miehe, J. M., Edel, J. B., Lexa, O., and Fairhead, D. (2014). Geophysical constraints for terrane boundaries in southern Mongolia. Journal of Geophysical Research: Solid Earth, 119(10), 7966-7991.

Guy, A., Schulmann, K., Janoušek, V., Štípská, P., Armstrong, R., Belousova, E., ... and Hanžl, P. (2015). Geophysical and geochemical nature of relaminated arc-derived lower crust underneath oceanic domain in southern Mongolia. Tectonics, 34(5), 1030-1053.

Hubbert M.K. (1937) Theory of scale models as applied to the study of geological structures. Geological Society of America Bulletin, 48, 1459-1520.

Jiang, Y.D., Schulmann, K., Sun, M., Štípská, P., Guy, A., Janoušek, V., Lexa, O. and Yuan, C. (2016) Anatexis of accretionary wedge, Pacific-type magmatism, and formation of vertically stratified continental crust in the Altai Orogenic Belt. Tectonics, 35(12), pp.3095-3118.

Jiang, Y.D., Schulmann, K., Kröner, A., Sun, M., Lexa, O., Janoušek, V., Buriánek, D., Yuan, C. and Hanžl, P. (2017) Neoproterozoic-Early Paleozoic Peri-Pacific Accretionary Evolution of the Mongolian Collage System: Insights From Geochemical and U-Pb Zircon Data From the Ordovician Sedimentary Wedge in the Mongolian Altai. Tectonics, 36(11), pp.2305-2331.

Jiang, Y. D., Schulmann, K., Sun, M., Weinberg, R. F., Štípská, P., Li, P.F., Zhang, J., Chopin, F., Wang, S., Xia, X. P., Xiao, W. J. (2019) Structural and Geochronological Constraints on Devonian Suprasubduction Tectonic Switching and Permian Collisional Dynamics in the Chinese Altai, Central Asia. Tectonics, 38(1), 253-280.

Kovalenko, V. I., Yarmolyuk, V. V., Kovach, V. P., Kotov, A. B., Kozakov, I. K., Salnikova, E. B., and Larin, A. M. (2004). Isotope provinces, mechanisms of generation and sources of the continental crust in the Central Asian mobile belt: geological and isotopic evidence. Journal of Asian Earth Sciences, 23(5), 605-627.

Koyi, H. A. and Mancktelow, N. S. (2001) Tectonic Modeling: A Volume in Honor of Hans Ramberg. Geological Society of America, 193.

Krýza, O., Závada, P., Lexa, O. (2019) Advanced strain and mass transfer analysis in crustal-scale oroclinal buckling and detachment folding analogue models. Tectonophysics, In Press (DOI: 10.1016/j.tecto.2019.05.001).

Lehmann J., Schulmann K., Lexa O., Corsini M., Kröner A., Štípská P., Tomurhuu D. and Otgonbator D. (2010) Structural Constraints of the Evolution of the Central Asian Orogenic Belt in sw Mongolia. American Journal of Science, 310, 575– 628.

Li, Z. L., H. L. Chen, S. F. Yang, C. W. Dong, W. J. Xiao, J. L. Li, Y. Ye, and J. Wang (2004), Discovery and genetic mechanism of basic granulite in the Altay orogenic belt, Xinjiang, NW China, Acta Geologica Sinica-English Edition, 78, 177-185.

Luján, M., Rossetti, F., Storti, F., Ranalli, G., and Socquet, A. (2010). Flow trajectories in analogue viscous orogenic wedges: Insights on natural orogens. Tectonophysics, 484(1), 119-126.

Maierová, P., Čadek, O., Lexa, O., and Schulmann, K. (2012). A numerical model of exhumation of the orogenic lower crust in the Bohemian Massif during the Variscan orogeny. Studia Geophysica et Geodaetica, 56(2), 595-619.

Maierová, P., Lexa, O., Schulmann, K., and Štípská, P. (2014). Contrasting tectonometamorphic evolution of orogenic lower crust in the Bohemian Massif: a numerical model. Gondwana Research, 25(2), 509-521.

Maierová, P., Schulmann, K., and Gerya, T. (2018). Relamination Styles in Collisional Orogens. Tectonics, 37(1), 224-250.

Maus, S., et al. (2009), EMAG2: A 2–arc min resolution Earth Magnetic Anomaly Grid compiled from satellite, airborne, and marine magnetic measurements, Geochemistry, Geophysics, Geosystems, 10(8)

Meffre, S., Berry, R. F., and Hall, M. (2000). Cambrian metamorphic complexes in Tasmania: tectonic implications. Australian Journal of Earth Sciences, 47(6), 971-985.

Menant, A., Sternai, P., Jolivet, L., Guillou-Frottier, L., and Gerya, T. (2016). 3D numerical modeling of mantle flow, crustal dynamics and magma genesis associated with slab roll-back and tearing: The eastern Mediterranean case. Earth and Planetary Science Letters, 442, 93-107.

Midtkandal, I., Brun, J. P., Gabrielsen, R. H., and Huismans, R. S. (2013). Control of lithosphere rheology on subduction polarity at initiation: Insights from 3D analogue modeling. Earth and Planetary Science Letters, 361, 219-228.

Nguyen, H., Hanžl, P., Janoušek, V., Schulmann, K., Ulrich, M., Jiang, Y., Lexa, O., Altanbaatar, B. and Deiller, P. (2018) Geochemistry and geochronology of Mis-

sissippian volcanic rocks from SW Mongolia: Implications for terrane subdivision and magmatic arc activity in the Trans-Altai Zone. Journal of Asian Earth Sciences, 164, pp.322-343.

Pastor-Galán D., Gutiérrez-Alonso G., Zulauf G. and Zanella F. (2012) Analogue modeling of lithospheric-scale orocline buckling: Constraints on the evolution of the Iberian-Armorican Arc. Geological Society of America Bulletin, 124, 1293-1309.

Pavlis, N. K., S. A. Holmes, S. C. Kenyon, and J. K. Factor (2012), The development and evaluation of the Earth Gravitational Model 2008 (EGM2008), Journal of Geophysical Research: Solid Earth, 117(B4)

Petit, C., Déverchère, J., Calais, E., San'kov, V., and Fairhead, D. (2002). Deep structure and mechanical behavior of the lithosphere in the Hangai–Hövsgöl region, Mongolia: new constraints from gravity modeling. Earth and Planetary Science Letters, 197(3-4), 133-149.

Ramberg H. (1981) Gravity, Deformation and the Earth Crust. Academic Press, London and New York.

Ratschbacher L., Merle O., Davy P. and Cobbold P. R. (1991) Lateral extrusion in the Eastern Alps, Part 1: Boundary conditions and experimental experiments scaled for gravity. Tectonics, 10, 245-256.

Ratschbacher, L., Frisch, W., Linzer, H. G., and Merle, O. (1991). Lateral extrusion in the Eastern Alps, part 2: structural analysis. Tectonics, 10(2), 257-271.

Rosenbaum, G. (2012). Oroclines of the southern New England orogen, eastern Australia. Episodes, 35(1), 187-194.

Rosenbaum, G. (2014). Geodynamics of oroclinal bending: Insights from the Mediterranean. Journal of Geodynamics, 82, 5-15.

Rosenbaum, G., and Lister, G. S. (2004). Formation of arcuate orogenic belts in the western Mediterranean region. Geological Society of America Special Papers, 383, 41-56.

Schöpfer M. P. J. and Zulauf G. (2002) Strain-dependent rheology and the memory of plasticine. Tectonophysics. 354, 85 – 99.

Seltmann, R., D. Konopelko, G. Biske, F. Divaev, and S. Sergeev (2011), Hercynian post-collisional magmatism in the context of Paleozoic magmatic evolution of the Tien Shan orogenic belt, Journal of Asian Earth Sciences, 42(5), 821-838

Slagstad, T., Pin, C., Roberts, D., Kirkland, C. L., Grenne, T., Dunning, G., Sauer, S. and Andersen, T. (2014). Tectonomagmatic evolution of the Early Ordovician suprasubduction-zone ophiolites of the Trondheim Region, Mid-Norwegian Caledonides. Geological Society, London, Special Publications, 390(1), 541-561.

Şengör, A. M. C., Natal'In, B. A., and Burtman, V. S. (1993). Evolution of the Altaid tectonic collage and Palaeozoic crustal growth in Eurasia. Nature, 364(6435), 299.

Sengör, A. C., and Natal'In, B. A. (1996). Turkic-type orogeny and its role in the making of the continental crust. Annual Review of Earth and Planetary Sciences, 24(1), 263-337.

Tapponier P., Peltzer G., Le Dain Y., Armijo R. and Cobbold P. (1982) Propagating extrusion tectonics in Asia: New insights from simple experiments with plasticine. Geology, 10, 611-616.

Thielicke, W., and Stamhuis, E. (2014). PIVlab–towards user-friendly, affordable and accurate digital particle image velocimetry in MATLAB. Journal of Open Research Software, 2(1).

Tikoff, B., Teyssier, C., and Waters, C. (2002). Clutch tectonics and the partial attachment of lithospheric layers. EGU Stephan Mueller Special Publication Series, 1, 57-73.

Thompson, A. B., Schulmann, K., Jezek, J., and Tolar, V. (2001). Thermally softened continental extensional zones (arcs and rifts) as precursors to thickened orogenic belts. Tectonophysics, 332(1-2), 115-141.

Tomurtogoo, O., Windley, B. F., Kröner, A., Badarch, G., and Liu, D. Y. (2005). Zircon age and occurrence of the Adaatsag ophiolite and Muron shear zone, central Mongolia: constraints on the evolution of the Mongol–Okhotsk ocean, suture and orogen. Journal of the Geological Society, 162(1), 125-134.

Weil, A. B., Van der Voo, R., and van der Pluijm, B. A. (2001). Oroclinal bending and evidence against the Pangea megashear: The Cantabria-Asturias arc (northern Spain). Geology, 29(11), 991-994.

Wilhem, C., Windley, B. F., and Stampfli, G. M. (2012). The Altaids of Central Asia: a tectonic and evolutionary innovative review. Earth-Science Reviews, 113(3-4), 303-341.

Xiao, W., B. Windley, S. Sun, J. Li, B. Huang, C. Han, C. Yuan, M. Sun, and H.

Chen (2015), A tale of amalgamation of three collage systems in the Permian-Middle Triassic in Central Asia: Oroclines, sutures and terminal accretion, Annual Review of Earth and Planetary Sciences, 43, 477-507

Xiao, W., Windley, B.F., Han, C., Liu, W., Wan, B., Zhang, J.E., Ao, S., Zhang, Z. and Song, D. (2018) Late Paleozoic to early Triassic multiple roll-back and oroclinal bending of the Mongolia collage in Central Asia. Earth-Science Reviews, 186, pp.94-128.

Yakubchuk, A. S. (2005). Gold and base metal metallogeny of the Central Asian orogenic supercollage. Econ. Geol., 100, 1035-1068.

Yarmolyuk, V. V., Kudryashova, E. A., Kozlovsky, A. M., and Savatenkov, V. M. (2007). Late Cretaceous-Early Cenozoic volcanism of Southern Mongolia: A trace of the South Khangai mantle hot spot. Journal of Volcanology and Seismology, 1(1), 1-27.

Zhang, P.Z., Shen, Z., Wang, M., Gan, W., Bürgmann, R., Molnar, P., Wang, Q., Niu, Z., Sun, J., Wu, J. and Hanrong, S. (2004) Continuous deformation of the Tibetan Plateau from global positioning system data. Geology, 32(9), pp.809-812.

Zheng, D., Zhang, P.Z., Wan, J., Yuan, D., Li, C., Yin, G., Zhang, G., Wang, Z., Min, W. and Chen, J. (2006). Rapid exhumation at 8 Ma on the Liupan Shan thrust fault from apatite fission-track thermochronology: Implications for growth of the northeastern Tibetan Plateau margin. Earth and Planetary Science Letters, 248(1-2), pp.198-208.

3 Advanced strain and mass transfer analysis in crustal-scale oroclinal buckling and detachment folding analogue models

Ondřej Krýza, Prokop Závada and Ondrej Lexa

3.1 Abstract

The PIV (particle image velocimetry) method became a standard tool for the calculation of displacement fields in physical geodynamic models. For understanding the deformation dynamics of geodynamic models, in our study, we implemented several post-processing algorithms on the derived displacement field and calculated the velocity and strain(-rate) components, such as the divergence of the velocity field, vorticity and shear strain-rate.

In the model of oroclinal buckling, we focused on strain analysis of the upper crust and correlated the shear strain-rate, vorticity and divergence anomalies with visual deformation patterns in the upper crust. The divergence of velocity fields in these models correspond to the pop-up and pop-down belts oriented along the axial trace of the oroclinal bends. High shear strain-rate domains correlate with horizontal, isovolumic shear zones alongside these belts, while vorticity shows rotational trend of fold axial traces of the pop-up and pop-down belts, around orocline inflection.

In another series of models, we simulated the development of melt-cored crustal scale detachment folds and employed the same set of parameters to investigate the ductile deformation visible in side-view of the model domain. We developed a method that allows tracing the divergence in subcells locked on target subdomains. We tracked and quantified melt flow between the melt source area at the bottom of the model and progressively developing folds. This mass transfer analysis revealed polyphase fold evolution, where initial fold perturbations quickly amplify as the melt accumulates in the triangular hinge sector below and between the rotating fold limbs. While the early amplification leads to decompression driving the melt into the hinge zone area between the limbs, the fold lock-up stage and continued attenuation of the vertical limbs is associated with melt expulsion from the fold interlimb domain back into the source layer, where it can be transferred laterally to the foreland.

Keywords: analogue modelling, PIV method, oroclinal buckling, detachment folding, strain-rate, divergence

Highlights:

- Models of oroclinal buckling and detachment folding were investigated by the PIV method.

- Several model parameters related to the velocity and strain were used to analyze the deformation features in both models.
- The divergence of the velocity field reflects distortion of the model surface.
- Analysis of the divergence reflects mass transfer budget in detachment folds.
- The fold growth rate is driven by the degree of melt flux into the axial zone.

3.2 Introduction

Analogue modelling represents a powerful tool for understanding geodynamic processes and therefore requires precise analysis of internal kinematics and deformation. The PIV (particle image velocimetry) technique is often employed to calculate the displacement/velocity field in the models to understand the model evolution on a global scale (e.g. Adrian, 2005; Adam et al., 2005; Krézsek et al., 2007; Schmatz et al., 2010; Warsitzka et al., 2013; Adam et al., 2013; Kettermann and Urai, 2015; Kettermann et al., 2016; Schellart and Strak, 2016; Boutelier, 2016). The core of the PIV method is based on tracing individual image elements (image patterns that consist of a specific arrangement of individual pixels or voxels) in the time-sequence of images (Fig. 23). Displacement vectors are then calculated on the basis of redistribution of these elements between the time steps. High resolution, fast calculations and relatively simple implementation of advanced scripting for data post-processing (vector validation, visualization, data smoothing) qualify the PIV method for deformation analysis of various physical laboratory models, especially for geometrically and rheologically complex simulations associated with high gradients in the velocity field (Adam et al., 2005; Krézsek et al., 2007; Schellart and Strak, 2016).

There are two major types of PIV methods employed in the analogue geodynamical modelling (e.g. Adam et al., 2005; Adam et al., 2013; Boutelier, 2016). First, the 2D PIV technique, which uses images recorded from one camera focused on a single plane, for example, the side-view or plan-view of thin-sheet experiments (e.g. Bajolet et al., 2012; Jang and Lee, 2008). The second type represents the stereoscopic and 3D PIV technique. The stereoscopic PIV technique enables calculating the surface velocity field with three velocity components (e.g. Hori and Sakakibara, 2004; Strak and Schellart, 2014) by tracking and correlating the image elements in photographs collected from several cameras targeted at the model domain from different angles. In contrast, the 3D PIV technique allows to compute the velocity components in a 3D space that consists of voxels (real 3D data), provided by e.g. CT scans, X-ray tomography etc. (e.g. Okamoto et al., 2000; Elsinga et al., 2007; Adam et al. 2013). For the 2D PIV technique, there are several open source software (PIVlab, openPIV, GeoPIV, MatPIV, PIVMat, etc.) or commercial platforms (e.g. LaVision - FlowMaster or StrainMaster, Dantec Dynamics - DynamicStudio, PIV 2D - Imagesystems, etc.). Similarly, for the stereo-PIV methods, that are usually

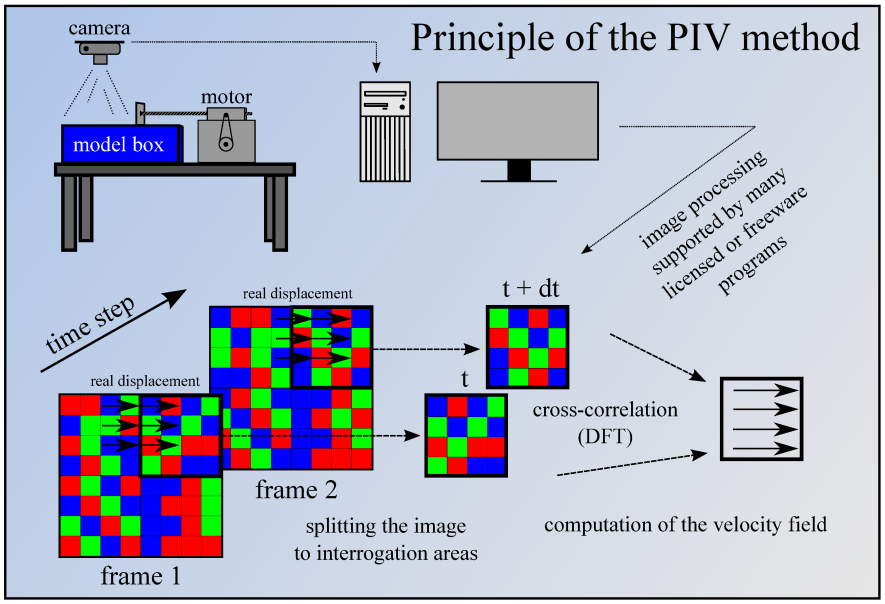


Fig. 23: Simplified scheme of the particle image velocimetry (PIV) analysis principle.

associated with specific camera systems, reconstruction of the surface displacement field can be provided by commercial software (e.g. DaVis from LaVision, etc.) or structure from motion (SFM) methods employing digital elevation models (DEM) that run on commercial platforms, such as Agisoft or open-source software, such as VisualSFM or MicMac (e.g. Galland et al., 2016). The displacement fields obtained from both PIV approaches (2D PIV and stereo-PIV) allow derivation of several model parameters that are associated directly with the velocity field or with strain(-rate) tensor describing the deformation in the model domain that help to quantify the kinematic evolution of the model and its internal dynamics.

Our study aims to illustrate the potential of the 2D PIV method for investigation of the surface deformation in complex analogue models of oroclinal buckling and inner mass transfer dynamics and material deformation in thin-sheet models of crustal-scale detachment folding. To calculate the displacement field, we employed the opensource PIVlab software that represents a good solution for analogue modelling laboratories that are not equipped with commercial systems (e.g. LaVision etc.). In both experiments, we used the calculated displacement field for the derivation of several model parameters, namely the velocity magnitude, shear strain(-rate), the divergence of the velocity field and vorticity and correlate their magnitude with observed deformation structures in the models. While the magnitude of the velocity field simply shows a gradient in displacement rate, the divergence of the velocity field in a plane represents local volumetric changes. Deformation-rate (shear-rate) of the crustal material, represented by the second invariant of the deviatoric strain(-rate) tensor (e.g. Gerya, 2009), corresponds to the isovolumic deformation independently of the global reference frame. The shear strain(-rate) is commonly expressed as

the exy component of the strain-tensor in analogue models that operates with the PIV method (e.g. Adam et al., 2005; Warsitzka et al., 2013; Chen et al., 2016). The vorticity of the velocity field (e.g. Schmatz et al., 2010; Bajolet et al., 2012; Warsitzka et al., 2013; Kettermann and Urai, 2015) displays a rotational trend of the material in the model domain.

The geometry of the first model is controlled by amplification of an orocline ribbon that influences the deformation of brittle upper crust and underlying ductile layers. We studied the deformation of the upper crust, marked by folds, strike-slip faults and development of thrusts and normal faults bounding the pop-up and pop-down systems, respectively. For mapping of the compression/extension subdomains related with the development of pop-up and pop-down belts in the upper-crust, we used the divergence of velocity field captured from the top-view of the model surface. This approach is sometimes used in analogue models that produce faults or thrusts (e.g. Reiter et al., 2011; Kettermann et al., 2016) or in models of subduction, where the lower plate is progressively undulated (e.g. Bajolet et al., 2012). Simple shear deformation is mapped by the isovolumic strain invariant and corresponds to strike-slips zones in the deformed model surface, developed in particular along the interface between the orocline and the surrounding material and along some of the pop-up or pop-down belts. The vorticity of the velocity field revealed progressive curvature of originally linear deformation features and rotation around the inflection point of the orocline.

In the second type of the model, the same model parameters serve for tracing the relative mass transfers in side-view of the model domain. This thin sheet experiment is designed to produce a series of crustal scale folds that are developed as a result of the buckling above a melt weakened lower crustal detachment layer. Here, the divergence is employed for tracing the local material flux between the pre-defined subdomains. The mass-transfer calculations required the implementation of additional routines that allow tracing the evolution of divergence in progressively geometrically modified subgrids.

3.3 Models of oroclinal buckling

3.3.1 Model background and setup

The first type of experiments were constructed in order to understand the relative mass transfers between the different lithospheric domains during oroclinal buckling. Formation of large arcuated orogens is related with rapid topography development associated with deformation of the upper crust (e.g. Pastor-Galán et al., 2012; Rosenbaum, 2012; Rosenbaum and Donchak, 2012; Rosenbaum, 2014), while middle to lower ductile crust is transferred laterally by gravity-driven flow or emplacement of a new material from the subduction wedge (Beaumont et al., 2006;

Pastor-Galán et al., 2012; Maierová et al., 2014, Menant et al., 2016; Maierová et al., 2018).

The model aims to mimic the formation of the Tuva-Mongol orocline (Xiao et al., 2015) after subduction of the Mongol-Okhotsk oceanic plate underneath the Mongolian microcontinent (Lehmann et al., 2010; Edel et al., 2014). The model is designed to simulate the amplification of a preexisting, gently folded, accretionary-subduction system surrounded by two neighbouring oceanic and continental lithospheric subdomains (Fig. 24a). In general, oroclinal buckling can be considered as a specific type of indentation tectonics setting which is accompanied with lateral movements of individual oroclinal hinges perpendicular to the movements of oceanic/continental blocks. Except for the complex material transfer in deeper lithospheric levels, deformation of the upper crust and related topography development represents an important part of the mechanical behaviour of such a system. The PIV technique was employed for deformation and displacement analysis of the model surface (upper crust) that is controlled by the deep material flows and mechanical coupling between the lithospheric mantle and the crust.

3.3.2 Model materials

The upper crust, in both oceanic and continental domains, is simulated by cohesionless Fontainebleau sand (Fig. 24a, Tab. 1). Silicone putties of various viscosity and density (GS1R gum from Rhone Poulenc, France) were used to simulate the ductile lower crust, continental lithospheric mantle and oceanic lithospheric mantle. Mechanical anisotropy in the model was implemented by incorporation of a plasticine layer between the two lithospheric domains as a beam to induce the oroclinal buckling and related mass redistribution. The inserted plasticine layer was pre-folded and represents an artificial element that controls the progressive amplification of the single wavelength orocline.

The model was scaled according to the standard modeling techniques (Hubbert, 1937) and uses the materials with physical properties that are comparable with the materials used in some of the previous 4-layer models (scaling according to Davy and Cobbold (1991) and Brun (2002) and material used according to Cagnard et al. (2006)), except for the incorporated plasticine layer (for model scaling see Tab. 2).

3.3.3 Experimental procedure and model development

Lateral compression was applied to the model at a rate of 2 cm/h up to 25, 37, 45 and 50% of finite shortening in eight simulations. Laboratory temperature was stable at around 19-20 °C during each experiment. The topographic images were captured every 10 minutes and saved in RAW (NEF) and JPG format (Digital SLR Camera Nikon D3200, 24.2MP, AF-S 18-55mm). The experiments show a similar evolution for all of the eight simulations with dominant deformation features that were

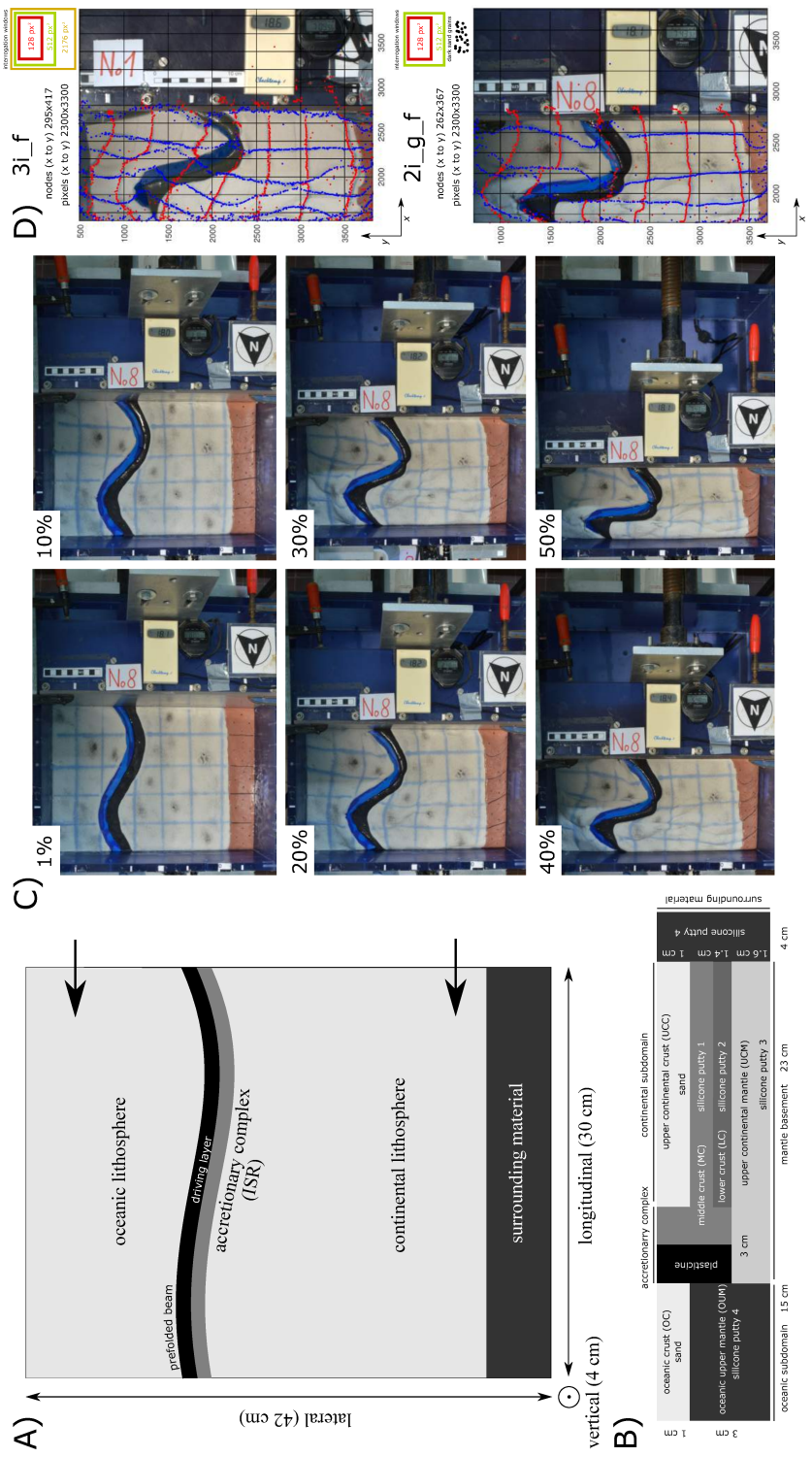


Fig. 24: Setup of the oroclinal buckling analogue model in plan-view (a) and lateral cross-section (b). Progressive evolution of the model domain during the lateral shortening is shown in (c). Qualitative test results of the displacement field obtained from the PIV (d,e), of variable image resolution, size of interrogation windows and type of PIV calculation. Red-blue grid is composed by individual markers that are transported by computed displacement in each time-step. Finite marker positions reflect well the finite deformation pattern. (d) 3i_f represents three interrogation windows and image filtering, while (e) 2i_g_f represents two interrogation windows, additional dark particles dispersed on the surface and image filtering.

initiated already between 7-10% of shortening. These features are manifested by 1) amplification of the orocline with hinges that buttress into both adjacent lithospheric domains, 2) build up of upper crustal topographic perturbations manifested by the development of pop-up structures confined by thrusts with strike-slip components, and 3) rotation of the central model domain parts around the inflection point of the orocline.

3.3.4 Application of the PIV method for oroclinal buckling models

For the PIV analysis of all eight simulations, we used the MATLAB freeware toolbox PIVlab (Thielicke and Stamhuis, 2014). The method was used for model domains with identical initial geometry. For the last three simulations, the model surface was powdered by dark-coloured grains of sand, to enhance the PIV accuracy. The PIV analysis was performed on the surface of the model domain and excluded the masked surrounding image parts. We analysed 47 TIFF (uncompressed, 24-bit(true color, RGB)) images for each experiment with finite shortening of 50% in pairs (i.e. sequence 1-2, 2-3, 3-4...). The resolution of all the images is 6016 × 4000 px (vertical to horizontal) where the analyzed domain represents 7590000 px^2. We employed three interrogation windows (2176 px^2, 512 px^2, 128 px^2) in PIVlab and allowed additional pre-processing features as intensity highpass or CLAHE (contrast-limited adaptive histogram equalization) (Thielicke and Stamhuis, 2014, Raffel et al., 2007). For data post-processing, we used a validation module implemented in PIVlab to reject irrelevant (distant/false) values of the displacement field according to normalized median test (Nogueira et al., 1997; Westerweel and Scarano, 2005). Missing data were interpolated by the 3×3 neighbourhood (3×3 mean) interpolation method (Nogueira et al., 1997; Thielcike and Stamhuis 2014; Boutelier, 2016).

The PIV procedure for our models comprised several post-processing algorithms. At first, we tested the accuracy of the calculated displacement field with respect to the different settings of the PIV calculations, input image formats and implementation of colour particles as physical markers (for increasing the PIVlab capability in recognizing the particle patterns in the image). The aim of the PIV tests was to achieve the best compromise between the resolution and accuracy of the resulting displacement field, evaluated by visual comparison of the real and calculated displacement. While the real displacement is defined by the movement of physical markers (an orthogonal grid of coloured sand lines or contrasting particles), the calculated displacement corresponds to the movement of virtual markers that match the original x, y positions of the pre-selected physical markers.

The testing procedure consists of the following steps: 1. Attribution of virtual point markers to initial physical markers (the finite position of physical markers that represent a surface sand grid) 2. application of a displacement to the virtual markers, 3. 2D interpolation of the displacement in new positions of the virtual markers from the surrounding nodal values (the calculated displacement grid is sparser than the

true displacement) for all time steps, and 4. imaging of the finite positions of virtual markers and their visual correlation with the position of physical markers. For all the tests, we scripted the associated procedures in MATLAB^{TM} environment. Based on the best PIV settings, for further analysis of the model, we first chose the dataset calculated with additional filtering and a triplet of interrogation windows. This setting regards models where the surface resolution of the model was not enhanced by distributed dark particles (coloured sand grains). The accuracy test for this setting revealed only several local deviations from real material displacement (Fig. 24d). In the second approach, two interrogation windows were used in experiments (Fig. 24e), where the sand layer was covered by distributed dark particles (coloured sand grains) to increase the PIV accuracy. The resultant accuracy in the displacement field is comparable for both approaches.

3.3.5 Derived model parameters

Several velocity and strain-related parameters were derived from the calculated displacement field (Fig. 25). The first parameter represents the normalized magnitude of the velocity field. The next three parameters are the divergence of the velocity field, shear strain rate (second invariant of the deviatoric part of the strain rate tensor) and vorticity.

First, the strain-rate tensor (Eq. 3.1) and its deviatoric part (Eq. 3.2) was derived from the displacement between each of the model points (represented by the discrete numerical grid). The elements of the main diagonal of the tensor represent the stretches that are associated with the x, y directions, while the elements of the anti-diagonal correspond to distortion (for the symmetric part of the tensor (Eq. 3.3a)) or rotation (for the antisymmetric part of tensor (Eq. 3.3b)). The divergence of the velocity field (Eq. 3.4), is represented by the sum of elements situated along the main diagonal of the strain-rate tensor. Shear deformation is defined as the second invariant of the deviatoric strain-rate tensor (e.g. Becker and Kaus, 2015; Gerya, 2009) that shows the magnitude of isovolumic deformation, independently to the reference frame of the model (Eq. 3.5). The tendency of the material to rotate is expressed by the vorticity (Eq. 3.6).

$$\dot{\epsilon} = \frac{1}{2}\left(\nabla \cdot \vec{v} + \nabla^T \cdot \vec{v}\right), \tag{3.1}$$

$$\dot{\varepsilon} = \begin{bmatrix} \epsilon_{xx} - \frac{1}{2}I_1 & \epsilon_{xy} \\ \epsilon_{yx} & \epsilon_{yy} - \frac{1}{2}I_1 \end{bmatrix}, \tag{3.2}$$

$$\dot{\varepsilon}_{\text{sym.}} = \begin{bmatrix} \frac{\partial v_x}{\partial x} & \frac{1}{2}\left(\frac{\partial v_x}{\partial y} + \frac{\partial v_y}{\partial x}\right) \\ \frac{1}{2}\left(\frac{\partial v_y}{\partial x} + \frac{\partial v_x}{\partial y}\right) & \frac{\partial v_y}{\partial y} \end{bmatrix}, \tag{3.3a}$$

$$\dot{\varepsilon}_{\text{antisym.}} = \begin{bmatrix} \frac{\partial v_x}{\partial x} & \frac{1}{2}\left(\frac{\partial v_x}{\partial y} - \frac{\partial v_y}{\partial x}\right) \\ \frac{1}{2}\left(\frac{\partial v_y}{\partial x} - \frac{\partial v_x}{\partial y}\right) & \frac{\partial v_y}{\partial y} \end{bmatrix}, \tag{3.3b}$$

$$\nabla \cdot \vec{v} = \dot{\epsilon}_{I_1} = \left(\frac{\partial v_x}{\partial x} + \frac{\partial v_y}{\partial y}\right), \tag{3.4}$$

$$\dot{\epsilon}_{I_2} = \varepsilon_{xx}\varepsilon_{yy} - (\varepsilon_{xy})^2, \tag{3.5}$$

$$\nabla \times \vec{v} = \left(\frac{\partial v_x}{\partial y} - \frac{\partial v_y}{\partial x}\right). \tag{3.6}$$

3.3.6 Correlation of the calculated parameters with deformation features

All calculated model parameters (magnitude of the velocity field, the divergence of the velocity field, shear strain and vorticity) were plotted for the three distinct stages of oroclinal buckling model evolution (Fig. 25) up to 20% of domain shortening. This initial deformation revealed a comprehensive correlation between the space-time changes of the strain-related parameters and the deformation features.

At first, we analyzed the velocity field which provides the first insight into the model dynamics (Fig. 25Aa-c) (All features that are described below are marked in the figure 25A by stars with corresponding numbering in the text). Here, the initial velocity increase reveals rapid amplification of the orocline hinge sector closer to the indenter side (1). The velocity field map reveals a curved frontline velocity gradient (Fig. 25Ab,c) (2) that is typical for arcuated deformation patterns in the indentation tectonics (Regard et al., 2005; Reiter et al., 2011) and accretionary wedge models confined between solid walls reflecting the Poisseuille type of flow (e.g. Grujic, 2006) (Fig. 25B). The zones of sharp velocity gradients are also related to the major deformation structures in the model that are also reflected by sharp space variations in other calculated parameters.

Negative anomalies in the divergence of the velocity field correspond to the thrust zones associated with the lateral propagation of the orocline hinges (Fig. 25e,f, (3)), thrusting (4) or underthrusting (5) outside of the orocline subdomains or pop-down structures (6) in the upper crust (Fig. 25f (6)). In contrast, positive values of divergence are related to areas of extension in crestal parts of upright folds, collapsing thrust belts or pop-up structures (7).

The contour diagram of shear strain (Fig. 25g,h,i) highlights two types of structures. First, the maximum values of shear rate reveals strong mechanical

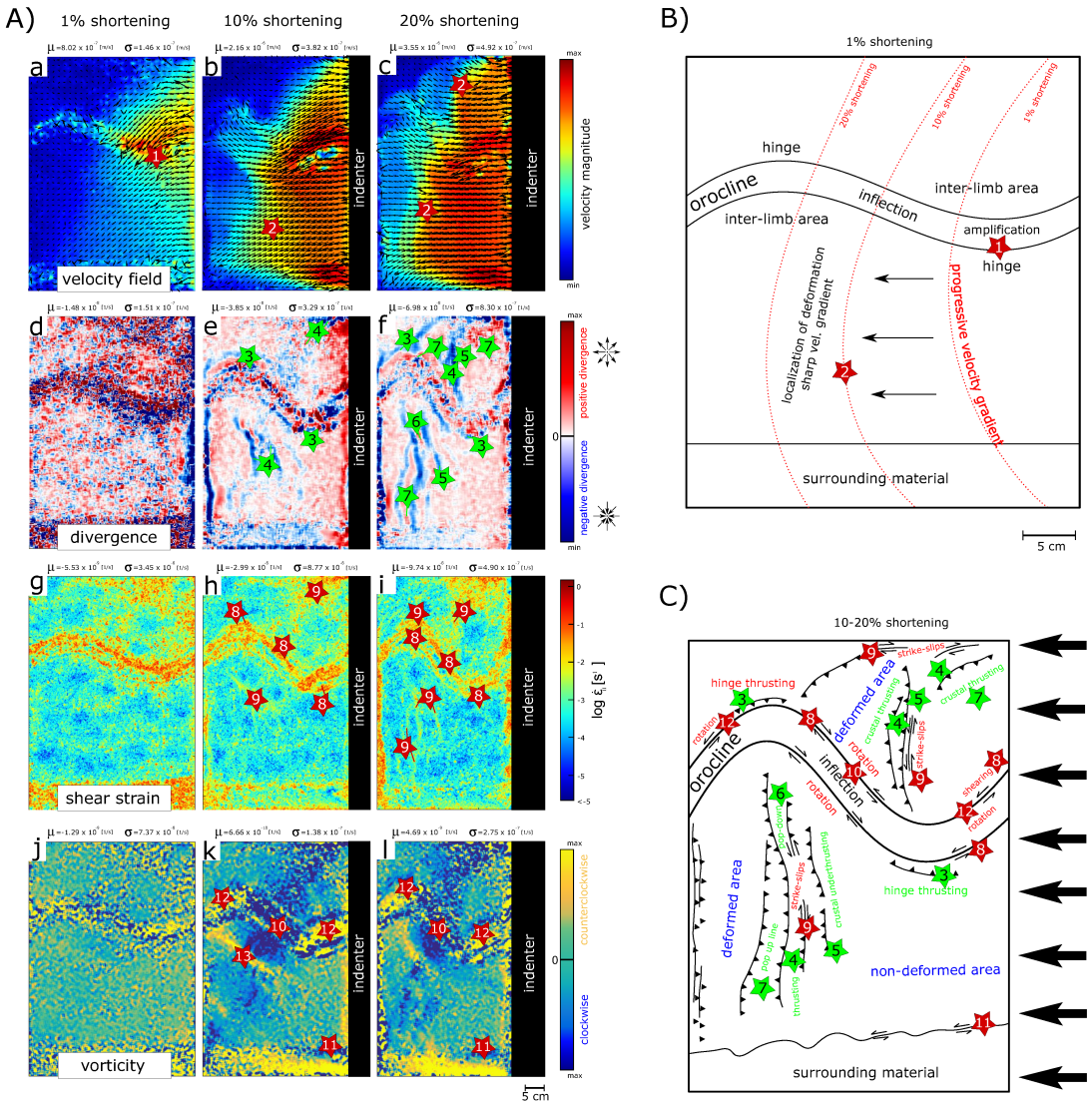


Fig. 25: Colour maps of PIV-derived parameters from the displacement field plotted for three distinct shortening stages (1%, 10% and 20%). From top to bottom (A), the parameters are: magnitude of displacement velocity with arrows representing vectors of displacement (a-c), divergence of velocity field (d-f), the second invariant of strain-rate tensor, equivalent to material shear strain-rate (g-i) and vorticity (j-l). All parameters except the strain-invariant are standardized (to obtain normalized z-scores for further analysis and to compare data from various experiments). Original average values and standard deviations are displayed in the small box above the current colour map. Panel (B) shows schematically the major features in the model domain as described in the text. Red lines show the progressive movement of the highest velocity gradient in time. Panel (C) represents a map of main deformation structures that are correlated with the variation of individual parameters displayed in panel (A). The red stars in the contour maps correspond with the deformation features that are described in the text and shown in panel (C).

decoupling along the rheological transition between the orocline and the surrounding subdomains (8). Second, elevated values of this parameter also correspond to strike-slip components of the thrusts and normal faults (9).

The restored vorticity field (Fig. 25j,k,l) reveals the clockwise movement of material elements around the inflection point sector of the orocline (10). This domain of clockwise rotation stretches in the direction parallel with the propagation direction of the orocline hinges. Another zone of relative clockwise rotation is situated in the lower right part of the model, in the confining silicone material adjacent to the brittle upper crustal domain (11). Counter-clockwise motion of the material is evident for the limbs on both ends of the orocline (12) and transitional zones (13) that divide subdomains of intense clockwise motion, dominated by rotational translation (orocline inflection) and regions, where deformation is dominated by volumetric distortion (pop-ups and pop-downs).

3.4 Models of detachment folding

3.4.1 Model background and setup

The motivation for the detachment folding experiments was to understand the dynamics of folding in accretionary systems with a melt-softened lower crustal subdomain. Rheological stratification marked by a middle to lower crustal migmatitic layer is typical for many of the Phanerozoic orogenic belts at convergent plate boundaries (Vanderhaeghe et al., 1999, 2009). Late stage development of these orogens is associated with lateral and vertical bulk flow of the melt weakened, migmatitic domains, extruded from the core domains of the orogens e.g. in form of metamorphic core-complexes (e.g. Beaumont et al., 2001; Schulmann et al., 2008; Vanderhaeghe et al., 2009). The softening of lower crust in such systems is facilitated by e.g. slab-retreat driven pre-orogenic thinning in hot back-arc domains (Collins, 2002) and/or by emplacement of voluminous partially molten layer between the crust and upper mantle during a process known as “relamination” (Hacker et al., 2011; Lehmann et al., 2017; Maierová et al., 2018). The setup of the experiment (Fig. 26) was designed to mimic the development of a late Devonian accretionary belt, the Chandman metamorphic dome in the Central Asian Orogenic Belt, originally formed by a strong brittle upper crust (∼15 km thick) and a weak partially molten layer (∼15 km thick) in the lower crust above a strong granulitic residuum (Lehmann et al., 2017).

The crustal scale detachment folding experiments were performed using a narrow sandbox with a mobile heating plate (sheet metal with inner heating body) confined between the glass walls (Fig. 26A). Stable thermal gradients in superposed layers were attained by heat input from the heating plate and the light bulbs mounted on the top of thermally insulated apparatus. These gradients are marked by ∼0.07 °C/mm and 0.06 °C/mm at the sides and the center of the model domain, respectively

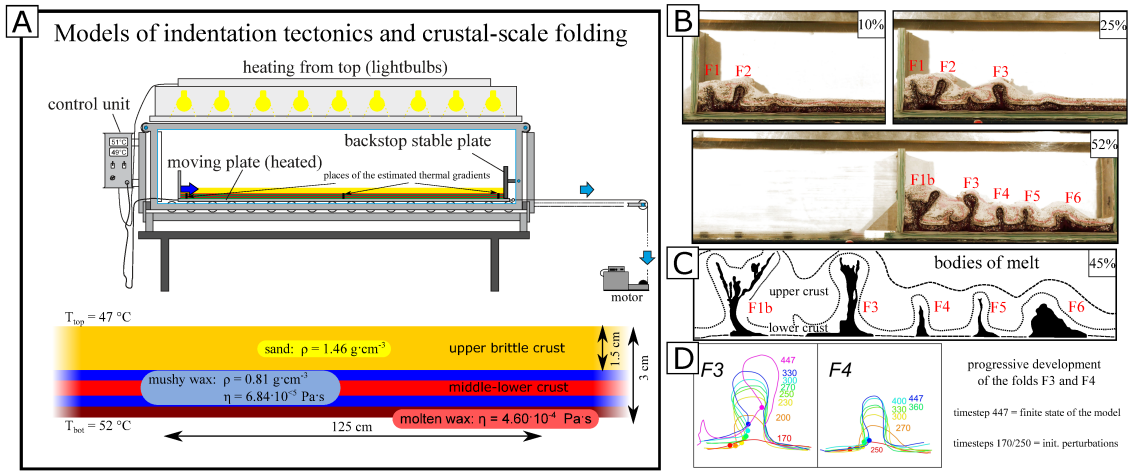


Fig. 26: Crustal scale detachment folding analogue model setup. Panel (A) shows experimental apparatus and model properties. Panel (B) represents progressive evolution of the model domain and sequential development of the folds for 10, 25 and 52% of shortening, respectively. Line drawing (C) highlights the boundaries between the different layers and the extent of redistributed wax melt in the fold cores (folds are marked F1b-F6, where F1b represents F1 and F2 that coalesced to the Y-shaped F1b fold). Progressive development of the folds F3 and F4 (D) show difference in body shape and mechanism of folding. Individual numbers represent timesteps where the actual shape was captured.

(Fig. 26, Tab. 3). During the experiments, the model domain on the mobile plate is pulled by a string reeled in by a motor at a constant rate against a stable vertical wall. The longitudinal, lateral and vertical dimensions of the model domain were 125 cm, 8 cm and 3 cm, respectively. The model consists of two layers, each 1.5 cm thick, the paraffin wax layer at the bottom and a fine-grained sand layer, representing the lower and upper crust, respectively.

The preliminary qualitative analysis of the resulting detachment folding experiments revealed that the amplification of the crustal scale detachment folds is associated with melt transfer from the bottom anatectic source to the core zones of growing folds. Therefore, in the following PIV quantitative analysis, we aimed to constrain the melt transfer dynamics between these subdomains. For related accuracy tests of the resulting displacement field after the post-processing (Fig. 28), we adopted the optimal PIV analysis setup, as applied for the oroclinal buckling models (Fig. 24D/24E).

3.4.2 Model materials and scaling

Paraffin wax *Paramo* with a melting point at 50 °C, manufactured by the *Paramo a.s.* Company in Czech Republic, was employed as the analogue of the thermally softened lower crust. The advantage of the paraffin wax is the thermally dependent rheology with Newtonian viscous properties in a molten state to slightly viscoplastic properties in a partially molten state below the melting point (Rossetti et al., 1999;

Tab. 3: Thermal profiles in the wax layer (see Fig. 26a for location of the profiles).

Depth (cm) / Temperature	left (°C)	central (°C)	right (°C)
T_surface	48,80	49,20	48,90
T_0.5	49,10	48,90	48,90
T_1.0	49,40	49,30	49,30
T_1.5	49,80	50,10	49,90
gradient (°C/mm)	0,07	0,06	0,07
gradient (°C/m)	66,67	60,00	66,67

* profiles are shown in Fig. 4a

Tab. 4: Wax viscosities. Dynamic viscosities of the wax measured at the temperatures that characterize the viscosity gradient of paraffin wax in the crustal scale detachment fold experiment. Value marked with * was obtained from the shear box experiments, value marked with ** was estimated according to shearing experiments and values published in Rossetti et al. (1999). The values for temperatures > 48 °C were obtained from rotational rheometer *VT 550 Haake* (Institute of Geophysics of the CAS, Prague).

Temperature (°C)	44*	46**	48	50	52
Viscosity (mPa.s)	1.01e9	1e5	0.85	0.53	0.46

Duarte et al., 2014). This range of rheological behaviour well corresponds to the rheological properties of anatectic lower crustal domains. The dynamic viscosities of the wax, that were measured by the *VT550 Haake viscometer* with coaxial cylinders (*MV1 cylinder*), range from 6.84 mPa.s at 44 °C to 0.46 mPa.s at 52 °C (Tab. 4).

The brittle upper crust in the models (1.5 cm thickness) is formed by pure quartz sand with an average size of 0.17 mm (quarried by *Sklopísek Střeleč co.*, Czech Republic). Ring shear test measurements revealed a friction coefficient of 0.7 and cohesion of 75 Pa (Klinkmüller et al., 2016; item 153-01 in the associated dataset). Before shortening of the model domain, a thermal and rheological gradient, marked by the low viscosity melt at the bottom and overlying visco(-elasto-)plastic partially molten wax, was attained after several hours of heating at the melting temperature of the wax (Fig. 26a). Before the experiment, the glass walls were sprayed with a low viscosity silicone to reduce the friction between the model domain and the glass walls.

The model was scaled according to the principles of geometric and dynamic-rheological similarity (Hubbert, 1937; Sokoutis et al., 2005). The geometric similarity is described by the scaling ratio $l^* = 2 \cdot 10^{-6}$ with respect to the 30 km original crustal thickness prior to the accretion and folding (e.g. in the Chandman dome area, Lehmann et al., 2017). The accuracy of the dynamic scaling was tested by calculating the non-dimensional numbers defined by the ratios between the forces acting on the models. For the ductile lower crustal layer, we calculated the Ramberg number (Eq.

3.7; see Eq. 1.10 - 1.13), representing the ratio between the gravitational and viscous forces (**Rm**; Weijermars and Schmeling, 1986; Sokoutis et al., 2005) as presented by Lehmann et al., (2017):

$$\mathrm{R_m} = \frac{gravitational\ stress}{viscous\ stress} = \frac{\rho_d g h_d}{\eta \dot{e}} = \frac{\rho_d g h_d^2}{\eta V}, \tag{3.7}$$

where the ρ_d and h_d are the density and thickness of the ductile layer (paraffin wax), respectively, g is the gravity acceleration ($g = 9.81m \cdot s^{-}2$), eta is the viscosity of the ductile layer and $\dot{e}$ the strain rate given by the ratio between the mean velocity of convergence V and the thickness of the ductile layer h_d.

Scaling of the brittle deformation in the upper crustal layer formed by the sand in the experiments was achieved by calculating the ratio between the gravitational stress and cohesive strength (**Rs**; Ramberg, 1981; Sokoutis et al., 2005):

$$\mathrm{R_S} = \frac{gravitational\ stress}{cohesive\ strength} = \frac{\rho_b g h_b}{\tau_c}, \tag{3.8}$$

where ρ_b and h_b represent the density and thickness of the brittle layer, respectively, g is the gravity acceleration and τ_c the cohesive strength of the brittle layer. For correctly dynamically scaled model, the R_m and R_S calculated for both the model and the original (e.g. the Chandman dome; Lehmann et al., 2017), respectively, should be similar (Tab. 5).

The scaling analysis (Tab. 5) compares the viscosities of the partially crystallized wax measured at 44 °C (6.84 mPa.s, Tab. 3) and a migmatite, for which the viscosity is indirectly estimated from the viscosity of a suspension of a hydrous granite (hydrous rhyolitic melt containing ∼ 1.5 wt.% water, Giordano et al., 2009) of ∼ 108 Pa.s and 60-80 vol.% of crystals that increases the effective viscosity of the crystal/free melt 6-7 orders of magnitude to maximum ∼ 1015 Pa.s (Costa et al, 2009). This scaling analysis (Tab. 5) shows similar values of both the Rm and Rs values for the experiment and the original, respectively. Alternatively, for the dynamic scaling analysis of the ductile layer, we can consider the viscosity of the completely molten wax (0.46 mPa.s at 52°C) as an equivalent to the same granite melt of ∼ 108 Pa.s, but with 40-50% crystals that will render effective viscosity of the melt+crystal suspension of ∼ 1013 Pa.s (Giordano et al., 2004, 2008; Costa et al., 2009). Calculating the corresponding R_m and R_S for both model and original will give again values within the same order of magnitude.

In summary, we can suggest that the rheological stratification of the sand and the wax quite well corresponds to the rheological stratification in thermally softened accretionary orogens, where the lower crust is formed by migmatites. The partially molten wax successfully implements a viscosity gradient from the completely molten

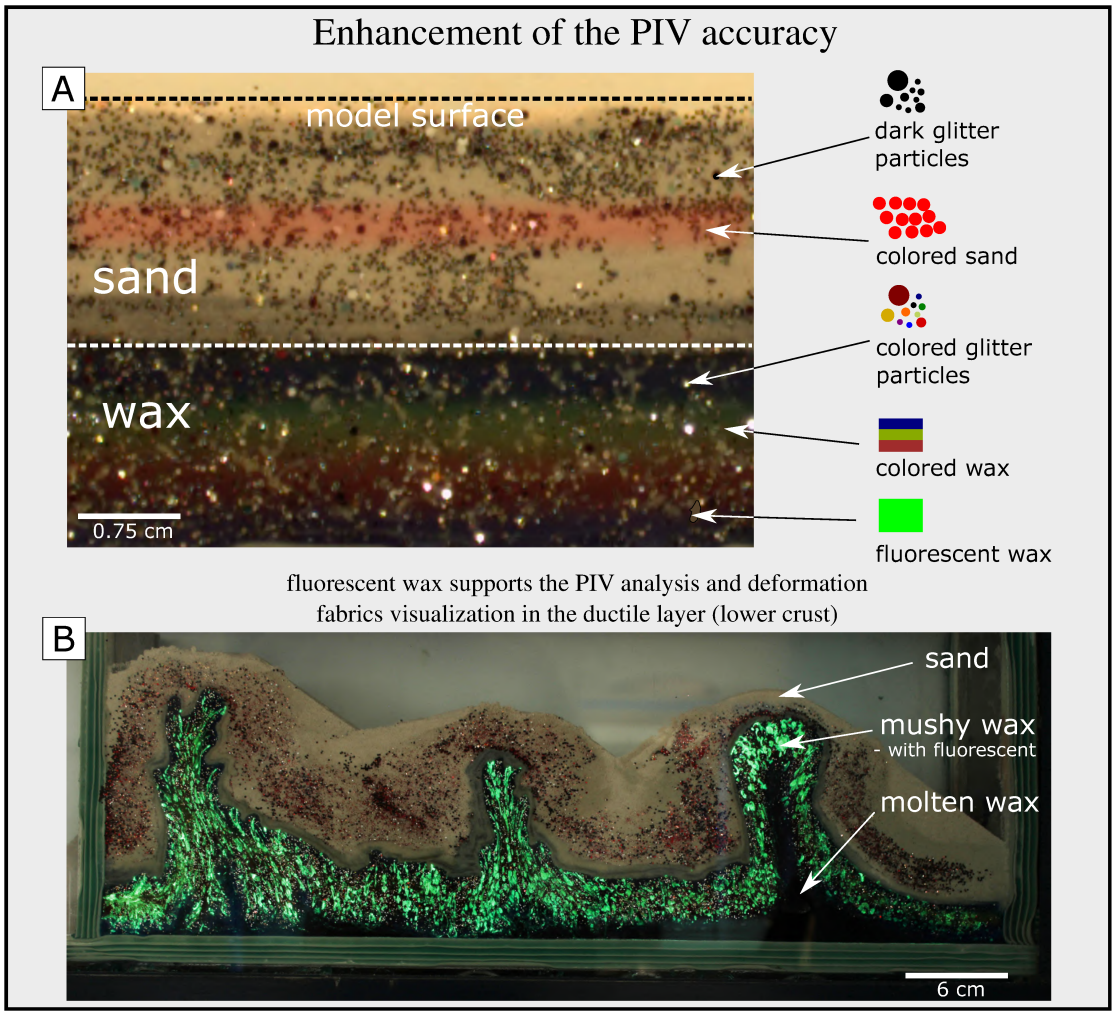


Fig. 27: Incorporated glitter particles in the sand and wax layers and additional shavings of fluorescent wax markers in the wax layer are shown in (a). Glowing markers of stretched fluorescent wax shavings in deformed model domain are shown in (b) (image was taken in dark room with long exposition). The black particles were incorporated into the sand layer while colour particles were superposed on the side wall of the wax layer. The setup of the illustrated model (b) represents the same physical properties of the analogue materials (i.e. sand, paraffin wax, fluorescent paraffin wax) as for the model described in Fig. 4, but with higher initial thickness of the model domain (3 cm sand layer, 3 cm wax layer) and shorter initial length (100 cm) than the model presented in Fig. 26 (120 cm). The 50% shortening of this model resulted in formation of three sequential detachment folds. The particles of the fluorescent wax highlight the finite deformation pattern in the mushy wax layer and are absent in the molten wax.

Tab. 5: Scaling analysis for the crustal scale detachment fold experiment.

	Upper crust (sand in the experiment)				Lower crust (wax in the experiment)						
parameters and units	ρ_b ($kg \cdot m^{-3}$)	h_b (m)	f_c	C (Pa)	ρ_d ($kg \cdot m^{-3}$)	h_d (m)	η_d (Pa·s)	g ($m \cdot s^{-2}$)	V ($m \cdot s^{-1}$)	R_m	R_s
model *	1460	0,015	0,63	156	810	0,015	$8.5 \cdot 10^{-4}$	9,81	$1.78 \cdot 10^{-4}$	11972360	3
nature *	2650	$1.5 \cdot 10^{4}$	0,6	$5 \cdot 10^{7}$	2750	$1.5 \cdot 10^{4}$	$1 \cdot 10^{15}$	9,81	$6.34 \cdot 10^{-10}$	9571077	8

* granitic melt with 1.5 wt.% water + 60-80 vol.% crystals; viscosity (melt+crystal) of $1 \cdot 10^{15}$ Pa·s

* mushy wax (48 °C)

layer at the bottom of the lower crust to a partially molten layer close to the interface between the weak lower crust and a brittle upper crust.

3.4.3 Experimental procedure and model development

After attainment of the stable thermal gradient across the wax-sand multilayer, 55-60% shortening of the model domain was provided by the motion of the mobile plate against a stable backstop at the constant velocity of 1.3 cm/h (Fig. 26). Front side images were captured every 10 seconds by a single camera (*Canon EOS 1300D, 18Mpx, lens Canon EF-S 18-55mm f3.5-5-6 IS II*) mounted on a tripod. Images were saved in both the JPG format and RAW (CR2), later converted to TIFF (uncompressed, 24-bit(true colour, RGB)). Two point light sources were used to suppress the shadows in the background of the model domain. To decrease the reflexivity of the model glass walls, a whiteboard was mounted in the back wall of the apparatus.

A sequence of experiments performed at similar settings exhibits comparable trends in the evolution of the model domain marked by the development of up to five folds that developed sequentially during increasing shortening (Fig. 26b,c, folds F1b-F6). During the first 3-5% of shortening of the model displayed in Fig. 26, the model domain reflects homogeneous thickening followed by amplification of the first two folds (Fig. 26b, 10% of shortening). These first two folds later merge into one large Y shaped fold during the subsequent amplification of the remaining set of folds (Fig. 26b). All folds are associated with melt inflow into their hinge zones along the axial planes (Fig. 26c). Such melt inflow is manifested for example by axial plane-parallel finger-shaped channels in the core zone of complex fold F1b (Fig. 26b, c) that formed by coalescence of the first two folds F1 and F2. Long-lasting evolution of fold F3 was coupled with strong attenuation of the vertical limbs. The vertical limbs were at a late-stage of the evolution of the fold pinched by the surrounding sand as the left limb and the associated inflection point of the fold were progressively uplifted during progressive shortening of the model domain (Fig. 26d). This evolution was associated with isolation of paraffin melt in the diapirically shaped upper part of the fold above the pinched zone. A relatively large amount of melt was trapped also in the triangular zone below the pinched zone and above the source layer of paraffin melt (Fig. 26d). In contrast, the two following folds, F4 and F5, are marked

by lower height than the folds F1b and F3, homogeneously attenuated fold limbs and a relatively small amount of captured melt (Fig. 26d). Finally, the last fold in the sequence (F6, Fig. 26b) is marked by the highest proportion of melt that accumulated in the asymmetrical triangular zone below the crestal part of the fold.

3.4.4 Improvement of colour variability for PIV analysis

Passive marker layers were incorporated in both, the wax and sand layers, to increase the visual resolution of the deformation features in the models. While the wax subdomain consists of a multilayer of five 0.3 mm thick layers of contrasting colour, only one stripe of red colour was included in the sand layer (Fig. 27b).

To enhance the PIV method resolution, we incorporated solid and circular passive markers that were randomly distributed on the front side of the model. These variably coloured markers are represented by small and flat glitter particles (Fig. 27a) of 0.1 - 0.5 mm in diameter. For the sand layer, we used the black colour dominated markers, while the more colourful glitter mixtures were superposed on the wax layer.

To visualize the finite deformation pattern, we tested the applicability of fluorescent wax shavings (Fig. 27a) that were again sprinkled on the frontal side of the wax layer. These variably shaped and elongated particles served as passive markers that were deformed during the domain shortening and were aligned and stretched parallel with the axial planes of the developing folds. The finite deformation pattern as visualized by these particles was then photographed with a long time exposure in darkness (Fig. 27c).

3.4.5 The PIV calculations and testing of accuracy

The displacement field was calculated from all the sequential pairs of 445 analyzed images (TIFF format). The images, with a resolution of 5202 × 3465 px (horizontal × vertical), were cropped by a mask, defining the model domain. The PIV calculations were performed with the setting corresponding to the PIV analysis of the oroclinal buckling models. We used three interrogation windows (2176 px^2, 512 px^2, 128 px^2) for subareas of the images (4801680 px^2 at an initial non-contracted state where the deformable model domain is represented by 885312 px^2) representing the deformed model domain. Image pre-processing (additional image filtering and contrast enhancement) were done using the PIVlab interface (see chapter 3.3.4 or 3.8.3). The resulting displacement field contains 319 × 57 (horizontal to vertical) node points.

As in the oroclinal buckling models, we tested the accuracy of the PIV post-processing using the virtual markers. The virtual markers were positioned along the horizontal line following the red stripe in the sand layer and one of the layers in the wax multilayer (Fig. 28). Application of the integrated displacement for each marker and for all the time steps resulted in a very good match with the finite state

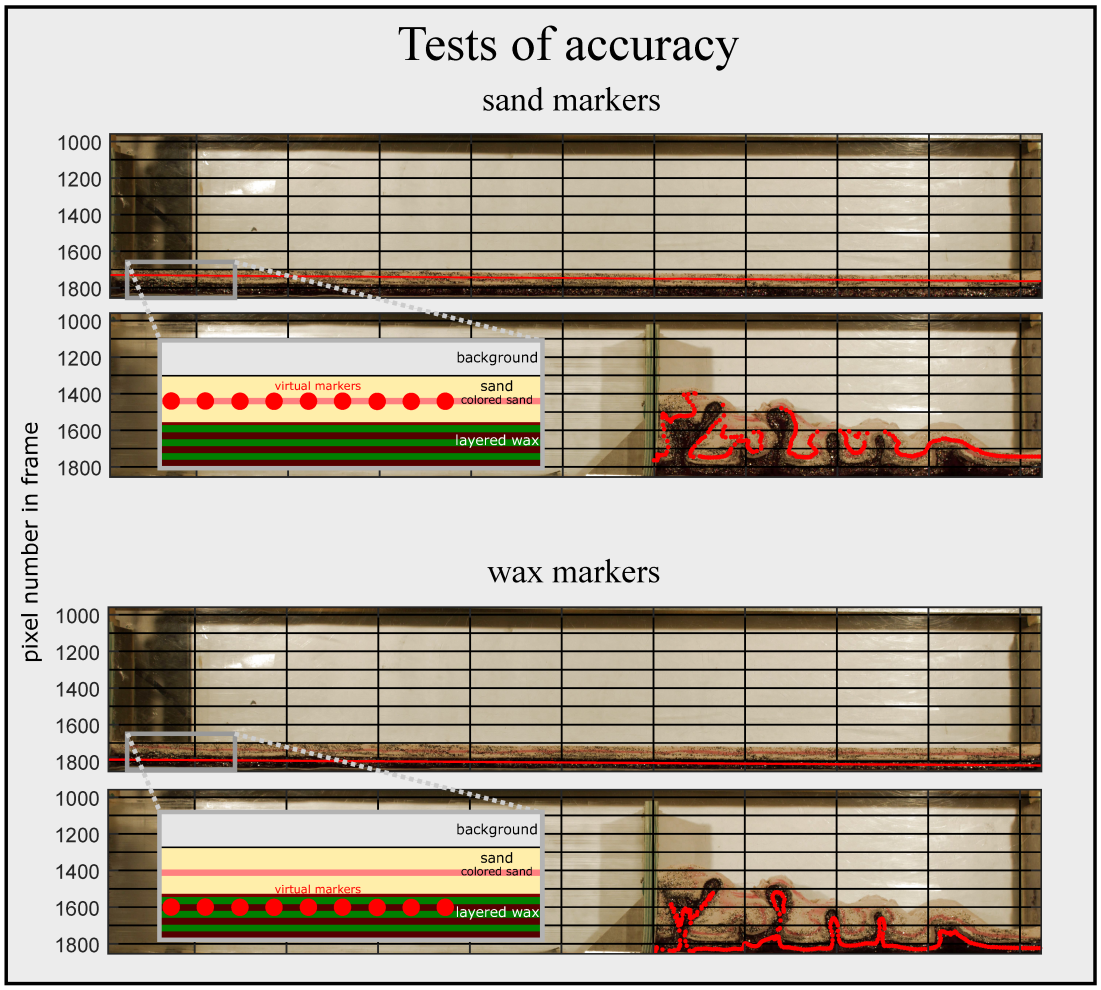


Fig. 28: Qualitative test results of the PIV for laboratory simulations of detachment folding. Top two figures show initial and final position of the markers distributed along the red line in the sand layer. Bottom two figures show a similar match for the initial and finite position of equivalent markers situated in the wax layer.

pattern of the experiment. The positions of the virtual markers trace the folded passive markers and displacement around the thrusts in the sand layer (Fig. 27b, 28). This test suggests that the calculated displacement field reliably reflects the final deformation pattern.

3.4.6 Derived model parameters

The contour maps of the strain-related parameters derived from the displacement field were analyzed only for the first 30% shortening since the evolution of the associated fields shows recurrent patterns during the sequential folding (Fig. 29). All the displacement field features that are described in the text below are marked by stars with corresponding numbering in figure 29A. The velocity displacement field map reveals a sharp gradient along the longitudinal direction that corresponds to the amplification of lastly developing fold (Fig. 29A-a (1)). From the ∼10% of shortening, the velocity gradient becomes more gradual.

The positive and negative divergence of the velocity field represents primarily the locations of extension and compression in the model domain, respectively. In the sand layer, the positive anomalies correspond to the extensional crestal part of the folds (Fig. 29A (2)), while the negative values match with the compressional, synclinal sectors located between the individual folds (3) and at the interface of the wax and sand above the initial fold perturbations (4). Aerially extensive domains of negative divergence in the foreland flanking fold limbs in the sand are associated with the motion of the model domain with respect to the immobile background (5). Therefore, these anomalies can be regarded as artefacts of the experimental setup and cannot be interpreted in terms of the inner deformation dynamics. Finally, pairs of close spatially associated negative and positive anomalies are situated in the triangular domains at the base of the developing detachment folds (6). These sites correspond to the visual inflow of melt from the source layer to the axial and crestal parts of the developing folds. While the left sides of these triangular zones are coupled with negative divergence, the right sides of these triangles show positive divergence values.

The second invariant of the strain-rate tensor (isovolumic strain-rate) reveals maximum shear rates at the surface of the model domain (7). This pattern is again linked to the movement of the model domain in front of the immobile background, similar to the negative divergence on the right side flanking slopes above the folds. In the interior of the model domain, high shear rates are linked with locations of fore- and back-thrusts in the sand (8) and axial planes of folds in the wax (9). The last significant localization of shear is associated with the triangular zones at the bottom of the melt-cored detachment folds (10).

In the vorticity field (Fig. 29A,j-l), we observe counterclockwise rotational movement at the model surface (11), which is again associated with the relative movement of the model domain with respect to the stable model background. In the

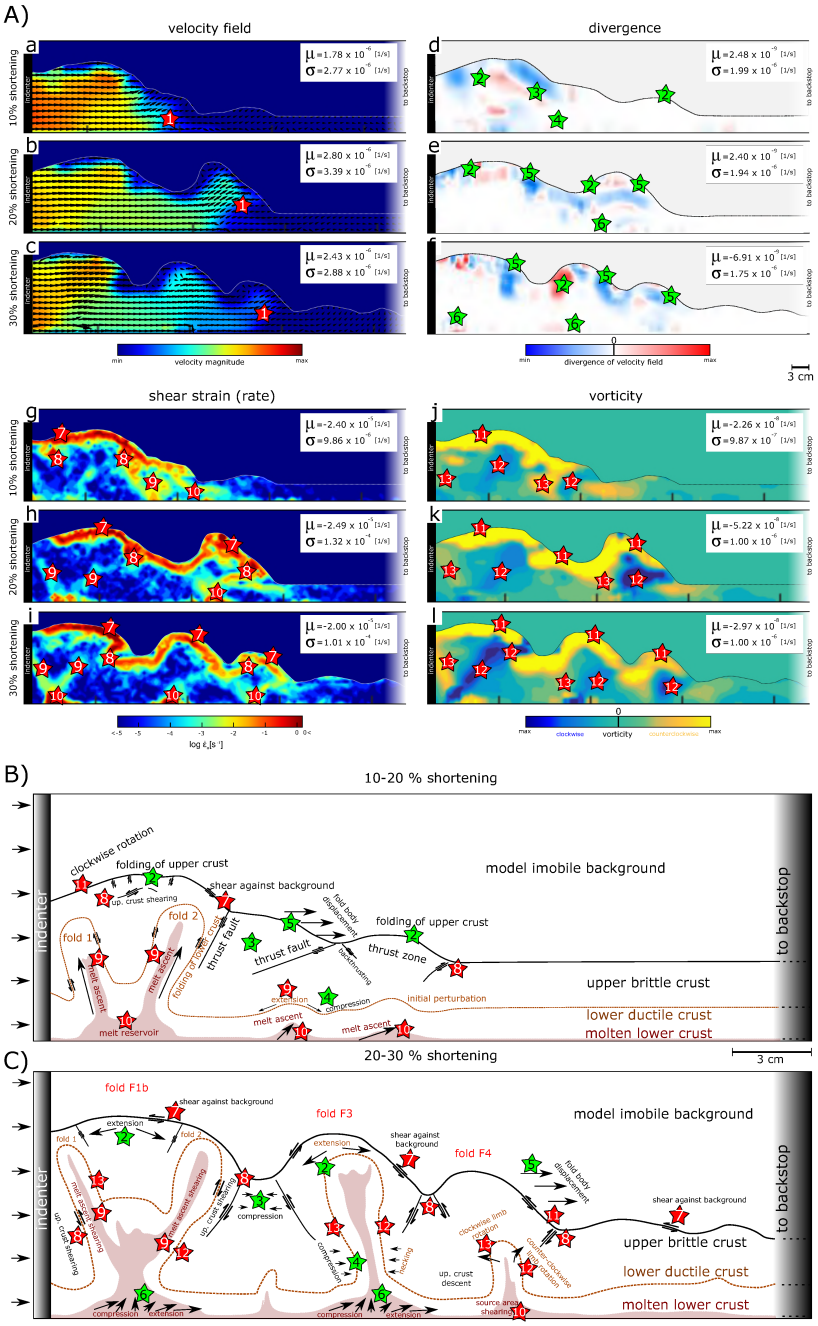


Fig. 29: Colour maps of PIV-derived parameters from the displacement field plotted for three shortening stages of the oroclinal buckling models (10, 20, 30% shortening). From top-left to bottom-right (panel A), the parameters are: magnitude of displacement velocity with arrows representing vectors of displacement (a-c), divergence of velocity field (d-f), the second invariant of strain-rate tensor, equivalent to material shear strain-rate (g-i) and vorticity (j-l). All parameters except the strain-invariant are standardized (to obtain normalized z-scores for further analysis). Original average values and standard deviations are displayed in the small box above the current colour map. Panel (B) shows schematically the evolution of the major features for 10-20% of the model domain shortening, while panel (C) shows the progressive evolution of these features for 20-30% of the model domain shortening. The red stars in the contour maps and panels (B) and (C) correspond with all the deformation features described in the text.

inner part of the model domain, the vorticity anomalies correspond to the clockwise and anti-clockwise motion related to the fore-thrusts (12) and back-thrusts (13), respectively.

3.5 Divergence and the volumetric flow on local scale in the detachment fold experiments

The divergence parameter in the detachment fold experiments was employed for tracing the volumetric changes derived from the velocity field that were analyzed from the cross-section of the accretionary system (side-view) (Fig. 26, 29). This approach is analogous to the oroclinal buckling models (Fig. 24, 25), where the divergence parameter was employed on plan-view image datasets for dynamics of topography evolution. The motivation for the detailed divergence analysis in the detachment fold experiments was a deeper understanding of the deformation and relative material transfers in the selected parts of the models.

In particular, we wanted to quantify the flow dynamics of melt and surrounding partially molten wax during the progressive development of the detachment folds, because the final fold shapes are apparently linked with the relative amount of melt available in the source layer (true amount of the melt transferred from the close surroundings of the amplifying folds) and the rate of vertical melt injection along the axial plane of the folds. Detailed inspection of the upward melt flow zones revealed that the melt is transferred in a coherent single channel (e.g. fold F3, Fig. 26; Fig. 27c) or through several discrete and narrow, finger-shaped channels surrounded by the mushy wax (e.g. fold F1b, Fig. 26). Since the geometry of the folds and the flow channels are clearly different across the studied sequence of the detachment folds in a single experiment, we decided to trace the variations of the divergence parameter in time and space.

At first, we focus on small-scale details of the models and analyze the displacement field in a predefined static image window. This window is fixed with respect to the background of the moving material in the model (Fig. 30) and locked at the original level of the mushy wax zone, where discrete melt channels develop at later stages of the model evolution (e.g. in fold F1b, Fig. 26, 29c). In the second approach, we develop the mobile and adaptive subgrids, fixed on pre-selected subdomains in the model domain (e.g. fixed on the axial plane of a specific fold), where the divergence is calculated.

3.5.1 Divergence in a static window

In order to understand the deformation pattern related with melt transfer on a local scale, the window used for the PIV calculations was fixed at a position in the foreland of the first two developed folds in the mushy wax layer (timestep 100/450; Fig. 30a). We traced the deformation field in this small window until the time step

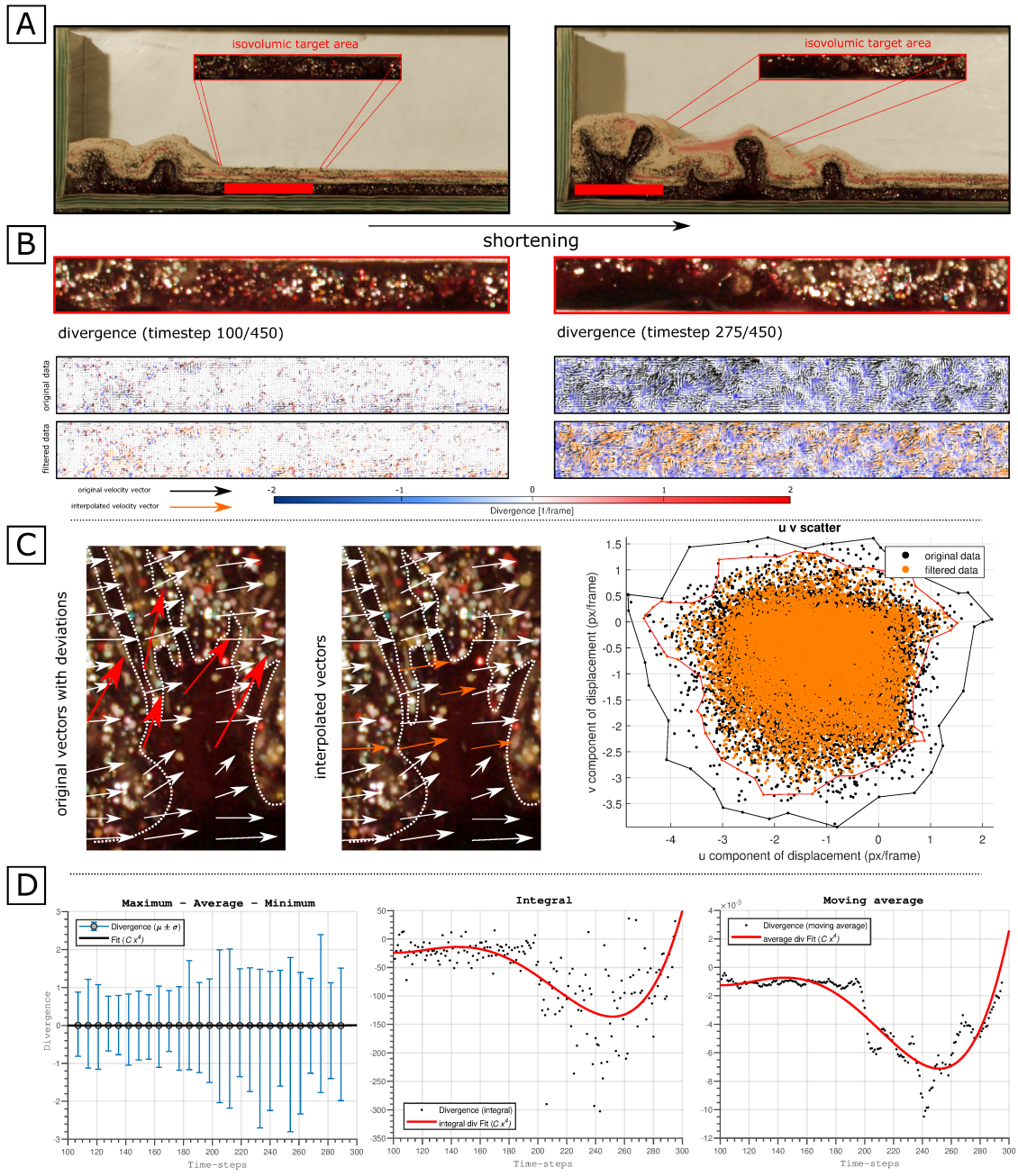


Fig. 30: Application of the divergence for investigation of volumetric flow. Panels A and B display the model domain in two distinct stages of the model evolution and a static window where the divergence of the velocity/displacement field was calculated. Panel B shows the displacement vectors and divergence field in the static window for corresponding time-steps, before and after filtering of the velocity field by substitution of vector deviations from the velocity background (filtration scheme follows the 3×3 median test: e.g. Nogueira et al., 1997; Westerweel and Scarano, 2005). The substitution of rejected vectors by 2D interpolation (c), includes scatterplot of u,v components of the velocity field before and after filtration. Red arrows represent the original displacement which is locally substituted by new interpolated values (yellow arrows). Diagrams of time-evolution of the divergence in static window shown in (D) were calculated from filtered displacement field (maximum - average - minimum divergence, integral divergence, moving average).

300/450, (Fig. 30a,b), when the core zone of fold F1b completely overlapped with this window during progressive shortening. At first, we calculated the divergence from the original displacement field obtained from the PIV with settings described in section 3.4.5. In the following calculations, we reshaped the interrogation windows in the PIV settings for the image subsamples corresponding to the dimensions of the static window (to 512 px^2, 128 px^2, 32 px^2). The analyzed image window represents the area of 75336 px^2 cut from the original image of the model domain with a size of 885312 px^2. The resultant vector field which is shown in Fig. 30b contains 49×391 nodes.

Preliminary analysis of the displacement field in the static window revealed velocity gradients on small scales (Fig. 30b) marked by e.g. anomalous vectors (Fig. 30c) that are associated with the melt flow through small finger-shaped channels in the lower parts of the model (Fig. 30c). This melt propagation and ascent into the cores of developing folds is apparently independent of the background displacement field which is related to the displacement of the whole model domain.

We realized that standard filtering procedures could significantly alter the distribution of divergence and interpretation of the local melt flow patterns. Therefore, we decided to intentionally attempt to filter all the anomalous vectors that are related with the small scale (finger shaped) channels transferring the melt from the source domain to the overlying folds (Fig. 30c). This procedure implements artificial distortions of the displacement field, where the anomalous vectors were replaced with interpolated values. As a result, the modified displacement field is characterized by non-zero values of integrated divergence that can be interpreted in terms of melt inflow, accumulation and outflow.

Figure 30d displays the local and areal divergence in the static isovolumic area (predefined static window) in time that corresponds to progressive folding of the model domain in front of, and later above, this area. The divergence values reveal a relatively small variation range for the first part of the studied image sequence (100-170/450) with average values close to zero (Fig. 30b,d). The difference between extreme values progressively increases with domain shortening from timestep 180. The integral values (areal divergence), as well as the average values of divergence (Fig. 30d), show a non-linear trend with decreasing values up to timesteps 240-260 followed by progressively increasing values up to a timestep 290.

This evolutionary trend may be attributed to an increasing melt transfer rate between the source area (basal layer) and the core of the growing fold (decreasing divergence). The minimum values are associated with a high rate of material inflow, resp. with an increasing amount of the melt which is distributed in the target area. As the amplification of the F1b fold is slowing down, the rate of the melt inflow decreases and the divergence increases back to zero values.

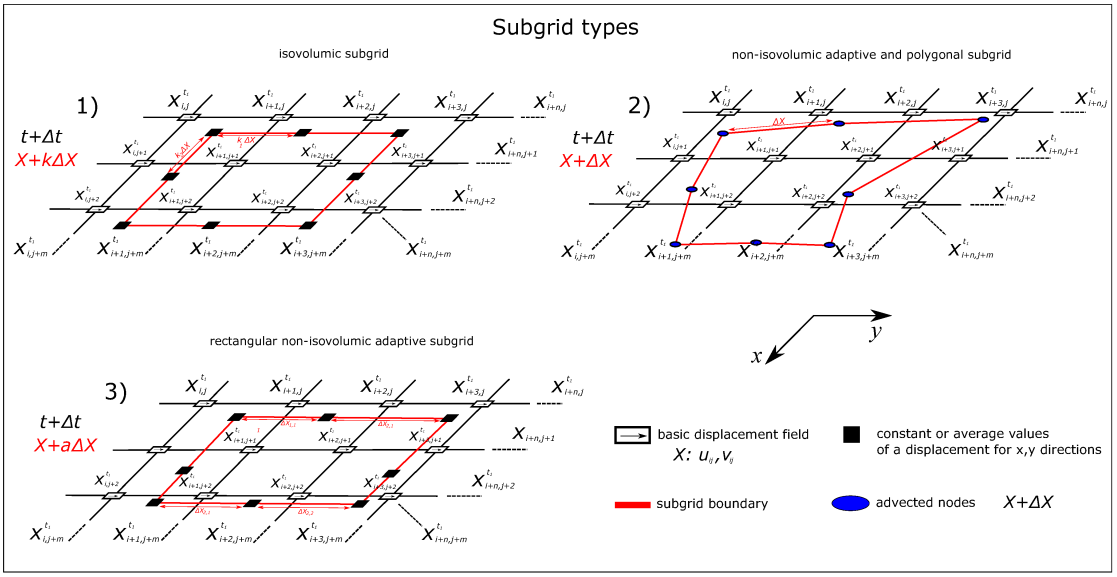


Fig. 31: Types and interpolation strategies for the interrogation subgrids. The three selected subgrid types are described in the text. Red lines show the shapes of the subgrids. The black rectangles at subgrid boundaries represent the constant or average values of displacement, while the blue ellipses correspond to subgrid boundary nodes with individual displacement in both directions.

3.5.2 Adaptive subgrids

We developed three types of numerical subgrids that were locked on the central parts of the evolving folds (target areas) (Fig. 31): 1. ***isovolumic subgrid*** with a constant factor of displacement ($k\Delta X$) of all boundary elements (Fig. 31.1, 2. ***non-isovolumic adaptive and polygonal subgrid*** with individual displacement (ΔX) of all boundary elements (Fig. 31.2), and 3. ***rectangular non-isovolumic adaptive subgrid***, where the displacement of boundaries is prescribed by average displacement ($a\Delta X$) of all boundary elements (Fig. 31.3).

For the ***isovolumic subgrid*** (Fig. 31.1), it was difficult to hold the subgrid on the central part of the target area (axial part of the fold). The application of the ***non-isovolumic and polygonal adaptive subgrid*** was finally rejected due to the numerical diffusivity problems that become more significant for complex geometries with sharp gradients in the relative motion of elements. In other words, the real perturbation of the interface between the rheologically contrasting domains shows a shorter wavelength than the displacement field grid, resulting in artificial distortion of the subgrid boundaries. Finally, the ***rectangular non-isovolumic adaptive subgrid*** proved as a fair compromise between the first two subgrid setting options. This subgrid remained centred on the domains of target areas during the progressive evolution of the displacement field. In addition, for two neighbouring target areas, individual boundaries remained parallel without any artificial development of gaps or overlaps.

3.5.3 Divergence in adaptive subgrids and mass balance

To trace the melt flow related mass balance in the developing detachment folds, we used two neighbouring cells of subgrids (***rectangular non-isovolumic adaptive subgrid***), where the first cell overlaps with the evolving fold structure and the second one confines the melt source area beneath that fold. For both subcells, we calculated the average values of divergence of the velocity field from all subcell nodal values and across all the time frames that capture the fold development. This allows to trace the time evolution of average divergence and study the relative mass balance between the amplifying fold and the melt source beneath the fold. We studied the time evolution of divergence for the target areas (Cell 1 and Cell 2; Fig. 32a) and compared the trends in this evolution with their modal amount of melt. The divergence/modal content vs. time diagrams reveal four distinct stages associated with fold development. In the fold structure (Cell 1), the average divergence decreases (minimum values), which is associated with the inflow of the weak wax and wax melt. At the same time, the average divergence increases in the source area (Cell 2) up to maximum values, which is coupled with melt outflow (Fig. 32b). Progressive amplification of the studied fold is associated with an increase of divergence up to zero, which coincides with the inflection point of the divergence/time curve for the studied fold (Fold 3). Subsequently, the source area (Cell 2) shows a decrease of divergence, which is attributed to the continuous loss of material that flows upwards into the fold area (Cell 1). The third stage in the fold development and associated mass transfer is marked by a further increase in divergence up to maximum values. This is linked with the increasing contribution of the extension in the sand layer and the wax in the hinge sector of the locked up folds. During this stage, the vertical limbs of the locked folds undergo attenuation and can be pinched by the surrounding sand, which results in the formation of diapirically shaped folds (Fig. 32c). This is complementary with decreasing positive divergence in the source domain (Cell 2), linked with a decreasing rate of melt outflow into the overlying region (Cell1).

The sum of the melt amount quantified in both subdomains (in folded and source areas) remains nearly equal for the incriminated timesteps and corresponding average divergence reveals opposite trends in both studied subdomains. This equilibrium serves well as an approximate test of mass conservation in the studied system.

We studied the mass balance for corresponding subdomains in all the sequential folds in the model domain (Fig. 33). The size of individual Cells is implicitly taken into account by calculation of average divergence in target areas. Although for the analytical solution, it is also possible to weight the integral divergence by the areal size of the current subgrid area, in this study, we calculated only the discrete (point) values of divergence for further analysis.

For folded areas, the range of divergence values comprising the maximum, inflection, minimum and finite point of the divergence evolution curve, respectively, progressively decreases in the sequence of melt-cored detachment folds (F1b, F3, F4, F5, F6; Fig. 26c, 33). A similar trend is also visible for the source area subdomains,

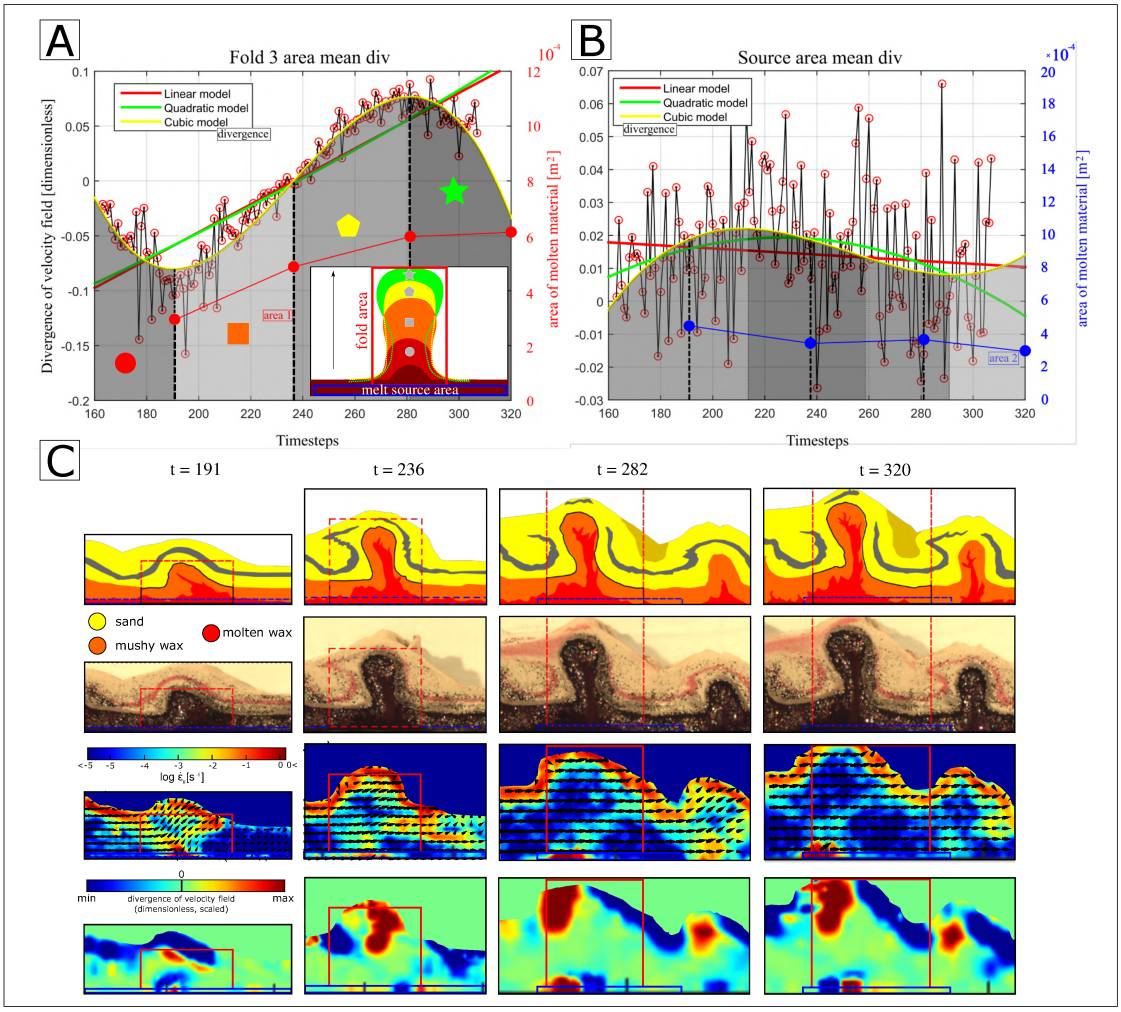


Fig. 32: Evolution of the divergence and melt content in the two traced subdomains in the detachment fold experiments (the fold and the source area) for the fold F3 (see Fig. 26c). Diagram A displays the average divergence evolution in the fold area. Key segments of the cubic interpolation curve (minimum, inflection, maximum, finite state) are also marked by the modal amount of the melt that was measured (red line with full red circles). Individual colored symbols correspond to the subsequent amplification stages of the fold as schematically illustrated in the inset. Diagram B displays the corresponding evolution of the divergence and the melt content in the source area. The blue line and blue circles show the melt amount content at specific time steps that correspond to the amplification stages (shown in inset of panel A). Panel C displays the redrawn shapes of the distorted layers, markers and the extent of remobilized melt in the fold cores, corresponding images and associated field contour-maps (divergence and shear strain-rate) for the individual amplification stages.

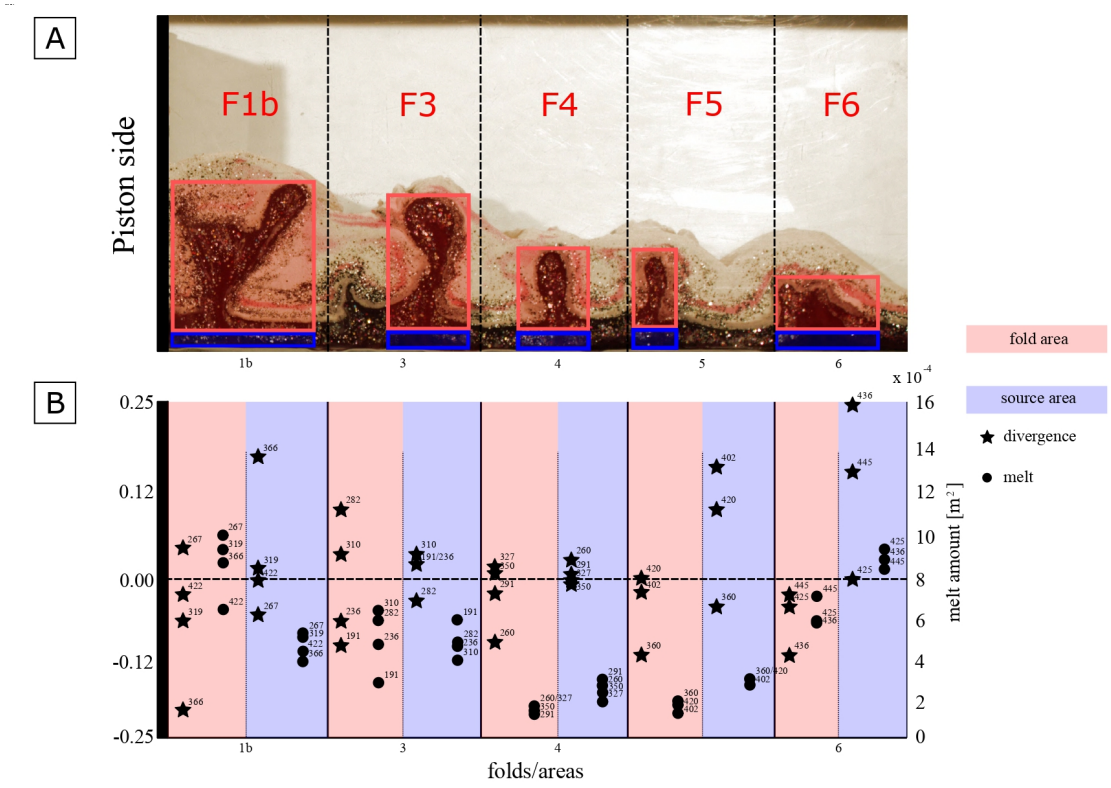


Fig. 33: Overview of the calculated divergence and measured melt amount for individual folds in the model domain. Red and blue rectangles schematically show positions and size of adaptive subgrids where divergence was calculated (fold and melt source areas). Lower panel compares the calculated mean divergence values and corresponding melt amount in significant fold evolution stages.

except for fold 5 and 6. The melt content values in associated stages partly follow this trend, except for fold 6.

The maximum values of average divergence decrease from fold 3 to fold 6 while in source areas, they reach the highest values for folds 1b and 6, situated at the edges of the model. The latter folds (1b and 6, Fig. 26c) also contain a significantly higher amount of melt in fold cores and source areas.

The minimum value of average divergence is characteristic for fold 1b and progressively increases with increasing distance from the indenter. A similar trend is also visible in respective source areas.

Generally, the time-steps with maximum average divergence in individual folds correspond to time-steps with minimum average divergence in their respective source areas. This opposite trend of evolution curves of average divergence represents clear evidence for mass conservation in neighbouring “melt source” and “fold core” subdomains.

3.6 Discussion

The two types of presented experiments illustrate complex lithospheric domains, where crustal scale transfers are controlled by the implemented stratification that induces mechanical anisotropy and promotes folding. The major aim of the present work was to illustrate the correlation of the deformation features with the variation of the velocity and strain-related parameters derived from the displacement field using the PIV technique, in order to explain the associated kinematic framework and relative mass redistribution on a local scale. We discuss briefly some of the geodynamic implications of the described models. Further detailed analysis of these models will be presented in separate studies.

3.6.1 Interpretation and significance of the calculated parameters in the oroclinal buckling models

Variations of all calculated parameters were neglected close to the margins of the model domains with anticipated edge effects at solid walls. The magnitude of the displacement field clearly reveals that the interface between the two subdomains is marked by contrasting element velocity in both models (Figs. 25a,b,c; 29a,b,c). This velocity gradient demarcates the deformation front with strong deformation localization. All parameters derived from the displacement field are well correlated with major deformation features developed exclusively at the surface of the orocline model domain. For example, the divergence of the velocity field map (Fig. 25d,e,f) indicates the convergent zones together with all the extensional zones. The divergence is rarely employed for the analysis of the displacement field (e.g. Kettermann et al., 2016, Reiter et al., 2011). Instead, the authors usually plot the horizontal and vertical components of strain (e.g. Adam et al., 2005; Krézsek et al., 2007; Boutelier and Oncken, 2011; Warsitzka et al., 2013). We suggest that the divergence represents a valuable parameter that reflects volumetric deformation and mass balance in the evaluated model domains.

In the oroclinal buckling models (Fig. 25), all negative values of divergence (convergent zones) are concentrated in elongated areas bound by thrust zones, while areas with positive divergence show extension, e.g. in crestal parts of upright folds, collapsing thrust belts or pop-up structures (Fig. 34, 35a). Formation of the thrusts, pop-up belts and elevated plateaus is primarily driven by mechanical coupling between the lower silicon layers and upper sand layer (Fig. 34c). Volumetric changes, associated with non-zero values of the divergence of the velocity field, inside and alongside the orocline, are then directly linked with internal deformation of the sand layer, e.g. marked by thrusting in front of the laterally propagating orocline hinges (Fig. 35a).

The second invariant of the deviatoric part of the strain-rate tensor (Fig. 25g,h,i) serves well for mapping of areas that are related with variations in the shear-strain component without the volume changes, independently to the referential frame. The

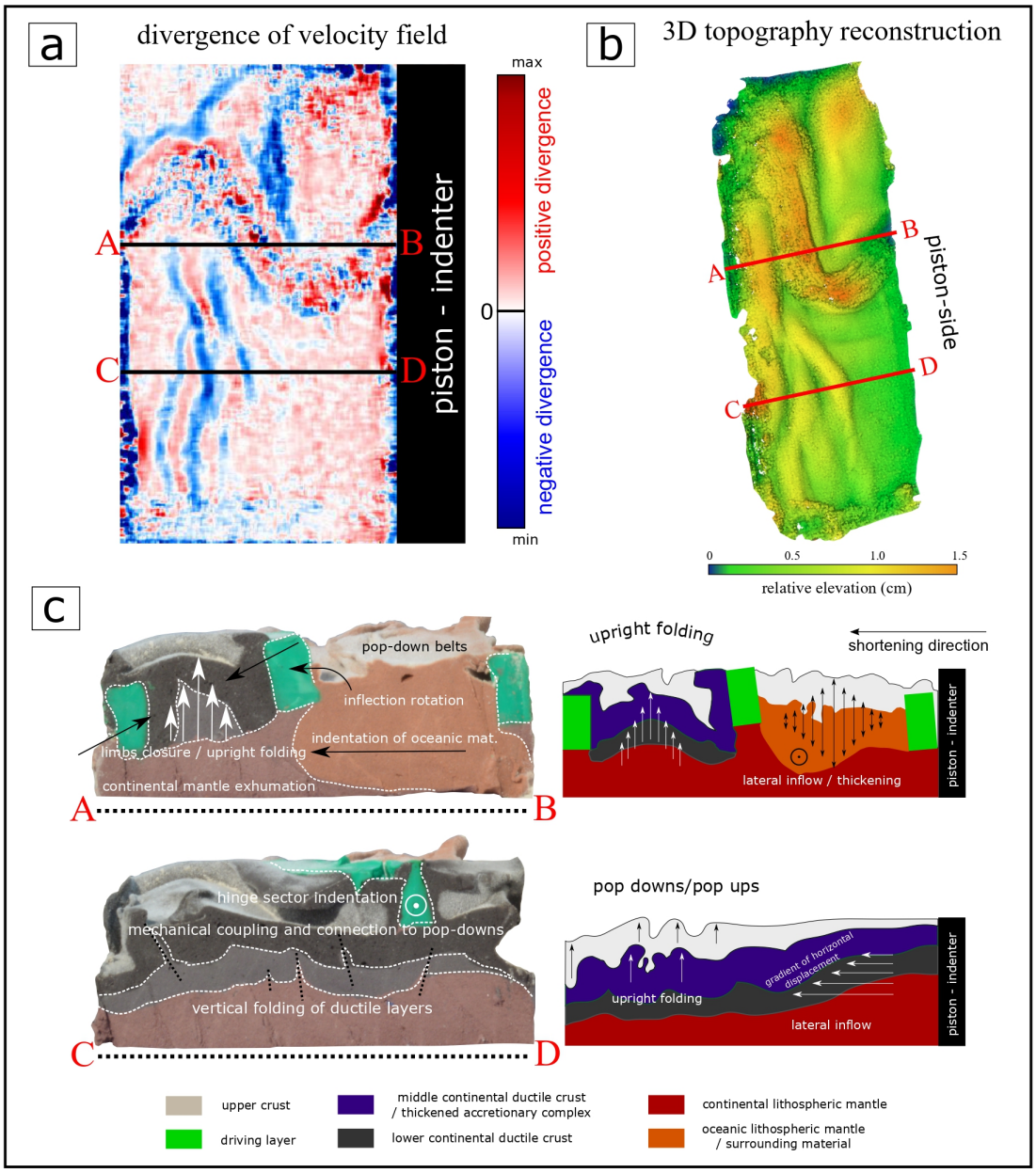


Fig. 34: Development of topography and a mechanical coupling between the upper crust and lower lithosphere in the model of oroclinal buckling. Panel A displays a contour map of the velocity divergence (after Fig. 25). The finite topography of the model surface (panel B) is represented by the DEM (digital elevation model), calculated by MicMac software (e.g. Galland et al., 2016). Sections A-B and C-D in panel C reveal the material transfer in the center of the model domain. Section A-B displays deformation of middle-lower crust and upper mantle segment between the orocline limbs, while section C-D displays development of pop-up and pop-down structures in the middle part of the model domain. Cross-sections of the model show the distorted silicone layers without the topmost sand layer (removed before the model slicing). Interpretative diagrams show the general deformation pattern that includes the sand layer.

zones of maximum shear strain values correlate primarily with the concentrated deformation along the rheological boundaries in the models and also reflect the development of major fault zones. We suggest that the total amount of shear strain with respect to the strain/-rate tensor is most conveniently expressed by the second invariant of its deviatoric part (equation 3.5) than simply by a single shear component (e.g. e_{xy}). In the vorticity of the velocity field (Fig. 25j,k,l), the most remarkable feature is seen in the rotation of the individual fold limbs around the inflection point of the orocline. It should be taken into account that the local tendency of the rotation is not related to the spinning movement of individual domain particles, but clusters of neighbouring particles.

The most of the deformation patterns in the upper crust are related to upright folding of lower ductile layers (Fig. 34c, section C-D) in both orocline hinge sectors. Subdomains of positive or negative divergence (Fig. 34a) can be correlated with the folded topography of the DEM (digital elevation model)(Fig. 34b). The upright folding and formation of pop-ups between the orocline limbs is supported by orocline amplification (Fig. 34c, section A-B). The pop-up and pop-down lines are curved and reveal a tendency to converge at the orocline inflection point. This pattern is also well shown in the vorticity field (Fig. 25A,j-l), where the rotational potential of the surface material around the inflection is obvious. The development of the finite topography pattern is associated with: 1. mechanical coupling between lower ductile layers and upper brittle material (e.g. Brun, 2002) and 2. amplification of the orocline, which is related with the rotational movement of the surrounding material.

3.6.2 Interpretation and significance of the calculated parameters in models of the detachment folding

The model parameters that were used for investigation of material transfer in the detachment folding models (Fig. 29) are the same as for the oroclinal buckling models. Here, the relevance of individual parameters interpretation is limited mostly by the distortion against the immobile background, as discussed above. The divergence of the velocity field (Fig. 29d,e,f) well correlates not only with sectors of extension or compression in the individual fold bodies but also with zones of melt ascent from the melt source layer. The triangular domains at the base of the folds (Fig. 29 (6),(10)) are clearly associated with melt coalescence from the source layer and later injection upwards along the axial planes of developing folds (Lehmann et al., 2017). While the inflow and vertical extrusion in mushy wax and wax melt are linked with negative anomalies of divergence, the neighbouring anomaly of positive divergence is attributed to the outflow of the melt from the melt source layer to the foreland part of the fold. The wax melt flow in the intrusion channel is then indicated by lower intensity negative anomalies that contribute to the negative part of the average divergence evolution curve (Fig. 32a).

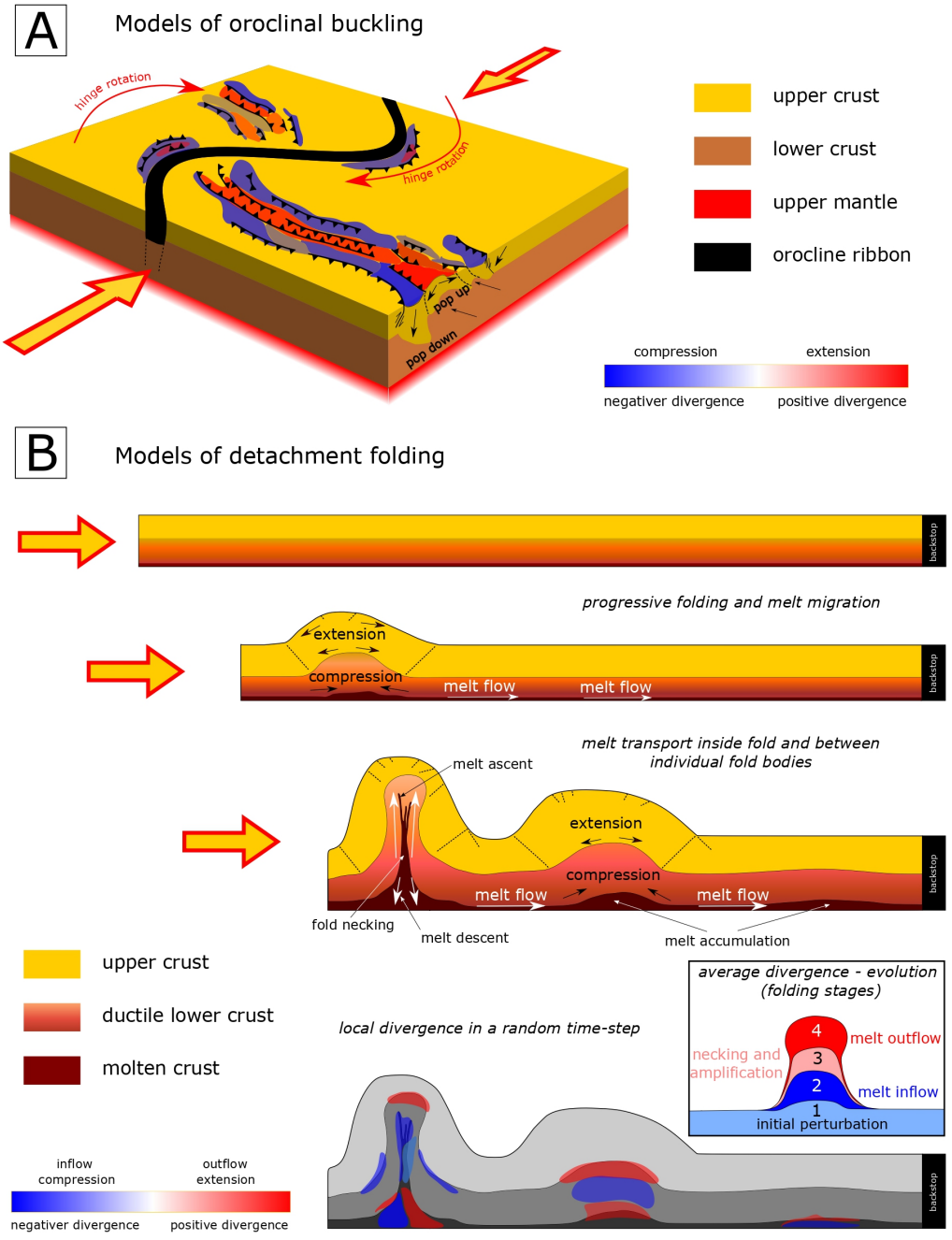


Fig. 35: The visualization of the main deformation features and material transport patterns in models of oroclinal buckling and detachment folding. Models of oroclinal buckling (A) reveal that the local positive and negative variations in divergence of the velocity field are associated with development of the pop-ups (positive values) and pop-downs (negative values). Models of detachment folding (B) show the inner transport alongside the axial plane of current fold and progressive migration of the molten material in the source layer towards the less amplified fold bodies in the frontal part of the accretionary system. Individual evolutionary stages of the detachment folds are complemented by a color pattern and a non-scaled color coding bar that corresponds to a relative range of average values of the divergence (small panel at lower-right part of (B)). All divergence polygons are only schematic (for real values see figures 25, 29 and 34).

As we discussed above, the shear strain component (Fig. 29g,h,i) is well expressed by scalar values of the second invariant (equation 3.5). Shear deformation corresponds with both the fore-thrusts and back-thrusts and also with the interface between the wax and the surrounding sand in the top part of the Y shaped fold (Fig. 29, features (8,9)). These shear zones are also reflected in both, the clockwise and counterclockwise domains in the vorticity field (Fig. 29, features (12, 13)).

3.6.3 Melt flow and mass balance in the sequence of detachment folds

The calculated average divergence of the velocity field for all individual folds (F1b-F6) in the time-plot and its correlation with the modal amount of melt in the areas of interest (melt source area in the basal layer below the fold and the folded area, Fig. 32), revealed progressively changing fold growth and associated melt flow dynamics in the sequence of developed detachment folds (Fig. 33).

The inner dynamics of the folds and the related divergence are characterized by several evolutionary stages (paragraph 3.5.3, Fig. 32a) that reflect initial perturbation, amplification and vertical extrusion of the fold body by attenuation of the verticalized limbs. The transition between these stages corresponds to the minimum, inflection and maximum (or maximum plateau), which can be followed by a slight drop in divergence during the final stages of the fold evolution. The distance between these evolutionary stages defines the magnitude of divergence scatter in the fold/source areas (Fig. 33, distance between black stars).

The maximum divergence scatter is characteristic for folds F1b, F3 and F6 that are situated close to the indenter and backstop regions and where also a higher amount of the melt was accumulated (Fig. 33, black circles).

The amplification associated with melt inflow in fold F3 was followed by the expulsion of some of that melt back into the melt source layer during the limb attenuation (Fig. 26d), which may be also reflected in the drop of the divergence values for the fold area (Fig. 33b). Simultaneously, as the folds lock up, the residual melt in the source layer flows laterally to the undeformed part of the model due to a pressure gradient driven by the load of the thickened portion of the model (Beaumont et al., 2001; Beaumont et al., 2004, Jamieson et al., 2004; Beaumont et al., 2006,; Gemmer et al., 2004; Albertz et al., 2010). This mobile melt thus thickens the detachment layer in the foreland (the melt source layer) and further assists decoupling of the overlying sequence and development of the sequential folds. This is clearly manifested by a large amount of melt trapped in the last fold of the fold array (Fig. 26c, 27c).

Small amplitude, low rate of melt transfer and low melt content in folds F4 and F5 in the middle part of the domain can be explained by 1) the difference in the thermal gradient - the lower thermal gradient in the centre of the model domain may be responsible for slightly softer wax with small buckling wavelength, 2) melt that was retained in the melt source region of fold F3 due to late stage uplift of the left

part of the fold (Fig. 26c,d), and 3) the short time interval for their growth with respect to the folds F1b and F3.

3.6.4 Application of modelling results to accretionary orogens with partially molten lower crust

Results of the detachment folding experiments presented in this study follow up on our earlier analogue modelling results that helped to identify detachment folding as a new mechanism for vertical extrusion of lower crustal rocks in accretionary orogens (Lehmann et al., 2017). A simple kinematic model of melt cored detachment folds presented by Lehmann et al., (2017) implies dynamic changes of the pressure gradients during the growth and lock up stage of these folds. In the first stage, "rapid fold amplification" is marked with an influx of melt driven by underpressure developed below the crestal domain of the fold, and associated with upright folding of the high-temperature flat layering. In the next stage, as the limbs of the fold rotated by 60°, the fold passes to "post-buckle flattening", marked by overpressurization of the melt in the fold core that may result in the failure of the ductile walls and expulsion of the melt from the core zone along the axial plane of the fold.

Similar melt transfer dynamics can be identified in the individual folds from the detailed analysis of the displacement field in a static window that passes through the mushy wax layer of a developing fold (Fig. 30) and the analysis of the developing fold in contact with the adjacent melt source domain using the subgrid areas (Fig. 32, 33). We suggest that some of the overpressured melt locked in the core zones of the folds may be evacuated back to the source layer (Fig. 35b). This melt can be transferred along the basal layer towards the foreland due to the gravity driven pressure gradient controlled by the crustal thickening in the wedge. Finally, this melt can become soaked up into the core zone of the subsequent fold in the fold array. In nature, such a scenario would imply significant magma assimilation and differentiation by percolation through different crustal levels back and forth vertically, and sideways in the source anatectic region.

The detailed analysis of displacement field in the present study allows comparison of the melt flux rates and relative melt flow directions, which is not yet possible in the crustal scale numerical models due to their low resolution and high viscosity/velocity gradients associated with the melt channels. Our results imply that the initial wavelength and thus the maximum height of the detachment folds are likely proportional to the amount of melt available in the imminent surroundings below the fold in the source layer. The early array of detachment folds can also later coalesce into branching structures cored by melt that represents weak zones prone to thrusting in the progressively thickened frontal part of the accretionary wedge (fold F1b, Fig. 29b,c). Some of the folds can also resemble diapirically shaped metamorphic core-complexes, where the surrounding sand (upper crust) in

the synclines indented the weak verticalized limbs of the folds during progressive shortening (fold F3, Fig. 26a,d, Fig. 35b).

3.7 Conclusions

The 2D PIV approach was tested on two examples of complex orogenic models, in topographic view of the oroclinal buckling models and side view of the crustal scale detachment fold models. Our structural and dynamical analysis of the analogue models is justified by fairly accurate test results comparing the calculated and real material displacement. The model parameters, derived by the decomposition of the strain rate tensor, highlight the evolution of major deformation structures in the models and allow interpretation of the local strain fields. In addition, the adaptive subgrids extend the quantification capabilities of the displacement field on a local scale, e.g. focussing on the divergence evolution during material transfer between individual target areas (melt inflow from the source layer into the core of a progressively amplifying fold). The results of this study are further summarized as follows:

1. The accuracy tests revealed that for optimal PIV post-processing and interpretation, it is convenient to combine the regular linear grid with randomly distributed contrasting particles sprinkled on the monitored surface. The accuracy of PIV calculations is also supported by the implementation of image filtering, additional interrogation windows and the TIFF format of input images.

2. In the oroclinal buckling models, isovolumic and non-isovolumic strain components, reflect the local distortions of the sand and dominantly the vertical displacement of the sand, respectively. This vertical displacement is interlinked with the amount of mechanical coupling between the lower ductile layers and the upper brittle crust (Fig. 35a).

3. The non-isovolumic component of the strain field (divergence) in the detachment fold experiments corresponds to 1) the extensional and compressional parts of crustal-scale folds, and 2) the dynamics of the molten material migration below and into the developing detachment folds (Fig. 35b). In contrast, the isovolumic strain field component (distortion) and vorticity correspond with dominant shearing in zones situated alongside the thrusts in the brittle part of the model and along the rheological interfaces, e.g. between the wax and sand layers or inside the folded partially molten wax layer.

4. The relative material transfer between the model subdomains can be quantified by average divergence evolution in the pre-defined subgrids and compared for example with the modal volume changes of the low viscosity and highly mobile material (molten wax).

5. The orocline buckling experiments reveal that the surface distortions reflect primarily the topography development of sand a) above the folded lower ductile layers, b) in front of laterally propagating orocline hinges, and c) orocline interlimb zones that are uplifted due to lateral inflow within the lower ductile layers (lower crust and lithospheric mantle).

6. The divergence analysis of the displacement field in the detachment folding experiments revealed systematic variations in the height of the folds and their modal melt content that are related to the inflow rate of melt into their cores. The overpressurization of the melt in the locked folds leads to melt expulsion back into the melt source layer, where it can be transferred further laterally into the foreland and facilitate detachment folding of the subsequent folds.

3.8 Appendix

3.8.1 Accuracy of the calculated displacement field

The accuracy testing of the displacement field in both models is an integral part of the present study (chapter 3.3.4 and 3.4.5). These tests justify the PIVlab based calculations for further parametric study and quantitative model evaluation. Many commercial softwares (e.g. *FlowMaster from LaVision, DynamicStudio etc.*) have implemented self-testing procedures where relevance of the calculated displacement/velocity respective to the real element displacement is tested. The PIV lab, as a freeware alternative to those software platforms, is also equipped with a self-testing procedure. This testing procedure creates synthetic particle images where real particle displacement is compared with the corresponding displacement calculations (Thielicke and Stamhuis, 2014 or Boutelier, 2016). The aim of the testing in our study was to evaluate the appropriate setting of the number of interrogation windows, surface colour conditions, image type and filtering, and geometrical setting of the models that can affect resultant displacement field (the best settings are described in chapter 3.3.4 and 3.4.5).

In general, the testing procedures revealed that the optimal set up of the PIV calculations in our models employs the TIFF image input format, additional filtering, colour variability of the model surface and multiple interrogation windows. The post-processing of the image sequences revealed that the calculations of the displacement field can be influenced or biased by several factors that should be taken into account during preparation of the model domain, image capturing and post-processing of the images. These factors comprise the analyzed image quantity, the image format, number of interrogation windows and resolution, light conditions and artificial motions of the model domains and camera position. We provide a summary of the testing results, which could be helpful for researchers that want to use the PIV (PIVlab toolbox) analysis for similar analogue models.

Quantity of analyzed images

The post-processing procedure revealed that the TIFF format is convenient for smaller image sets that cover the entire evolution of the model domain. In contrast, the JPG format can be employed for previewing the displacement fields of large image sequences. We suggest that further testing should focus on the optimal image capture frequency to decrease the computational and data storage requirements. However, the optimal capture frequency is important to achieve a good balance between small and large displacements between successive images. The finding of convenient sampling of image set for optimization of precision in resultant displacement field is a subject of empirical work. Too small increments result in a bad signal-noise ratio, whereas too large increments can result in loss of correlations/markers. These factors all well discussed in Thielicke (2014) and Thielicke and Stamhuis (2014).

Number of interrogation windows

Increasing the quantity and decreasing the size of interrogation windows results in higher resolution of the calculated displacement field. Although the large and dense field grids are convenient for detailed investigation of local deformation patterns, high resolution is conversely coupled with increasing number of artefacts. Sparser displacement fields do not authentically reflect real material movement on the local frame but can be employed for general development of the model dominated by homogeneous deformation. The effects related with sparse and dense displacement fields, according to numbering and sizing of interrogation windows, are discussed e.g. in Thielicke (2014)

Deformation artefacts during preparation and experimental runs

A crucial issue, negatively influencing the PIV calculated fields, arises from the changes in laboratory light conditions during the experimental runs. Slight light variations are introduced by passing by persons (or insects) or by propagation of shadows during motion of solid walls confining the model domain. Potential distortions can be also caused by the vibrations of the whole apparatus, produced e.g. by the stick-slip effect of the moving plate, the motor or by steps of passing by persons.

Image capture issues

The camera should be also conveniently positioned at a distance to cover the whole model domain with sufficient image resolution. For long rectangular domains, images should be corrected for the effect of *Petzval field curvature* (e.g. Riedl, 2001), associated with the curvature of the lens. Since the development of topography in the orocline models is associated with motions of particles in a direction towards the camera lens, the evaluated displacements in subdomains that are closer and farther

from the camera lens (deformed and non-deformed subdomains of the models, Fig. 25c) are not equivalent, but are likely negligible for small vertical topography as in the models of oroclinal buckling. It should be noted that these shifts are removable by correction techniques that are implemented in some commercial softwares (e.g. DaVis from LaVision) or potentially can be implemented in MATLAB (e.g. Boutelier, 2016) or Python environments.

3.8.2 Subgrid calculations and Marker in Cell method

The adaptive subgrid calculation is based on the same principle as the tracing of virtual markers. Every point of the subgrid is moved to a new position, where actual values of the displacement are interpolated from the surrounding nodal values. In summary, we can suggest that for the purpose of preliminary dynamic interpretations, the rectangular non-isovolumic adaptive subgrid was sufficient to reveal the relative mass balance between the domains of interest. Nevertheless, we also suggest that for reliable mass balance analysis in the subdomains, consisting of e.g. one type of material, the non-isovolumic adaptive and polygonal subgrid would be most appropriate. However, to suppress the effect of a numerical diffusion, it would be necessary to employ a second-order subgrid for local grid interpolations. This requires interpolation of new boundary positions using the displacement values not only from the surrounding nodal values but also from the equivalent grid values between the two subsequent time-steps. This approach is similar to the principle of the *Marker in Cell* technique (e.g. Gerya and Yuen, 2003).

3.8.3 Testing of the PIV resultant displacement field

For qualitative validation of the resultant displacement field acquired using the PIV, we tested different settings of the calculations and input image formats (Fig. 36). We compare processing results using both the JPG and TIFF images, colour variability of the studied surface, amount and size of the interrogation windows and optional image filtering (intensity highpass, intensity capping). The interrogation windows represent sub-samples of the images, where pixel clusters are identified and subsequently employed for cross-correlation analysis. The size and number of these sub-images corresponds to the order of cross-correlation analysis and final resolution of the calculated displacement field (Thielicke and Stamhuis, 2014). The aim of the PIV tests was to achieve the best compromise between the resolution and accuracy of the resulting displacement field, evaluated by visual comparison of the real and calculated displacement. While the real displacement is defined by movement of physical markers (an orthogonal grid of coloured sand lines or contrasting particles), the calculated displacement corresponds to the movement of virtual markers that match the original x, y positions of the pre-selected physical markers. The testing procedure consists of the following steps: 1. Attribution of virtual point markers to initial physical markers (the finite position of physical markers that represent

a surface sand grid) 2. application of a displacement to the virtual markers, 3. quadratic interpolation of the displacement in new positions of the virtual markers from the surrounding nodal values (the calculated displacement grid is sparser than the true displacement) for all time steps, and 4. imaging of the finite positions of virtual markers and their visual correlation with the position of physical markers. For all the tests, we scripted the associated procedures in MATLAB environment. The test results for the chosen PIV settings are summarized in Fig. 36. The default tested setting is marked by two embedded interrogation windows (Fig. 36e,e) and revealed relatively low degree of spatial correlation between the virtual and physical markers, irrespective to the chosen image format. The arrangement of virtual markers roughly follow the grid lines of the colored sand, but are scattered in highly distorted surface subdomains and locally form arbitrary isolated clusters, e.g. along the longitudinal linear (red) markers (Fig. 36a, 36e). Another test was performed for an experiment, where the color variability was enhanced by powdering the surface with dark sand (Fig. 36b,f). This test in general revealed a lower degree of virtual marker scattering with respect to the sand lines than for the default test. However, in several places and especially for the JPG format (Fig. 36b), the calculated solutions show high degree of scattering or completely incorrect positions (Fig. 36b,f). The third pair of tests represents the PIV analysis for three embedded interrogation windows, without additional surface powdering and applied image filtering (Fig. 36c,g). These tests resulted in a fairly good correlation of the virtual and physical markers in the central part, but increased degree of scattering close to the left boundary of the studied domain. The difference between the solutions for JPG and TIFF formats, respectively, is evident in slightly higher amount of erroneous solutions marked by isolated points for the JPG format (Fig. 36g). The last pair of tests characterizes the same PIV analysis setting, only the color variability of the surface was again enhanced by sand powdering (Fig. 36d,h). These tests resulted in the best match between the virtual and physical marker finite positions throughout the entire studied domain. There is only few clearly erroneous solutions that are again more abundant for the JPG format (Fig. 36d). For further analysis of the model, we chose the dataset from this last processed PIV calculation (Fig. 36h).

3.8.4 Rheometry of the analogue materials used in Part II and Part III

In the analogue modelling of the oroclinal buckling we used several silicone putties with various viscosities and densities according to a specified position in the model domain. The silicons which we used are modified GS1R gums from Rhone Poulenc in France (Cagnard et al., 2006). The measurement of viscosities of individual silicones before experiments (and re-measurement after a material recycling from the model after experimental procedure) was performed in a cylindrical viscometer (Reber et al., 2013) and density was calculated according to Archimédes law in high cylinder infilled by water. The scheme of concentric-cylinder viscometer (used in analogue modelling laboratory at Géoscience Rennes) is shown at Fig. 37 and

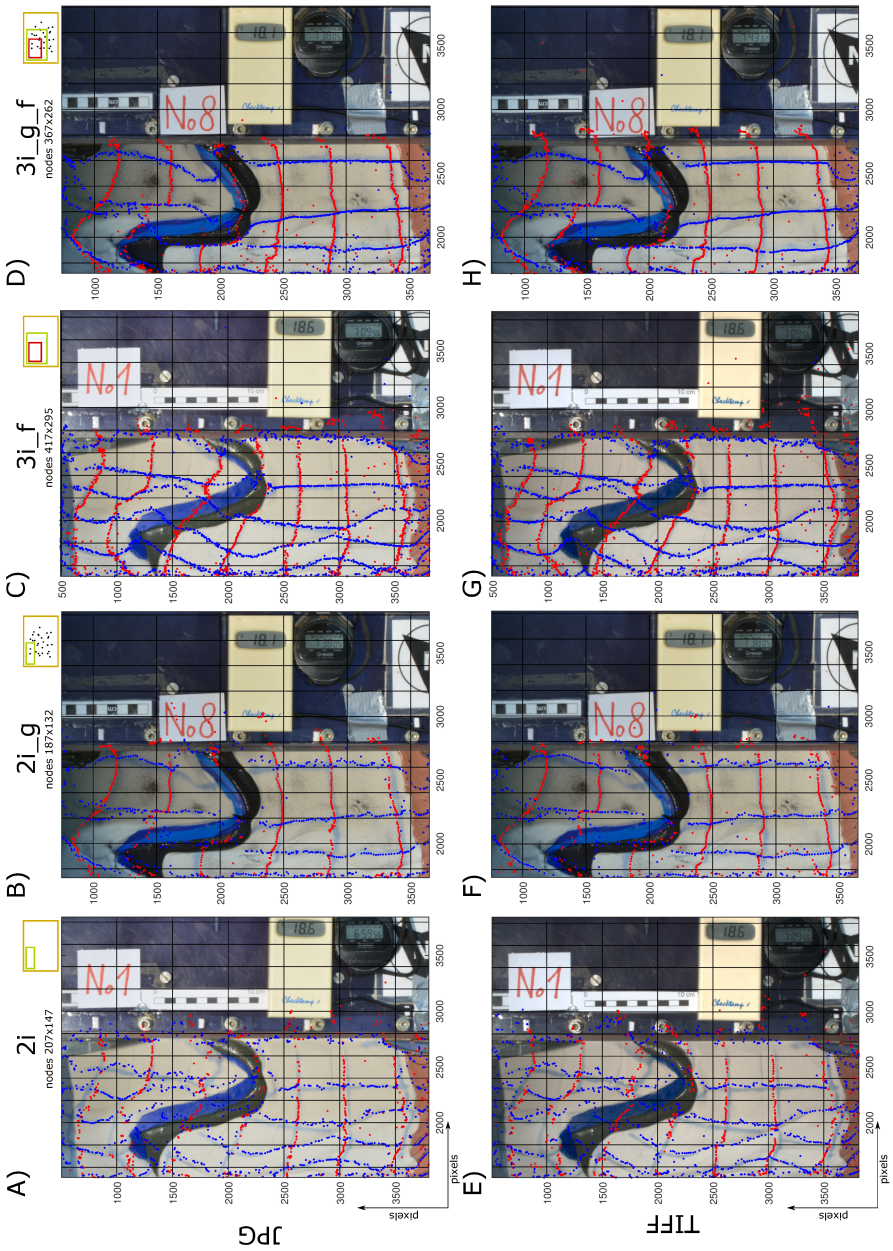


Fig. 36: Testing of the displacement field from the PIV for laboratory simulations of oroclinal buckling. Figures A-D represent the results for JPG format of input images, while figures E-H show the results with the TIFF input format. From left to the right, several PIV settings are compared; 2i - two applied interrogations windows (A,E), 2i_g - two interrogation windows and additional dark particles dispersed on the surface (B,F), 3i_f - three interrogation windows and image filtering (C,G), 3i_g_f - three interrogation windows with additional particles and image filtering (D,H)). The interrogation windows are defined by the following resolutions: 1st order: 64x64 px with step of 32 px; 2nd order: 32x32 px with step of 16 px; 3rd order: 16x16 px with step of 8 px. The blue markers originally corresponded to the lateral surface grid-lines, while red markers followed horizontal (longitudinal) direction of the grid-lines.

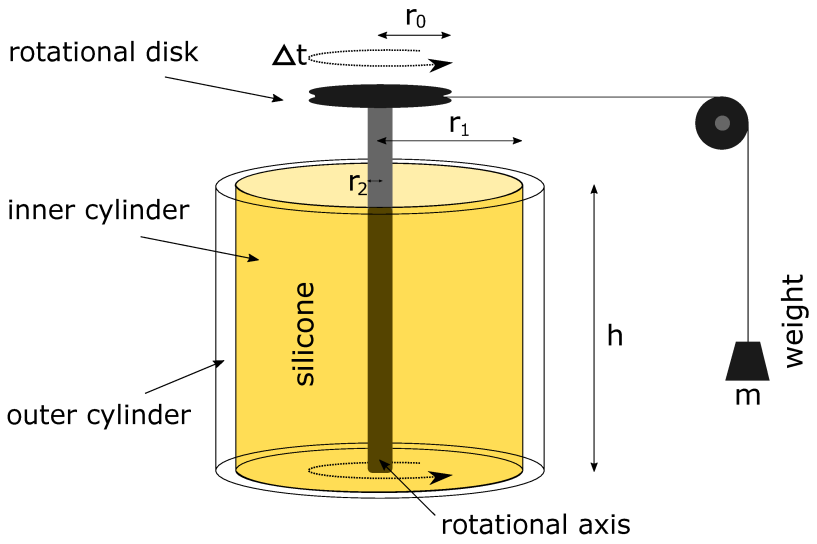


Fig. 37: Scheme of the cylindrical viscometer. The height of the cylinder (h) is 0.1 m, $r_0 = 0.05$ m, $r_1 = 0.05$ m, $r_2 = 0.008$ m and m = 200g.

appropriate relationship for viscosity calculation corresponds to equation (3.9). The viscosity measurement was divided into several steps, such as: 1. Filling of the cylinder by silicone and waiting for the removing of air bubbles; 2. Application of a drag to the silicone which surrounds the small central axial cylinder; 3. Manual measurement (using a stopwatch) of time Δt for one rotation of the axis in the cylinder and calculation of viscosity η according to the following relation:

$$\eta = \frac{\Delta t}{2\pi n} \times \frac{mgr_0}{2\pi h} \times \frac{1}{2}\left(\frac{1}{r_2^2} - \frac{1}{r_1^2}\right). \tag{3.9}$$

Here n is the dimensionless number of rotations, r_0 is the radius of the turning wheel, r_1 is the inner radius of the outer cylinder, r_2 is the radius of the inner axial cylinder, m is the mass of the pulling weight and $h(l)$ is the height of the outer cylinder. The determination of power-law numbers for chosen tested materials is described in Reber et al. (2013) and referring Betteguay (1986).

In the models of detachment folding we used a paraffin wax as suitable analogue material for simulation of lower ductile crust. Before we designed and built cylindrical viscometer with variable thermal conditions, we used translation shear apparatus (Fig. 38) for a measurement of the shear stress in a wax samples and then calculated

viscosity directly from relation between shear stress and velocity gradient:

$$\eta = \tau \left(\frac{\partial u}{\partial z} \right)^{-1}, \tag{3.10}$$

where τ is the shear stress, $\frac{\partial u}{\partial z}$ is the shear velocity gradient of the wax flow and η is the viscosity.

The cylindrical wax samples were heated in a water bath to a specified temperature (Tab. 6-8). Due to the low wax thermal conductivity we kept an appropriate temperature of the samples during the experiments with average deviation of ~ 0.8 °C at the top and bottom surface, ~ 0.5 °C at the side surface and 0.3 °C at 1 cm depth. The shear velocities were progressively set to three different rates (Tab. 6-8). The resultant shear stresses were used for calculation of viscosities reflecting individual temperatures and shear-rates. The velocity gradients were calculated from measured displacement gradients for selected samples (Fig. 39).

The resultant viscosities (Fig. 40) show a pseudo-linear decreasing of viscosity with minimum values at 45 °C corresponding to $\sim 9 \cdot 10^5$ Pa.s (with counting of an additional tested samples is scatter of values situated between $9 \cdot 10^4$ Pa.s and $1 \cdot 10^6$ Pa.s). Between 45 °C and 47 °C is a zone of a rapid viscosity decreasing up to the melting point at $\sim$ 51 °C. The viscosity measurements for wax with temperature in range $48 - 51$ °C were performed by rotational rheometer *VT 550 Haake* (supported by the Institute of Geophysics of the CAS in Prague). These viscosities are significantly lower than for $T < 47$ °C (Tab. 4,6-8) which is consistent with measurements of similar paraffin waxes used by Rossetti et al. (1999).

The general principle of the shear box experiments is in detail described in Mužík (2014).

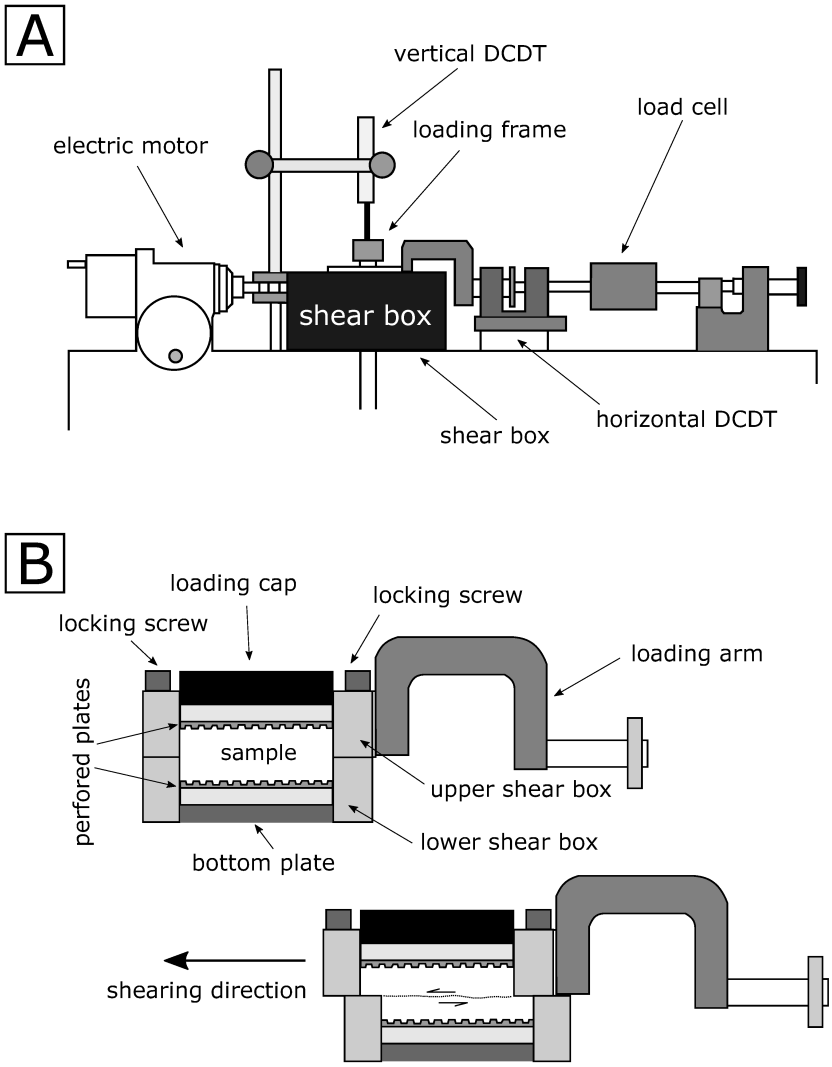


Fig. 38: Scheme of a translation shear box device. (A) lateral view to the device (developed by company *VJ Tech Ltd.* and situated at the department of Engineering Geology - Charles University) including holding frame, shear box and horizontal/vertical dynamometers (DCDT). (B) Details of the shear box core and shearing principle. Redrawn and modified after Mužík (2014).

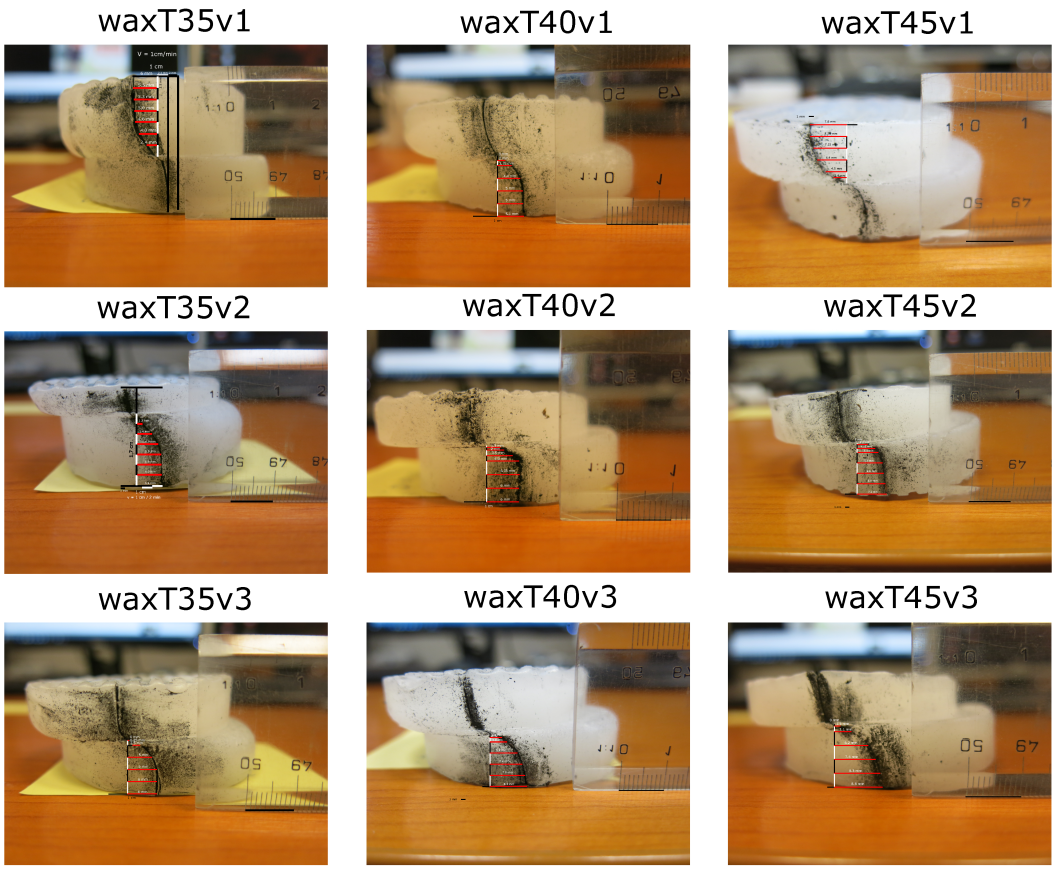


Fig. 39: Deformed wax cylinders. Selected 9 tested samples of the Paramo wax (used in modelling of the detachment folding). The temperature of a current sample is marked by T in the sample name and rate of the shearing is marked by v (see text for further details). The black and red lines are auxiliary scale-lines for measurement and calculation of the displacement/velocity gradient through shear zone of the sample. The black dust on the samples is a grinded graphite which was used for mapping of the shearing.

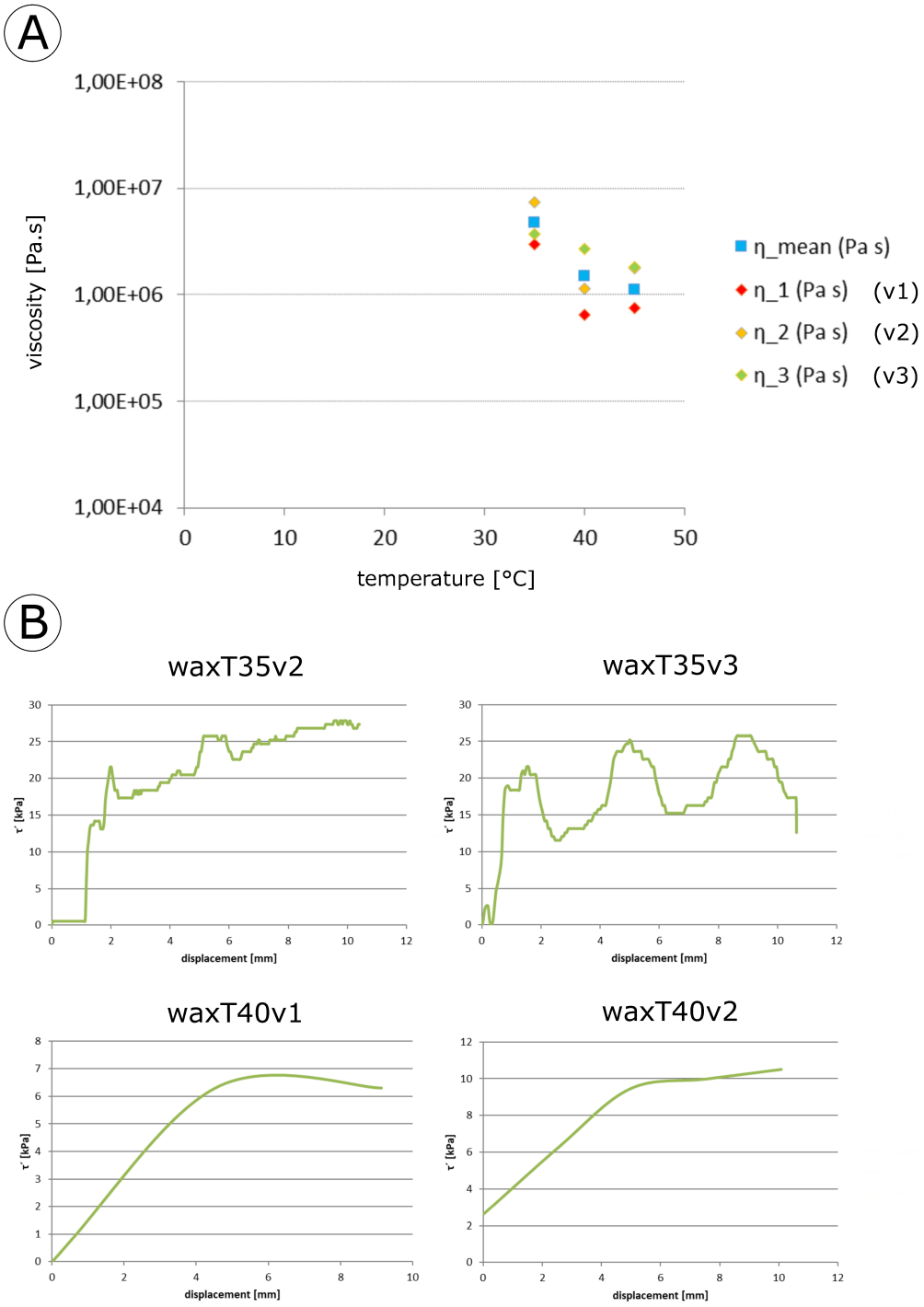


Fig. 40: Wax viscosities. Dynamic viscosities of the wax measured at the temperatures that characterize the viscosity gradient of paraffin wax in the crustal scale detachment fold experiment. Value marked with * was obtained from the shear box experiments, value marked with ** was estimated according to shearing experiments and values published in Rossetti et al. (1999). The values for temperatures > 48 °C were obtained from rotational rheometer *VT 550 Haake* (Institute of Geophysics of the CAS, Prague)

Tab. 6: Measured velocity gradient and calculated viscosity for samples with T = 35 °C.

waxT35v1	1cm/1min								
u (m)	y (m)	du	dy	v (m/s)	grad v (1/s)	n	tau (Pa)	mu (Pa s)	mu (exp)
0,006	0	-	-	-	-	7	17000	2975000	2.975E6
0,0055	0,0025	0,0005	-0,0025	8,33E-06	-0,00333333				
0,0053	0,005	0,0002	-0,0025	3,33E-06	-0,00133333				
0,005	0,0075	0,0003	-0,0025	0,000005	-0,002				
0,0046	0,01	0,0004	-0,0025	6,67E-06	-0,00266667				
0,004	0,0125	0,0006	-0,0025	0,00001	-0,004				
0,0024	0,015	0,0016	-0,0025	2,67E-05	-0,01066667				
0	0,0175	0,0024	-0,0025	0,00004	-0,016				
					-0,00571429				

waxT35v2	1cm/2min								
0,0062	0	-	-	-	-	7	22000	7451613	7.451E6
0,006	0,0025	0,0002	-0,0025	1,67E-06	-0,00066667				
0,0059	0,005	0,0001	-0,0025	8,33E-07	-0,00033333				
0,0058	0,0075	0,0001	-0,0025	8,33E-07	-0,00033333				
0,0049	0,01	0,0009	-0,0025	7,5E-06	-0,003				
0,0034	0,0125	0,0015	-0,0025	1,25E-05	-0,005				
0,0012	0,015	0,0022	-0,0025	1,83E-05	-0,00733333				
0	0,0175	0,0012	-0,0025	0,00001	-0,004				
					-0,00295238				

waxT35v3	1cm/3min								
0,006	0	-	-	-	-	6	21000	3687805	3.687E6
0,006	0,0025	0	-0,0025	0	0				
0,006	0,005	0	-0,0025	0	0				
0,005	0,0075	0,001	-0,0025	5,56E-06	-0,00222222				
0,0025	0,01	0,0025	-0,0025	1,39E-05	-0,00555556				
0,00025	0,011	0,00225	-0,001	1,25E-05	-0,0125				
0	0,0111	0,00025	-0,0001	1,39E-06	-0,01388889				
					-0,00569444				

Tab. 7: Measured velocity gradient and calculated viscosity for samples with T = 40 °C.

waxT40v1	1cm/1min								
u (m)	y (m)	du	dy	v (m/s)	grad v (1/s)	n	tau (Pa)	mu (Pa s)	mu (exp)
0,0051	0	-	-	-	-	6	7000	641221,4	6.412E5
0,005	0,0025	0,0001	-0,0025	1,67E-06	-0,00066667				
0,005	0,005	0	-0,0025	0	0				
0,0044	0,0075	0,0006	-0,0025	0,00001	-0,004				
0,00315	0,01	0,00125	-0,0025	2,08E-05	-0,00833333				
0,002	0,011	0,00115	-0,001	1,92E-05	-0,01916667				
0	0,012	0,002	-0,001	3,33E-05	-0,03333333				
					-0,01091667				
waxT40v2	1cm/2min								
0,006	0	-	-	-	-	7	10000	1144414	1.144E6
0,006	0,0025	0	-0,0025	0	0				
0,00603	0,005	-3E-05	-0,0025	-2,5E-07	1E-04				
0,0049	0,0075	0,00113	-0,0025	9,42E-06	-0,00376667				
0,0035	0,0085	0,0014	-0,001	1,17E-05	-0,01166667				
0,002	0,0095	0,0015	-0,001	1,25E-05	-0,0125				
1,3	0,01	-1,298	-0,0005	-0,010817	21,6333333				
0	0,0105	1,3	-0,0005	0,010833	-21,6666667				
					-0,0087381				
waxT35v3	1cm/3min								
0,0083	0	-	-	-	-	6	14000	2671378	2.671E6
0,0078	0,0025	0,0005	-0,0025	2,78E-06	-0,00111111				
0,0072	0,005	0,0006	-0,0025	3,33E-06	-0,00133333				
0,0062	0,0075	0,001	-0,0025	5,56E-06	-0,00222222				
0,0039	0,01	0,0023	-0,0025	1,28E-05	-0,00511111				
0,0028	0,011	0,0011	-0,001	6,11E-06	-0,00611111				
0	0,012	0,0028	-0,001	1,56E-05	-0,01555556				
					-0,00524074				

Tab. 8: Measured velocity gradient and calculated viscosity for samples with T = 45 °C.

waxT45v1	1cm/1min								
u (m)	y (m)	du	dy	v (m/s)	grad v (1/s)	n	tau (Pa)	mu (Pa s)	mu (exp)
0,0078	0	-	-	-	-	6	8000	494845,4	4.948E5
0,00775	0,0025	5E-05	-0,0025	8,33E-07	-0,00033333		12000		
0,00715	0,005	0,0006	-0,0025	0,00001	-0,004				
0,0064	0,0075	0,00075	-0,0025	1,25E-05	-0,005				
0,0045	0,01	0,0019	-0,0025	3,17E-05	-0,01266667				
0,0029	0,011	0,0016	-0,001	2,67E-05	-0,02666667				
0	0,012	0,0029	-0,001	4,83E-05	-0,04833333				
					-0,01616667				

waxT45v2	1cm/2min								
0,0072	0	-	-	-	-	7	6000	1507809	1.507E6
0,0069	0,0025	0,0003	-0,0025	2,5E-06	-0,001		7000		
0,0066	0,005	0,0003	-0,0025	2,5E-06	-0,001				
0,0062	0,0075	0,0004	-0,0025	3,33E-06	-0,00133333				
0,0051	0,01	0,0011	-0,0025	9,17E-06	-0,00366667				
0,00435	0,011	0,00075	-0,001	6,25E-06	-0,00625				
0,0026	0,012	0,00175	-0,001	1,46E-05	-0,01458333				
0	1,013	0,0026	-1,001	2,17E-05	-2,1645E-05				
					-0,00397928				

waxT45v3	1cm/3min								
0,0088	0	-	-	-	-	6	8000	1333333	1.333E6
0,0083	0,0025	0,0005	-0,0025	2,78E-06	-0,00111111		11000		
0,0076	0,005	0,0007	-0,0025	3,89E-06	-0,00155556				
0,0062	0,0075	0,0014	-0,0025	7,78E-06	-0,00311111				
0,0031	0,01	0,0031	-0,0025	1,72E-05	-0,00688889				
0,0011	0,011	0,002	-0,001	1,11E-05	-0,01111111				
0	0,0115	0,0011	-0,0005	6,11E-06	-0,01222222				
					-0,006				

3.9 Acknowledgements

3.9.1 Funding

This work was supported by the Czech Science Foundation grant No.: 16-17457S and the Center for Geosphere Dynamics project UNCE/SCI/006.

3.9.2 Author Contributions Statement

This research represents an integral part of the PhD project of OK. This PhD project is aimed to the analogue and numerical modelling of the material/heat transfer in large and hot orogens. All calculations in this article were provided by OK. OK performed all the oroclinal buckling models. OK and PZ cooperated on preparation of the detachment folding experiments. Primary text and figures were produced by OK and all corrections and improvements were supported by PZ. OL and OK are responsible for an idea to use the divergence theorem for investigation of mass transfer and mass balance in the model domain of the detachment folding experiments. OK performed all PIV calculations and associated scripting of routines calculating the divergence and flux balance.

3.10 References

Adam, J., Klinkmüller, M., Schreurs, G., and Wieneke, B. (2013). Quantitative 3D strain analysis in analogue experiments simulating tectonic deformation: Integration of X-ray computed tomography and digital volume correlation techniques. Journal of Structural Geology, 55, 127-149.

Adam, J., Urai, J. L., Wieneke, B., Oncken, O., Pfeiffer, K., Kukowski, N., Lohrmann, J., Hoth, S., van der Zee, W. and Schmatz, J. (2005). Shear localisation and strain distribution during tectonic faulting—New insights from granular-flow experiments and high-resolution optical image correlation techniques. Journal of Structural Geology, 27(2), 283-301.

Adrian, R. J. (2005). Twenty years of particle image velocimetry. Experiments in fluids, 39(2), 159-169.

Albertz, M., Beaumont, C., Shimeld, J.W., Ings, S.J., and Gradmann, S., (2010). An investigation of salt tectonic structural styles in the scotian basin, offshore atlantic canada: 1. comparison of observations with geometrically simple numerical models. Tectonics, 29, TC4017, doi: 10.1029/2009TC002539.

Bajolet, F., Galeano, J., Funiciello, F., Moroni, M., Negredo, A. M., and Faccenna, C.

(2012). Continental delamination: Insights from laboratory models. Geochemistry, Geophysics, Geosystems, 13(2).

Beaumont, C., Nguyen M. H., Jamieson, R. A. and Ellis, S. (2006) Crustal flow modes in large hot orogens. Geological Society, London, Special Publications, 268, 91-145.

Beaumont, C., Jamieson, R. A., Nguyen, M. H., and Medvedev, S. (2004). Crustal channel flows: 1. Numerical models with applications to the tectonics of the Himalayan-Tibetan orogen. Journal of Geophysical Research: Solid Earth, 109(B6).

Beaumont, C., Jamieson, R. A., Nguyen, M. H., and Lee, B. (2001). Himalayan tectonics explained by extrusion of a low-viscosity crustal channel coupled to focused surface denudation. Nature, 414(6865), 738.

Becker, Thorsten; Kaus, Boris (2015): Numerical Modeling of Earth Systems: An introduction to computational methods with focus on solid Earth applications of continuum mechanics. figshare. Paper.

Batteguay, G. (1986). Mise au point d'une technique de viscosimetrie dun materiau analogique (silicone) utilistl en modtlisation expthimentale. Memoire de DEA, Univ. Paris XI.

Boutelier, D., and Oncken, O. (2011). 3-D thermo-mechanical laboratory modeling of plate-tectonics: modeling scheme, technique and first experiments. Solid Earth, 2(1), 35.

Boutelier, D. (2016). TecPIV—A MATLAB-based application for PIV-analysis of experimental tectonics. Computers and Geosciences, 89, 186-199.

Brun, J. P. (2002). Deformation of the continental lithosphere: Insights from brittle-ductile models. Geological Society, London, Special Publications, 200(1), 355-370.

Cagnard, F., Brun, J.-P., Gapais, D. (2006) Modes of thickening of analogue weak lithospheres. Tectonophysics, 421(1-2), 145–160.

Chen, Z., Schellart, W. P., Strak, V., and Duarte, J. C. (2016). Does subduction-induced mantle flow drive backarc extension?. Earth and Planetary Science Letters, 441, 200-210.

Collins, W. J. (2002). Hot orogens, tectonic switching, and creation of continental crust. Geology, 30(6), 535-538.

Costa, A., Caricchi, L., and Bagdassarov, N. (2009). A model for the rheology of particle-bearing suspensions and partially molten rocks. Geochemistry, Geophysics, Geosystems, 10(3).

Davy, P., and Cobbold, P. R. (1991). Experiments on shortening of a 4-layer model of the continental lithosphere. Tectonophysics, 188(1-2), 1-25.

Duarte, J. C., Schellart, W. P., and Cruden, A. R. (2014). Rheology of petrolatum–paraffin oil mixtures: applications to analogue modelling of geological processes. Journal of Structural Geology, 63, 1-11.

Elsinga, G. E., Wieneke, B., Scarano, F., and Schröder, A. (2007). Tomographic 3D-PIV and applications. In Particle image velocimetry (pp. 103-125). Springer, Berlin, Heidelberg.

Edel J.-B., Schulmann K., Hanžl P., Lexa O. (2014) Palaeomagnetic and structural constraints on 90° anticlockwise rotation in SW Mongolia during the Permo-Triassic: implications for Altaid oroclinal bending. Journal of Asian Earth Sciences, 94, 157–171.

Galland, O., Bertelsen, H. S., Guldstrand, F., Girod, L., Johannessen, R. F., Bjugger, F., Burchardt, S. and Mair, K. (2016). Application of open-source photogrammetric software MicMac for monitoring surface deformation in laboratory models. Journal of Geophysical Research: Solid Earth, 121(4), 2852-2872.

Gemmer, L., Ings, S.J., Medvedev, S., and Beaumont, C., (2004). Salt tectonics driven by differential sediment loading: stability analysis and finite-element experiments: Basin Research, 16(2), 199–218, doi: 10.1111/j.1365-2117.2004.00229.x.

Gerya, T. (2009). Introduction to numerical geodynamic modelling. Cambridge University Press.

Gerya, T. V., and Yuen, D. A. (2003). Characteristics-based marker-in-cell method with conservative finite-differences schemes for modeling geological flows with strongly variable transport properties. Physics of the Earth and Planetary Interiors, 140(4), 293-318.

Giordano, D., Ardia, P., Romano, C., Dingwell, D. B., Di Muro, A., Schmidt, M. W., Mangiacapra, A. and Hess, K. U. (2009). The rheological evolution of alkaline Vesuvius magmas and comparison with alkaline series from the Phlegrean Fields, Etna, Stromboli and Teide. Geochimica et Cosmochimica Acta, 73(21), 6613-6630.

Giordano, D., Russell, J. K., and Dingwell, D. B. (2008). Viscosity of magmatic

liquids: a model. Earth and Planetary Science Letters, 271(1-4), 123-134.

Giordano, D., Romano, C., Papale, P., and Dingwell, D. B. (2004). The viscosity of trachytes, and comparison with basalts, phonolites, and rhyolites. Chemical Geology, 213(1-3), 49-61.

Grujic, D. (2006). Channel flow and continental collision tectonics: an overview. Geological Society, London, Special Publications, 268(1), 25-37.

Hacker, B. R., Kelemen, P. B., and Behn, M. D. (2011). Differentiation of the continental crust by relamination. Earth and Planetary Science Letters, 307(3-4), 501-516.

Hori, T., and Sakakibara, J. (2004). High-speed scanning stereoscopic PIV for 3D vorticity measurement in liquids. Measurement Science and Technology, 15(6), 1067.

Hubbert, M. K. (1937). Theory of scale models as applied to the study of geologic structures. Bulletin of the Geological Society of America, 48(10), 1459-1520.

Jamieson, R. A., Beaumont, C., Medvedev, S., and Nguyen, M. H. (2004). Crustal channel flows: 2. Numerical models with implications for metamorphism in the Himalayan-Tibetan orogen. Journal of Geophysical Research: Solid Earth, 109(B6).

Jang, Y. I., and Lee, S. J. (2008). PIV analysis of near-wake behind a sphere at a subcritical Reynolds number. Experiments in Fluids, 44(6), 905-914.

Kettermann, M., von Hagke, Ch., van Gent, H. W., Grützner, Ch., and Urai, J. L. (2016). Dilatant normal faulting in jointed cohesive rocks: a physical model study. Solid Earth, 7(3), 843.

Kettermann, M., and Urai, J. L. (2015). Changes in structural style of normal faults due to failure mode transition: first results from excavated scale models. Journal of Structural Geology, 74, 105-116.

Klinkmüller, M., Schreurs, G., Rosenau, M., and Kemnitz, H. (2016). Properties of granular analogue model materials: A community wide survey. Tectonophysics, 684, 23-38.

Krézsek, C., Adam, J., and Grujic, D. (2007). Mechanics of fault and expulsion rollover systems developed on passive margins detached on salt: insights from analogue modelling and optical strain monitoring. Geological Society, London, Special Publications, 292(1), 103-121.

Lehmann, J., Schulmann, K., Lexa, O., Závada, P., Štípská, P., Hasalová, P., Belyanin, G. and Corsini, M. (2017). Detachment folding of partially molten crust in accretionary orogens: A new magma-enhanced vertical mass and heat transfer mechanism. Lithosphere, 9(6), 889-909.

Lehmann, J., Schulmann, K., Lexa, O., Corsini, M., Kröner, A., Štípská, P., Tomurhuu, D. and Otgonbator, D. (2010) Structural Constraints of the Evolution of the Central Asian Orogenic Belt in sw Mongolia. American Journal of Science, 310, 575– 628.

Maierová, P., Schulmann, K., and Gerya, T. (2018). Relamination Styles in Collisional Orogens. Tectonics, 37(1), 224-250.

Maierová, P., Lexa, O., Schulmann, K., and Štípská, P. (2014). Contrasting tectonometamorphic evolution of orogenic lower crust in the Bohemian Massif: a numerical model. Gondwana Research, 25(2), 509-521.

Menant, A., Sternai, P., Jolivet, L., Guillou-Frottier, L., and Gerya, T. (2016) 3D numerical modeling of mantle flow, crustal dynamics and magma genesis associated with slab roll-back and tearing: The eastern Mediterranean case. Earth and Planetary Science Letters, 442, 93-107.

Mužík, V. (2014). Analysis of peak and critical strength of remoulded clay from Jiří mine. Master thesis, Charles University, Prague

Nogueira, J., Lecuona, A., and Rodriguez, P. A. (1997). Data validation, false vectors correction and derived magnitudes calculation on PIV data. Measurement Science and Technology, 8(12), 1493.

Okamoto, K., Nishio, S., Kobayashi, T., Saga, T., and Takehara, K. (2000). Evaluation of the 3D-PIV standard images (PIV-STD project). Journal of Visualization, 3(2), 115-123.

Pastor-Galán, D., Gutiérrez-Alonso, G., Zulauf, G. and Zanella, F. (2012) Analogue modeling of lithospheric-scale orocline buckling: Constraints on the evolution of the Iberian-Armorican Arc. Geological Society of America Bulletin, 124, 1293-1309.

Raffel, M., Willert, C. E., and Kompenhans, J. (2007). Particle image velocimetry: a practical guide. Springer Science and Business Media.

Ramberg, H. (1981). The role of gravity in orogenic belts. Geological Society, London, Special Publications, 9(1), 125-140.

Reber, J. E., Galland, O., Cobbold, P. R., and de Veslud, C. L. C. (2013). Experimental study of sheath fold development around a weak inclusion in a mechanically layered matrix. Tectonophysics, 586, 130-144.

Regard, V., Faccenna, C., Martinod, J., and Bellier, O. (2005). Slab pull and indentation tectonics: insights from 3D laboratory experiments. Physics of the Earth and Planetary Interiors, 149(1-2), 99-113.

Reiter, K., Kukowski, N., and Ratschbacher, L. (2011). The interaction of two indenters in analogue experiments and implications for curved fold-and-thrust belts. Earth and Planetary Science Letters, 302(1-2), 132-146.

Riedl, M. J. (2001). Optical design fundamentals for infrared systems (Vol. 48). SPIE press.

Rosenbaum, G. (2014). Geodynamics of oroclinal bending: Insights from the Mediterranean. Journal of Geodynamics, 82, 5-15.

Rosenbaum, G. (2012). Oroclines of the southern New England orogen, eastern Australia. Episodes, 35(1), 187-194.

Rosenbaum, G., and Donchak, P. J. (2012). Structural evolution of the Texas Orocline, eastern Australia. Gondwana Research, 22(1), 279-289.

Rossetti, F., Ranalli, G., and Faccenna, C. (1999). Rheological properties of paraffin as an analogue material for viscous crustal deformation. Journal of Structural Geology, 21(4), 413-417.

Schellart, W. P., and Strak, V. (2016). A review of analogue modelling of geodynamic processes: Approaches, scaling, materials and quantification, with an application to subduction experiments. Journal of Geodynamics, 100, 7-32.

Schmatz, J., Holland, M., Giese, S., Van Der Zee, W., and Urai, J. L. (2010). Clay smear processes in mechanically layered sequences—Results of water-saturated model experiments with free top surface. Journal of the Geological Society of India, 75(1), 74-88.

Schulmann, K., Lexa, O., Štípská, P., Racek, M., Tajčmanová, L., Konopásek, J., Edel, J.-B., Peschler, A. and Lehmann, J. (2008). Vertical extrusion and horizontal channel flow of orogenic lower crust: key exhumation mechanisms in large hot orogens?. Journal of metamorphic Geology, 26(2), 273-297.

Sokoutis, D., Burg, J. P., Bonini, M., Corti, G., and Cloetingh, S. (2005).

Lithospheric-scale structures from the perspective of analogue continental collision. Tectonophysics, 406(1-2), 1-15.

Strak, V., and Schellart, W. P. (2014). Evolution of 3-D subduction-induced mantle flow around lateral slab edges in analogue models of free subduction analysed by stereoscopic particle image velocimetry technique. Earth and Planetary Science Letters, 403, 368-379.

Thielicke, W. (2014). The flapping flight of birds—analysis and application. Rijksuniversiteit Groningen (Doctoral dissertation, PhD Dissertation).

Thielicke, W., and Stamhuis, E. (2014). PIVlab–towards user-friendly, affordable and accurate digital particle image velocimetry in MATLAB. Journal of Open Research Software, 2(1).

Vanderhaeghe, O. (2009). Migmatites, granites and orogeny: Flow modes of partially-molten rocks and magmas associated with melt/solid segregation in orogenic belts. Tectonophysics, 477(3-4), 119-134.

Vanderhaeghe, O., Burg, J. P., and Teyssier, C. (1999). Exhumation of migmatites in two collapsed orogens: Canadian Cordillera and French Variscides. Geological Society, London, Special Publications, 154(1), 181-204.

Warsitzka, M., Kley, J., and Kukowski, N. (2013). Salt diapirism driven by differential loading—Some insights from analogue modelling. Tectonophysics, 591, 83-97.

Weijermars, R., and Schmeling, H. (1986). Scaling of Newtonian and non-Newtonian fluid dynamics without inertia for quantitative modelling of rock flow due to gravity (including the concept of rheological similarity). Physics of the Earth and Planetary Interiors, 43(4), 316-330.

Westerweel, J., and Scarano, F. (2005). Universal outlier detection for PIV data. Experiments in fluids, 39(6), 1096-1100.

Xiao, W., Windley, B. F., Sun, S., Li, J., Huang, B., Han, C., Yuan, C., Sun, M., and Chen, H. (2015). A tale of amalgamation of three Permo-Triassic collage systems in Central Asia: oroclines, sutures, and terminal accretion. Annual review of earth and planetary sciences, 43, 477-507.

4 Numerical modelling of crustal-scale Rayleigh-Taylor instabilities

4.1 Introduction

In this chapter a numerical model of crustal-scale diapirism will be described and discussed, this model is derived from the time-evolution of a Rayleigh-Taylor instability. This scenario follows recent studies that are aimed at describing crustal inversion due to the presence of a high density mafic lower crust which is underlain by a light felsic relaminant (Schulmann et al., 2009; Lexa et al., 2011; Maierová et al., 2012, 2014). The presence of the relaminant assumes one of the relamination scenarios which are described in Maierová et al. (2018): 1. Intra-crustal relamination, whereby felsic material which is originally derived from the subducted slab and relaminated into the crustal part of the overriding plate; 2. Sub-lithospheric relamination, where the delaminated felsic upper part of the subducting slab is progressively detached and relaminated underneath the overriding plate - into weak asthenospheric mantle; 3. Redistribution of the felsic material along the subduction channel with partial underlying of the lithospheric mantle. The presented numerical model is most relevant to the first two scenarios, where the buoyancy of relaminated material produces lithospheric-scale diapirism.

The first scenario assumes a weak and hot upper plate which could typically be the product of back-arc thinning, flexure and rapid heating due to higher thermal gradient during continuous subduction (Faccenna et al., 1996; Yasui et al., 2012, Jolivet et al., 2015). In this scenario the weak, low-viscosity relaminant could be transported in the form of a horizontal channel flow through the crustal segment (Beaumont et al., 2001; Jamieson et al., 2007) or be emplaced along the lower (MOHO) level of the crust (Maierová et al., 2012).

The second scenario assumes continuing subduction with a typically thin overriding plate and melt weakening at the lower lithospheric levels. The strength of the overriding plate is higher than in scenario 1. and the relaminant is distributed in deeper positions beneath the lithospheric mantle. Progressive heating and melt weakening is responsible for ascent of this material in the form of gravitationally driven vertical flow and later emplacement at the base of crustal levels. This relaminant later represents a source material for the development of HP granulitic domes (Schulmann et al., 2009; Lexa et al., 2011; Maierová et al., 2012; Schulmann et al, 2014; Maierová et al., 2016) and(/or) Mg-K magmas (Hacker et al., 2000, 2005; Maierová et al., 2016) that are typical for large accretionary systems such as e.g. Tibetan-Himalayan orogen (Chemenda et al., 2000; Hacker et al., 2011) or Variscan orogen (Massonne, 2001; Maierová et al., 2016).

In the previous part, where we discussed the development and dynamics of detachment folds related to the migration of anatectic lower crust, we followed a complex scenario which combines both above described situations. The assumption for those models was a significantly heated crust and the potential melting of the lower felsic crust at MOHO levels. In those models, under a continuous compressional regime, a sequence of fold-like dome structures were produced depending on crustal thickness and the total amount of melt in the system. The kinematics and dynamics of these structures combines the buckling and bending and is also associated with the intrusion of a various melt amount into the individual folds (domes) - depending on the position of folding in the whole compressed system (Krýza et al., 2019). This model is based on a constant shortening rate and non-scaled Earth gravitational acceleration. The model reflected folding and doming of the lower ductile crust which is associated with the development of pop-ups and pop-downs in the upper crust. The scenario where the lower felsic crust is significantly less dense than upper part of the lower crust or middle crust (e.g. Lexa et al., 2011 or Maierová et al., 2012), and where gravitational inversion of such layers is induced, could not be involved in this approach due to problematics of the gravity scaling ($g_M = g_N$). However, we suggest that gravitationally driven diapiric exhumation is a native component of the processes associated to doming and uplift of the lower crust, including the molten component of the lower crust.

In this part the evolution of a crustal-scale Rayleigh-Taylor instability which is associated with inversion of a density stratified crustal segment of the lithosphere and with the diapiric exhumation of the weak felsic lower crust will be studied and discussed. The modelling follows the scheme presented in Krýza (2013) where parametric statistical study was employed and revealed that the density contrast (affected in time by radiogenic heat productivity) represents the most influential parameter which drives the rate and dynamics of crustal diapirism.

In this study we present new data that are complementary to Krýza (2013) and compare simulations that reflect various density contrasts, undulation of the interface of the basal layers and radiogenic heat productivity. Plotted strain(-rate) maps, material distributions, viscosity contrasts and GPE (gravitational potential energy) curves for selected simulations are discussed in the frame of the analogue models that are presented in *Chapter 3*. The model results are used to discuss the possibility of gravity driven uplift of the lower weak crust in frame of convergent models.

4.2 Model setup

The model domain represents a crustal-mantle segment (150 km × 120 km, horizontal to vertical) that contains two, pre-defined material perturbations before crustal gravitational inversion (Fig. 41). The model domain is vertically stratified and individual layers represent the unified upper-middle crust (UC/MC), mafic lower

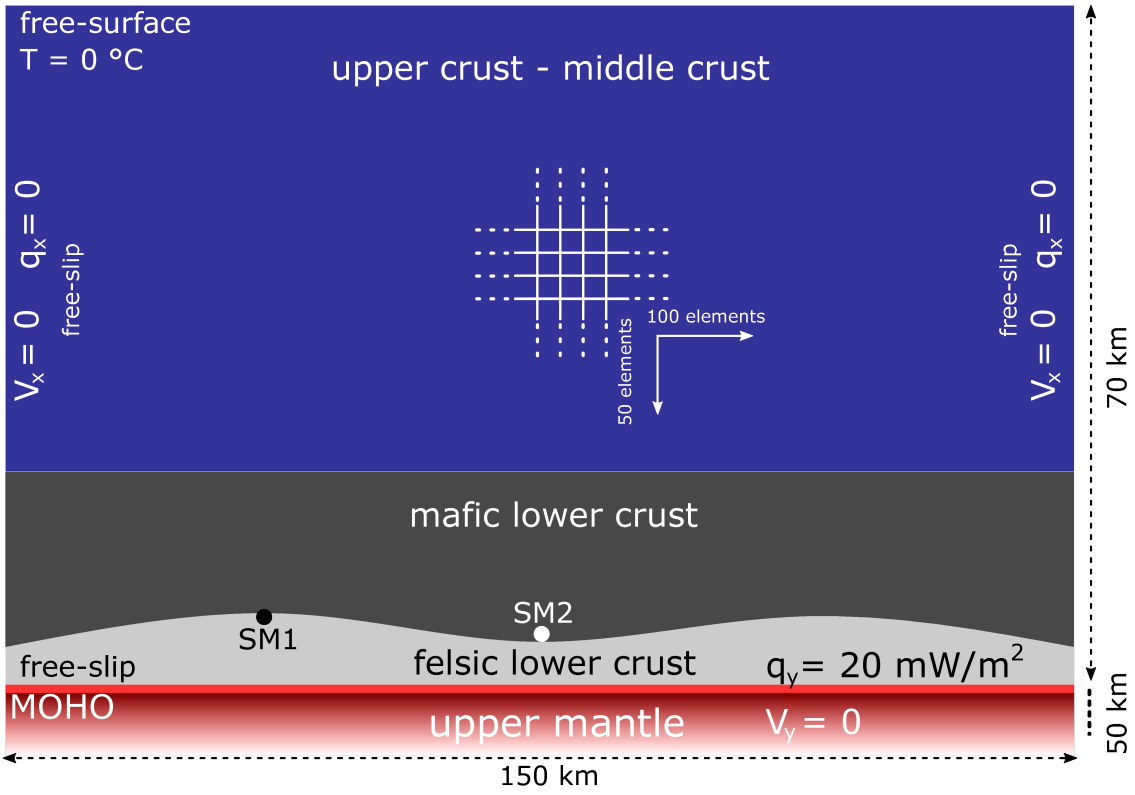


Fig. 41: Geometry and boundary conditions of the model domain. The upper boundary is deformable due to the free-surface b.c. and remeshing routine. For the top part is prescribed the Dirichlet b.c. with zero temperature. Both vertical boundaries are impermeable with prescribed free-slip b.c. in the vertical direction and zero heat flux in the horizontal direction. The base of the model is represented by the Neumann boundary condition with the heat flux in the vertical direction and with zero velocity in both directions. The MOHO line is represented by free-slip and represents the mechanical separation of the crustal and mantle segment. White points represent the special markers where the target output model parameters are traced.

crust (MLC), felsic lower crust (FLC) and upper mantle (UM). The UC/MC is defined as an initially colder, less dense segment with defined radiogenic heat productivity. The MLC represents the original high-density basement of a crustal segment which is stronger than the layer situated above and has no thermal productivity associated with radioactive decay. The FLC is a low-density and higher radiogenic heat productivity layer which represents a relaminant incorporated into the lithosphere during a convergent event (according to models of Maierová et al., 2012, 2016). The whole crustal segment is underlain by the upper part of the UM segment. This part does not play a significant role for mechanical evolution of the crustal segment in models with no longitudinal shortening but is important for heat transfer from the model base. In the presented model, and for each simulation, we do not consider this part as being mechanically coupled with the crustal segment. All model physical parameters all described in Fab. 9.

The model is set in a 2D domain (with Cartesian geometry) represented by numerical grid with resolution of 100 (horizontal) to 70 (vertical) bilinear quadrilateral (Q4) elements (size of individual element corresponds to 1.5 km to 1.7 km). The resolution of the crustal segment is 100 x 50 elements while the mantle segment has a resolution of a 100 × 20 elements (vertical spacing of elements in the mantle segment is progressively increasing from MOHO to model base while in the crustal segment the spacing is constant).

4.2.1 Governing equations

The model describes the complex deformation of a heterogeneous lithospheric environment related to heat flow between individual subdomains. The flow of incompressible material with neglected inertia is described by following equations (generally described for compressible solution in the section 1.6.2):

$$\begin{aligned} \nabla p - \nabla \cdot \sigma &= -\rho g e_z, \\ \nabla \cdot v &= 0, \end{aligned} \tag{4.1}$$

where ρ is the density, g is the gravitational acceleration, σ is the stress tensor, p is the pressure, v is the velocity and e_z is the unit vector in direction of z-axis. The equation follows the solution of the Stokes problem (e.g. Gerya, 2009). The heat transport in the model domain is represented by a prescribed heat transfer equation (following eq. 1.27 - subsection 1.6.3) with reduced source member to only radiogenic heat productivity H_r (other sources as latent, adiabatic or shear heating are neglected) as follows:

$$\rho c_p \frac{DT}{Dt} - \nabla \cdot \lambda(\nabla T) = H, \tag{4.2}$$

where c_p is the specific heat capacity under constant pressure, T is the temperature, t is the time, ρ is the density and λ is the thermal conductivity. In the model we assumed a non-diffusive evolution of the material composition on the geological time-scale:

$$\frac{Dc_i}{Dt} = 0, \quad \forall i > 0. \tag{4.3}$$

Density in our model is a function of the temperature and material composition:

$$\rho = \rho(T, \{c_i\}) = \rho_{\text{ref}}\left(\{c_i\}\right)\left[1 - \alpha\left(\{c_i\}\right)\left(T - T_{\text{ref}}\right)\right], \tag{4.4}$$

Tab. 9: The model parameters.

Physical parameters	Symbols	Values	Units
thermal conductivity	κ	**2.5**	$Wm^{-1}K^{-1}$
specific heat	c_p	**800**	$Jkg^{-1}K^{-1}$
gravitational acceleration	g	**9.81**	ms^{-2}
gass constant	R	**8.314**	$JK^{-1}m^{-1}$
mantle density	ρ	**3300**	$kg\ m^{-3}$
temperature at the surface of the model domain	T_p	**273**	K
heat flow at the base of the model domain	q_b	**20**	$mW\ m^{-2}$
switch-off of the thermal sources	T_f	**1170**	K
minimum and maximum viscosity (exp)	$\eta_{min/max}$	**14 / 26**	Pa s
referential values of plastic strain	$\varepsilon_{0,inf}$	**0 ; 1**	
cohesion	C	**1**	Mpa
UC/MC - sediments, quarzit (Hirth et al., 2001; Ranalli, 1995):			
coefficient of thermal expansion	α	**2e-5**	
initial angle of internal friction	φ_0	**15**	°
finite angle of internal friction	φ_{inf}	**7.5**	°
viscosity exponent	n	**3**	
pre-exponential parameter	B	**1.89e8**	$Pa\ s^{1/n}$
activation energy	E_A	**156**	$kJ\ mol^{-1}$
referential density	ρ_0	**2800**	$kg\ m^{-3}$
radiogenic heat productivity	H_r	**2e-6**	$\mu W\ m^{-3}$
thickness	m	**50**	km
MMC - plagioklas (Ranalli, 1995):			
coefficient of thermal expansion	α	**2e-5**	
initial angle of internal friction	φ_0	**30**	°
finite angle of internal friction	φ_{inf}	**15**	°
viscosity exponent	n	**3.2**	
pre-exponential parameter	B	**3.69e6**	$Pa\ s^{1/n}$
activation energy	E_A	**238**	$kJ\ mol^{-1}$
referential density	ρ_{0A}	**2950**	$kg\ m^{-3}$
varied referential density (for various simulations)	ρ_{0B}	**2800-3100**	$kg\ m^{-3}$
radiogenic heat productivity	H	**0**	$\mu W\ m^{-3}$
thickness (varied from 5 to 15 km - according to FLC thickness)	m	**5**	km
FLC - granite (Ranalli, 1995):			
coefficient of thermal expansion	α	**3e-5**	
initial angle of internal friction	φ_0	**30**	°
finite angle of internal friction	φ_{inf}	**15**	°
viscosity exponent	n	**1.9**	
pre-exponential parameter	B	**2.75e7**	$Pa\ s^{1/n}$
activation energy	E_A	**137**	$kJ\ mol^{-1}$
referential density	ρ_{0A}	**2750**	$kg\ m^{-3}$
varied referential density (for various simulations)	ρ_{0B}	**2650-2950**	$kg\ m^{-3}$
radiogenic heat productivity (for various simulations)	H	**2e-6 - 6e-6**	$\mu W\ m^{-3}$
thickness (referential)	m	**10**	km
thickness (for various simulations)	m_A	**5 - 15**	km
undulation amplitude (referential)	A	**3**	km
undulation amplitude (for various simulations)	A_A	**2 - 4**	km

Tab. 10: The varied model parameters. Individual parameters are: amplitude of the interface undulation between MLC and FLC (A_F), thickness of the FLC, (Th_F), density of the MLC (D_M), density of the FLC (D_F) and radiogenic heat productivity of the FLC (H_F)

number of current value	A_F [km]	Th_F [km]	D_M [kg.m^{-3}]	D_F [kg.m^{-3}]	H_F [μW.m^{-3}]
1	2	5	2800	2650	2
2	2.5	7.5	2875	2725	3
3	3	10	2950	2800	4
4	3.5	12.5	3025	2875	5
5	4	15	3100	2950	6

where ρ_{ref} is the referential density - which is chosen according to defined material (see Tab. 10), T_{ref} is a referential temperature - chosen always as 273 K and α is a heat expansion coefficient which depends on a given material.

Heat sources (radiogenic heat productivity H_r) are dependent on material composition:

$$H = H\left(\{c_i\}\right), \tag{4.5}$$

where non-zero values are initially prescribed for UC and FLC with variable initial values for FLC according to individual simulations.

The deviatoric stress tensor is a function of strain-rate, temperature, pressure and composition:

$$\begin{aligned} \sigma &= \sigma(\dot{\varepsilon}, T, p, \{c_i\}) \\ \sigma &= \begin{pmatrix} \sigma_{xx} & \sigma_{xz} \\ \sigma_{zx} & \sigma_{zz} \end{pmatrix} e_x \times e_z. \end{aligned} \tag{4.6}$$

In the whole model domain we prescribed a non-linear visco-plastic rheology affected by stress acting on crustal material. The plastic deformation in the UC also represents an approximation of a brittle failure which dominates in low T systems with high strain-rates while high T systems with low deformation rates are affected by viscous flow. The viscous flow is characterized by irreversible deformation of a material where the strain-rate depends on acting stress. The plastic deformation is also irreversible but is considered when differential stress yield limit is reached (σ_{yield}). This functional dependency of deviatoric stress (equation 4.6) is possible to express for visco-plastic regime by using the effective viscosity (η_{eff}) as:

$$\sigma = 2\eta_{\text{eff}}\dot{\varepsilon}, \tag{4.7}$$

where ($\dot{\varepsilon}$) represents the deviatoric strain-rate tensor (see section 3.3.5 and eq. 3.2). For a viscous regime (when the value of the second invariant of the deviatoric stress tensor is smaller than a yield stress ($\sigma_{II} < \sigma$yield)) is a deformation represented by dislocation creep which is defined by non-linear relationship between stress tensor and strain-rate tensor. This could be expressed as:

$$\dot{\varepsilon} = A\frac{3^{\frac{n+1}{2}}}{2}\sigma_{II}^{n-1}\exp\left(-\frac{E_A}{RT}\right)\sigma, \tag{4.8}$$

where R is the gas constant, $\sigma_{II} = \sqrt{1/2\sigma : \sigma}$ is the second invariant of the deviatoric stress tensor, E_A is the activation energy, n is the power of the viscosity (stress invariant, respective) and A is the material constant. These parameters are experimentally stated (see Tab. 9; Hirth et al., 2001; Ranalli, 1995). Based on these relations, it is possible to derive the effective viscosity as follows (e.g. Maierová et al., 2012):

$$\eta_{\text{eff}} = B\dot{\varepsilon}_{II}^{1/n-1}\exp\left(-\frac{E_A}{nRT}\right), \text{ where } B = \frac{1}{2}(A)^{-1/n}\frac{2^{(1-n)/n}}{3^{(n+1)/2n}}. \tag{4.9}$$

Here $\dot{\varepsilon} = \sqrt{1/2\dot{\varepsilon} : \dot{\varepsilon}}$ is the second invariant of the strain-rate tensor and B is the pre-exponential parameter. In the plastic regime is $\sigma_{II} = \sigma_{\text{yield}}$ (see subsection 1.3.1) and effective viscosity is derived from the equation 4.7 as follows:

$$\sigma_{\text{eff}} = \frac{\sigma_{\text{y}}}{\dot{\varepsilon}_{II}}. \tag{4.10}$$

The yield stress for various materials is not constant but directly depends on some other parameters related to current material (such as porosity, grain size and grain distribution, chemical composition, temperature, pressure etc.). For rock behavior which is pressure-dependent we used *Drucker-Prager yield criterion* (according to Maierová et al., 2012):

$$\sigma_{\text{y}} = p\sin\phi + C\cos\phi, \tag{4.11}$$

where p is the pressure, C is the cohesion and ϕ is the internal friction angle. The parameters (B, E_A, n, ϕ, C) are dependent on the material composition ($\{c_i\}$) (see Tab. 9). The angle of internal friction ϕ depends on the plastic strain (defined as integration of the second invariant of the plastic strain-rate tensor - along trajectory

of the current material particle). This dependency is possible to express as follows (after Maierová et al., 2012):

$$\begin{aligned} \phi &= \phi_0 \ \text{ if } \ \varepsilon_{II} \leq \varepsilon_0, \\ \phi &= \phi_0 + (\phi_\infty - \phi_0)\tfrac{\varepsilon_{II}-\varepsilon_0}{\varepsilon_\infty-\varepsilon_0} \ \text{ if } \ \varepsilon_0 < \varepsilon_{II} < \varepsilon_\infty, \\ \phi &= \phi_\infty \ \text{ if } \ \varepsilon_{II} \geq \varepsilon_\infty, \end{aligned} \tag{4.12}$$

where ϕ_0, ϕ_∞, ε_0 and ε_∞ are parameters while ε_{II} is the integrated invariant of the plastic strain-rate.

For the evolution of the material composition the *particle-in-cell method* is used (Maierová et al., 2012; for the *marker-in-cell method* follow Gerya and Yuen (2003)). The principle of this technique is saving the information about material properties due to representative material markers (particles) that have supported advecting in the model domain by the velocity field. Each particle contains information about the material composition - which is not changed due to the time evolution - and about the commulated plastic deformation (represented by value of σ_{II}). The displacement of the particle is solved by fourth-order *Runge-Kutta method*. The material properties for every single particle in each timestep in each numerical grid element are evaluated at the integration points. In these points are calculated average values of a given material properties for all particles in current mesh element. In our model we followed the scheme of Maierová et al. (2012) where the effective viscosity is calculated from geometrical average as follows:

$$\log(\eta_{\text{eff}}) = \sum_i c_i \log(\eta_{\text{eff},i}), \tag{4.13}$$

while other quantities are calculated from arithmetic average as:

$$P = \sum_i c_i P_i, \tag{4.14}$$

where i denotes the component of the material and c_i is a fraction of this component in the calculation of the current quantity. During the computation of the c_i and $\epsilon_{II,i}$ in current point which is given by coordinates x, z (for two-dimensional domain), we used the following relationship (Maierová et al. (2012) after Gerya and Yuen (2003)):

$$c_i = \frac{\sum_{n_i} w_{n_i}}{\sum_n w_n}, \quad \varepsilon_{II,i} = \frac{\sum_{n_i} \varepsilon_{II,n_i} w_{n_i}}{\sum_n w_{ni}}, \tag{4.15}$$

where n_i represents the marker which corresponds to the current material, n is the index for summing over all markers for current mesh element and w_i is the weight for respective marker which is calculated as follows:

$$w_n = \frac{1}{\Delta x^{\max} \Delta z^{\max}} \left(1 - \frac{\Delta x_n}{\Delta x^{\max}}\right) \left(1 - \frac{\Delta z_n}{\Delta z^{\max}}\right), \tag{4.16}$$

where Δx_n and Δz_n are distances of the markers from point $\{x, z\}$ and $\Delta x^{\max}$ and $\Delta z^{\max}$ represents the maximum value of those distance for all markers in the current element.

4.2.2 Boundary conditions

At the boundaries of the model domain we imposed boundary conditions (b.c.) describing how the model is related to the potentially surrounding regions. The topography effect of the model surface and the mantle bulging are neglected (model has implemented free-surface boundary condition but the finite shape of the model surface does not affect the inner dynamics. Lateral deformation (shortening) of the domain is not included in the model setup.

For the top of the model we set a free-surface boundary condition without sedimentation/erosion factors which would not play a significant role in our model scenario (for incorporation of the sedimentation or erosion processes follow Maierová et al. (2012). Both lateral boundaries and the bottom of the crustal segment have prescribed free-slip b.c. while side boundaries and bottom of the mantle segments have no-slip b.c. (mantle segment is in most of the simulations used only for heat transfer to the crustal segment). Thermal b.c. is set as *Dirichlet* b.c. for the model surface where $T = 0$ K while for model base is set *Neumann* b.c. where the heat flux is $q = 20$ mW/m^2. Both model sides are thermally isolated from outer regions, i.e. $q = 0$ mW/m^2.

4.2.3 Initial conditions

In the model we tested variations of the several input parameters as is described above. These parameters are set as: 1. amplitude of undulation of the interface between MLC and FLC ($A_F = 2 - 4$ km with step of 0.5 km); 2. thickness of the FLC (ratio of thickness of the FLC and MLC, respectively) which is related to the amount of radiogenic heating produced by the FLC ($Th_F = 5 - 15$ km with step of 2.5 km); 3. radiogenic heat productivity of a FLC ($H_F = 2 - 6$ μWm^{-3} with step of 1 μWm^{-3}); 4. density of FLC ($D_F = 2650 - 2950$ kg.m^{-3} with step of 75 kg.m^{-3}); 5. Density of MLC ($D_M = 2800 - 3100$ kg.m^{-3} with step of 75 kg.m^{-3}). All parameters are shown in Tab. 9 and 10 (amplification of undulated interface between the MLC and FLC is represented by median value of sinus in the predefined boundary line position).

4.2.4 Numerical implementation

All of the simulations are considered under the same numerical approach where the system of partial differential equations is solved. For solution of above prescribed equations we used multiphysical open-source software *ELMER FEM* which is based on the principle of the finite element method. The structure of numerical calculations is following (including procedures implemented to extend applicability to geodynamical modelling (Maierová et al., 2012) such as markers initiation and integration of plastic deformation, free-surface b.c. etc.):

1. Initialization of a thermal field - stationary solution of the heat transfer equation ($-k\nabla T$ from Eq. 1.27)
2. Estimation of the time-step
3. Interpolation of the viscosity and marker density to an integration point in the current mesh element - solution of the Stoke's problem (Eq. 4.1)
4. Interpolation of thermal sources and density from current markers to integration points - non-stationary solution of the heat transfer equation (Eq. 4.2)
5. Calculation of the advection of the free-surface
6. Deformation of the numerical mesh
7. Advection of the markers in the model domain and integration of the plastic strain
8. Saving of the calculated values and export to *.vtk* data file
9. Return to point 2.

4.3 Results

In this part will be described the general evolution of the model domain reflecting the variation of the model parameters with variation of the prescribed initial conditions. For further analysis of the diapir development and vertical extrusion is used only the set of simulations which reflects extreme values of the chosen initial conditions such as the density contrast of the MLC/FLC, amplitude of the Rayleigh-Taylor instability (A_f), radiogenic heating (H_f) in the FLC and contrast of thickness of both lower crust layers. All combinations of the prescribed initial conditions, and associated output model parameters, will not be described in this study (for details follow Krýza (2013)).

4.3.1 The output model parameters

Two series of parameters, that describe both global and local material properties and physical conditions in the model domain, serve well as relevant indicator of model behaviour (Fig. 42). The global parameters are related to the global model quantities (e.g. temperature, bulk strain(-rate), bulk stress, gravitational potential energy (GPE), kinetic energy, characteristic time of the simulation, position/movement of the gravitational centre of specified material - such as gravity center of the FLC material, etc.). On the small-scale of the model domain it is possible to trace the local model parameters which describe changes in some specific model subdomain (Fig. 42b)(e.g. maximum/minimum temperature and pressure, maximum pressure and temperature differences, pressure and temperature differences respective to aimed areas, specific time related to this P-T parameters, elevations of the material element or pathes, etc). Except previous, it is also possible to use kinematic and geometric parameters (Fig. 42c) that could be related to changes in a surfaces curvature (such as tracing the evolution of a curvature along specific material boundary - e.g. curvature of a diapiric surface), particle movement described by the absolute and relative distances (e.g. tortuosity of a particle trajectory) and others.

Global output model parameters

The set of these parameters is based on investigation of gravitational potential GPE (Fig. 42d) evolution in the model domain through model evolution. The curve which represents the GPE is unique for each simulation and is characterized by a lower plateau, inflection and upper plateau that corresponds to the maximum GPE, higher dynamics during material inversion and minimum GPE of the system. The GPE is in the model represented by distribution of FLC material in current time-step which reflects progress in the material inversion. Initial state of the model is then represented by higher values of the GPE while finite state correlates with a minimum values. The GPE in each timestep is expressed as:

$$U = mgh, \tag{4.17}$$

and change of the GPE is expressed as:

$$\Delta U = mg\Delta h, \tag{4.18}$$

respective. Here $m = m^t_{(}\rho_i)$ is the mass of the material element and U is calculated as the integral over the area related to the felsic material in each time-step. The mass is related to the density with dependence on t while h represents the vertical position of the material element with respect to the base of the crustal part of the model (MOHO). The GPE in each simulation is possible to substitute by calculation

of the gravitational center of the FLC material. The inflection of the curve which represents the vertical position of the FLC mass center in time corresponds to the most dynamic event of the model evolution - related to vertical extrusion (driven by density contrast of the FLC and MLC) of the felsic material. The individual global model output parameters are then related to:

- Inflection of the GPE curve (maximum dynamics of the system - maximum vertical extrusion rate)
- Difference between ∼maximum and ∼minimum of the GPE related to the lower and upper plateaus
- Corresponding time for both features described above

While the slope of the first part of the curve (part of which is represented by the distance from the beginning to the inflection) is typically reflecting the acceleration of the vertical extrusion, the upper plateau is defined as the site of higher deceleration of the extrusion (marked as *rp*). This threshold is defined as the time where the increment of the extrusion (negative increment of the GPE) is evaluated as smaller than the average value from the interval between inflection and finite time-step of the simulation.

The following set of parameters is based on the above described features of the GPE evolutionary curve (Fig. 42d):

1. D_max (the characteristic time of the maximum system dynamics - inflection of the GPE curve [Ma])
2. T_dom (average integral temperature of the model domain in D_max [K])
3. S_dom (average bulk strain-rate in the model domain in D_max [$\log \dot{\varepsilon}[s^{-1}]$])
4. dh (difference between the original position of the gravitational center of the FLC material and position of this gravity center in time of rp [km])
5. t_dh (corresponding time to dh [Ma])
6. H_max (maximum reached vertical position of the FLC material in the model domain - corresponds to rp position [km])

Local output model parameters

This set of the parameters is based on the P-T-t-d (pressure-temperature-time-space) conditions of the aimed markers in the model domain. The figure 42(a,b) displays strategy and position for special markers (SM or M) where target output parameters are calculated that are defined as:

1. T1_max (maximum reached temperature in the special marker SM1 [K])
2. P1_min (minimum reached pressure in the special marker SM1 [kbar])

3. T2_max (maximum reached temperature in the special marker SM2 [K])
4. P2_min (minimum reached pressure in the special marker SM2 [kbar])
5. h_t (specific time of between minimum and maximum depth reached by SM1 [Ma])
6. h_d (maximum vertical difference in the position of SM1 [km])
7. T_d (temperature difference corresponding to minimum and maximum elevation points of SM1 [K])

All the analyzed global model output parameters are sorted in the table 11. The correlation analysis and principal component analysis (PCA) of all input and output model parameters is possible to find in Krýza (2013). In the following text, the analysis will be restricted to qualitative comparison of the target parameters and description of thermal and mechanical features of the developed diapiric structure.

4.3.2 Initial thermal field and geotherm

A steady-state thermal field is generated during the first time-step by solution of the *Poisson* (conduction) equation and reflects well a laterally isotropic thermal field which has the same characteristic vertical gradient along this lateral direction (Fig. 43). The thermal field in this first time-step does not reflect the prescribed geometry of the upper-middle-lower crust. This is due to the time-dependent rheology and thermal parameters (such as radiogenic productivity) that are related to the model evolution after time-step 1. The thermal field corresponds to the conditions in massively thickened orogenic root before erosion which typically removes the upper crust (thickening, erosion and sedimentation are typically reflected by isostatic compensation). However, the erosion/sedimentation factor and the isostatic response are not prescribed in our model.

4.3.3 Evolutionary stages and the main simulation differences

The different evolutions which reflects the effect of individually prescribed initial conditions (Tab. 10) for each simulation can be divided into the three basic classes of the evolutionary trends (Fig. 44): 1. Gravitationally driven inversion of the lower crust which is associated with the diapiric exhumation of the FLC through the middle(-upper) crust; 2. Gravitationally driven inversion of the FLC and MLC with the stabilisation of the FLC at the level of the originally positioned MLC; 3. Gravitationally driven collapse and stabilisation-equilibration of the felsic lower crust along the MOHO level.

For further reading, the notation of various simulations will be introduced here. All variations in the initial parameters are numbered after labeling of an appropriate parameter (e.g. D_M1 corresponds to the first value of the density of the MLC

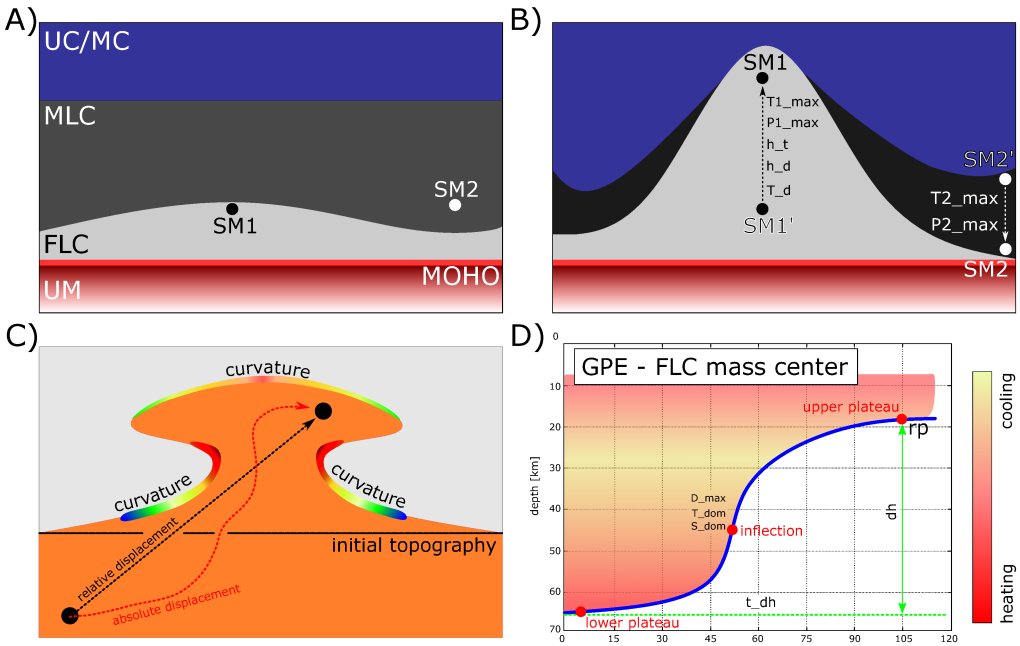


Fig. 42: Model output parameters. In the panels (a,b) are shown positions of the special markers where the local model output parameters are traced inside the model domain (for resultant values see Tab. 11). Panel (c) shows example of the strategy chosen for selection of the global output model parameters. The chosen model output parameters are related to the time-evolution of the gravitational potential energy (GPE) in the model domain. The GPE is related to the position of the felsic material mass center in the model domain in current time-step. This curve is associated with the minimum, maximum and inflection of the evolutionary trend (d). The inflection point reflects the time-step where the model dynamics is at the highest (maximum kinetic energy of FLC mass center - also derived from FLC material particles) while the high plateau of this curve represents a convergence of the GPE to a stable state. The difference between lower and upper plateau of the GPE curve represents the specific time for the vertical extrusion of the FLC material. All parameters derived from this GPE evolution and related to curve target point are described in the text.

Tab. 11: The model output parameters.

Set 1						
model parameters	n	Minimum	Maximum	Average	Variance	Std deviation
A_F [km]	125	2.000	4.000	3.000	0.500	0.707
Th_F [km]	125	5.000	15.000	10.000	12.500	3.535
H_F [$\mu W.m^{-3}$]	125	2.000	6.000	4.000	2.000	1.414
D_max [Ma]	125	3.740	10.411	6.295	2.684	1.638
T_dom [K]	125	719.390	882.379	756.947	1204.205	34.701
S_dom (log) [s^{-1}]	125	-14.540	-13.971	-14.2376	0.025	0.157
dh [km]	125	21.860	38.662	30.826	17.650	4.201
t_dh [Ma]	125	12.059	35.413	19.553	21.424	4.629
H_max [km]	-	-	-	-	-	-
T1_max [K]	125	929.638	1169.953	1027.456	3737.193	61.132
P1_min [kbar]	125	5.044	9.779	6.827	0.647	0.804
T2_max [K]	125	1129.329	1173.801	1136.441	83.492	9.137
P2_min [kbar]	125	16.501	18.907	17.890	0.691	0.831
h_t [Ma]	125	12.158	38.540	25.266	55.888	7.476
h_d [km]	125	31.950	49.576	42.951	8.952	2.992
T_d [K]	125	18.597	253.678	113.159	3574.243	59.785
Set 2						
D_M [$kg.m^{-3}$]	120	2800.000	3100.000	2956.250	10742.188	103.645
D_F [$kg.m^{-3}$]	120	2650.000	2950.000	2793.750	10742.188	103.645
H_F [$\mu W.m^{-3}$]	120	2.000	6.000	4.000	2.000	1.414
D_max [Ma]	120	0.935	67.346	9.400	173.309	13.165
T_dom [K]	120	658.946	984.0756	760.768	5403.794	73.510
S_dom (log) [s^{-1}]	120	-15.527	-13.853	-14.373	0.126	0.355
dh [km]	120	6.470	39.938	23.721	141.360	11.890
t_dh [Ma]	120	15.412	98.312	27.024	242.023	15.557
H_max [km]	-	-	-	-	-	-
T1_max [K]	120	934.514	1317.510	1113.665	8516.532	92.285
P1_min [kbar]	120	4.455	18.683	9.500	14.278	3.779
T2_max [K]	120	1149.738	1322.327	1191.4635	1699.604	41.226
P2_min [kbar]	120	14.753	19.147	18.248	0.667	0.817
h_t [Ma]	120	7.039	120.112	30.443	843.229	29.038
h_d [km]	120	0.867	51.798	33.230	188.076	13.714
T_d [K]	120	0.942	402.029	102.264	7849.330	88.596
Individual simulations	[$D_M1D_F1H_F1$]	[$D_M1D_F1H_F5$]	[$D_M1D_F5H_F1$]	[$D_M1D_F5H_F5$]	[$D_M5D_F5H_F1$]	[$D_M5D_F5H_F5$]
D_max [Ma]	5.800	4.865	79.990	51.896	5.001	4.005
T_dom [K]	736.268	751.312	988.380	981.173	717.954	725.568
S_dom (log) [s^{-1}]	-14.029	-13.917	-16.285	-16.339	-14.625	-14.394
dh [km]	37.814	40.592	0.224	0.580	9.020	9.691
t_dh [Ma]	26.460	19.000	119.310	119.215	21.530	24.010
H_max [km]	27.186	24.407	64.776	64.420	56.020	55.309

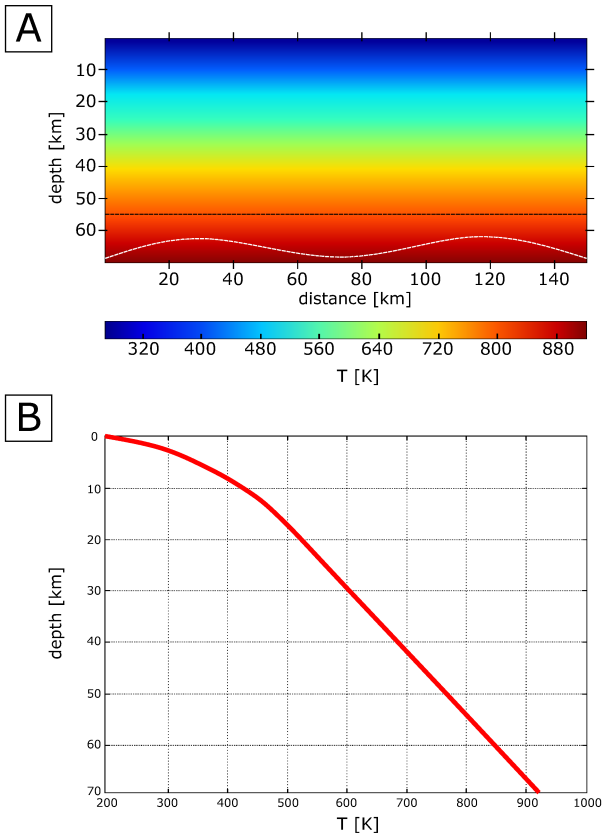


Fig. 43: Initial thermal field. The heat distribution after the time-step 1 is visualized in (a). Corresponding interfaces between UC, MLC and FLC are displayed by black and white dashed lines. Initial geotherm corresponding to calculated thermal field is shown in (b).

according to table 10). All tested initial parameters are listed in this table and the individual simulations from the series with varied parameters are marked as e.g. D_M*1-5* (example for various MLC densities). The model output parameters (Tab. 11) are not compared in detail for all the sets of simulations but rather discussed for selected simulations. The simulations reflect extreme values of initial varied parameters (covering extreme differences in the model evolution) and are described below (this selection is used to describe and discuss strain(-rate) characteristics for the crustal-scale diapiric systems - see paragraph 4.3.4 and discussion).

Simulation class D_M1-5D_F5H_F1-5 (a)

The setting of the simulation $D_M1D_F5H_F1$ corresponds to higher density of the FLC than MLC and minimum radiogenic heating of the FLC (see Tab. 10). In this simulation is not observed any inversion of the lower crustal layers and corresponding development of a diapiric body (Fig. 44A). Initial perturbation of the interface between MLC and FLC is progressively smoothened until the gravitational equilibration is reached at a time of 119 Ma. The corresponding thermal evolution reflects heat transfer from the mantle segment and also thermal increment from the FLC with maximum temperatures higher than 1300 K at the MOHO level. The material markers (M1 and M2) show no significant change in the vertical position of the corresponding material (Fig. 44B) which is related with stable position at $\sim$ 19 kbar (M1) and $\sim$ 15 kbar (M2). The maximum reached temperature for M1 is $\sim$ 1285 K while M2 is heated to $\sim$ 1230 K. For increasing density of the MLC (simulations D_M*1-5*D_F5H_F1) the gravitational instability is developed and leads to the ascent of the FLC material (e.g. Fig 44G - will be described below). The results for high values of the radiogenic heating of the FLC (D_M*1-5*D_F5H_F5) are similar in terms of the material flow and ascent. The temperature of the M1 for high H_F is $\sim$ 1300 K and M2 has approximately the same temperature evolution as simulations D_M*1-5*D_F1H_F1.

Simulation class D_M1-5D_F1H_F1-5

These simulations are characterized by gravitational inversion of the MLC and FLC and progressive development of the crustal-scale diapiric structures (Fig. 44C). The elevation level of the FLC here depends on the initial value of the density. For the lowest densities of the FLC (that correspond to 2650 kg.m^{-3}) occurs the inversion of the UC and FLC with partial exhumation of the MLC material at the head of the diapir body. The model domain is generally heated less than in the case of the simulations with small or reverse density gradient (described above) and model base reached $\sim$ 1076 K. The most heated parts of the model domain also reflects the exhumation trace of the FLC material with temperature higher than 1000 K. The simulations with higher radiogenic heating are characterized by higher maximum temperatures in the diapiric body ($<$ 1075 K) but with approximately the same temperatures close to the MOHO levels. The P-T diagram (Fig. 44D) reflects progressive

exhumation of the FLC material which is accelerated between approximately first 10-30% of the simulation time. The material which is associated with the position of M1 is rapidly exhumed and for the higher positive density contrast between the basal layers (D_M5D_F1) is lifted rapidly. The peak temperature is $\sim$ 1028 K which is reached at the bottom part of the diapir head while the pressure peak is $\sim$ 7.2 kbar. For the lower density of the MLC (D_M1D_F1) the FLC material reached a higher crustal level with a pressure peak at 6.2 kbar and maximum temperature of $\sim$ 895 K. The marker M2 reflects a sinking of the MLC material (respective to current density contrast) with finite positions at $\sim$ 17.4 kbar, peak pressure depth at $18.2 - 18.8$ kbar and peak temperature at $1065 - 1078$ K. The H_F affected dominantly felsic diapir body and moved peak value of M1 to $\sim$ 1070 K for higher density contrast while a smaller density contrast leads to slightly different inner dynamics of the diapir and M1 reached higher levels of the crust (typically 5 kbar with 920 K).

Simulation class A_F1-5Th_F5H_F1-5

In this class of the simulations, the gravitational inversion and the crustal diapirism occurred similarly to the previous case (Fig. 44E). The exhumation rate of the FLC material is driven by the amplitude of the undulation of the lower crust A_F as well as by radiogenic heating H_F. The elevation level is similar for all values of the amplitude and radiogenic heat productivity. The P-T diagrams (Fig. 44F) revealed that for smaller amplitudes of the FLC-MLC interface, the thermal evolution of the marker M1 is similar for the higher values of the amplitude. The variation of the maximum temperatures varies from $\sim$ 925 K to $\sim$ 970 K ($910 - 1075$ K for the highest H_F). The pressure peak corresponds to $\sim$ 6.8 kbar. The temperature differences show that the smaller amplification of the FLC-MLC interface leads the material ascent less significantly than higher values. The marker M2 has the same initial and finite P-T values for all values of the H_F. The significant differences in the P-T conditions occur only for the first 40% of the model evolution.

Simulation class D_M1-5D_F1H_F1-5

These simulations are characterized by a bimodal evolutionary trend which reflects variable density contrast with respect to the fixed and generally highest density of the FLC (Fig. 44G). The situation when $D_M<D_F>D_{UC}$ represents relaxation of the felsic material at the MOHO level and is described above (Fig. 44A). The second subclass of those simulations where $D_M>D_F>D_{UC}$ is characterized by inversion of both lower crust layers without the development of the crustal-scale diapiric body. The P-T diagrams (Fig. 44B and Fig. 44H) show the rapid increasing of the pressure due to fast elevation of the FLC material (M1) which is exhumed to maximum levels corresponding to $\sim$ 13.5 kbar and associated temperatures $\sim$ 950 K. Due to the inner convection-like dynamics of the FLC material, the M1 markers are progressively buried back to the lower crustal level with the maximum depth at $\sim$ 60 km - 62 km

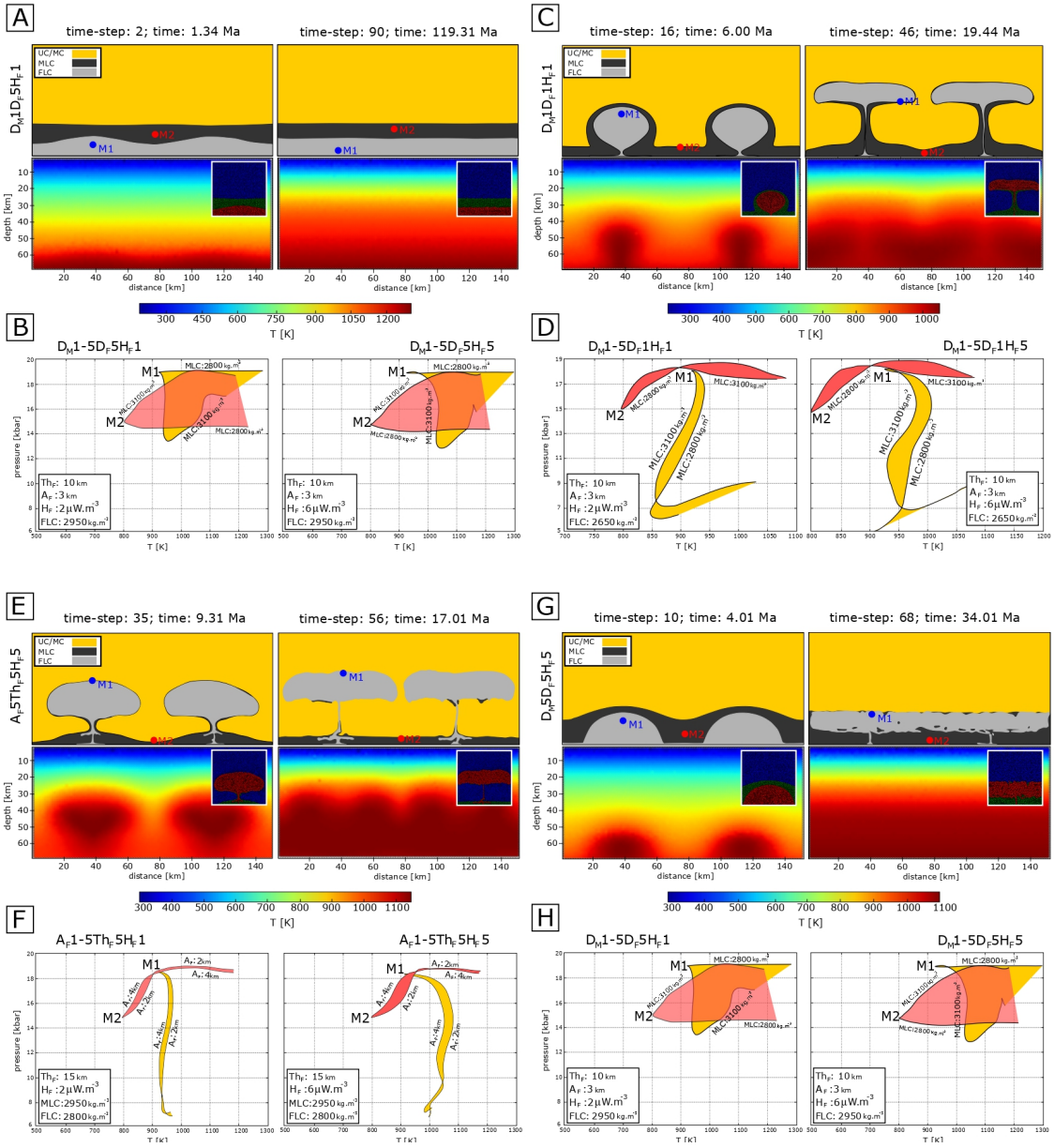


Fig. 44: Material and thermal evolution of various simulations. Each panel in the figure displays the redrawn position of the crustal material due to the specific time-steps, corresponding thermal field and overview of P-T evolutionary paths for special markers (M1,M2). Dispersion of P-T paths is covered by colored fields (yellow and red) with side paths marked by information about the value of modified initial parameters (here for density of MLC and initial amplitude of surface of the FLC). These P-T plots are displayed twice to reflect effect of radiogenic heating (extreme values from chosen simulations). The position of selected special markers is shown in material distribution diagram and small square windows in the thermal maps display real positions of the material particles in the model domains. All other variable parameters for whole simulation class are displayed in a small window in the P-T diagram field.

and pressure $\sim$ 17 kbar with associated temperature of 1150 K. The evolutionary trend for high H_F is similar in pressure ranges (minimum P is 12.9 kbar and finite P is $\sim$ 16 kbar). The initial temperature for M1 is the same as for the low heating values ($\sim$ 925 K), the temperature in the highest position is $\sim$ 1040 K and finite temperature is $\sim$ 1160 K. However, the marker M2 is characterized by very similar trends for both values of H_F with the same ranges of the P-T conditions.

Model output parameters

For the simulation class $D_M1\text{-}5D_F1H_F1\text{-}5$ is the maximum average temperature of the model domain (T_dom) 984 K and maximum average logarithmic strain-rate is -13.8 s^{-1} which corresponds to maximum rate of exhumation after 0.9 Ma (average is 9.4 Ma). Maximum vertical displacement of the FLC mass center corresponds to 39.9 km. The maximum reached temperature in M1 is 1070 K and minimum pressure is 4.9 kbar. Maximum differential temperature for initial and finite position of M1 is 195 K. The marker M2 reached a maximum temperature of 1322 K and minimum pressure is 14.8 kbar. The simulation in the class $A_F1\text{-}5Th_F5H_F1\text{-}5$ are characterized by the maximum temperature of the model domain which is between 719 K and 882 K (depends on thickness of the FLC) and average strain-rate $\sim$-14.2 s^{-1}. Average exhumation rates closely correspond to time at 6 Ma and maximum reached vertical extrusion distance of the FLC mass center is $\sim$ 35 km. The maximum reached temperature in the marker M1 is 1079 K and minimum reached pressure is 6.5 kbar (higher than for variable density simulations). The maximum differential temperature corresponds to 170 K. The marker M2 generally recorded the maximum temperature of 1173 K (average 1136 K) and minimum pressure of 15 kbar (maximum is $\sim$ 19 kbar). The statistical overview for the simulation sets and for the individual simulations is listed in the Table 11.

4.3.4 The velocity field and strain(-rate) in the model domain

The individual FLC material perturbation (diapiric body) was studied in terms of the strain, velocity field, strain-rate and rate of the exhumation of the FLC mass center (Fig. 45). In this paragraph is described the dynamics of the selected simulations, that distinguish three different scenarios of the mass transfer in the crustal domain according to various initial conditions (Tab. 11 - individual simulations). The characteristical evolution of the GPE for the specific simulation has typically three significant points as is defined in the paragraph 4.3.1. These evolutionary trends are in good correlation with the position of the mass center of the FLC material in the model domain during the time in current simulation. Each plotted strain diagram corresponds to one of all three points at the "GPE - FLC mass center" curve.

Simulations $D_M1D_F5H_F1$ and $D_M1D_F5H_F5$

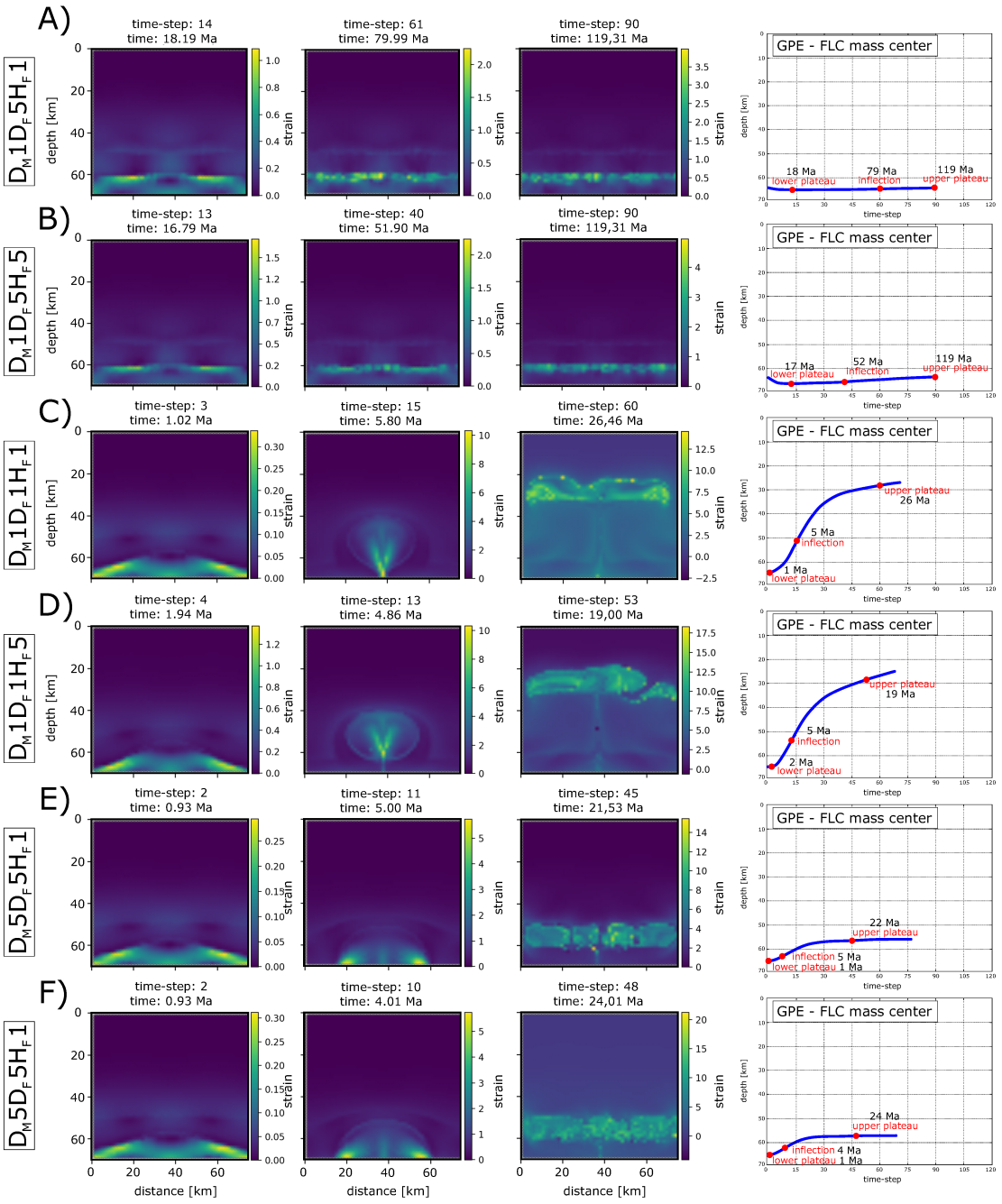


Fig. 45: Strain maps and GPE evolution curves for selected simulations. Each triplet of strain contour maps shows strain values and distribution in the crust for target time-steps (lower plateau, inflection and upper plateau of the GPE curve). The GPE - FLC mass center diagrams show evolutionary trend and positions of the felsic material mass center for each time-step with marked (red filled circles) target points for crucial time-steps (and associated time) corresponding to strain diagrams.

These simulations are characterized by the progressive relaxation of the FLC material along the MOHO level without any material inversion (Fig 45A, 45B). The strain is mainly concentrated at the sides of the initial FLC undulation with small localization along the axis of the perturbation. This state corresponds to the time where the lower plateau of the GPE is situated. The inflection of the GPE evolution (at a time of 79 Ma) reflects higher strain which is distributed mainly along the interface between MLC and FLC. The finite strain pattern is similar as in time of the inflection (except the magnitude which is higher).

The situation for high H_F is similar as in the case of low H_F. The main difference is in the higher strain values and earlier inflection event of the GPE evolution (52 Ma). This reflects decreased density of the FLC due to higher heating.

Simulations $D_M1D_F1H_F1$ and $D_M1D_F1H_F5$

Both simulations corresponds to the situation when the felsic material is exhumed to the UC/MC levels due to the lower density in contrast to the MLC (Fig. 45C, 45D). The time of the maximum rate of the material exhumation corresponds to 5 Ma while decreasing rate of the uplift differ between 19 Ma and 26 Ma as a function of H_F. In both simulations, the main strain zones corresponds progressively to both sides and central part of the material perturbation. During the late evolution, the maximum strain is exclusively localized in diapir neck and head. During the accumulation of the FLC material in the central diapiric part (exhumation channel), the strain is localized along 'V' shaped deformation zones. When the FLC material reached the position corresponding to the interface between the upper and middle crust, the strain is distributed through the diapir head and material has tendency to be equilibrated at depths $20-30$ km (in dependence on density contrast).

Simulations $D_M5D_F5H_F1$ and $D_M5D_F5H_F5$

The evolutionary trend in these simulations (Fig. 45E, 45F) reflects high densities of both basal layers (MLC and FLC). Due to the significant density contrast between both layers, the inversion became relatively fast. However, the high density contrast between both basal layers and UC/MC leads the inversion exclusively for both basal layers without a development of classic diapiric body as in the previous case. The maximum rate of the FLC exhumation corresponds to 5 Ma (4 Ma for high H_F) and zones of the maximum strain converged to the central part of the bulge of the exhumed FLC. Before the development of the 'V' shaped strain pattern in the exhumation channel (as in the previous situation) the FLC bulge fell apart and material is redistributed along the base of the UC/MC. The strain is higher and more distributed than during earlier stages and has the maxima at 22 Ma (low H_F) and 24 Ma (high H_F). The result of the inversion is the fully relaminated felsic layer above the mafic lower crust.

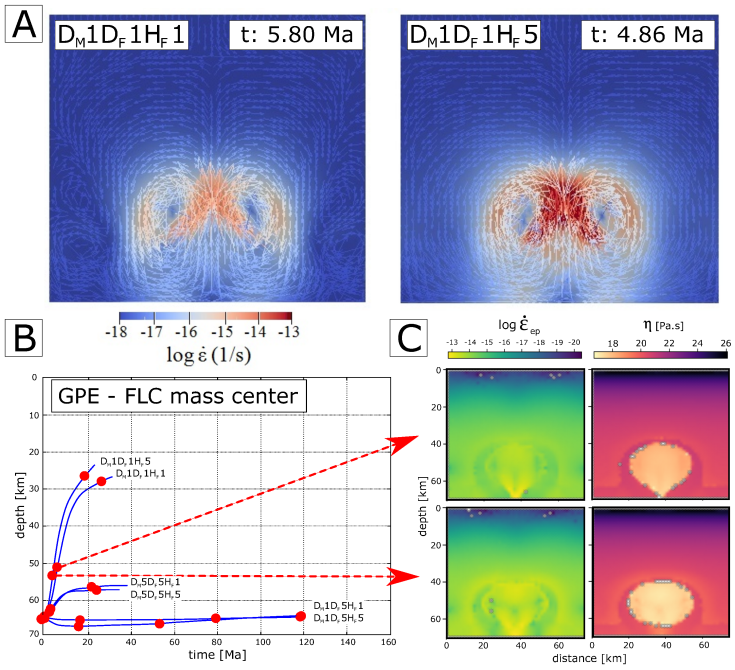


Fig. 46: The strain-rate and rheological structure of developed diapiric body. Diagram (a) displays the strain-rate distribution in the lifted felsic material and sinking surrounding felsic material in the diapiric body for simulations with the same density contrast of both basal layers (side members of H_F). Overview of the GPE diagrams (b) show comparison of three main types of the FLC material transfer and dynamics as is described in text and visualized at Fig. 45. For the simulations with higher density MLC and low density FLC *($D_M1D_F1H_F1$* and *$D_M1D_F1H_F5$)* (corresponding to fully developed diapiric body with the maximum exhumation of the FLC mass center) is displayed *Epsr* (effective plastic strain-rate) and viscosity contour maps (displayed diagrams are shown for inflection of the GPE curve).

Dynamics of the diapir body for simulations $D_M1D_F1H_F1$ and $D_M1D_F1H_F5$

As was described above, the simulations with the higher density contrast of the basal layers ($D_M >> D_F$) are characterized by a fully developed diapir body with the relamination of the felsic material at the level of the upper crust. The evolution of the diapir has four main stages: 1. Accumulation of the felsic material into the bulge shape; 2. Vertical extrusion and flattening of the bulge; 3. Development of a head and narrow neck (saturation channel) of the diapir; 4. Horizontal relamination of the felsic material.

The velocity field and magnitude of the strain-rate (Fig. 46A) reveal the convection-like dynamics in the inner part of developed diapir. Both mirrored convection cells are symmetric along the axis of the diapir with the higher strain-rates inside the upper-central part of the diapir (diapir head). The maximum values of the strain-rate varies from $10^{-13,8}$ s^{-1} to 10^{-15} s^{-1} for simulation with low H_F in time of the maximum rate of the vertical uplift (GPE inflection). For the simulation with the high H_F, the inner dynamics is faster and strain-rates varies between 10^{-13} s^{-1} to $10^{-14,7}$ s^{-1} for earlier time of the inflection point. The highest strain-rates correspond to the central part of the diapir where the fast vertical flow of the felsic material occurs - in the area of the highest horizontal and vertical gradient of the velocity.

Both simulations have identically shaped diapir body and the main difference is in the higher exhumation-rate of the FLC for higher H_F. From all studied simulations (at the Fig. 45) this class represents the higher rates of the exhumation of the FLC material. Here the inflection time of the GPE is comparable with the simulations that are characterized by high D_M and D_F (Fig. 46B). The effective plastic strain-rate (Epsr) and viscosity in the model domain are shown in the Fig. 46C. The maximum Epsr is concentrated along two 'V'-shaped shear zones in the lower part of the diapir and also in the head of the diapir. The characteristic values of the Epsr in these areas are typically between 10^{-13} s^{-1} and 10^{-14} s^{-1}. The viscosity in the diapiric body varies between 10^{19} Pa.s and 10^{17} Pa.s depending on the position and time.

4.4 Discussion

Lithosphere-scale diapirism is a native component of hot accretionary orogenic systems where negative density gradients of the lower crust play a significant role for the development of Rayleigh-Taylor instabilities (Conrad and Molnar, 1997; Beaumont et al., 2006; Schulmann et al., 2008; Lexa et al., 2011; Maierová et al., 2012, 2014, 2016). In the presented model we tested several initial conditions as driving parameters of the model dynamics. The statistical analysis was performed in Krýza (2013) while new insight into the model dynamics which is based on the additional modelling data is a subject of this chapter.

4.4.1 The effect of the heating on diapiric extrusion

The multivariate statistics revealed that the most influencing initial parameter is a density contrast which is leading the whole dynamics and associated factors as the integral field temperature, local temperature, heat distribution in time, strain(-rate) distribution and intensity, viscosity changes, general material flow, etc. (Krýza, 2013).

All simulations that were described in the sections 4.3.3 and 4.3.4 revealed that the radiogenic heating of the felsic lower crust affects the typical time where the inflection of the GPE is reached. With increasing H_F, the lower crustal segment gains significantly higher temperatures and its density and viscosity are decreased. The density contrast of the layers is then indirectly affected and changed during the model evolution. Typically, the vertical extrusion of the felsic material is faster due to this contrast. However, the simulations where the stratification is preserved (the simulation class with reverse density contrast of the MLC and FLC) occur also for a smaller time for the inflection for the GPE evolution. This could be related with the viscosity decreasing which can affect the effectivity of the material transport. Also, long-term decreasing of the inverted density contrast changes in the structure of the GPE evolution (Fig. 45A,B and 46B).

The simulations that are characterized by a typically diapiric-shaped FLC exhumation, reflects the higher H_F by the maximum strain and maximum reached crustal level where the felsic material is later relaminated (Fig. 45C,D and Fig. 46B). In general, the FLC material with high H_F has a potential to reach higher crustal levels and its ascent is faster than for the simulations with low H_F. This is well-proven by the global output model parameters (see Tab. 11 - the section of individual simulations).

The weakening of the lower crust, in response to radiogenic heating, typically affects the style of the crustal-scale material transfer in the hot orogens (Maierová et al., 2014, 2016, Faccenda et al., 2008; Jiménez-Munt and Platt, 2006; Arnold et al., 2001; Moresi et al., 2007). Based on the various heating source distribution and intensity, different thermal gradients are produced and characteristic P-T conditions for a different areas of the lithosphere are reached (e.g. Hasterok and Chapman, 2011). Rapid heating of the FLC increases peak temperatures for the felsic material which then progressively form a diapir body ($\sim$ 1000 K - 1175 K (marker M1); 1317 K (maximum FLC temperature)) and also for the maffic material ($\sim$ 1165 K - 1220 K (marker M2); 1322 K (maximum MLC temperature)) which is in contact (or sufficiently close) with the felsic material. These marker values are in quite good agreement with the peak temperatures presented in Maierová et al. (2014) for the FLC and MLC material. However, the mafic material, which in the diapiric-evolved simulations sank to the bottom of the model domain, is heated by two sources: 1. Heat flow from the MOHO level; 2. Heat exchanges with the thermally productive felsic material. For the models where the domain shortening does not occur, the material is heated equally from the sides and symmetric diapirism is produced (this

study). This situation is comparable with the diapiric exhumation of granulitic rocks in the Bohemian massif (Maierová et al., 2012, 2014; Lexa et al., 2011). For large accretionary systems where the sequence of the diapiric bodies is produced (Maierová et al., 2016), the furthermost diapirs from the indenter are formed similarly as in the static, non-contracted domain. On the other hand, the diapirs that are situated close to the indenter are affected by side shortening and the material of the lower crust is later transported in the form of a channel-flow (Maierová et al., 2012; Duretz et al., 2011).

The heating and the weakening of the lower crust depends strongly on the combination of the H_F and exhumation rate of the felsic material as well as on the amount of the thermally productive material. In contrast to the diapirism, the folding of the MMC occured when no (or low) radiogenic heating ($H_F = 0 - 2$ mW.m^{-3}) of the FLC and at the same time medium shortening rates (1.5 cm.yr^{-1}) of the model domain are employed (Maierová et al., 2014). If the time for the weakening of the basal layers is sufficient then a switch from the folding to diapirism may occur afterwards. For pre-developed folds/diapirs the density contrast plays a key role. And the initial style and rate of the exhumation will be affected by the shape of such material perturbations (Krýza, 2013).

4.4.2 The density contrast of the lower crust

While the viscosity contrast of the different crustal layers affects the shape of the diapir (and the folding mechanism), the density contrast leads to the exhumation potential and rate of the material exchanges along the vertical direction. The simulations with the initially lower density ratio and with the higher density of the FLC, which typically produces a horizontal layering (e.g. Bittner and Schmeling, 1995), represent a good precondition to the folding of the lower crust (after transition to the compression regime). With the rapid heating of the basement along the MOHO and with high radiogenic thermal productivity (simulations with $H_F > 3$), the partial melting of the FLC and melt accumulation can occur. If the system is in a contraction regime then detachment folding (Fig. 47A) can produce a sequence of the folds and leads the ascent of the melt such as in the scenario which is described in Krýza et al. (2019) (Chapter 3) or in Lehmann et al. (2017). The hot lithosphere and the weak middle and lower crust that are in the contraction regime can also produce a bending and the brittle-ductile deformation response in the upper crust (Zeitler et al., 2001). The buckling of the lower crust leads the decompressional melting and the gravity driven ascent of the partially molten material (Nelson et al., 1996). The buckling mechanism without the associated melt ascent, where a detachment is the product of horizontal shortening and mechanical decoupling (e.g. Carry et al., 2009; Handy and Brun, 2004; Smit et al., 2003; Groshong and Epard, 1994) of the layers with contrasting strength, is similar to the salt-tectonics and detachment folding in the Central and Eastern Zagros fold-belt (e.g. Sherkati et al., 2005). The difference between weak-hot and stronger-cold lower crust can affect the gravitationally driven

exhumation (as in fig. 47A) of the lower crust where the weak and partially molten lower crust can contribute to the areal exhumation (as is described in the previous section). The mechanical contrast of the lower crustal layers and the potential of gravitationally driven exhumation are also mutually related with (iso-)volumetric detachment folding (Groshong and Epard, 1994) and its characteristic kinematics (Epard and Groshong, 1995; Hardy and Finch, 2005) that will affect the amount and the physical properties of the material which is migrating along the fold axial planes (e.g. Krýza et al., 2019; Lehmann et al., 2017).

In the static models of the crustal domain without the MOHO parallel shortening where $D_F > D_M$, no diapirism will be produced. This scenario corresponds to the models where the felsic material is stable at the basement of the crustal segment (horizontal layering as is described in Bittner and Schmeling (1995)). However, the situation when the low density felsic material is covered by the high density maffic material leads typically to the inversion of both layers (e.g. Maierová et al., 2012; Lexa et al., 2011; Bittner and Schmeling, 1995; Weinberg and Podladchikov, 1994) and a characteristic density contrast (variable in time) determines the maximum exhumation level of the light material (Bittner and Schmeling, 1995). This contractionless scenario typically corresponds to the evolution of a distant Rayleigh-Taylor instabilities such as in the back-stop region in the models of Maierová et al. (2012, 2014, 2016).

4.4.3 The role of the perturbation shape for diapiric exhumation rate

The amplitude and wavelength of the material perturbation play a significant role during the geometrical evolution of the Rayleigh-Taylor instability (Polavarapu et al., 2019; Anuchina et al., 2004; Elgowainy and Ashgriz, 1997; Bittner and Schmeling, 1995). In our models we also tested the effect of the initial amplitude of the material undulation (A_F) against the exhumation rate and other related model output parameters (see Tab. 11) rather than against the geometrical differences in the finite diapir shape. The results show that the simulations with higher amplitude of the undulation of the FLC (A_F) lead to a faster initial exhumation with typically earlier inflection of the GPE evolution. However, the previous work (Krýza, 2013) revealed that in the tested range of the A_F the correlation with all the model output parameters is insignificant with respect to the maximum correlation with D_{max} (lower in range of 1-2 orders). For the lower density contrast of the mafic and felsic crust, the A_F still affects the characteristic time of the exhumation and time where the GPE inflection is reached. Unlike the study of Bittner and Schmeling (1995) where the shape of the diapiric body of the partially molten granite is affected by initial amplification, the large crustal-scale diapiric body is not strongly geometrically affected by the amplification but rather by the wavelength of the material perturbation - similarly to the mantle-scale diapirism (e.g. Wilcock and Whitehead, 1991; Schmeling, 1987). Generally, the long-wavelength perturbations will lead to the dome-like exhumations while the short-wavelength perturbations with the same amplitude will lead to finger-like exhumations. However, the testing of a wide spectra of the wavelengths is not

the subject of this study and according to prescribed range of the A_F, the three main situations can occur according to the different amplification of the lower crust interface: 1. Very low A_F - long term initial stage of the FLC exhumation; 2. Medium A_F - short time for the material accumulation close to the axis of the perturbation, followed by fast exhumation; 3. The highest A_F - rapid initial exhumation, early deceleration of the exhumation rate.

In general, the amplification of the MLC/FLC crustal interface leads to the initial acceleration of the dipirism for the simulations with the positive density contrast of the layers of the lower crust ($D_M < D_F$). Even for the small and positive density contrast of the layers, the A_F supports the material inversion. The A_F plays a key role during the first stages of the diapirism while later prevails the density contrast of both lower crust layers.

4.4.4 Diapiric or detachment folding?

Recent studies show that large accretionary systems are related with (exponentially) slowing convergence rate (Clark, 2012; van Hinsbergen et al., 2011; Toussaint et al., 2004; McQuarrie et al., 2003; Patriat and Achache, 1984; Dewey et al., 1989). The slowing convergence rate is interpreted as a response to several events, including: demise of a mantle plume (Morodova plume in case of India-Asia convergence) → decreasing the driving pull force, cooling and hardening of the mobile plate (van Hinsbergen et al., 2011); the effect of the deformation of the viscous mantle lithosphere related with the constant bulk strain-rate in the upper plate (Clark, 2012).

The previous analysis revealed that the convergence rate and horizontal shortening play a significant role for the deformation and horizontal-vertical flow of the lower crust. If the shortening rate is high then buckling of the strong layers prevails over the diapiric exhumation of the weak/anatectic material of the lower crust (Fig. 47A,B - detachment folding). For a slow shortening rate, the deformation response will be longer and due to radiogenic heating and thermal flow from the mantle, crustal diapirism will dominate the vertical uplift of the lower crust (Fig. 47A,B - crustal diapirism). However, long-term convergence and shortening are related with the exponential slowing of the plate motions. In this scenario, the initially high convergence-rate may be associated with buckling and with the development of material perturbations in the form of long-wave folds and flexures in the lower crust. As in the previous case, the lower crust will be heated (in dependence on heating potential of the FLC and heat transfer from the mantle). During the progressive slowing of the shortening-rate, the gravitational instability gains in time to effectively produce the crustal-scale diapirism (Fig.47A,B - detachment folding/diapirism).

The weak and anatectic lower crust, which is near to the rigid indenter, might be transported in the form of a channel flow alongside the indenter (Maierová et al., 2012; Duretz et al., 2011). When the indentation rate is progressively decreased, then the drag force for the material transport is also decreased and the material perturbations

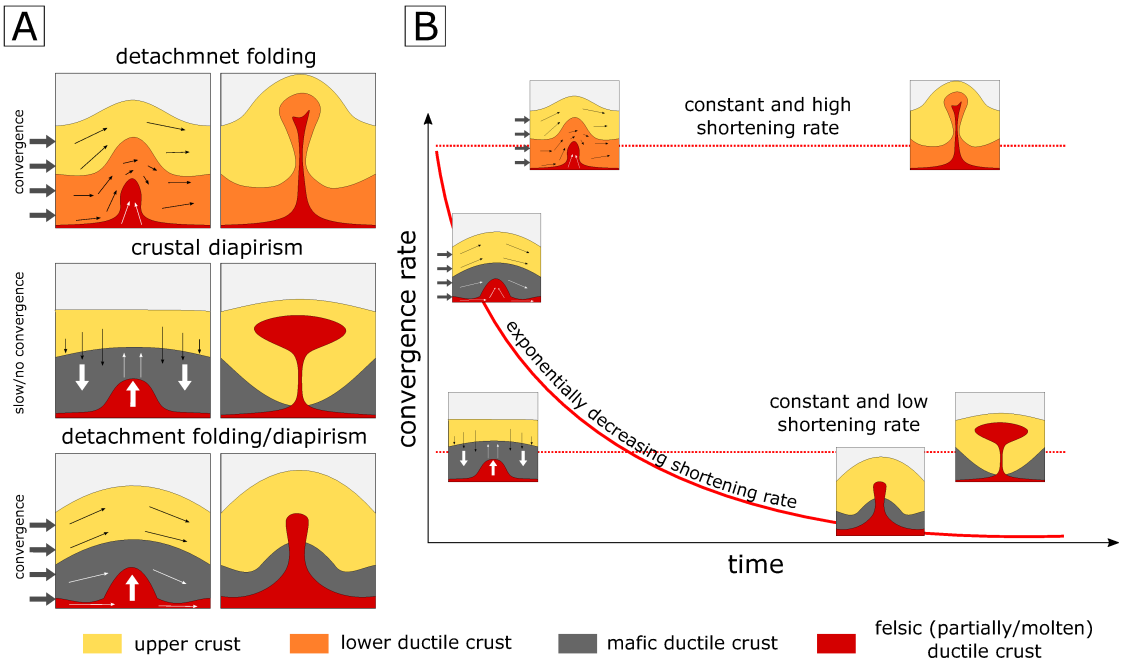


Fig. 47: Comparison of diapiric/folding evolution of the lower crust for various rates of convergence in the collision systems. Contrasting styles of lower crust flow/deformation are shown in (a). Thick bold arrows show general (external) forces inducing the inner deformation while thin arrows show consequential material movement in the crustal domain. Diagram of the time evolution of the convergence-rate (b) represents three main types of contracted systems with representative behavior of the crust material (as is described in text).

may produce the Rayleigh-Taylor instability that support the secondary diapirism. The diapirism of the material which is remote from the indentation area will be progressively affected by the approaching indenter and inclined (as in Maierová et al (2012, 2014, 2016)). If the indenter will be effectively slowed, as in the case of the exponential decreasing of the convergence rate, then the sufficiently distant diapirs will not be significantly affected in a term of the shape and exhumation rate.

Interaction of developing diapiris with the pre-folded crust can be reflected by inflow of the material along axial plane of the fold in the case of antiforms (as is described in chapter 3). The exhumaed material will then be surrounded and isolated by limbs. The perturbations that are situated benath the synforms will probably not be fully developed but material will flow-up rather than around the hinge zone. However, the smaller strength contrast between pre-folded layers and ascending material will increase diapiric potential not only in the hinges of the antiforms but also will support the exhumation potential of the light material undeneath the hinge areas of the synform.

4.5 Conclusions

The numerical simulations revealed the complex behavior of the lower crust for the various tested initial conditions. The parametric study shows that the major driving parameter for crustal-scale diapirism is a density contrast between the MLC and FLC. A detailed analysis of the additional simulations described the inner dynamics, P-T conditions, geometry and strain(-rate) distribution as they are affected by prescribed initial conditions and related with the output model parameters.

There are three main groups of the transfer specifics of the lower crust: 1. the systems where the lowest part of the lower crust has a typically higher density than the layers above (e.g. $D_F > D_M > D_{UC}$), 2. the systems with the highest density of the upper part of the lower crust (e.g. $D_{UC} > D_F < D_M$; $D_M > D_{UC}$), 3. the systems where the lower part of the lower crust is less dense than upper lower crust but denser than upper crust (e.g. $D_{UC} < D_F < D_M$). The first scenario is characterized by pure relamination of the lowest crust (FLC) along the MOHO level while the second scenario leads to typical crustal-scale diapirism and vertical exhumation of the lowest crust (FLC) with typical relamination at the depths corresponding to the mid-levels of the upper crust. The last scenario is characterized by inversion of the lower crust (exchange of the FLC and MLC).

- The amount of radiogenic heating affects the P-T-t conditions at individual crustal levels. If the density contrast of the individual crustal layers is not significant, the higher heating of the FLC may support the vertical transfer. Higher radiogenic heating also decreases the time where maximum dynamics of the systems occurs. The effect of the heating is also conditioned by the amount of productive material.

- The amplitude and wavelength of the initial material perturbation support diapiric potential, partly affect the finite shape and rate of the exhumation. The higher amplitudes decrease the time of the maximum dynamics.
- The viscosity contrast affects the incremental geometry and finite shape of the diapir.
- The maximum strain(-rate) distribution is typical for the scenario 1 and 3 while the maximum strain(-rate) localization occurs in scenario 2. Higher density contrast, heat production and amplification of the material perturbation are responsible for higher strain-rates in more localized strain zones.

The density and size of the initial perturbation also represent different initial stages (various times and reached distances) of the material transfer in dependence on the indenter distance from this perturbation. In systems that are characterised by high convergence rates and low heating (or short term heating), where the weakening of the lower crust is insufficient (strong lower crust), buckling or detachment folding of the lower crust is more typical than diapirism. The systems where the convergence rate is low and where heating and weakening of the lower crust occurs (weak lower crust), the diapirism represents the dominant mechanism responsible for vertical transfer of the lower crust. The systems with the progressively decreasing convergence rate may be characterized by a combination or switching of both described mechanisms. The distance of the Rayleigh-Taylor instabilities from the indenter (variable in time) also affects their inner dynamics. Distant instabilities will be evolved as is described in this study while growing of near positioned instabilities may be suppressed by indentation and folding.

The presented model is aimed to describe and understand how the material of the lower crust is transfered, how this vertical transfer is affected by geometric and material properties and how the potential of the crustal diapirism is related to convergence rate in the collision systems. The analogue (and numerical) modeling of the systems with characteristic slowing convergence is a subject of ongoing research. The future studies will be focused also to the testing of the system dynamics affected by mantle presence, isostatic response, erosion effects etc.

4.6 References

Anuchina, N. N., Volkov, V. I., Gordeychuk, V. A., Es' kov, N. S., Ilyutina, O. S., and Kozyrev, O. M. (2004). Numerical simulations of Rayleigh–Taylor and Richtmyer–Meshkov instability using MAH-3 code. Journal of computational and applied mathematics, 168(1-2), 11-20.

Arnold, J. W. S. H., Jacoby, W. R., Schmeling, H., and Schott, B. (2001). Continental collision and the dynamic and thermal evolution of the Variscan orogenic crustal root—numerical models. Journal of Geodynamics, 31(3), 273-291.

Beaumont, C., Jamieson, R. A., Nguyen, M., and Lee, B. (2001). Himalayan tectonics explained by extrusion of a low-viscosity crustal channel coupled to focused surface denudation. Nature, 414(6865), 738–742.

Beaumont, C., Nguyen, M. H., Jamieson, R. A., and Ellis, S. (2006). Crustal flow modes in large hot orogens. Geological Society, London, Special Publications, 268(1), 91-145.

Bittner, D., and Schmeling, H. (1995). Numerical modelling of melting processes and induced diapirism in the lower crust. Geophysical Journal International, 123(1), 59-70.

Carry, N., Gueydan, F., Brun, J. P., and Marquer, D. (2009). Mechanical decoupling of high-pressure crustal units during continental subduction. Earth and Planetary Science Letters, 278(1-2), 13-25.

Clark, M. K. (2012). Continental collision slowing due to viscous mantle lithosphere rather than topography. Nature, 483(7387), 74.

Chemenda, A. I., Burg, J. P., and Mattauer, M. (2000). Evolutionary model of the Himalaya–Tibet system: geopoem: based on new modelling, geological and geophysical data. Earth and Planetary Science Letters, 174(3-4), 397-409.

Conrad, C. P., and Molnar, P. (1997). The growth of Rayleigh—Taylor-type instabilities in the lithosphere for various rheological and density structures. Geophysical Journal International, 129(1), 95-112.

Dewey, J., Cande, S., and Pitman, W. C. I. I. I. (1989). The tectonic evolution of the India/Eurasia collision zone. Ecolgae Geologicae Helvetiae, 82, 717-734.

Duretz, T., Kaus, B. J. P., Schulmann, K., Gapais, D., and Kermarrec, J. J. (2011). Indentation as an extrusion mechanism of lower crustal rocks: Insight from analogue and numerical modelling, application to the Eastern Bohemian Massif. Lithos, 124(1-2), 158-168.

Elgowainy, A., and Ashgriz, N. (1997). The Rayleigh–Taylor instability of viscous fluid layers. Physics of Fluids, 9(6), 1635-1649.

Epard, J. L., and Groshong Jr, R. H. (1995). Kinematic model of detachment folding including limb rotation, fixed hinges and layer-parallel strain. Tectonophysics, 247(1-4), 85-103.

Faccenda, M., Gerya, T. V., and Chakraborty, S. (2008). Styles of post-subduction

collisional orogeny: Influence of convergence velocity, crustal rheology and radiogenic heat production. Lithos, 103(1-2), 257-287.

Faccenna, C., Davy, P., Brun, J. P., Funiciello, R., Giardini, D., Mattei, M., and Nalpas, T. (1996). The dynamics of back-arc extension: an experimental approach to the opening of the Tyrrhenian Sea. Geophysical Journal International, 126(3), 781-795.

Gerya, T. (2009). Introduction to numerical geodynamic modelling. Cambridge University Press.

Gerya, T. V., and Yuen, D. A. (2003). Characteristics-based marker-in-cell method with conservative finite-differences schemes for modeling geological flows with strongly variable transport properties. Physics of the Earth and Planetary Interiors, 140(4), 293-318.

Groshong Jr, R. H., and Epard, J. L. (1994). The role of strain in area-constant detachment folding. Journal of Structural Geology, 16(5), 613-618.

Hacker, B. R., Gnos, E., Ratschbacher, L., Grove, M., McWilliams, M., Sobolev, S. V., ... and Zhenhan, W. (2000). Hot and dry deep crustal xenoliths from Tibet. Science, 287(5462), 2463-2466.

Hacker, B., Luffi, P., Lutkov, V., Minaev, V., Ratschbacher, L., Plank, T., ... and Metcalf, J. I. M. (2005). Near-ultrahigh pressure processing of continental crust: Miocene crustal xenoliths from the Pamir. Journal of Petrology, 46(8), 1661-1687.

Hacker, B. R., Kelemen, P. B., and Behn, M. D. (2011). Differentiation of the continental crust by relamination. Earth and Planetary Science Letters, 307(3), 501–516.

Handy, M. R., and Brun, J. P. (2004). Seismicity, structure and strength of the continental lithosphere. Earth and Planetary Science Letters, 223(3-4), 427-441.

Hardy, S., and Finch, E. (2005). Discrete-element modelling of detachment folding. Basin Research, 17(4), 507-520.

Hasterok, D., and Chapman, D. S. (2011). Heat production and geotherms for the continental lithosphere. Earth and Planetary Science Letters, 307(1-2), 59-70.

Hirth, G., Teyssier, C., and Dunlap, J. W. (2001). An evaluation of quartzite flow laws based on comparisons between experimentally and naturally deformed rocks. International Journal of Earth Sciences, 90(1), 77-87.

Jamieson, R. A., Beaumont, C., Nguyen, M., and Culshaw, N. (2007). Synconvergent ductile flow in variable-strength continental crust: Numerical models with application to the western Grenville orogen. Tectonics, 26, TC5005. https://doi.org/10.1029/2006TC002036

Jiménez-Munt, I., and Platt, J. P. (2006). Influence of mantle dynamics on the topographic evolution of the Tibetan Plateau: Results from numerical modeling. Tectonics, 25(6).

Jolivet, L., Gorini, C., Smit, J., and Leroy, S. (2015). Continental breakup and the dynamics of rifting in back-arc basins: The Gulf of Lion margin. Tectonics, 34(4), 662-679.

Krýza, O. (2013). Application of multivariate statistical methods for analysis of 2D thermo-mechanical numerical models of diapirism. Master thesis, Charles University.

Krýza, O., Závada, P., and Lexa, O. (2019). Advanced strain and mass transfer analysis in crustal-scale oroclinal buckling and detachment folding analogue models. Tectonophysics (In Press). https://doi.org/10.1016/j.tecto.2019.05.001

Lehmann, J., Schulmann, K., Lexa, O., Závada, P., Štípská, P., Hasalová, P., ... and Corsini, M. (2017). Detachment folding of partially molten crust in accretionary orogens: A new magma-enhanced vertical mass and heat transfer mechanism. Lithosphere, 9(6), 889-909.

Lexa, O., Schulmann, K., Janoušek, V., Štípská, P., Guy, A., and Racek, M. (2011). Heat sources and trigger mechanisms of exhumation of HP granulites in Variscan orogenic root. Journal of Metamorphic Geology, 29(1), 79-102.

Maierová, P., Čadek, O., Lexa, O., and Schulmann, K. (2012). A numerical model of exhumation of the orogenic lower crust in the Bohemian Massif during the Variscan orogeny. Studia Geophysica et Geodaetica, 56(2), 595-619.

Maierová, P., Lexa, O., Schulmann, K., and Štípská, P. (2014). Contrasting tectonometamorphic evolution of orogenic lower crust in the Bohemian Massif: a numerical model. Gondwana Research, 25(2), 509-521.

Maierová, P., Schulmann, K., Lexa, O., Guillot, S., Štípská, P., Janoušek, V., and Čadek, O. (2016). European Variscan orogenic evolution as an analogue of Tibetan-Himalayan orogen: Insights from petrology and numerical modeling. Tectonics, 35(7), 1760-1780.

Maierová, P., Schulmann, K., and Gerya, T. (2018). Relamination styles in collisional

orogens. Tectonics, 37(1), 224-250.

Massonne, H.-J. (2001). First find of coesite in the ultrahigh-pressure metamorphic area of the central Erzgebirge, Germany. European Journal of Mineralogy, 13(3), 565–570.

McQuarrie, N., Stock, J. M., Verdel, C., and Wernicke, B. P. (2003). Cenozoic evolution of Neotethys and implications for the causes of plate motions. Geophysical research letters, 30(20).

Moresi, L., Quenette, S., Lemiale, V., Meriaux, C., Appelbe, B., and Mühlhaus, H. B. (2007). Computational approaches to studying non-linear dynamics of the crust and mantle. Physics of the Earth and Planetary Interiors, 163(1-4), 69-82.

Nelson, K. D., Zhao, W., Brown, L. D., Kuo, J., Che, J., Liu, X., ... and Kind, R. (1996). Partially molten middle crust beneath southern Tibet: synthesis of project INDEPTH results. Science, 274(5293), 1684-1688.

Patriat, P., and Achache, J. (1984). India–Eurasia collision chronology has implications for crustal shortening and driving mechanism of plates. Nature, 311(5987), 615.

Polavarapu, R., Roach, P., and Banerjee, A. (2019). Rayleigh-Taylor-instability experiments with elastic-plastic materials. Physical Review E, 99(5), 053104.

Ranalli, G. (1995). Rheology of the Earth. Springer Science and Business Media.

Schmeling, H. (1987). On the relation between initial conditions and late stages of Rayleigh-Taylor instabilities. Tectonophysics, 133(1-2), 65-80.

Schulmann, K., Lexa, O., Štípská, P., Racek, M., Tajčmanová, L., Konopásek, J., ... and Lehmann, J. (2008). Vertical extrusion and horizontal channel flow of orogenic lower crust: key exhumation mechanisms in large hot orogens?. Journal of metamorphic Geology, 26(2), 273-297.

Schulmann, K., Konopásek, J., Janoušek, V., Lexa, O., Lardeaux, J. M., Edel, J. B., Štípská, P. and Ulrich, S. (2009). An Andean type Palaeozoic convergence in the Bohemian massif. Comptes Rendus Geoscience, 341(2-3), 266-286.

Schulmann, K., Lexa, O., Janoušek, V., Lardeaux, J. M., and Edel, J. B. (2014). Anatomy of a diffuse cryptic suture zone: an example from the Bohemian Massif, European Variscides. Geology, 42(4), 275-278.

Sherkati, S., Molinaro, M., de Lamotte, D. F., and Letouzey, J. (2005). Detachment folding in the Central and Eastern Zagros fold-belt (Iran): salt mobility, multiple detachments and late basement control. Journal of Structural Geology, 27(9), 1680-1696.

Smit, J. H. W., Brun, J. P., and Sokoutis, D. (2003). Deformation of brittle-ductile thrust wedges in experiments and nature. Journal of Geophysical Research: Solid Earth, 108(B10).

Toussaint, G., Burov, E., and Jolivet, L. (2004). Continental plate collision: Unstable vs. stable slab dynamics. Geology, 32(1), 33-36.

van Hinsbergen, D. J., Steinberger, B., Doubrovine, P. V., and Gassmöller, R. (2011). Acceleration and deceleration of India-Asia convergence since the Cretaceous: Roles of mantle plumes and continental collision. Journal of Geophysical Research: Solid Earth, 116(B6).

Weinberg, R. F., and Podladchikov, Y. (1994). Diapiric ascent of magmas through power law crust and mantle. Journal of Geophysical Research: Solid Earth, 99(B5), 9543-9559.

Wilcock, W. S., and Whitehead, J. A. (1991). The Rayleigh-Taylor instability of an embedded layer of low-viscosity fluid. Journal of Geophysical Research: Solid Earth, 96(B7), 12193-12200.

Yasui, M., Kishii, T., Watanabe, T., and Uyeda, S. (2012). Heat flow in the Sea of Japan. The crust and upper mantle of the Pacific area, 12, 3-16.

Zeitler, P. K., Koons, P. O., Bishop, M. P., Chamberlain, C. P., Craw, D., Edwards, M. A., ... and Kidd, W. S. (2001). Crustal reworking at Nanga Parbat, Pakistan: Metamorphic consequences of thermal-mechanical coupling facilitated by erosion. Tectonics, 20(5), 712-728.

Part III

Mud flows under the Martian conditions

5 Lava-like mud flows on Mars

Petr Brož, **Ondřej Krýza**, Lionel Wilson , Susan J. Conway, Ernst Hauber, Adriano Mazzini, Jan Raack, Manish R. Patel, Matthew R. Balme, and Matthew E. Sylvest

5.1 Abstract

Ever since the presence of methane in the martian atmosphere was first reported (Formisano et al, 2004; Mumma et al., 2003), mud volcanism has been hypothesised to be a possible source (Oehler and Etiope, 2017) and its surface expression has been sought in remote sensing data. Possible martian mud volcano fields (and other signs of subsurface sediment mobilisation) have been identified based on similarities to terrestrial analogues (Skinner and Tanaka, 2007; Okubo, 2016; Komatsu et al., 2016). However, their identification on Mars is not straightforward because similar-looking landforms can result from igneous volcanism (Brož and Hauber, 2016; Brož et al., 2017) and the behaviour of extruded mud and resultant morphologies under martian conditions are poorly constrained. Here, we present experimental results performed inside a low pressure chamber at cold temperatures to investigate the mechanisms of mud propagation on Mars. Our results show that low viscosity mud under such conditions propagates differently than on Earth, because of rapid freezing and the formation of an icy-crust. The mud flow propagates in a similar manner to pahoehoe lava flows, liquid mud spilling from ruptures in the frozen crust, then refreezing at the surface to form a new 'flow lobe'. Our findings open new ways of interpreting flow-like morphologies on Mars that were previously attributed to igneous volcanism, and also provides new understanding of the physics behind cryovolcanic extrusions on other icy bodies in the Solar System.

5.2 Introduction

Although the physics behind igneous volcanism on Mars is relatively well studied and understood (e.g. Wilson and Head, 1994; Brož et al., 2015; Parfitt and Wilson, 2008; Fagents et al., 2013), this is not the case for sedimentary volcanism in which mixtures of water and sediments, subsequently simply referred to as mud, are extruded onto the surface. On Earth, sedimentary volcanism (or mud volcanism) manifests at the surface as an eruption of fluids (water, gas and occasionally oil), fine grained sediments (e.g. clays) and clasts from the country-rock penetrated by the conduit. These geological phenomena are the result of fluid (typically methane) overpressure generated at depth combined with gravitational instability of more buoyant sedimentary units buried at deeper stratigraphic intervals (Mazzini and Etiope, 2017). Numerous aspects of sedimentary volcanism and mud behaviour remain unknown, particularly for extraterrestrial examples where it is unclear if

the main driving mechanisms identified on Earth are also present. Therefore the term "mud volcanism" for extraterrestrial phenomena is often loosely used. An initial study by (Wilson and Mouginis-Mark, 2014) discussed an overview of mud propagation on the surface of Mars. However, there is a lack of basic theoretical and empirical knowledge about the behaviour of mud at low atmospheric pressure, temperature and gravity. This knowledge gap represents an obstacle in the study of landforms interpreted to be formed from mud extruded onto the surfaces of terrestrial or icy bodies across the Solar system, and more specifically on Mars. Currently, the low martian atmospheric pressure inhibits the sustained presence of liquid water on the surface (e.g. Bargery et al., 2010), so evaporation and ice formation cause the rheology of the extruded mud to change rapidly and, as a consequence, mud flows may propagate differently than on Earth (Brož et al., 2019).

Here we present the results of analogue experiments performed in a low pressure chamber where we examined how low viscosity, water-dominated mud (12.7 mPa.s at $\sim$ 276 K and 10.7 mPa.s at $\sim$ 296 K) propagates over a cold surface ($<\sim$ 273 K) under both terrestrial and martian ($\sim$ 7 mbar) atmospheric pressures. These experiments enabled us to compare the flow mechanisms at different pressures and reveal unique propagation behaviours under martian conditions. Based on these observations we show that this suite of processes is scalable to kilometre-sized mud flows conjectured to be present on the martian surface (e.g. Skinner and Tanaka, 2007; Komatsu et al., 2016; Wilson and Mouginis-Mark, 2014 Brož et al., 2019).

5.3 Model setup and experimental procedure

The low viscosity mud used in our experiments was a mixture of water that contains 0.5% w/w dissolved magnesium sulphate ($MgSO_4$) salts corresponding to the average river water salinity and clay obtained from the claystone named after the *Rokle* locality operated by the company *Keramost*, which is situated near the town of *Kadaň* in the Czech Republic. The clay was a bentonite composed of 76% montmorillonite, 23% illite, and 1% kaolinite which has been formed by alteration of pyroclastic rocks. As there is no direct in-situ knowledge of which types of clays could be present on Mars during subsurface sediment mobilization and as explosive volcanism was once present on Mars (Platz et al., 2014), to the first approximation this material seems to be a suitable analogue. To exclude the presence of potentially more lithified clayey aggregates, the clay was mixed with water and salt and homogenized in a blender for 3 minutes. Adding the small amount of the salt was necessary to allow submillimetre particles to get into suspension within the mixture (Corradi et al., 1994) and also realistic for the martian surface (e.g. Clark, 1978; Vaniman et al., 2004; Hecht, 2009). The resulting viscosity of the mud was 12.7 mPa.s at $\sim$ 276 K and 10.7 mPa.s at $\sim$ 296 K and the average density of the mixture was 1037.5 $kg.m^{-3}$. The viscosity was measured with *Haake Rotovisco RV 20 and Viscotester VT 550 rheometers* (Institute of Hydrodynamics of the Czech Academy

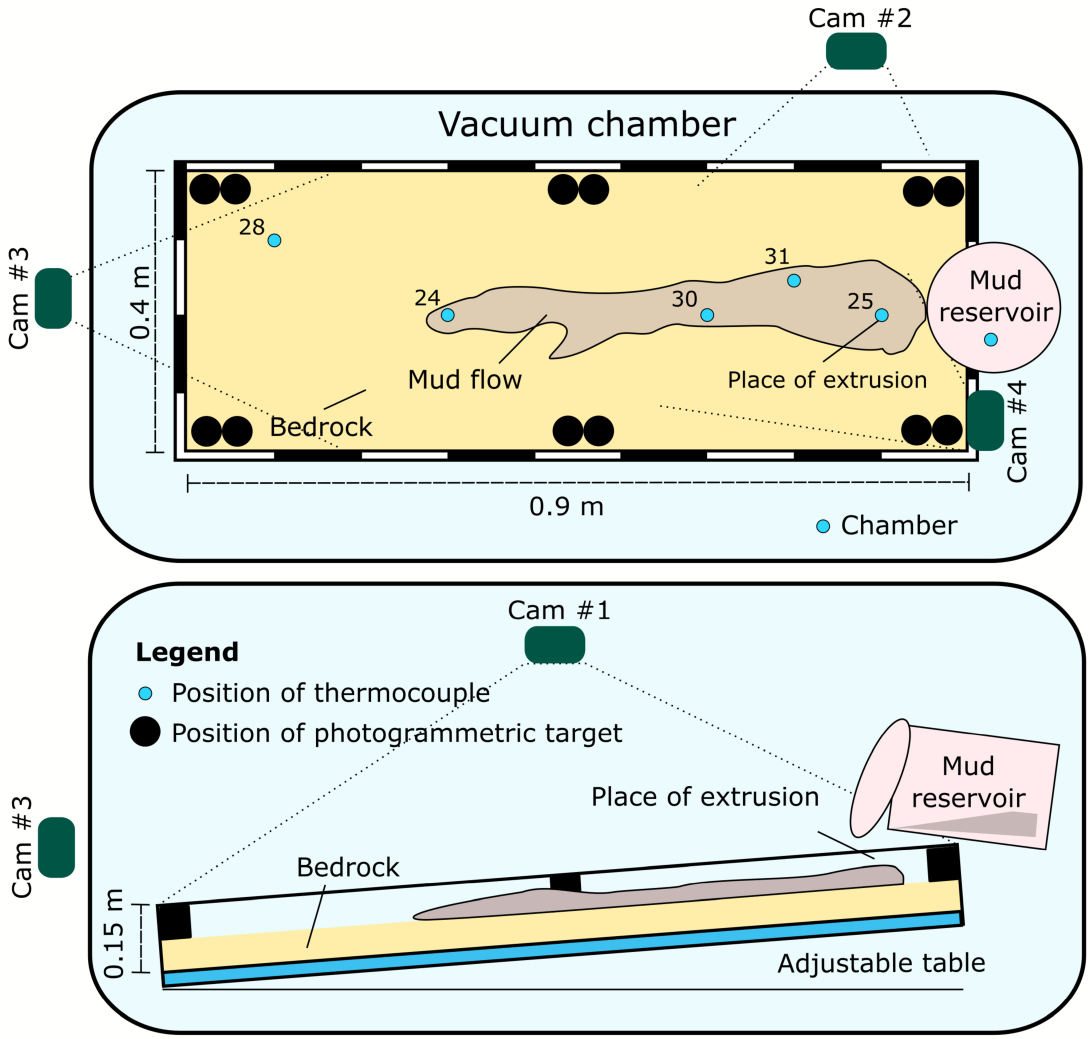


Fig. 48: Schematic illustration showing the experimental setup with the position of thermocouples, photogrammetric targets and four cameras marked.

of Science) with ledges on the *MV2 cylinder* to prevent slip of the measured material on its walls.

Each experimental run (for details see Tab. 12) started by inserting the 0.9 × 0.4 m aluminium tray filled with (a) a ∼ 2 cm deep substrate bed (natural sand, ∼ 200 μm), or b) a plastic plate, and similarly sized copper plate inside the freezer to pre-cool the tray and the plate to temperatures around 238 K. Once the required temperature was reached, the plate and the tray were inserted inside the vacuum chamber. At the same time the 500 ml of liquid mud was poured inside the tilting container equipped with one thermocouple to record the temperature of the mud, and the container was installed inside the chamber. The temperature of the mud varied from 274 to 297 K before the pressure drop. The temperature within the chamber

Tab. 12: Summary of measured and controlled variables for each experimental run.

Exp #	Pressure range [mbar]	Inclination [°]	Release time* [s]	Surface T** [°K]	Mud T*** [°K]	Type of surface	Salinity****
5	6.55 - 7.33	5	15	265	294	sand	D.I. water
6	7.16 - 7.66	5	26	264	292	sand	tape water
7	6.43 - 7.02	5	27	258	296	sand	saline water
8	7.11 - 7.37	5	25	261	294	sand	saline water
9	7.09 - 7.63	5	27	262	294	sand	saline water
10	1000	5	21	258	290	sand	saline water
11	1000	5	19	264	274	sand	saline water
15	1000	5	15	258	293	sand	saline water
16	6.32 - 6.54	5	46	256	290	sand	saline water
17	6.57 - 6.94	5	34	252	278	sand	saline water
18	6.37 - 6.58	5	15	260	290	sand	saline water
19	6.06 - 6.81	10	35	258	286	sand	saline water
21	6.55 - 6.77	10	34	253	293	sand	saline water
22	7.08 - 7.36	10	37	254	294	sand	saline water
23	6.43 - 6.97	5	40	265	293	plastic plate	saline water
24	6.66 - 7.11	5	28	254	295	plastic plate	saline water
29	6.55 - 7.08	5	40	259	295	plastic plate	saline water
34	5.29 - 6.55	5	failed exp.	259	297	plastic plate	saline water
41	1000	5	42	244	295	plastic plate	saline water
49	1000	5	34	247	290	plastic plate	saline water
54	1000	5	34	249	277	plastic plate	saline water

* Time period over which the mud was poured from the container

** Temperature of the surface before the release of the mud from the flipping container

*** Temperature of the mud within the container before the pressure drop

**** Saline water refers to a mixture of water that contains 0.5% w/w dissolved magnesium sulphate ($MgSO_4$)

was also monitored by another thermocouple. Additionally, five thermocouples were set in a grid (see Fig. 48 for details about the positioning of thermocouples) within the tray in order to monitor the temperature of the surface over which the mud propagated.

Once the tray was in place inside the chamber, a series of images were taken by a single-lens reflex camera from different angles to obtain the digital elevation model of the pristine surface before the experimental ran. Subsequently the chamber was closed and the process of depressurization started. To achieve the pressure drop from ambient terrestrial pressure to 7 mbar took usually around 6 minutes. Once the pressure started to drop, the decrease in the temperature of the mud within the container was measured. Every time the mud self-cooled close to 273 K during the pressure drop, but it remained liquid. When the pressure of $\sim$ 7 mbar was reached, the container was manually flipped by the operator and hence mud was poured from the height of $\sim$ 5 cm to the surface.

The movement of the mud over the surface was recorded by four video cameras. Once the mud propagation stopped, the resulting mud flow feature was left in the low pressure environment for various lengths of time ranging from several minutes to about one hour. After that the process of re-pressurization of the chamber to terrestrial values started, typically before temperature of the tray surface rose above $\sim$ 273 K. Once the pressure inside the chamber reached atmospheric pressure, the chamber

was opened and the resulting flow features were documented by taking images from different angles to acquire data for subsequent DEM production. Ultimately the mud flows produced were sectioned and their inner structure was investigated and documented.

5.3.1 DEM calculation

To compare the elevation profiles along and perpendicular to the flow directions of the mud flows we calculated a series of digital elevation models (DEM). The sedimentary bed was photographed after each experimental procedure $\sim 30 - 70$ times from multiple viewpoints. The reconstruction of a 3D model surface was produced by using the 'Structure-from-Motion' (Westoby et al., 2012) commercial software Agisoft PhotoScan. For image orientation correlation and scaling of the 3D models we used twelve fixed black-on-white printed markers which were affixed onto flat topped cylindrical posts. The posts had two different elevations (4.6 cm and 9.6 cm) and the markers were ~ 2.67 cm in diameter. Typical discrepancies between actual and calculated marker positions were $\sim 0.8 - 1.6$ mm. Exported DEMs and orthophotos (TIFF format) were imported to QGIS for further analysis and production of the elevation profiles.

5.4 Results and discussion

We performed 21 experiments (for details see Tab. 12 and Fig. 48) using the *Mars Chambe*r located at the *Open University* (UK). During each experiment 500 ml of low viscosity mud was poured over a 0.9×0.4 m aluminium tray containing either (a) a ~ 2 cm deep sand bed ($\sim 63\check{}200$ μm grain diameter; 14 experiments), or (b) a plastic plate (7 experiments) to resemble icy non-permeable surfaces. Fifteen experiments were performed at a reduced atmospheric pressure of $\sim 7 \pm 0.5$ mbar and six experiments at terrestrial pressure of ~ 1 bar (Tab. 12). The mud was released over the surface from a tilting container situated inside the chamber and manually operated from the outside. This design allowed us to investigate the propagation of mud over the surface rather than the ascent through a conduit and its final extrusion. At the beginning of the experiment the mud inside the container was kept above the freezing point of water. The temperature of the surface of the sand bed or plastic plate ranged from ~ 244 K to 265 K and gradually increased with time as no active cooling of the experiment was performed. The aluminium tray was inclined at 5° (18 experiments) or 10° (3 experiments) to force the mud to move by various velocities. These variations in the experimental parameters allowed us to investigate how the behaviour of the mud was controlled by pressure, temperature, slope angle, and the erodibility of the surface onto which the mud flowed. Each experimental run was performed at least in triplicate and was recorded with four cameras. The experiments inevitably neglected the effect of the reduced gravity which would be present on Mars.

At the beginning of each experiment the atmospheric pressure was gradually reduced, thus triggering the boiling of the water in the mud because of its instability in the low pressure environment (Bargery et al., 2010; Raack et al., 2017). This resulted in the ejection of particles outside the container due to bursting mud bubbles. The boiling intensified as the pressure approached $12-14$ mbar and remained intense down to $\sim$ 7 mbar. During the pressure decrease the temperature of the mud decreased due to evaporative cooling (Bargery et al., 2010) and hence the mud within the container self-cooled closer to its freezing point before it was poured onto the surface, occurring when the pressure reached $\sim 7 \pm 0.5$ mbar (Tab. 12). Once in contact with the cold surface, the mud rapidly began to freeze at the bottom and edges of the flow, and at the flow upper surface (Fig. 49a or associated movies linked in the Supplementary Information). The freezing resulted in the formation of an ice-mud crust which modified the propagation, hampering the ability of the flow to spread laterally (Fig. 50).

Mud propagation occurred through an intricate system of narrow flow lobes (Fig. 50b) or several lobate flows (Fig. 50c) which developed positive topography (Fig. 50d). The formation of these lobes was controlled by the development of frozen marginal ridges that confined the flow of the liquid mud inside a central channel. With time as freezing continued, icy crystals floated to the surface and started to merge together. However, mud still propagated within the crust via a network of "mud tubes", in an analogous way to lava tubes (Fig. 49c). When new mud batches arrived at the flow front or the central part of a flow, they caused breakouts and the formation of further lobes (Fig. 49b). The newly extruded material rapidly developed a frozen crust on exposure to the ambient environment. This process repeated itself as long as the system provided more liquid mud such that enough internal pressure was maintained to breach the previously-formed crust.

The presence of internal mud tubes was confirmed by sectioning the frozen mud flows after the re-pressurization of the chamber. A liquid mud core was present in the interiors of the lobes – even in the experiments where mud was exposed to low pressure for several tens of minutes (Fig. 49d, e). Vesicles ranging in size from 1 to 10 mm were observed within the crusts (Fig. 49d). These vesicles appear to have been formed by vapour bubbles that did not escape from the interior of the flow, and the vesicular nature of the crust probably reduced its ability to conduct heat (Smith et al., 2013).

During flow formation, newly supplied mud was observed to increase the thickness of lobes by up to several centimetres (Fig. 50d) by lifting the protective crust. This occurred when the terminal part of the flow was frozen and the mud release was blocked, but newly supplied mud was still intruding the lobe via mud tubes. This created overpressure within the mud which was able to vertically lift the crust of the lobes. Once a sufficient volume of the mud had accumulated within the lobe, the overpressure of mud was able to break the crust at the terminal part of the lobe and a new lobe formed. The mud flow was hence inflating in a manner analogous to

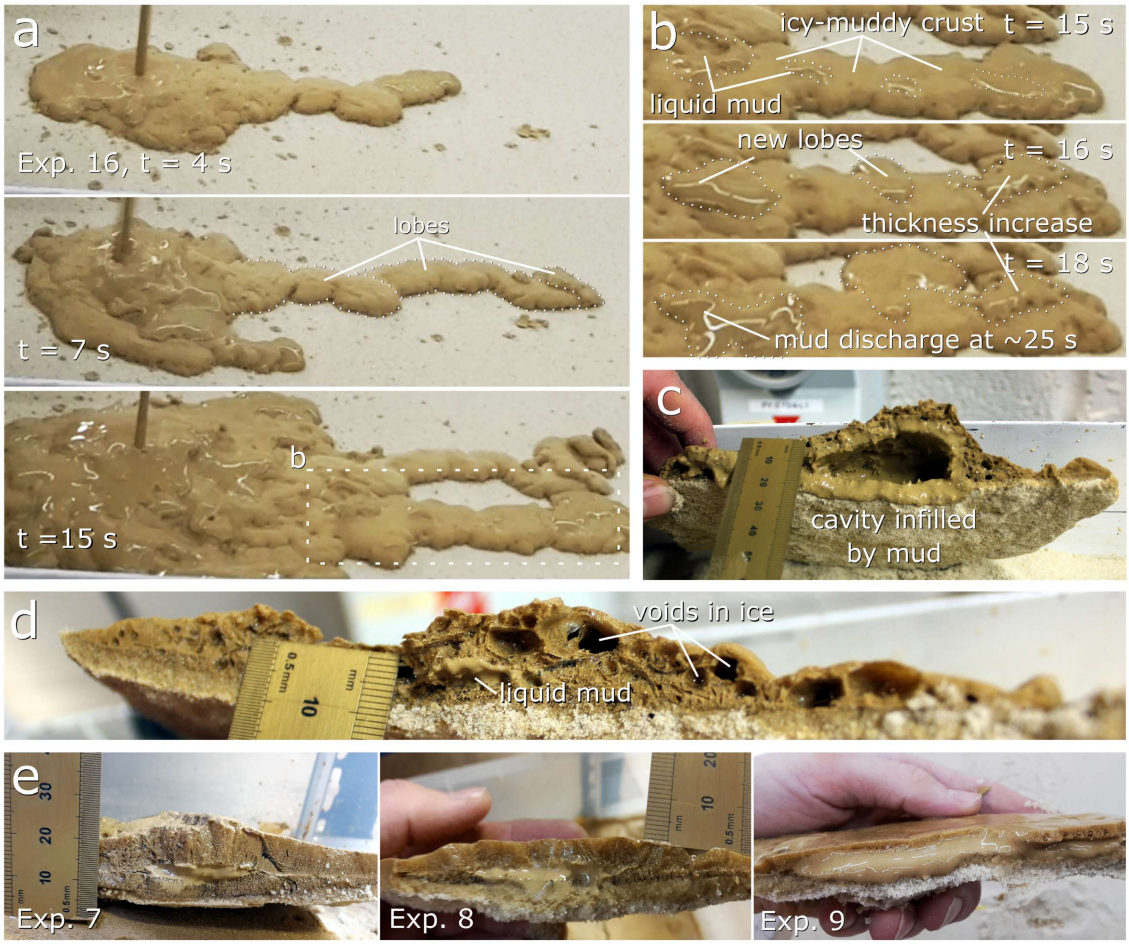


Fig. 49: Example of the development of a mud flow in a low-pressure environment (panels a, b) and details of their interior structure, sampled once the chamber was re-pressurized (c, d, e). Panel a shows three frames from video taken by Cam #2 covering experiment #16 in which the formation of a narrow, thick mud flow occurred. Panel b shows in detail the formation of the icy crust and several outbreaks of new mud batches from beneath the crust. Once the resulting mud flow features were sectioned, large cavities filled with liquid mud (c), or voids in the ice were observed. A liquid mud core was commonly observed in the flow interior (e).

that of pahoehoe lava flows (Hon et al., 1994). Flow thickening was also observed on shallow slopes and when the inclination was increased to 10°, and occurred whether the substrate was unconsolidated sand or plastic board. Comparative experiments performed under terrestrial conditions (i.e. room pressure and temperature) revealed that the mud flow moving over a cold surface under ambient pressure did not form lobes, did not inflate, and had no icy crust (Fig. 50d) regardless of the temperature of the mud poured onto the cold surface (tested for mud with temperatures of $\sim$ 274, $\sim$ 290, and $\sim$ 293 K). Instead the mud spread out over the sand in a broad sheet only a few millimetres thick which was in the liquid phase over the entire length of the flow (Fig. 50a, d). Only minor freezing was observed in the form of icy crystals on the margins of the flow after several minutes.

In a similar manner to basaltic lavas on Earth, the low viscosity mud flows produce laterally extensive structures with lower relief than those resulting from high viscosity flows (Mazzini and Etiope, 2017). Because the mud used in our experiments is water-dominated with a solid fraction less than $\sim$ 6.5% of the mud mass, it is initially behaving as a Newtonian fluid. Our experiments revealed that in the low pressure environment, the instability of water against evaporative cooling changes this behaviour as ice crystals increase the solid content and a protecting crust is formed. The mud therefore now behaves as non-Newtonian fluid with a yield strength. As a consequence, its behaviour is very similar to that of low viscosity basaltic lavas whose movement is also significantly affected by the formation of an external crust, which forms by solidification of the molten rock due to cooling (Cashman et al., 2006). In both cases the strength of the external crust is able to inhibit lateral spreading and allows fluid accumulation and vertical propagation; in other words flow inflation. The resulting thickness to which the flow can inflate is linked to the thickness and strength of the crust.

Calculations of the processes occurring during the cooling and freezing of the mud are reported in the Appendix (5.6.1). Through time, the volume of remaining water – which was not lost by evaporation – had been frozen to ice in the crust, and hence by definition only the solid content was within the crust. Thus, during the freezing process, the thin crust layer must have developed an ever-increasing yield strength simply due to the presence of solids in the liquid (see rheology references in (Chevrel et al., 2014)). At some point the ice crystal snetwork must have become continuously interconnected between the clay particles and a mechanical strength similar to that between the mineral crystals of a silicate rock would have replaced the rheological yield strength. Thus the strength of the crust would have increased with time, preventing breakout unless the internal pressure became large enough, but likely requiring greater inflation before breakout in the distal parts of the compound flow fields, as was observed. There is no reason to assume that the mechanical strength of the crust would be different on Mars for mud with the same clay content. Since the rate, as well as the mode, of its formation are controlled by the non-equilibrium thermodynamics of vapour loss, specifically the transfer of sensible heat to latent heat in the liquid surrounding each nucleating vapour bubble (Bargery et al., 2010),

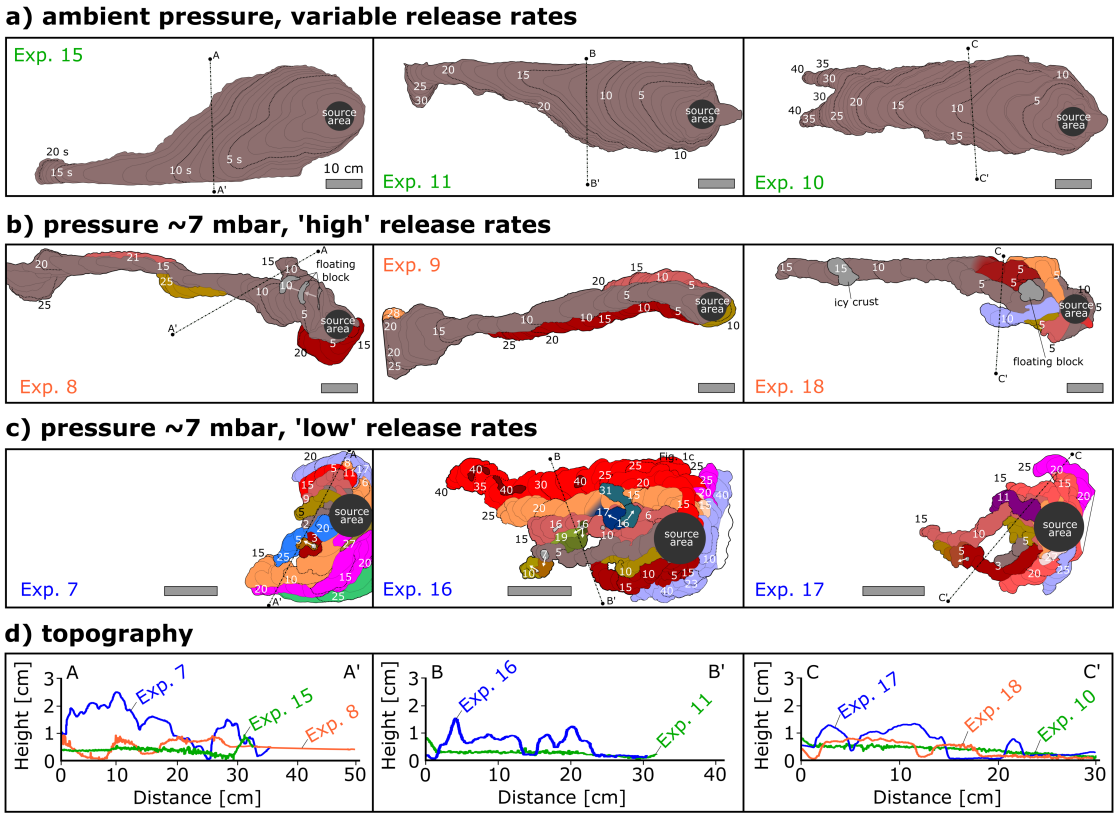


Fig. 50: Timeline maps derived from the videos summarising the progression of 9 selected experiments in which 500 ml low viscosity mud was poured onto a cold sand surface inclined at 5° in terrestrial (a) and low pressure environments (b,c). Panel (b) shows experiments with high release rates and panel (c) those with low release rates. The numbered bold lines in panels a, b, and c represent the margins of the flows at 5 s intervals, the other lines are 1 s intervals. Panel (d) shows the topographic cross sections of the final mud flow structures measured after the chamber was re-pressurized. The position of each topographic profile is marked in panels a, b and c. Experiments revealed that when mud moves under terrestrial pressure a broad, mm-thick flow formed and was liquid throughout. In a low pressure environment, a narrow and thick flow formed in which the mud propagated from the source area to the flow margins via mud tubes.

the time scale of crust development should also be the same on Mars. The spatial scales of inflation from lobe breakouts will then be determined mainly by the flow speed of the mud, and this will be determined by the thickness of the mud, the ground slope, and the rheology of the mud in the same way that the spatial scales of silicate lava flows are determined. The above arguments assume that, as in the experiments, the motion of the mud is laminar. However, it is inevitable that on a large enough spatial scale the Reynolds number of the mud motion will be so large that the fluid motion is turbulent. For mud viscosities of 0.01, 0.1, 1 and 10 Pa.s on 0.6° slopes under martian gravity, the transition to turbulence will occur for mud flows with thicknesses of 17 mm, 8 cm, 36 cm and 1.7 m, respectively (see equations in Wilson and Mouginis-Mark, 2014). Thus any mud flow thicker than $\sim$ 1 metre on Mars is likely to be turbulent.

The present experimental system is not large enough to simulate such conditions directly but reveals an important point. In a model of mud flow dynamics on Mars, Wilson and Mouginis-Mark (2014) considered the effects of high solid contents on the non-Newtonian rheology of mud, but they assumed that those rheological properties were constant everywhere along the flow. The present experiments underlines the vital importance of considering the thermodynamics of the processes that are likely to occur when mud is exposed to the martian environment. Specifically, if a mud flow is turbulent, then mud from all depths within the flow will be exposed to the low pressures near the surface of the flow and will have the opportunity to boil, lose vapour, and cool. Thus the initial cooling rate of the whole of the flow, not just a surface skin, will be large, and as long as the flow remains turbulent it will cool and eventually evolve a non-Newtonian rheology. At some point this will force a transition to laminar flow, but the bulk viscosity of the mud will now be much larger than that of the mud in the core of a laminar flow, with complex implications for the formation of lobes and breakouts.

5.5 Conclusions

These findings have important implications for the interpretation of flow morphologies at the martian surface (Fig. 51). Our results show that both igneous and mud volcanism can produce surface expressions which share morphological characteristics (e.g. Wilson and Mouginis-Mark, 2014; Brož et al., 2019). This would make it very difficult to distinguish between them based on currently available remote sensing data (Wilson and Mouginis-Mark, 2014). This is because inflation of decimetre-thick lobes could occur both at the edges of mud flows and lava flows. Our numerical modelling shows that the morphologies of mud flows at scales larger than those covered by our experiments could be affected by the same processes. Hence martian mud volcanoes may differ substantially in shape from their terrestrial counterparts (Brož et al., 2019). Additionally, sedimentary volcanism has also been proposed for the dwarf planet Ceres (Sori, 2017; Ruesch et al., 2019) which may have

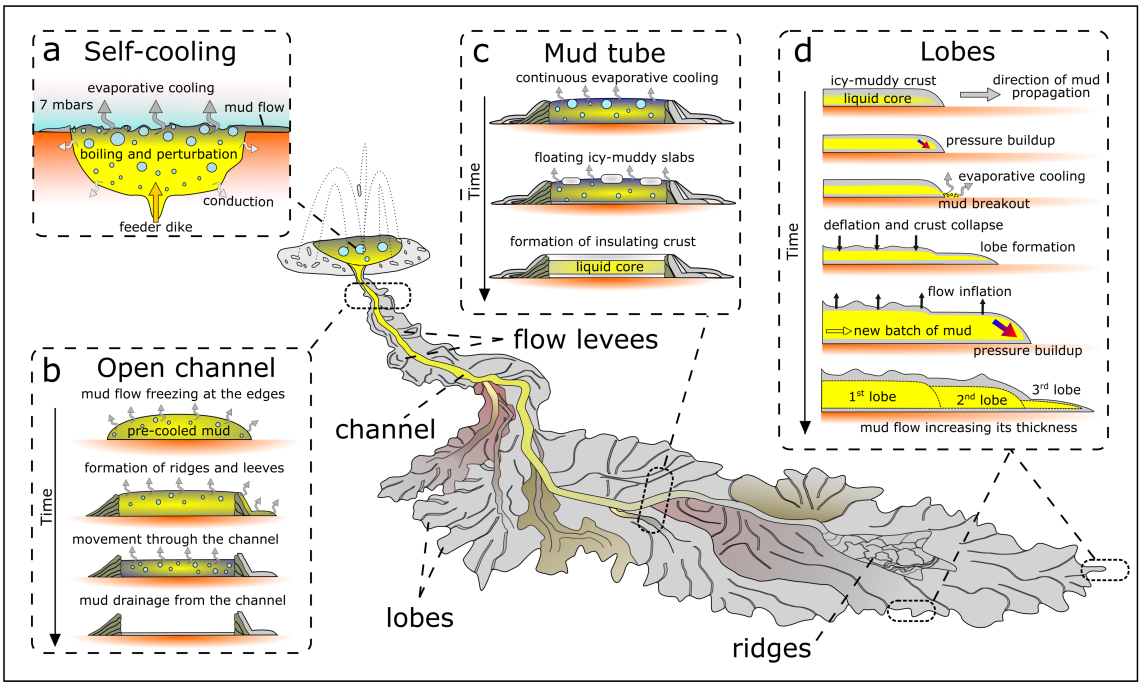


Fig. 51: (a) The ascending mud would self-cool through evaporative cooling once it reaches the surface. The instability of water leads to boiling and hence perturbation of the mud by exiting gas bubbles capable to fragment the mud. (b) Once enough material is extruded, the mud flow would develop. Close to the vent the mud would move through a relatively narrow open channel which would arise from freezing at the edges of the flow forming confining ridges (levees). The ridges may be overrun by mud and hence short flows would form. Once the mud source is depleted, an empty channel would be formed. (c) As the flow continues ice crystals would start to form within the flow which would float to the surface, then coalesce as freezing progresses. An insulating crust would then form on top of the flow inhibiting the process of the evaporative cooling. The mud would continue to move within an isolated mud tube. (d) Mud would be transported via mud tubes to the flow front where mud would be spreading by lobes. The icy-muddy crust prevents the mud from freely moving over the surface so continued input of new material increases the pressure inside the lobe. Eventually, the pressure is large enough to break the icy-muddy crust or to lift the crust up, and hence to release the mud and expose it to the martian environment and hence trigger evaporative cooling again.

a water-muddy ocean beneath a crust made of clays, salts, clathrates and ice (Ruesch et al., 2019; Marchi et al., 2018). The process of evaporative cooling and associated freezing should also occur there, effecting morphologies of resulting effusive features; probably even more on Ceres than on Mars as Ceres lacks an atmosphere. This is because once cryomagma, a solid-liquid mixture, reaches the surface of Ceres, water would be unstable and start to evaporate or freeze or both (Ruesch et al., 2019). The same principles would be applicable for other small bodies and icy moons elsewhere within the Solar system where effusive cryovolcanism has been postulated, and so our experimental results should be considered when interpreting possible effusive cryovolcanic surface features on these bodies (e.g. Allison and Clifford, 1987; Fagents, 2003). Our results highlight that it is critical to consider the effects of the differing environmental conditions on other planetary surfaces when comparing analogue landforms observed on Earth with apparently similar effusive morphologies on other bodies.

5.6 Appendix

5.6.1 Cooling and freezing of mud when the external pressure is less than the saturation vapour pressure of the water.

Both the silicate component and the water that has not yet vaporized will cool from the initial temperature until the freezing point is reached. After the freezing point is reached, the temperature remains constant and vapour continues to be lost until all of the remaining water has been converted to ice. If the external pressure is less than the saturation vapour pressure of the ice, evaporation continues, the frozen mud surface cools, and a wave of cooling propagates into the frozen mud. The bulk density of the mud changes continuously throughout these stages as a function of the initial mass fractions of silicate and water in the mud. Let the initial masses of water and silicate in a given sample of the mud be m_w and m_s, respectively, the volumes of water and solid be v_w and v_s, respectively, and the corresponding densities be ρ_w and ρ_s Let the bulk density of the mud be β. Then

$$\beta = \frac{(m_w + m_s)}{(v_w + v_s)} = \frac{(m_w + m_s)}{[(m_w/\rho_w) + (m_s/\rho_s)]}. \tag{5.1}$$

Expanding, collecting terms and simplifying:

$$\frac{m_w}{m_s} = (\frac{\rho_w}{\rho_s})\frac{(\rho_s - \beta)}{(\beta - \rho_w)}. \tag{5.2}$$

We next find the mass of vapour, M_{vc}, that must be lost from the water to cool the remaining water and silicate to any given lower temperature. Let the initial mud

temperature be θ_i and the final temperature be θ_f. The heat H_v removed from the water by the formation of the vapour is

$$H_v = M_{vc} L_v, \tag{5.3}$$

where L_v is the latent heat of vapourization, 2.46×10^6 J kg^{-1}. During this cooling process, the liquid water mass decreases from its initial value m_w to a smaller final value m_f, where by definition

$$m_f = m_w - M_{vc}. \tag{5.4}$$

Thus, the average mass of water, m_a, during the cooling process is

$$m_a = 0.5(m_w + m_f) = 0.5(m_w + m_w - M_{vc}) = (m_w - 0.5 M_{vc}). \tag{5.5}$$

As long as the specific heat of the water can be approximated as a constant, the heat the water loses while cooling is H_c where

$$H_c = m_s C_s (\theta_i - \theta_f). \tag{5.6}$$

and C_w is the specific heat of water, 4186 J kg^{-1} K^{-1}. The silicate mass ms also cools, and loses an amount of heat equal to H_s where

$$H_s = m_s C_s (\theta_i - \theta_f). \tag{5.7}$$

Here C_s is the specific heat of the silicate, say 1000 J kg^{-1} K^{-1}. Equating the sum of H_c and H_s to H_v,

$$(m_w - 0.5 M_{vc}) C_w (\theta_i - \theta_f) + m_s C_s (\theta_i - \theta_f) = M_{vc} H_v \tag{5.8}$$

and regrouping,

$$M_{vc}[H_v + 0.5 C_w (\theta_i - \theta_f)] = (m_w C_w + m_s C_s)(\theta_i - \theta_f) \tag{5.9}$$

or

$$\frac{M_{vc}}{m_s} = \{[(m_w/m_s) C_w + C_s](\theta_i - \theta_f)\} / [H_v + 0.5 C_w (\theta_i - \theta_f)]. \tag{5.10}$$

Using equation (5.2) for (m_w/m_s) we can also find (M_{vc}/m_s) as a function of the assumed value of ρ_s. Finally, the ratio, R, of the mass of water converted to vapour to the initial water mass, i.e. $R = (M_{vc}/m_w)$, is equal to $[(M_{vc}/m_s)(m_s/m_w)]$ or more conveniently

$$R = \frac{(M_{vc}/m_s)}{(m_w/m_s)}. \tag{5.11}$$

The mass of water remaining in the mud after the cooling phase, m_f, is therefore

$$m_f = (1 - R)m_w. \tag{5.12}$$

The above equations apply between any pair of temperatures θ_i and θ_f until θ_f becomes equal to the freezing point, θ_{fr}. After the freezing point is reached, the temperature remains constant while liquid water continues to evaporate and the latent heat of vaporization is extracted from the remaining water, progressively freezing into ice all of the water that is not lost as vapour. The latent heat of vaporization in the $10 - 20$ Kelvin range is 2.46×10^6 J kg^{-1} and the latent heat of solidification is 3.34×10^5 J kg^{-1}. The ratio of these is $Q = (3.34 \times 10^5/2.46 \times 1^6) = 0.13577$. Thus, to freeze 1 kg of liquid water to ice we would have to evaporate 0.13577 kg of water into vapour from an initial total mass of 1.13577 kg of water. A fraction $[Q/(1 + Q)]$ of the water mass remaining after cooling must become vapour and a fraction $[1/(1 + Q)]$ of the water mass remaining after cooling becomes ice. The final ice mass, m_i, is

$$m_i = [1/(1 + Q)][(1 - R)m_w] \tag{5.13}$$

and the mass of water converted to vapour during the freezing phase is M_{vf} where

$$M_{vf} = [Q/(1 + Q)](1 - R)m_w. \tag{5.14}$$

The total mass of vapour generated by the whole process is $M_v = M_{vc} + M_{vf}$.

As a result of the loss of vapour, the bulk density of the frozen mud will be different from the density of the initial mixture. The ice has a density ρ_i of 916.8 kg m^{-3} so the mass m_i of ice has a volume of $v_i = (m_i/\rho_i$. The silicate volume is still vs and so the final bulk density is β_f where

$$\beta_f = \frac{(m_i + m_s)}{(v_i + v_s)} = \frac{(m_i + m_s)}{[(m_i/\rho_i) + (m_s/\rho_s)]}. \tag{5.15}$$

Equation (5.12) gives (m_i/m_w) and equation (5.2) gives (m_w/m_s) so in terms of these,

$$\beta_f = [(m_i/m_w)(m_w + m_s)^{-1}]/\left\{[(m_i/m_w)/\rho_i] + [\rho_s(m_w/m_s)]^{-1}\right\}. \quad (5.16)$$

The density, ρ_s, of the clay minerals in the experimental mud was ~ 2500 kg m^{-3} and the bulk density of the mud was ~ 1040 kg m^{-3}, implying that the clay component formed $\sim 6.5\%$ of the mud mass. The mud was released into ambient experimental chamber pressures in the range $650-700$ Pa, and initial mud temperatures were up to ~ 275.5 K. Taking account of the weight of the overlying mud and the experimental chamber pressure, the saturation vapour pressure of water, with values up to ~ 730 Pa (Lide, 2004), would have been reached at depths up to $5-6$ mm in the experiments. The relative values of the specific heat and the latent heat of evaporation of water are such that while the mud was cooling from ~ 275.5 K to its freezing point, $\sim 0.34\%$ of its water would have been lost, having a trivially small effect on its essentially Newtonian rheology. By the time subsequent vapour loss had frozen the remaining water, $\sim 88\%$ of the initial mass of water would have been converted to ice at the expense of losing $\sim 12\%$ of the initial water mass as vapour, leaving solid mud with a density of ~ 961 kg m^{-3}, slightly less dense than the original liquid mud. This should have produced a frozen crust, again of thickness $5-6$ mm, beneath which the mud would have been partially liquid, as observed in the experiments. In similar scale flows under martian gravity, the thermodynamics of this process would have been the same, as it involves only heat transfer by conduction, but the thickness of the frozen outer crust would have been greater, $14-17$ mm, because the pressure in the mud depends on the acceleration due to gravity.

5.7 Acknowledgements

The access to the Mars Chamber at the Open University was provided by Europlanet 2020 RI which has received funding from the European Union's Horizon 2020 research and innovation program under grant agreement No 654208. LW was supported by the Leverhulme Trust through an Emeritus Fellowship. OK was supported by Center for Geosphere Dynamics (Faculty of Science at Charles University) project UNCE/SCI/006. AM was funded by the ERC grant agreement 308126 (LUSI LAB) and the Research Council of Norway (Centers of Excellence funding scheme, project 223272). The authors thank Steve Lane and Ondřej Čadek for valuable discussions.

5.8 Author contribution

The experimental set-up and the methodology was conceived and designed by P.B. and O.K. with the help and advice of S.J.C., J.R., M.R.P., M.R.B., A.M., and

E.H. The technical support was provided by M.R.S. The data analysis was done by P.B. with significant feedback from O.K., L.W., S.J.C., E.H. and A.M. The DEM production was done by O.K. and the theoretical considerations associated with scaling were done by L.W. All authors contributed to discussion, interpretation and writing of the manuscript.

5.9 Data availability

The movies and temperature and pressure data that support the findings of this study are available in Zenodo with the identifier 3457148 [https://doi.org/10.5281/zenodo.3457148]. These materials, which are now restricted from being view publicly, can be downloaded and viewed by using this link: https://zenodo.org/record/3457148?token=eyJhbGciOiJIUzUxMiIsImV4cCI6MTU3MTY5NTE5OSwiaWF0IjoxNTY5MDkzNDAx
eyJkYXRhIjp7InJlY2lkIjozNDU3MTQ4fSwiaWQiOjQxMzEsInJuZCI6ImFlMjM4ODY3In0.
26aX16mbbLTTzAeIwWKMWqoPAY7sXwaaiZFEVund254uIjqmA1M3v7623ib3j_F6bpNGqai5Xhzt3xzpBBt8-
(file has around 20 GB).

5.10 References

Allison, M. L. and Clifford, S. M. (1987). Ice-covered water volcanism on Ganymede, J. Geophys. Res., 92, 7865– 7876.

Bargery, A. S., Lane, S. J., Barrett, A., Wilson, L., and Gilbert, J. S. (2010). The initial responses of hot liquid water released under low atmospheric pressures: Experimental insights. Icarus, 210(1), 488–506, https://doi.org/10.1016/j.icarus.2010.06.019

Brož, P., Hauber, E., van de Burgt, I., Špillar, V., and Michael, G. (2019). Subsurface sediment mobilization in the southern Chryse Planitia on Mars. Journal of Geophysical Research: Planets, 124. https://doi.org/10.1029/2018JE005868

Brož, P., Hauber, E., Wray, J. J., and Michael, G. (2017). Amazonian volcanism inside Valles Marineris on Mars. Earth and Planetary Science Letters, 473, 122–130. https://doi.org/10.1016/j.epsl.2017.06.003

Brož, P., Čadek, O., Hauber, E., and Rossi, A. P. (2015). Scoria cones on Mars: Detailed investigation of morphometry based on high-resolution digital elevation models. Journal of Geophysical Research: Planets, 120, 1512–1527. https://doi.org/10.1002/2015JE004873

Brož, P., and Hauber, E. (2013). Hydrovolcanic tuff rings and cones as indicators for phreatomagmatic explosive eruptions on Mars. Journal of Geophysical

Research: Planets, 118, 1656–1675. https://doi.org/10.1002/jgre.20120

Cashman, K. V., Kerr, R. C., and Griffiths, R. W. (2006). A laboratory model of surface crust formation and disruption on lava flows through non-uniform channels. Bulletin of Volcanology, 68(7-8), 753-770.

Chevrel M. O., Baratoux, D., Hess, K.-U., Dingwell, D. B. (2014). Viscous flow behavior of tholeiitic and alkaline Fe-rich martian basalts. Geochimica et Cosmochimica Acta, 124, 348–365.

Clark, B. C. (1978). Implications of abundant hygroscopic minerals in the martian regolith. Icarus 34, 645–665.

Corradi, A. B., Manfredini T., Pellacani, G. C. and Pozzi, P. (1994), Deflocculation of Concentrated Aqueous Clay Suspensions with Sodium Polymethacrylates, Journal of the American Ceramic Society 77, Issue 2. https://doi.org/10.1111/j.1151-2916.1994.tb07022.x.

Fagents, S.A. (2003). Considerations for effusive cryovolcanism on Europa: The post-Galileo perspective. J. Geophys. Res.-Planets 108 (E12), 5139.

Fagents, S. A, Gregg, T. K. P., and Lopes, R. M. C. (2013). Modelling volcanic processes: the physics and mathematics of volcanism, pp. 421, Cambridge University Press, Cambridge, ISBN: 9781139021562.

Formisano, V., Atreya, S., Encrenaz, T., Ignatiev, N., and Giuranna, M. (2004). Detection of methane in the atmosphere of Mars. Science, 306(5702), 1758–1761. https://doi.org/10.1126/science.1101732

Hecht, M. H., et al. (2009), Detection of perchlorate and the soluble chemistry of martian soil at the Phoenix lander site, Science, 325, 64– 67.

Hecht, M. H. (2002). Metastability of liquid water on Mars. Icarus, 156(2), 373–386. https://doi.org/10.1006/icar.2001.6794

Hon, K., Kauahikaua, J., Denlinger, R., Mackay, K., 1994. Emplacement and inflation of pahoehoe sheet flows: observation and measurements of active lava flows on Kilauea Volcano, Hawaii. Geol. Soc. Am. Bull.106, 351–370.

Komatsu, G., Okubo, C. H., Wray, J. J., Ojha, L., Cardinale, M., Murana, A., et al. (2016). Small edifice features in Chryse Planitia, Mars: Assessment of a mud volcano hypothesis. Icarus, 268, 56–75. https://doi.org/10.1016/j.icarus.2015.12.032

Lide, D. R. (ed.) (2004). CRC Handbook of Chemistry and Physics (85th edition), CRC Press.

Marchi, S., Raponi, A., Prettyman, T., De Sanctis, M. C., Castillo-Rogez, J., Raymond, C., et al. (2018). An aqueously altered carbon-rich Ceres. Nature Astronomy, 3, 140–145. https://doi.org/10.1038/s41550-018-0656-0

Mazzini, A., and Etiope, G. (2017). Mud volcanism: An updated review. Earth-Science Reviews, 168, 81–112. https://doi.org/10.1016/j.earscirev.2017.03.001

Mumma, M. J., Villanueva, G. L., Novak, R. E., Hewagame, T., Bonev, B. P., DiSanti, M. A., et al. (2009). Strong release of methane on Mars in northern summer 2003. Science, 323(5917), 1041–1045. https://doi.org/10.1126/science.1165243

Oehler, D. Z., and Etiope, G. (2017). Methane seepage on Mars: Where to look and why. Astrobiology, 17(12), 1233–1264. https://doi.org/10.1089/ast.2017.1657

Okubo, C. H. (2016). Morphologic evidence of subsurface sediment mobilization and mud volcanism in candor and Coprates Chasmata, Valles Marineris, Mars. Icarus, 269, 23–37. https://doi.org/10.1016/j.icarus.2015.12.051

Parfitt, E. A., and Wilson L. (2008), Fundamentals of Physical Volcanology, 256 pp., Blackwell, Oxford, U. K., ISBN: 978-0-632-05443-5

Platz, T., Byrne, P. K., Massironi, M. and Hiesinger, H. (2014). Volcanism and tectonism across the inner solar system: an overview. Geol. Soc. Lond. Spec. Publ. 401, 1–56.

Raack, J., Conway, S. J., Herny, C., Balme, M. R., Carpy, S., and Patel, M. R. (2017). Water-induced sediment levitation enhances downslope transport on Mars, Nature Communications 8. https://doi.org/10.1038/s41467-017-01213-z

Ruesch, O., Genova A., Neumann W., Quick L. C., Castillo-Rogez J. C., Raymond C. A., Russel Ch. T., and Zuber, M. T. (2019). Slurry extrusion on Ceres from a convective mud-bearing mantle. Nature Geoscience, 12, 505-509. https://doi.org/10.1038/s41561-019-0378-7

Skinner, J. A., and Tanaka, K. L. (2007). Evidence for and implications of sedimentary diapirism and mud volcanism in the southern Utopia highland-lowland boundary plain, Mars. Icarus, 186(1), 41–59. https://doi.org/10.1016/j.icarus.2006.08.013

Smith, D., Alzina, A., Bourret, J., Nait-Ali, B., Pennec, F., Tessier-Doyen, N., Otsu, K., Matsubara, H.,.Elser, P., Gonzenbach, U. (2013). Thermal conductivity of porous materials. Journal of Materials Research, 28(17), 2260-2272. https://doi.org/10.1557/jmr.2013.179

Sori, M. M. et al. (2017). The vanishing cryovolcanoes of Ceres. Geophys. Res. Lett. 44, 1243–1250.

Vaniman, D. T., Bish, D. L. , Chipewa, S. J. , Fialips, C. I. , Carrey, J. W. and Feldman, W. C. (2004). Magnesium sulphate salts and the history of water on Mars, Nature, 431, 663– 665.

Westoby, M. J., Brasington, J., Glasser, N. F., Hambrey, M. J. and Reynolds, J. M. (2012). 'Structure-from-motion' photogrammetry: a low-cost, effective tool for geoscience applications. Geomorphology 179, 300–314.

Wilson, L., and Mouginis-Mark, P. J. (2014). Dynamics of a fluid flow on Mars: Lava or mud? Icarus, 233, 268–280. https://doi.org/10.1016/j.icarus.2014.01.041

Wilson, L., and Head, J. W. (1994). Review and analysis of volcanic eruption theory and relationships to observed landforms. Reviews of Geophysics, 32(3), 221–263. https://doi.org/10.1029/94RG01113

6 Mud Flow Levitation on Mars: Insights from Laboratory Simulations

Petr Brož, **Ondřej Krýza**, S. J. Conway, N. T. Mueller, E. Hauber, A. Mazzini, J. Raack, M.R. Patel, M.R. Balme, and M.E. Sylvest

6.1 Abstract

Sediment mobilisation occurring at depth and ultimately manifesting at the surface, is a process which may have operated on Mars. However the propagation behaviour of this mixture of water and sediments (hereafter simply referred to as mud) over the martian surface, remains uncertain. Although most of the martian surface is below freezing today, locally warmer surface temperatures do occur, and our current knowledge suggests that similar conditions prevailed in the recent past. Here, we present the results of experiments performed inside a low pressure chamber to investigate mud propagation over a warm (295 K) unconsolidated sand surface under martian atmospheric pressure conditions (7 mbar). Results show that the mud boils while flowing over the warm surface. The gas released during this process can displace the underlying sand particles and hence erode part of the substrate. This "entrenched" flow can act as a platform for further mud propagation over the surface. The escaping gas causes intermittent levitation of the mud resulting in enhanced flow rates. The mud flow morphologies produced by these phenomena differ from those produced when mud flows over a frozen martian surface as well as from their terrestrial counterparts. The intense boiling removes the latent heat both from the mud and the subsurface, meaning that the mud flow would eventually start to freeze and hence changing again the way it propagates. The diverse morphology expressed by our experimental mudflows implies that caution should be exercised when interpreting flow features on the surface of Mars and other celestial bodies.

6.2 Introduction

The surface of Mars is characterized by features of various shapes ranging from decimetres to kilometres scale whose origin has been attributed to the action of sedimentary volcanism (e.g., Allen et al., 2013; Hemmi and Miyamoto, 2018; Oehler and Allen, 2012; Pondrelli et al., 2011; Salvatore and Christensen, 2015; Skinner and Mazzini, 2009; Skinner and Tanaka, 2007; Okubo, 2016; Komatsu et al., 2016; Rubin et al., 2017; Brož et al., 2019, Wheatley et al., 2019; Kumar et al., 2019). However, such interpretation is not unanimous, since igneous volcanism has also been proposed as a formation mechanism for several of these features (e.g. Brož and Hauber, 2013; Brož et al., 2017). Regardless of this ambiguity, if sedimentary volcanism (Oehler and Etiope, 2017) has ever been present on Mars, the mud would propagate in an

environment significantly different from the terrestrial one, in particular with respect to atmospheric pressure and gravity.

Until recently it has remained unclear as to whether such different environmental properties would allow the mud to propagate over the martian surface. This uncertainty was related to the fact that the martian low-pressure environment inhibits the sustained presence of liquid water on the planet's surface (e.g., Bargery et al., 2010; Hecht, 2002). Previous studies have shown that water would boil and this would significantly affect the transportation of particles (Conway et al., 2011; Massé et al., 2016; Raack et al., 2017; Herny et al., 2018). This suggests that the different environmental conditions on Mars may have profound effects on mud rheology and hence mud propagation on Mars may vary from our terrestrial experience.

While the behaviour of mud during the emplacement and its rheology under terrestrial conditions is well studied and understood (e.g., O'Brien and Julien, 1988; Laigle and Coussot, 1997 and references therein), this is not the case for Mars nor for other planetary bodies within the Solar System, where sedimentary volcanism has been proposed (e.g., Ruesch et al., 2019). An initial study examining the general behaviour of kilometre-sized mud flows in a low pressure environment was performed by Wilson and Mouginis-Mark (2014), where some aspects of mud propagation over the martian surface were discussed from a theoretical point of view. The authors proposed that the water present in the mud would be unstable and hence evaporate from the mud flow, ultimately removing the latent heat from the mixture. As a consequence, the residual water within mud should freeze in a relatively short period of time, hours to days. Additional insight came from experimental work of Brož et al. (under review) in which the behaviour of low viscosity mud was experimentally studied in a low pressure chamber that partly simulated the environment of Mars. Their work revealed that low viscosity mud flows would actually be able to propagate over a cold (< 273 K) surface under martian atmospheric pressure, however, the mechanism of such propagation would be very different from that observed on Earth. On Mars, mud would rapidly freeze due to evaporative cooling (Bargery et al., 2010) forming an icy-crust leading to the propagation of the decimetre thick mud flows in a similar manner to pahoehoe lava flows on Earth.

The average temperature of the martian surface is today far below the freezing point of water, but thermal infrared observations (e.g. Sinton and Strong, 1960; Kiefer et al., 1977; Christensen et al., 2001) show locally higher temperatures can occur at appropriate locations at favourable seasonal times (Hecht, 2002). This is mainly because the redistribution of solar heat is impeded by the low atmospheric pressure, which limits advective heat transport by the atmosphere, and by the low thermal conductivity of the regolith covering most of the surface (e.g. Presley and Christensen, 1997). Numerical thermal models of the surface have been developed to derive regolith thermophysical properties such as albedo and thermal inertia from the observed temperatures (e.g. Kieffer et al., 1977, Putzig and Mellon, 2007). Conversely, we can use such models and the thermophysical properties to calculate

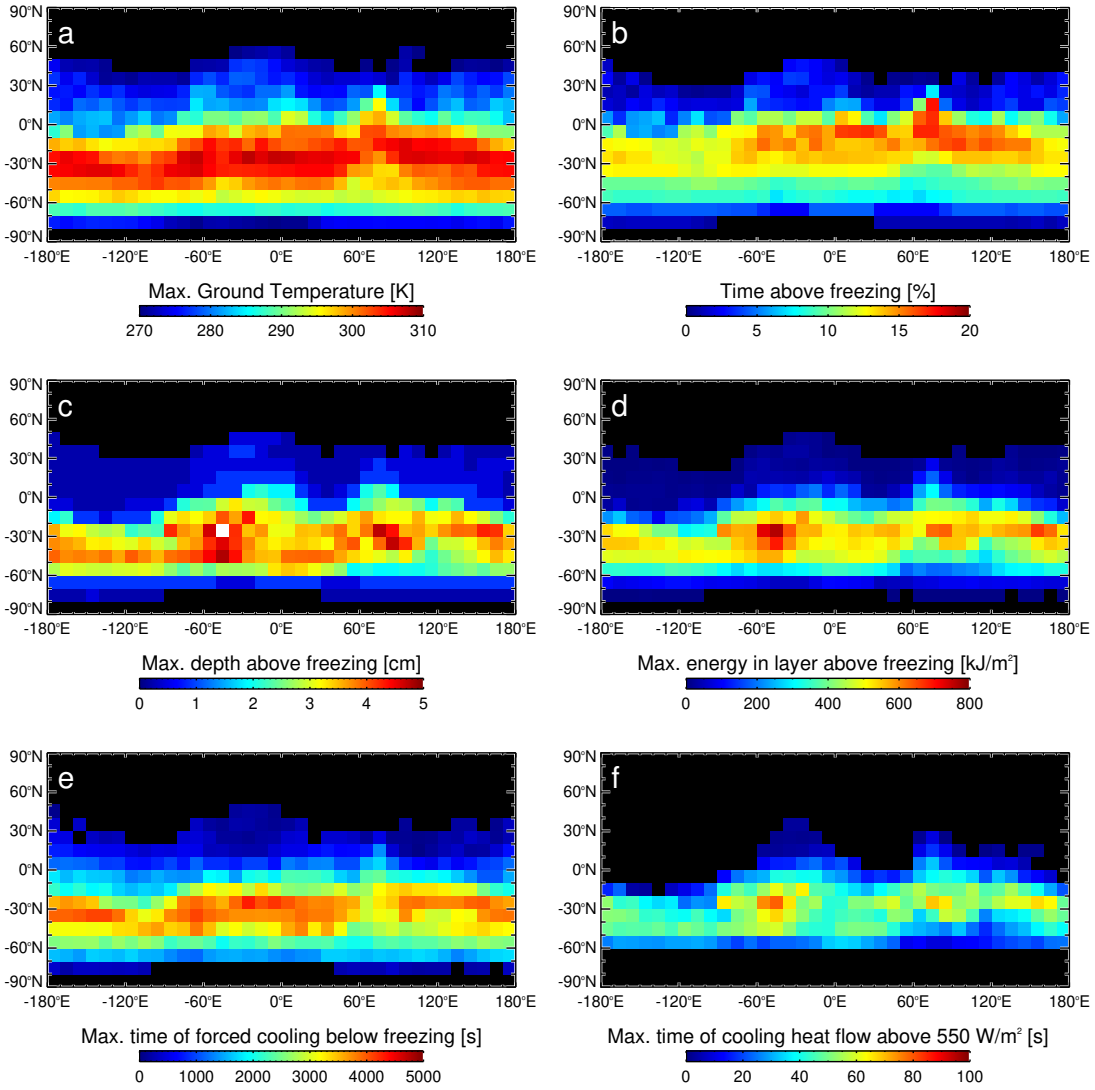


Fig. 52: Results of thermal model calculations described in the Section 6.3.2. Panel a) is the map of the maximum temperature the surface can be expected to attain in an average current martian climate. b) is the total percentage of a Mars Year that the surface is above 273.16 K. c) shows the maximum depth of the layer that experiences temperatures above 273.16 K. d) shows the maximum energy that can be released before the entire surface layer is cooled below 273.16 K. e) shows the time needed to cool the subsurface from the maximum temperature case (a) to below 273.16 K when the substrate top is forced to be at 273.16 K. f) shows the time needed until the heat flow conducted through the surface drops below 550 W/m^2 under the same conditions as in e).

the subsurface temperature structure that is consistent with observed temperatures. The results are shown in Fig. 52 and the details of calculations are described below in Section 6.3.2. The results show that conditions above freezing are not rare on Mars and that some significant amount of heat can be released to potentially keep a mud flow from freezing.

The goal of this manuscript is therefore to investigate the behaviour of low viscosity mud flowing under martian pressure conditions over a warm (from $\sim$ 292 K to $\sim$ 296 K) surface. More specifically, we examine how the instability of water within the mud would change its flow behaviour during the phase change from liquid to gaseous. Hence, we aim to reveal which transport processes would be reasonable to expect during sedimentary volcanism on Mars and how they may affect the final morphology of the resulting mud flows.

6.3 Methods

6.3.1 Experimental setup

We performed a set of experiments (see Tab. 13 for details) using the *Mars Simulation Chamber* at the Open University (UK). The chamber was equipped with a 0.9 $\times$ 0.4 m aluminium tray filled with a $\sim$ 2 cm deep sediment bed (natural sand, $\sim$ 200 μm) together with a reservoir containing 500 ml of low viscosity, and hence water-dominated, mud (12.7 mPa.s at $\sim$ 276 K and 10.7 mPa.s at $\sim$ 296 K). The container with the mud hung $\sim$ 5 cm above the tray (Fig. 53). Before depressurisation, the mud and sand were at room temperature (from $\sim$ 292 K to $\sim$ 296 K). The tray was inclined by 5° and 10° to force the mud to move under gravity once poured on to the surface. The mud was released from the container under reduced pressure ($\sim$ 7 mbar) and the movement of the mixture was observed and recorded by four cameras from different angles. In some experiments the sand bed was replaced by a smooth plastic plate inclined by 5° to assess if the observed processes were dependent on the presence of unconsolidated and porous material. We also performed comparative experiments under terrestrial pressure to get a reference set of experiments. In an additional experimental setup, a plastic box (0.6 $\times$ 0.4 m) infilled by a 33 cm thick layer of sand was used to investigate the depth to which the mud is able to propagate in a low pressure environment. Each experiment was performed in triplicate to confirm the reproducibility of the results.

The mud used for the experiments was a mixture of deionised water with 0.5% w/w of dissolved magnesium sulphate salts ($MgSO_4$) and clay at $\sim$ 6.5% of the mud mass (the mass ratio between deionised water and clay was 4:1). The magnesium sulphate salt, which was previously detected on the martian surface (Clark, 1978; Vaniman et al., 2004; Hecht et al., 2009), was added to achieve the average river water salinity which is necessary to suspend submillimetre clay particles (Corradi et al.,

Tab. 13: Summary of measured and controlled variables for each experimental run.

Exp #	Pressure range* [mbar]	Inclination [°]	Release time** [s]	Type of surface
exp_31	7.1-8.1	5	52	~2 cm sand layer
exp_32	6.9-7.6	5	29	~2 cm sand layer
exp_33	6.9-7.4	5	21	~2 cm sand layer
exp_51	7.0-7.7	5	45	~33 cm sand layer
exp_52	6.6-7.1	5	34	~33 cm sand layer
exp_53	6.6-8.5	5	22	~33 cm sand layer
exp_12	1000	5	19	~2 cm sand layer
exp_13	1000	5	20	~2 cm sand layer
exp_14	1000	5	18	~2 cm sand layer
exp_26	6.7-7.4	10	36	~2 cm sand layer
exp_27	7.1-8.1	10	23	~2 cm sand layer
exp_28	7.1-7.8	10	43	~2 cm sand layer
exp_46	6.7-7.6	5	34	plastic plate
exp_47	6.9-7.3	5	50	plastic plate
exp_48	6.8-7.4	5	60	plastic plate
exp_43	1000	5	45	plastic plate
exp_44	1000	5	40	plastic plate
exp_45	1000	5	37	plastic plate

* Pressure range during the first two minutes of the experimental run
** Time period over which the mud was poured from the container

1994). As there is no direct in-situ knowledge of which types of clays could be involved in the subsurface sediment mobilisation on Mars, we decided to use the clay obtained from the claystone named after the Rokle locality situated near the town Kadaň in the Czech Republic and operated by the private company Keramost. This clay is a bentonite composed of 76% of montmorillonite, 23% of illite, and 1% of kaolinite which has been formed by alteration of pyroclastic rocks. As explosive volcanism was likely common on Mars (e.g., Wilson and Head, 1994), to a first approximation this material is a suitable analogue. The mud mixture was obtained using a blender for 3 minutes to reduce the presence of more lithified clayey aggregates. The average density of the resulting mixture was 1037.5 kg.m^3. The viscosity was measured at the Institute of Hydrodynamics of the Czech Academy of Science by using *Haake Rotovisco RV 20 and Viscotester VT 550 rheometers* with ledges on the MV2 cylinder to prevent slip of the measured material on its walls.

6.3.2 Modeling of Mars surface temperatures

To model the subsurface temperature on Mars we used the albedo and thermal inertia maps derived by Putzig and Mellon (2007) from Thermal Emission Spectrometer data (Christensen et al., 2001). Thermal inertia is the square root of the product of thermal conductivity, bulk density, and specific heat capacity. Since the latter

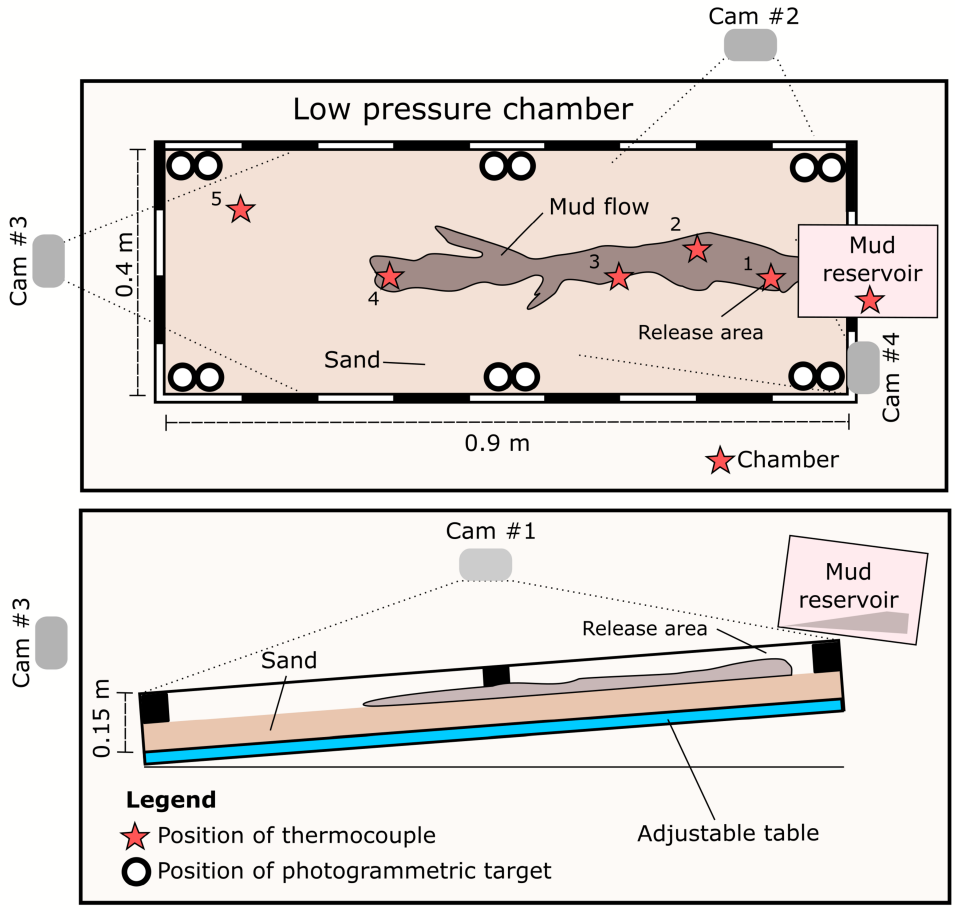


Fig. 53: Schematic illustration showing the experimental setup with the position of thermocouples, photogrammetric targets and four cameras marked. Data from thermocouples are not discussed within this study, however, they are provided in the Supplementary materials uploaded on Zenodo.org for those who are interested.

two exhibit much less variability in regolith than the former, we assume them to be constant. Density is assumed to be 1300 kg/m^3 and heat capacity is assumed to be 630 J/kg/K from the numbers recommended for the InSight landing site (Morgan et al., 2018).

The variables governing the boundary conditions are Mars' orbit and spin axis obliquity, as well as atmospheric pressure and dust optical thickness. For our modeling we use the timeseries output of the local surface atmospheric pressure and local dust optical thickness at the 610 Pa pressure level provided by the average climatology scenario of the Mars Climate Database (MCD, Forget et al. 1999, Millour et al. 2017). The database covers the average of TES observations over martian years 24 – 31, with planet encircling dust events excluded (Montabone et al., 2015). We scale the dust opacity to the local atmospheric column by multiplying with the ratio of local pressure to 610 Pa (Montabone et al., 2015). For the calculations of

subsurface temperature, we use a 1-D version of the Mars Climate Database MCD, which calculates the downwelling visible and infrared fluxes and solves the heat conduction equation in the subsurface, assuming a zero heat flux lower boundary condition. The calculations are done for 10×10 degree tiles, with each tile having the average surface albedo and thermal inertia, and the average from the surface pressure and dust opacity timelines. The output is generated at intervals of 15° of solar longitude and 0.5 h of local solar time for the duration of one Mars year. The results are validated by comparison with version 5.3 of the MCD and found to be consistent within a few Kelvin. This dataset is searched to find the maximum surface temperatures, presented in Fig. 52a. The percentage of the total time of a Mars year when the surface temperatures are above freezing is presented in Fig. 52b. The maximum depth of subsurface layer above freezing is shown in Fig. 52c and the maximum heat that can be released from that layer before everything is below freezing in Fig. 52d.

6.4 Observations

Once the atmospheric pressure was reduced inside the chamber, the mud in the container started to boil and to cool down due to evaporative cooling. The boiling intensified as the pressure decreased to 12-14 mbar and continued to 7 mbar. When a pressure of $\sim$ 7 mbar was reached, the mud had a temperature slightly above freezing and was manually released by tipping the container, letting it flow over the 'warm' (from $\sim$ 292 K to $\sim$ 296 K) sand surface inclined at 5°. The contact of the mud with the warm surface triggered boiling, which caused ejection of sand grains to a height of several centimetres. The particles landed both on the mud and on the surrounding sand. The deposition of the sand grains formed a small raised rim around the contact area resulting in a crater-like depression (Fig. 54, t=10 s). The explosive activity decreased with time. At the beginning, the mud was not visible inside the crater area, as it was covered by a layer of loose sand grains, which was repeatedly disturbed by bubbling (Fig. 54, t=10 s). Within seconds, mud could be observed on the surface – not necessarily at the site where it was directly poured from the container – propagating inside the crater (Fig. 54, t=22 s). At the boundary between the mud and the sand layer, a large number of millimetre-scale explosion pits formed, from which gas continued to eject particles over several minutes. This enabled a progressive expansion of the rim.

Continued mud supply caused the flow to breach the sandy rim and a lobe of mud advanced over the warm sand (Fig. 54, t=22 s). This flow front triggered new explosions as the mud propagated and it sank into the surface of the sand. The boiling caused the release of gases, which caused transient levitation of a part of the flow lobe. The escape of gas at the base of the mud flow caused the lobe to vibrate vertically and to quickly propagate over the first few centimetres of the sand surface (Fig. 54, t=26 s; Fig. 4a). This decreased the friction between the mud and the sand

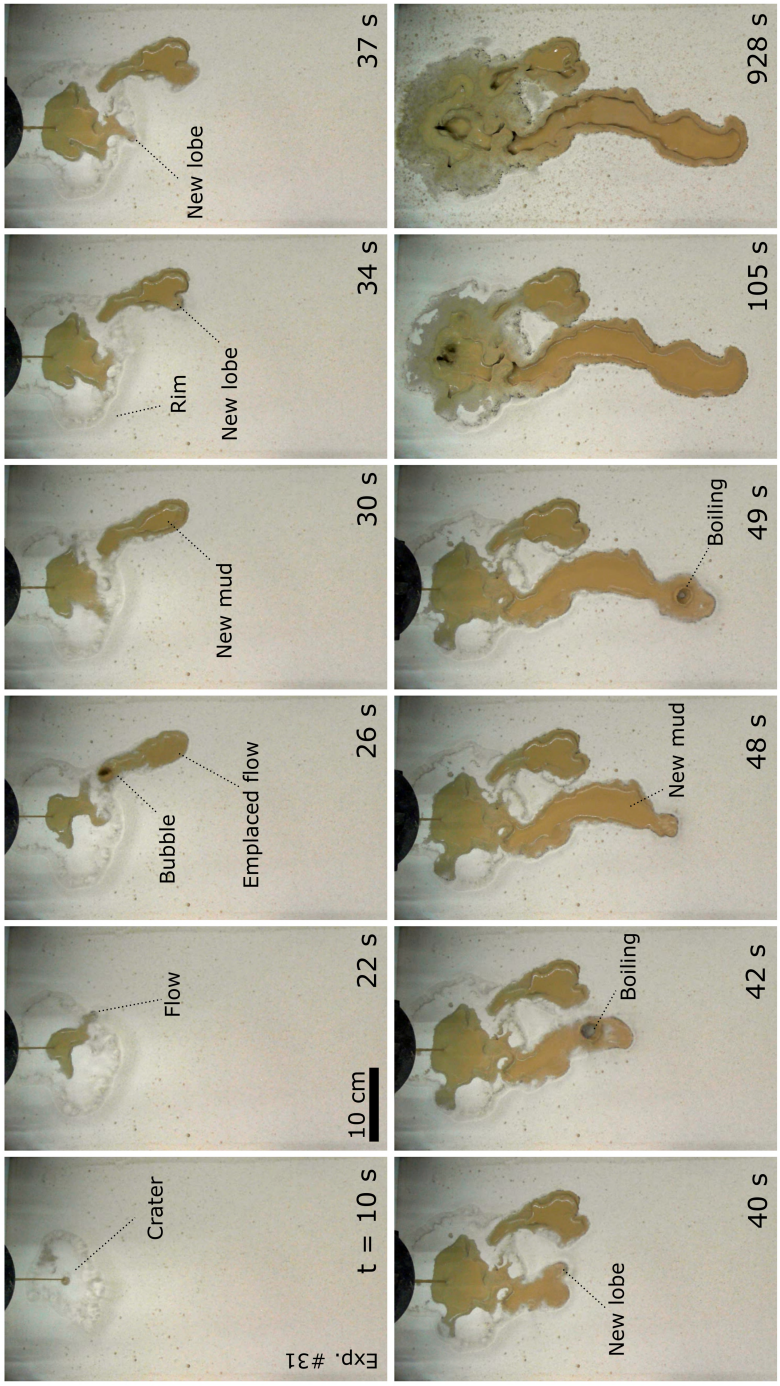


Fig. 54: A sequence of images from different time steps (in seconds) capturing the propagation of low viscosity mud over a warm surface inclined by 5° under low pressure mimicking conditions on Mars. The mud was poured on the surface from a hanging container. Once the mud touched the surface, intense boiling occurred, and a central crater-like depression started to form (t=10 s). Soon a surface mud flow developed (t=22 s) and started to propagate downslope a few centimetres at a time in the form of a narrow lobe which was levitating and sliding/creeping over the sand surface (t=26 s). After a while, the flow stopped its propagation (t=30 s) and a new lobe developed (t=34 s). This process repeated as long as mud was being poured onto the surface (t=37 s; t=40 s). The boiling also caused the formation of rims surrounding the lobes. The images were obtained from the video recorded by camera #1 observing experiment #31 from above.

surface. Once the boiling was not capable of lifting the entire weight of the mud flow anymore, the flow lobes slid/crept over the surface entraining the sand particles. Then the lobe stalled and small millimetre-scale explosions occurred around its edge causing the formation of small ridges. Simultaneously fresh mud outpouring from the crater started to propagate over the lobe's surface and accumulate at the front of the flow (Fig. 54, t=30 s). Once enough material had accumulated to overcome the small ridges at the edges, a new lobe formed (Fig. 54, t=34 s to t=48 s) and the process repeated until the supply of new mud was exhausted (Fig. 54, t=49 s and t=105 s). The movement of mud through the lobes created an interior trough with a curvy and irregular shape (Fig. 54, t=928 s).

When the same experiment was repeated with the surface inclined at 10°, a similar behaviour was observed (Fig. 56). However, the higher inclination did somewhat affect the way the mud advanced. The flow lobes travelled faster and further than lobes at 5° inclination. The resulting deposited lobes were also longer and narrower than in the previous set of experiments (Fig. 56, t=30 s). In some cases, the flow lobe became separated from the main flow and/or from the source crater by a layer of sand grains ejected by escaping gases from the sand layer (see the evolution of the left flow lobe on Fig. 56 from t=25 s to t=35 s), giving the flow a discontinuous appearance.

The boiling within the bulk volume of the mud also caused the nucleation of variously sized bubbles which moved upwards to the surface of the mud. Once they reached the surface, they dramatically expanded and as a result some portions of the mud were fragmented into small droplets (Fig. 55b). These droplets were then ejected along ballistic pathways and deposited close to the active mud flow (e.g. Fig. 54, note the presence of small dark droplets whose frequency increased around the flow between times t=30 s and t=105 s). The influence of the mud fragmentation on the total transported mud volume was only minor, however, it occurred over the entire length of the mud flow wherever the bubbles were able to form and move through the mud. This transport mechanism was not active during the experiments performed under terrestrial pressure conditions. Part of the ejected sand and mud was also deposited on the mud flow where it formed a sandy-muddy crust (Fig. 55b) which partly hindered the mud flow. The crust was either later destroyed by a new batch of mud or by a gas release, or it survived until the end of the experiment.

We also observed the release of gases in the form of centimetre-sized bubbles for dozens of minutes in the pouring area and in several other areas along the entire length of the flow providing evidence that the mud remained liquid in the subsurface (Fig. 55b). The presence of liquid mud covered by sand was later confirmed once the chamber was recompressed and the interior of the resulting features were studied by breaking them apart from their edges to the source area (Fig. 57). By using an additional experimental setup, a plastic box infilled by a 33 cm thick layer of sand, we found that the mud flow was capable of eroding into the sand layer to a depth of several centimetres as mud was observed beneath the original sand surface. This

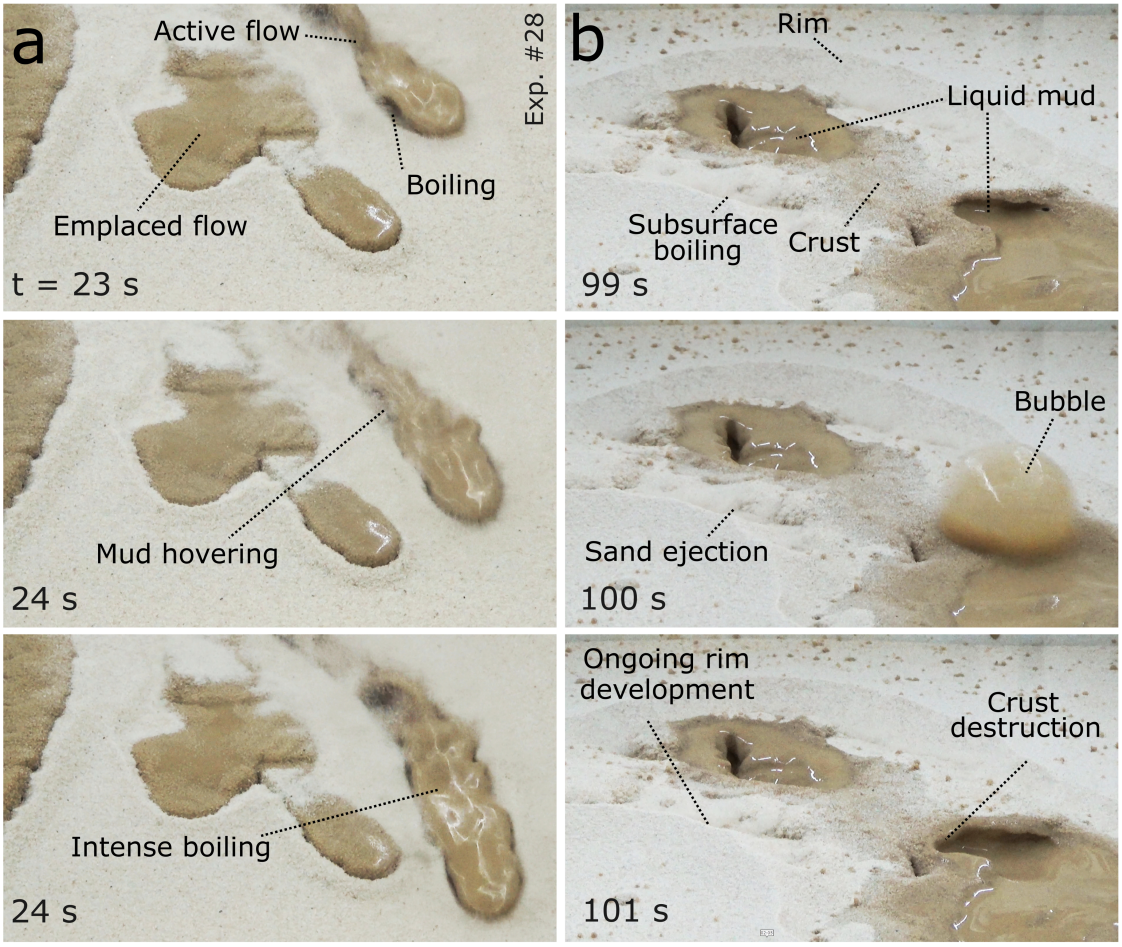


Fig. 55: Two-time sequences of images showing (a) the levitating and sliding mud over an unconsolidated surface and (b) the continuous explosions indicating the presence of liquid mud in the subsurface. Note the irregular shape of the propagating active mud flow in the vertical direction in panel (a) revealing intense boiling within the flow and associated release of water vapour from the flow. Such releases caused levitation of the material and rapid propagation of the flow over the surface. The images were obtained from the video recorded by camera #3 observing experiment #28 from front.

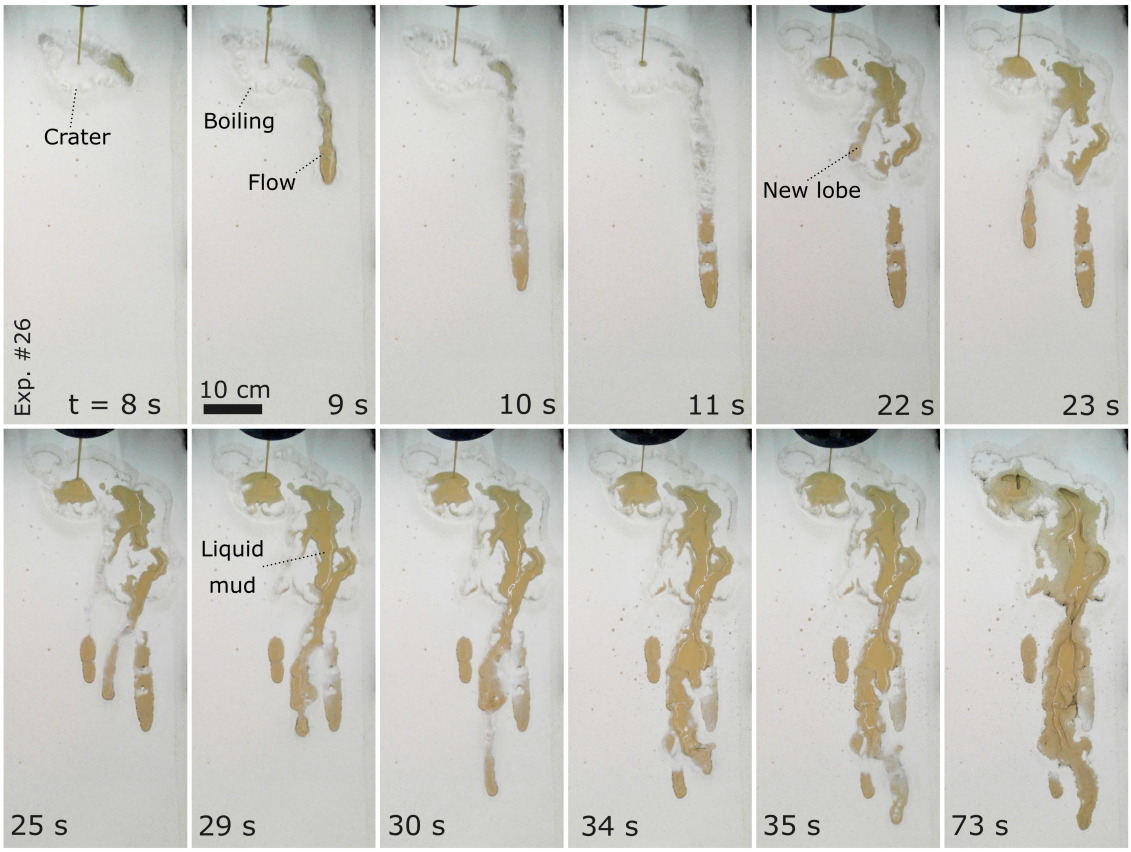


Fig. 56: A time series of images (time steps in seconds) capturing the propagation of low viscosity mud over a warm surface inclined by 10° under low pressure, mimicking conditions on Mars. The mud was poured to the surface from a hanging container. Similarly to the results captured in Figure 3, intense boiling occurred (t=8 s) and after a while a narrow mud lobe developed (t=9 s). Due to the higher inclination of the surface the mud lobe travelled faster and further (t=11 s) than in those experiments performed at a slope of 5°. The narrow, long lobes were partly or fully covered by ejecting sandy grains (t=25 s) which caused a seemingly discontinuous appearance of the final morphology. The images were obtained from the video recorded by camera #1 observing experiment #26 from above.

setup also revealed that the mud flow was surrounded by a layer of sand saturated by water (Figs. 57b-d).

The inspection of the final morphology of the mud flows once the chamber was recompressed revealed that the internal structures of the flows were supported by a hardened mixture of mud and sand allowing the formation of vertical cliffs or overhangs forming crusts which fully or partially covered the flow channels. These crusts enclosed cavities through which the flows had propagated cavities through which flows had propagated (Fig. 58). We also observed that the bottoms of the troughs were covered by fine-grained clay. Repetitive explosions caused by escaping gases formed holes which were located above small subsurface pockets infilled by mud.

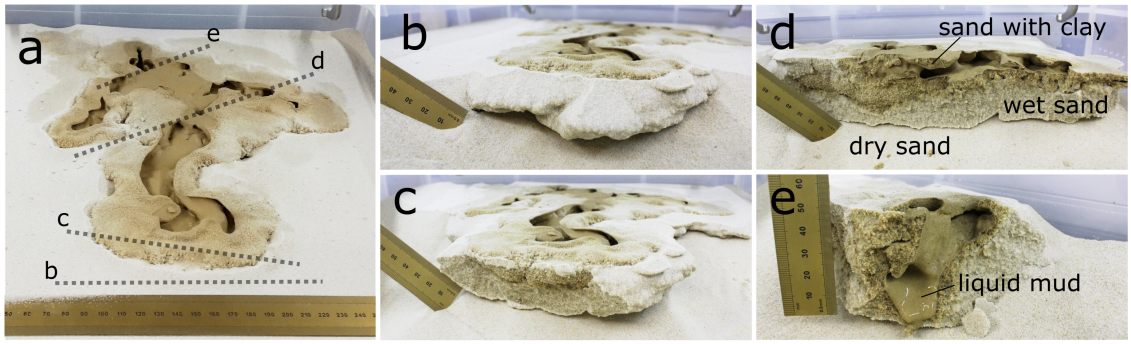


Fig. 57: An example of the resulting morphology of a low viscosity mud flow and its inner structure formed by the movement over "warm" sand in a low pressure environment. (a) The edge of the flow is surrounded by set of sandy ridges and several central troughs through which the mud propagated. The dashed line at b marks the position at which the mud flow was exposed by removing the sand (shown in panel b) and the dashed lines c to e mark where the flow was sectioned to reveal the inner structure of the flow (shown in the corresponding panels). The flow was composed of a layer in which clay-particles dominated and by a layer in which the sand was saturated by water (marked on panel d). In some cases, the liquid mud was still present in the subsurface (e).

The experiments performed under terrestrial pressure did not show the same behaviour or morphologies as those at martian pressure (Fig. 59). The mud within the container before pouring did not boil and its internal temperature did not drop. Once the mud was poured from the container (Fig. 59, t=5 s), it started to flow relatively uniformly over the sand surface (Fig. 59) and, as a consequence, a broad and thin mud flow formed (Fig. 59, t=20 s). In some cases, centimetre-sized flow lobes formed on the edge of the propagating flow (Fig. 59, t=25 s and t=85 s) as a result of topographic irregularities in the sand layer. The flow did not significantly erode into the sand surface and vertical cliffs or protective muddy-sandy crust were not observed to form.

The experiments performed under reduced atmospheric pressure over the 5° inclined plastic plate showed that boiling still occurred, but it was not able to lift the propagating mud flow. Once the mud was poured from the container, it started to flow over the surface forming a several centimetres wide and a dozens of centimetres long flow. As no unconsolidated material was available, the flow did not erode to the subsurface and hence the direction of the propagation of the mud flow was only controlled by gravity. Analogue experiments performed under terrestrial pressure lead to the formation of similarly looking mud flows, however, no boiling was observed.

6.5 Discussion

6.5.1 Application to Mars

Experiments revealed that a low pressure environment has a significant effect on the propagation of low viscosity mud over a warm unconsolidated surface (Fig.

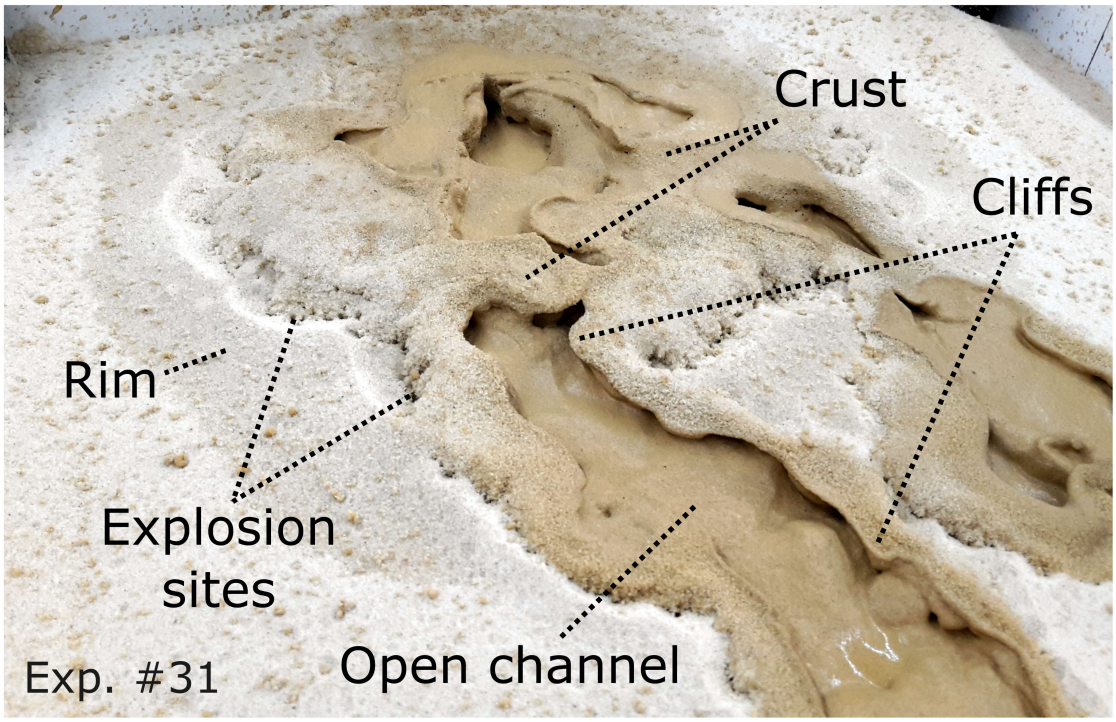


Fig. 58: Detail of the resulting low viscosity mud flow morphology, which was characterised by a network of open central channels of varying depths surrounded by rims composed of sandy particles ejected from multiple small explosion sites. These explosion sites mark the boundary between the liquid mud and surrounding dry sand. In some places a protective crust developed by gluing together clay and sand particles. The width of the main channel is around 2 cm. Note the cliffs which can be vertical or overhangs can be formed.

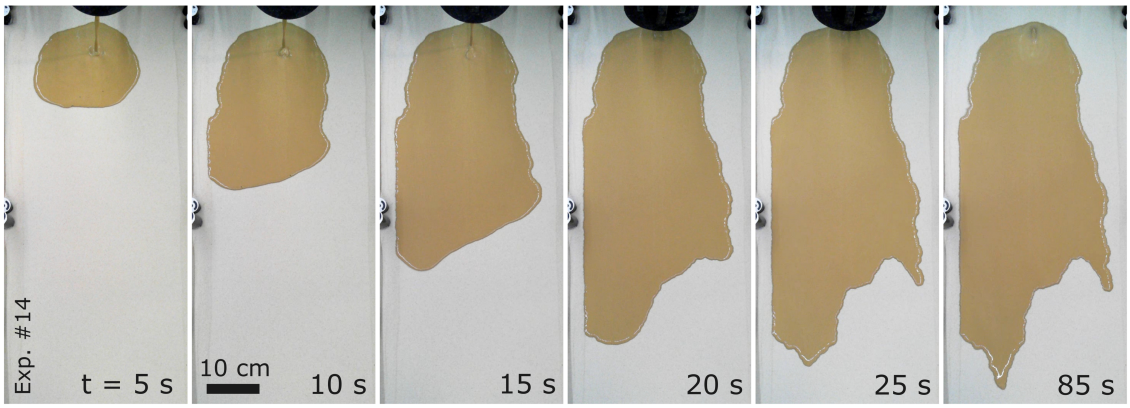


Fig. 59: A sequence of images taken at different time steps (t) capturing the propagation of low viscosity mud over a warm surface inclined by 5° under terrestrial ambient pressure conditions. The mud propagates as a tens of centimetres wide and a few mm thick sheet-like mud flow. Images obtained from the clip recorded by camera #1 observing the experiment #14 from above.

60)). The reason for this different behaviour is the instability of water (Bargery et al., 2010) that leads to boiling and the formation of water vapour bubbles which escape violently from the mud to the surrounding atmosphere and partly also into the subsurface. The strongest influence of the boiling on the mud movement occurs at the contact between the mud and the warm material over which the mud propagates. Here the boiling is most intense as the heat stored within the substrate is available to support boiling. As a result, a large quantity of water vapour is produced at this interface (Fig. 55)a). The release of water vapour can then modify the way the mud moves leading to levitation and sliding/creeping of the advancing mud lobes.

This is similar to the transport mechanism described by Raack et al. (2017) and Herny et al. (2018), who studied the downslope movement of water-saturated sediments in a low pressure environment, albeit with one major difference. Whereas Raack et al. (2017) and Herny et al. (2018) observed that the water-saturated sediments propagated in the form of individual small pellets, the levitating mud observed herein moves as a coherent fluid (Figs. 52), 53) and 56)a). The entire flow lobe is therefore affected by the levitation. Once the gas production in the advancing lobe decreases, the mud seems to propagate over the inclined unconsolidated surface by sliding and/or creeping (Figs. 52), 53) and 56)a) as the gas release can only partly lift the mud lobe. These mechanisms cause an increase in the speed of mud propagation over the unconsolidated surface under martian ambient pressure (Figs. 52) and 53)) as compared to terrestrial ambient pressure (Fig. 59)).

The boiling of water has also another effect on mud flow propagation in regard to its stability in the martian environment. This is because the ejection of sandy grains by expanding gas and their re-deposition on top of the mud flow can form a sandy-muddy crust by coalescing sand and finer-grained clay particles together. The crust can partly isolate the liquid mud from the atmosphere and prolongs its lifetime on the surface. The mud can then propagate under the crust giving rise to the formation of an interconnected network of mud channels beneath the crust (e.g. experiment #26 and #31).

The crust which developed in our experiments extended along the flow over several centimetres of the mud flow channel (e.g., Figs. 54, 55, 56 and 57), but real mudflows are likely to be longer and wider, so it is difficult to estimate the efficacy of this process at field-scale. We hypothesize that the limited coverage of the flow in our experiments was caused by the fact that these experiments were volume-limited and the processes associated with the development of the mud flow operated for only a relatively short period of time. If the mud volume was larger, the flow would last for longer and more mud-sand interaction would occur and perhaps a crust may be formed over a larger surface area of the mud channel. If a larger section of the channel were covered by the crust, this may fully isolate the flow from the low atmospheric pressure, causing boiling to cease. Under such scenario, boiling would only occur at the active edges of the mud flow where the mud would be exposed to the atmosphere. Even if the crust could only cover part of the channel over its

entire length, our observations suggest that mud propagating over a warm surface – similarly to the mud propagating over a cold surface (Brož et al., under review) – is capable of developing a protective crust prolonging the lifetime of the flow on the surface of Mars. This is an aspect of mud propagation that has not previously considered and should be investigated further. However, it should be noted that this process may only be important for those martian mud flows whose width is in the range of centimetres to decimetres, and less significant for wider ones. This is because even under the reduced martian gravity the ballistic trajectory of the particles is limited and at the same time the larger width of the flow would mean that the volume of ballistically transported particles necessary to form a sufficiently thick crust would significantly increase. As the consequence it would be difficult to form a crust over a flow more than several tens of centimetres wide. Similarly, a crust would only be formed on martian mud flows propagating over mobile substrates, such as, unconsolidated sandy regolith. As shown by the experiment setup using the plastic plate, if the mud propagated over impermeable rocky or crusty surfaces, even though boiling would still occur, the crust would not be formed because of the absence of small particles that could be ejected onto the mud. The properties of the substrate could significantly influence the way the mud propagates and the final morphology observed at the surface.

We also observed that mixing of the mud and sand at the flow boundaries produced vertical cliffs or even overhangs which were relatively stable as shown by their capacity to survive the processes of chamber repressurisation (Figs. 57a,d and 58). We expect that within the range of centimetres to decimetres wide mud flows such cliffs may result in atypical morphologies compared to those typically found in terrestrial mud flows suggesting that comparison to terrestrial analogues could be misleading. However, we do not expect that shapes of metre- or kilometre-sized mud flows would be affected as the mechanical strength of such cliffs would be limited, and whereas centimetre-sized cliffs can be attained, a metre-sized cliffs would collapse. Small mud flows can therefore share some similarities with terrestrial low viscosity lava flows for which vertical cliffs or overhangs are common (e.g., Kilburn, 2000) as lava solidification is capable of forming such landforms.

6.5.2 Temperature drop within the mud and substrate

Additionally, our experiments show that there is another crucial factor which deserves further investigations when studying surface expressions of possible martian mud flows. The instability of the water causes a temperature drop in the mud due to evaporative cooling which removes latent heat from the mud and from the subsurface (Bargery et al., 2010; Brož et al., under review). So, once the ascending mud reaches the martian surface, the mixture would rapidly self-cool close to the freezing point.

More specifically, when the mud initially propagates over a warm surface, and the flow continues over the same area for a certain amount of time, evaporative

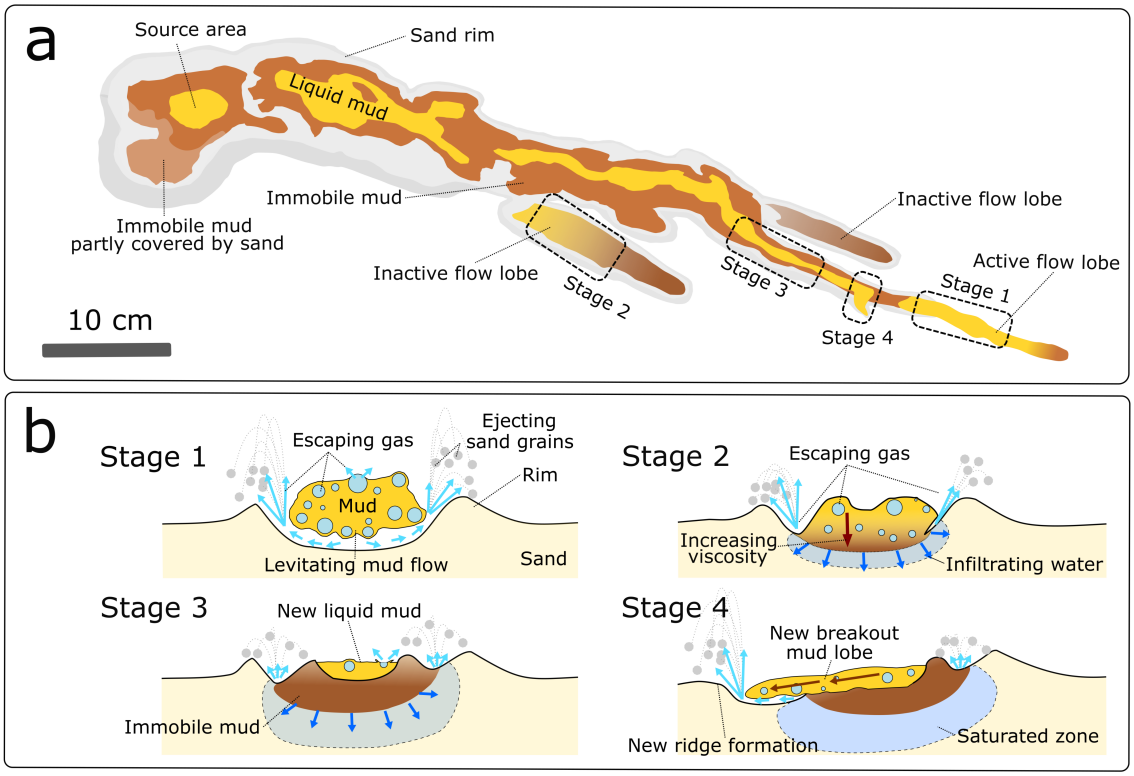


Fig. 60: Schematic illustration showing the development of a low viscosity mud flow during the movement over the 'warm' inclined surface under martian conditions with insets showing the main processes operating during its emplacement. (a) The ascending mud would move downhill from the source area via partly overlapping flow lobes. The instability of water within the mud would cause redeposition of unconsolidated sandy surface as well as fast propagation of the fronts of the active lobes. The different colours mark different states of the mud; brown indicates immobile mud, while orange indicates liquid, and hence mobile, mud. The black dashed rectangles mark the position of small insets in panel b (b) Stage 1 shows mud propagation by levitation over the inclined sand surface. The levitation is caused by boiling water releasing gases from the base of the mixture. Escaping gases are additionally able to trigger ejections of sand grains and hence cause self-burying of the mud flow under the surface. Stage 2 shows the situation when the mud flow lobe stops propagating by levitation and when the water from the mud starts to infiltrate into the subsurface. Stage 3 then shows the input of new liquid mud flows over the older mud flow. Finally, at Stage 4 the new batch of mud overcomes the margins of the older mud flow and hence the mud flow would be again be exposed to a warm surface. This then causes the levitation of the mud flow and repetition of the whole process.

cooling removes the available heat both from the mud and the substrate. This results in gradual freezing of the mud and the subsequent formation of an icy-muddy crust (Brož et al., under review), altering the mechanisms of mud propagation. Ultimately the mud would propagate via frozen mud tubes in similar fashion as pahoehoe lava (Brož et al., under review). This leads us to conclude that mud movement over today's martian surface involves a complex process in which the movement is governed both by levitation and/or sliding at the front and by freezing as the flow progresses. Both mechanisms may occur during the formation of a single mud flow and this suggests that the resulting morphologies may record these variations of mud transport.

To obtain a first order of understanding regarding what happens in case of a mud flow over a warm surface, we use the subsurface temperature profiles corresponding to the maximum ground temperature case in Fig. 52a as the initial temperature state. We force the top of that temperature profile to be at 273 K, representing the coldest possible temperature in contact with boiling water. We then solve the heat conduction equation starting from the above described condition, using the explicit Euler finite difference method with 1 mm depth resolution and 0.1 s time resolution. The model is stopped when the entire profile is below 273 K, the time until at that moment is presented in Fig. 52e. For comparison we also conduct this cooling model with a profile resembling the laboratory setup: i.e. assuming a thermal conductivity of 0.04 $Wm^{-1}K^{-1}$ for the 0.2 mm particle diameter sand at 700 Pa (Presley and Christensen, 1997) and an initial constant temperature of 273 K. The timescale of cooling below freezing everywhere is not meaningful in this context, but we can calculate the heat flow conducted through the surface as a function of time. This heat flow q with unit Wm^{-2} can be translated into a vapour column production rate v with unit of m s^{-1}, which is the thickness of the vapour layer produced per second:

$$v = qRT/(L_v m_{H_2O} P), \tag{6.1}$$

where R = 8.314 J K^{-1} mol^{-1} is the ideal gas constant, T = 273 K is the assumed gas temperature, $L_v = 2.46 \times 10^6$ J.kg^{-1} is the latent heat of water vaporization, m_{H2O} = 0.018 kg is the weight of 1 mol of water, and P = 611 Pa is the saturation pressure of water at temperature T. Temperature and pressure below a levitating flow will likely be higher, and the volume lower, than these assumed values, since it must compensate for hydrostatic and ambient pressure. It is likely that for levitation a critical production rate, proportional to the heat flow out of the top of the substrate must be sustained. In the laboratory experiments the levitating is intermittent, with a typical duration on the order of 10 s after the emplacement of fresh mud flow lobes (Fig. 54). In the thermal model of the laboratory setup with the top of the substrate forced to 273 K, the heat flow conducted from the surface is > 550 Wm^{-2} in the first 10 seconds. This corresponds to column of vapour produced per second of v = 46 cm s^{-1}. It should be noted that not all of the heat from the subsurface will produce water vapour from the mud flow, some heat will be transported away by the vapour.

Nevertheless, taking 550 Wm^{-2} as requirement for mud levitation, we can apply it to the model of the forced cooling of Mars surface to estimate how long flows could levitate on Mars, Fig. 52f shows the duration of heat flow > 550 Wm^{-2} conducted through the substrate surface forced to a temperature of 273 K starting from the maximum modelled temperature conditions (Fig. 52a). This map shows that over a band of latitudes of 60°S to the equator, levitation is possible if a mud flow occurs close to noon during the warmest season. In the northern hemisphere this also applies to parts of Syrtis Major Planum and Chryse Planitia, due to their relatively high albedo.

We are also aware that the environmental properties on Mars will have varied over time, due to the chaotic variation in Mars' orbital parameters, which affects the distribution of incoming insolation (Laskar et al., 2004). For example, during periods of higher obliquity (Ward, 1973) areas where surface temperatures could be above the freezing point of water would vary in magnitude and position. Also, the depth to which the freezing point would descend would vary (Costard et al., 2002) and hence the amount of available heat necessary to keep the process of the violent boiling active would be different. The time required by the evaporative cooling to remove the available heat from the subsurface increases proportionally with the depth of the freezing point. Variations in surface temperatures caused by variations in Mars' orbital parameters may therefore prolong or foreshorten the period over which boiling would dominate the behaviour of the mud. This means that the mechanisms dominating in mud propagation should change through time.

Additionally, the complex magmatic history of Mars (e.g. Grott et al., 2013) suggests that the heat flux within the martian crust has not been steady. In fact it varied through time at various localities producing geothermal anomalies (e.g. Plesa et al., 2016). These sites may represent ideal places where sedimentary eruptions may result due to the melting of subsurface water ice or hydrothermal activity. Higher heat flux may also imply that the surface can be sufficiently warm to prevent the freezing of the extruded mud for extended periods of time, or even completely inhibited. Under such a scenario, it may be possible that the described processes, which operated in our experiments at the centimetre-scale only, would be able to affect even wider surfaces and therefore produce larger scale mud features. It should therefore be taken into account that some morphologies which are present at the surface of Mars today, and which may have an origin associated with mud eruptions, may be linked to the intense boiling and the above described transport mechanisms.

6.5.3 Scaling to Mars and experimental limitations

The presented experimental approach has several limitations as it can not fully attempt to simulate all the conditions of sedimentary volcanism on Mars or even on Earth. Firstly, our experiments were performed with a fixed volume of mud (500 ml). This limits the size of the resulting flows to a length of several decimetres,

the width to several centimetres and the thickness to less than 1-2 centimetres. On Earth, sedimentary volcanism can extrude mud volumes several orders of magnitudes larger than those in our experiments (e.g. Kopf, 2002; Mazzini and Etiope, 2017) resulting in metre- to kilometre-long mud flows. Obviously, we were not able to perform experiments at this scale due to the size limitation of the available low pressure chamber. Nevertheless our work can still provide valuable insights into mud propagation in a low pressure environment due to the chosen mud viscosity. This is because the low viscosity mud flows, naturally occurring on Earth, propagate over flat surfaces and form centimetres-thick mud lobes (Mazzini and Etiope, 2017; Miller and Mazzini, 2018) similar to those observed in our experimental setup. Therefore, we are capable to directly address the differences between those terrestrial flows and putative martian analogues. However, our experiments do not provide appropriate insights about the propagation of thicker low viscosity flows, for example, when the mud becomes channelized or a large quantity of mud is extruded over a short period of time. This is because in thick mud flows the flow regime may change. This should significantly change the way the mud propagates in the low pressure environment as heat will be transported differently within the flow and there is a need for further experimental or theoretical investigation of this problem.

An additional limitation is associated with the inability to perform experiments in a reduced gravity environment, mimicking the gravity of Mars (3.7 m s^{-2}). Our experiments were performed under terrestrial gravity (9.8 m s^{-2}), which has an influence on the way the mud propagates. Terrestrial gravity limited the height to which the vibrating mud could levitate as well as the total volume of mud which could be lifted. A similar limitation can be applied to the study of Raack et al. (2017) in which the different gravitational force effects the levitation of the sedimentary pellets propagating over the hot surface. These authors showed that the reduced gravity would allow pellets to levitate up to 48 times longer on Mars than on Earth and that the lifted pellets can be up to seven times heavier compared to those lifted in their experiments. These calculations suggest that, on Mars, mud would levitate for a longer period of time and to a greater height than observed in our experiments. The lower martian gravity would also affect the distance to which the sand grains and small mud droplets would be ejected. Brož et al. (2014) showed that ballistically emplaced scoria particles can travel about 20 times further on Mars than on Earth due to the lower gravity and lower atmospheric pressure. Therefore, the ejected material would be spread over much wider area than observed in our experiments. This means that on Mars more transported material would be necessary to build a steep-sided rim which in part affect the flow of material over the flat surface. As a consequence the role of marginal rims to, at least partly, guide the flow direction may be limited on Mars as the rims may be much broader but shallower than those observed in our experiments. Ultimately gravity may also affect the way the flow erodes the subsurface as sand and rocky particles would be more easily shifted by releasing gases from the advancing mud flow.

6.6 Conclusions

Our experiments show that a warm (from ∼ 292 K to ∼ 296 K) and unconsolidated surface has a profound effect on the behaviour of flowing low viscosity mud in a low-pressure environment (Fig. 60). The resulting boiling occurring during the mass flow, causes transient levitation of the mud above the warm surface as well as the erosion of the unconsolidated sandy substrate. Both mechanisms alter mud propagation in a low pressure environment. Moreover, we expect that these processes would be even more effective on Mars which has a lower gravitational acceleration than on Earth. On Mars gravity does not change the boiling rate, but the sediments can be more easily entrained (Raack et al., 2017; Herny et al., 2018). The gas release should levitate mud for a longer period of time than observed in our experiments, as also similarly suggested for wet sand (Raack et al., 2017; Herny et al., 2018), hence allowing the mud to propagate over larger distances than modelled within the low pressure chamber. Additionally, as the process of evaporative cooling would remove the latent heat from the mud and from the surface over which it is propagating, at a certain point, the mud would start to freeze. This would cause the formation of a protective icy-muddy crust affecting the way the mud moves (Brož et al., submitted) switching from levitation and sliding/creeping to the propagation via mud tubes. The mechanisms of mud propagation on Earth at different P-T conditions are well studied. The mud propagation, during this relatively simple process, is controlled by mass gravity flow. In contrast, very little is known on the modes controlling the same events on e.g. Mars and other bodies within or absent atmospheres where mud eruptions may be present (e.g., Ruesch et al., 2019). Our new data demonstrate that the behaviour of mud and its propagation in a low-pressure environment, is strongly controlled by the surface temperature since freezing or rapid boiling give rise to different transport mechanisms than simple liquid flow. We conclude that mud eruption activity on other celestial bodies may produce profoundly different morphologies compared to those commonly observed on Earth.

6.7 Acknowledgements

The access to the Large Mars Chamber at the Open University was provided by *Europlanet 2020 RI* which has received funding from the European Union's Horizon 2020 research and innovation program under *grant agreement No 654208*. OK was supported by Center for Geosphere Dynamics (Faculty of Science at Charles University) *project UNCE/SCI/006*. AM was funded by the *ERC grant agreement 308126* (LUSI LAB) and the Research Council of Norway (Centers of Excellence funding scheme, *project 223272*). The movies and temperature and pressure data that support the findings of this study are available in *Zenodo.org* with the identifier 3520947 (https://doi.org/10.5281/zenodo.3520947). These materials, which are now during the re view restricted from being view publicly, can be downloaded and viewed by using this link: https://zenodo.org/record/3520947?token=

eyJhbGciOiJIUzUxMiIsImV4cCI6MTU4NTM0OTk5OSwiaWF0IjoxNTcyMjk3MzY0fQ.eyJkYXRhIjp7In
_VxA9eaaMuzDSRq_q3TBaaKLsqkwA6daOuzVIJuqAa9EE7q5W_-GJMxH59rL0vPwe5h52l7K20L791iiQ
.XbdapNV7lz0).

6.8 References

Allen, C. C., Oehler, D., Etiope, G., van Rensbergen, P., Baciu, C., Feyzullayev, A., et al., 2013. Fluid expulsion in terrestrial sedimentary basins: A process providing potential analogs for giant polygons and mounds in the Martian lowlands. Icarus, 224(2), 424–432. https://doi.org/10.1016/j.icarus.2012.09.018.

Bargery, A. S., Lane, S. J., Barrett, A., Wilson, L., Gilbert, J. S., 2010. The initial responses of hot liquid water released under low atmospheric pressures: Experimental insights. Icarus 210(1), 488–506. https://doi.org/10.1016/j.icarus.2010.06.019.

Brož, P., Hauber, E., 2013. Hydrovolcanic tuff rings and cones as indicators for phreatomagmatic explosive eruptions on Mars. Journal of Geophysical Research: Planets 118, 1656–1675. https://doi.org/10.1002/jgre.20120.

Brož, P., Čadek, O., Hauber, E., Rossi, A. P., 2014. Shape of scoria cones on Mars: Insights from numerical modeling of ballistic pathways, Earth and Planetary Science Letters 406, 14–23, https://doi.org/10.1016/j.epsl.2014.09.002.

Brož, P., Hauber, E., Wray, J. J., Michael, G., 2017. Amazonian volcanism inside Valles Marineris on Mars. Earth and Planetary Science Letters 473, 122–130. https://doi.org/10.1016/j.epsl.2017.06.003.

Brož, P., Hauber, E., van de Burgt, I., Špillar, V., Michael, G., 2019. Subsurface sediment mobilization in the southern Chryse Planitia on Mars. Journal of Geophysical Research: Planets 124. https://doi.org/10.1029/2018JE005868.

Brož, P., Krýza, O., Wilson, L., Conway, S. J., Hauber, E., Mazzini, A., Raack, J., Patel, M. R., Balme, M. R., Sylvest, M. E., under review. Lava-like mud flows on Mars. Nature Geoscience.

Christensen, P.R., et al., 2001. Mars Global Surveyor Thermal Emission Spectrometerexperiment: Investigation description and surface science results. Journal of Geophysical Research 106, 23823–23872. https://doi.org/10.1029/2000JE001370.

Clark, B. C., 1978. Implications of abundant hygroscopic minerals in the martian regolith. Icarus 34, 645–665. https://doi.org/10.1016/0019-1035(78)90052-0.

Conway, S. J., Lamb, M. P., Balme, M. R., Towner, M. C., Murray, J. B., 2011. Enhanced runout and erosion by overland flow at low pressure and sub-freezing conditions: experiments and application to Mars. Icarus 211, 443–457. https://doi.org/10.1016/j.icarus.2010.08.026.

Corradi, A. B., Manfredini T., Pellacani, G. C., Pozzi, P., 1994. Deflocculation of Concentrated Aqueous Clay Suspensions with Sodium Polymethacrylates, Journal of the American Ceramic Society 77, Issue 2. https://doi.org/10.1111/j.1151-2916.1994.tb07022.x.

Costard, F., Forget, F., Mangold, N., Peulvast, J. P., 2002. Formation of recent martian debris flows by melting of near-surface ground ice at high obliquity. Science 295, 110–113. https://doi.org/10.1126/science.1066698.

Forget, F., Hourdin, F., Fournier, R., Hourdin, C., Talagrand, O., Collins, M., Lewis, S. R., Read, P. L., Huot, J.-P., 1999. Improved general circulation models of the Martian atmosphere from the surface to above 80 km. Journal of Geophysical Research 104, 24155. https://doi.org/10.1029/1999JE001025.

Grott, M., Baratoux, D., Hauber, E., Sautter, V., Mustard, J., Gasnault, O., Ruff, S. W., Karato, S.-I., Debaille, V., Knapmeyer, M., Sohl, F., Van Hoolst, T., Breuer, D., Morschhauser, A., Toplis, M. J., 2013. Long-Term Evolution of the Martian Crust-Mantle System, Space Science Reviews 174, 49–111. https://doi.org/10.1007/s11214-012-9948-3.

Hecht, M. H., 2002. Metastability of liquid water on Mars, Icarus 156, 373-386. https://doi.org/10.1006/icar.2001.6794.

Hecht, M. H., et al., 2009. Detection of perchlorate and the soluble chemistry of martian soil at the Phoenix lander site, Science 325, 64–67. https://doi.org/10.1126/science.1172466.

Herny, C., Conway, S.J., Raack, J., Carpy, S., Colleubanse, T., Patel, M.R., 2018. Downslope sediment transport by boiling liquid water under Mars-like conditions: experiments and potential implications for Martian gullies. In: Conway, S.J., Carrivick, J.L., Carling, P.A., De Haas, T. Harrison, T.N. (eds) Martian Gullies and their Earth Analogues. Geological Society, London, Special Publications 467. https://doi.org/10.1144/SP467.10.

Hemmi, R., Miyamoto, H., 2018. High resolution topographic analyses of mounds in southern Acidalia Planitia, Mars: Implications for possible mud volcanism in submarine and subaerial environments. Geosciences 8(5), 152. https://doi.org/10.3390/geosciences8050152.

Kiefer, H.H., Martin, T.Z., Peterfreund, A.R., Jakosky, B.M., Miner, E.D., Palluconi, F.D., 1977. Thermal and albedo mapping of Mars during the Viking primary mission. Journal of Geophysical Research 82, 4249–4291. https://doi.org/10.1029/JS082i028p04249.

Kilburn, C. R. J., 2000. Lava flows and flow fields, in Encyclopedia of Volcanoes, pp. 291 – 305, Elsevier, New York.

Komatsu, G., Okubo, C. H., Wray, J. J., Ojha, L., Cardinale, M., Murana, A., Orosei, R., Chan, M. A., Ormö, J., Gallagher, R., 2016. Small edifice features in Chryse Planitia, Mars: assessment of a mud volcano hypothesis, Icarus 268, 56–75. http://dx.doi.org/10.1016/j.icarus.2015.12.032.

Kopf, A. J., 2002. Significance of mud volcanism. Review of Geophysics 40, 1–52. https://doi.org/10.1029/2000RG000093.

Kumar, P.S, Krishna, N., Prasanna Lakshmi, K.J., Raghukanth, S.T.G., Dhabu, A., Platz, T., 2019. Recent seismicity in Valles Marineris, Mars: Insights from young faults, landslides, boulder falls and possible mud volcanoes. Earth and Planetary Science Letters 505, 51–64. https://doi.org/10.1016/j.epsl.2018.10.008.

Laskar J., Correia A. C. M., Gastineau M., Joutel F., Levrard B., Robutel P., 2004. Long term evolution and chaotic diffusion of the insolation quantities of Mars. Icarus 170, 343–364. https://doi.org/10.1016/j.icarus.2004.04.005.

Laigle, D., Coussot, P., 1997. Numerical modelling of mudflows. Journal of Hydraulic Engineering 123, 617–623. https://doi.org/10.1061/(ASCE)0733-9429(1997)123:7(617).

Massé, M., S. J. Conway, J. Gargani, M. R. Patel, K. Pasquon, A. McEwen, S. Carpy, V. Chevrier, M. R. Balme, L. Ojha, et al., 2016. Transport processes induced by metastable boiling water under Martian surface conditions, Nature Geoscience 9, 425–428. http://doi.org/10.1038/ngeo2706.

Mazzini, A., Etiope, G., 2017. Mud volcanism: An updated review. Earth-Science Reviews 168, 81–112. https://doi.org/10.1016/j.earscirev.2017.03.001

Miller, S. A., Mazzini, A., 2018. More than ten years of Lusi: A review of facts, coincidences, and past and future studies. Marine and Petroleum Geology 90, 10–25. https://doi.org/10.1016/j.marpetgeo.2017.06.019.

Montabone, L., Forget, F., Millour, E., Wilson, R. J., Lewis, S. R., Cantor, B., Kass, D., Kleinböhl, A., Lemmon, M. T., Smith, M. D.,Wolff, M. J., 2015.

Eight-year climatology of dust optical depth on Mars. Icarus 251, 65. https://doi.org/10.1016/j.icarus.2014.12.034.

Morgan, P., Grott, M., Knapmeyer-Endrun, B., Golombek, M., Delage, P., Lognonné, P., Piqueux, S., Daubar, I., Murdoch, N., Charalambous, C., Pike, W. T., Müller, N., Hagermann, A., Siegler, M., Lichtenheldt, R., Teanby, N., Kedar, S., 2018. A Pre-Landing Assessment of Regolith Properties at the InSight Landing Site. Space Science Reviews 214, 104. https://doi.org/10.1007/s11214-018-0537-y.

O'Brien, J. S., Julien, P. Y., 1988. Laboratory analysis of mudflow properties, J. Hydraul. Eng. 114, 877–887. https://doi.org/10.1061/(ASCE)0733-9429(1988)114:8(877).

Oehler, D. Z., Allen, C. C., 2012. Giant polygons and mounds in the lowlands of Mars: Signatures of an Ancient Ocean? Astrobiology 12(6), 601–615. https://doi.org/10.1089/ast.2011.0803.

Oehler, D. Z., Etiope, G., 2017. Methane seepage on Mars: where to look and why, Astrobiology 17. https://doi.org/10.1089/ast.2017.1657.

Okubo, C. H., 2016. Morphologic evidence of subsurface sediment mobilization and mud volcanism in Candor and Coprates Chasmata, Valles Marineris, Mars, Icarus 269, 23–27. https://doi.org/10.1016/j.icarus.2015.12.051.

Plesa, A.-C., Grott, M., Tosi, N., Breuer, D., Spohn, T., Wieczorek, M. A., 2016. How large are present-day heat flux variations across the surface of Mars? J. Geophys. Res. Planets 121, 2386– 2403. https://doi.org/10.1002/2016JE005126.

Pondrelli, M., Rossi, A. P., Ori, G. G., van Gasselt, S., Praeg, D., Ceramicola, S., 2011. Mud volcanoes in the geologic record of Mars: The case of Firsoff crater. Earth and Planetary Science Letters 304(3-4), 511–519. https://doi.org/10.1016/j.epsl.2011.02.027.

Presley, M. A., Christensen, P. R., 1997. Thermal conductivity measurements of particulate materials 2. Results. Journal of Geophysical Research 102, 6551–6566. https://doi.org/10.1029/96JE03303.

Putzig, N. E., Mellon, M. T., 2007. Apparent thermal inertia and the surface heterogeneity of Mars. Icarus 191, 68–94. https://doi.org/10.1016/j.icarus.2007.05.013.

Raack, J., S. J. Conway, C. Herny, M. R. Balme, S. Carpy, Patel, M. R., 2017. Water-induced sediment levitation enhances downslope transport on Mars, Nature

Communications 8, https://doi.org/10.1038/s41467-017-01213-z.

Ruesch, O., Genova A., Neumann W., Quick L. C., Castillo-Rogez J. C., Raymond C. A., Russel Ch. T., Zuber, M. T., 2019. Slurry extrusion on Ceres from a convective mud-bearing mantle. Nature Geoscience 12, 505–509. https://doi.org/10.1038/s41561-019-0378-7.

Rubin, D.M, Faíren, A., Martínez-Frías, J., Frydenvang, J., Gasnault, O., Galfenbaum, G., Goetz, W., Grotzinger, J.P., Le Moue´lic, S., Mangold, N., Newsom, H., Oehler, D.Z., Rapin, W., Schieber, J., Weins, R.C., 2017. Fluidized-sediment pipes in Gale Crater, Mars, and possible Earth analogs. Geology 45, 7–10. https://doi.org/10.1130/G38339.1.

Salvatore, M. R., Christensen, P. R., 2015. On the origin of the Vastitas Borealis formation in Chryse and Acidalia Planitiae, Mars. Journal of Geophysical Research: Planets 119, 2437–2456. https://doi.org/10.1002/2014JE004682.

Sinton, W., Strong, J., 1960. Radiometric observations of Mars, Astrophysical Journal 131, 459–469. https://doi.org/10.1086/146852.

Skinner, J. A., Tanaka, K. L., 2007. Evidence for and implications of sedimentary diapirism and mud volcanism in the southern Utopia highland-lowland boundary plain, Mars, Icarus 186, 41–59, http://dx.doi.org/10.1016/j.icarus.2006.08.013.

Skinner, J. A., Mazzini, A., 2009. Martian mud volcanism: Terrestrial analogs and implications for formational scenarios. Marine and Petroleum Geology 26(9), 1866–1878. https://doi.org/10.1016/j.marpetgeo.2009.02.006.

Vaniman, D. T., Bish, D. L., Chipewa, S. J., Fialips, C. I., Carrey, J. W. Feldman, W. C., 2004. Magnesium sulphate salts and the history of water on Mars. Nature 431, 663– 665. https://doi.org/10.1038/nature02973.

Ward, W. R., 1973. Large-scale variations in the obliquity of Mars. Science 181, 260–262. https://doi.org/10.1126/science.181.4096.260.

Whaetley, D. F., Chan, M. A., Okubo, C. H., 2019. Clastic pipes and mud volcanism across Mars: Terrestrial analog evidence of past martian groundwater and subsurface fluid mobilization. Icarus 328, 141-151. https://doi.org/10.1016/j.icarus.2019.02.002.

Wilson, L., Head, J.W., 1994. Mars: review and analysis of volcanic eruption theory and relationships to observed landforms. Rev. Geophys. 32, 221–263. https://doi.org/10.1029/94RG01113.

Wilson, L., and Mouginis-Mark, P. J., 2014. Dynamics of a fluid flow on Mars: Lava or mud? Icarus 233, 268–280. https://doi.org/10.1016/j.icarus.2014.01.041.

Part IV
Concluding summary

7 General conclusions

In this thesis we present two topics that are related to analogue and numerical modelling of the large-scale plate tectonic systems on the Earth and to the exogenic processes associated with mudflows on the surface of Mars. The first part is conceived as a brief overview of the methods, history and physical background of modelling in geosciences. The second part introduces two analogue models of oroclinal buckling and detachment folding where the techniques of advanced numerical image analysis were employed to support strain and flow dynamics investigation. Both models are supplemented by numerical modelling of the Rayleigh-Taylor instability in the systems with expected crustal-scale inversion. The third part is aimed at the study of the morphology and dynamics of mud flows situated on the surface of Mars with potential implications for rocky-icy moons and dwarf planets. In this final part we summarize the main conclusions from each part and chapter.

7.1 Conclusions of the Part II

Models of oroclinal buckling

The modelling which simulates the lateral shortening of the pre-arcuated multi-layer (accretionary belt) shows the development of two regional-scale types of folds: 1. upright folds which are developed in both the oceanic domain and continental ribbon; 2. Steeply plunging orocline. The general deformation pattern is characterized by significant thickening and exhumation of the lower ductile crust and upper mantle that are oriented near the indenter part which is accommodated by thickening of the upper crustal material at the back-stop side.

The overthrusting of oceanic and continental crust along the orocline hinges is associated with material vortex flow around the inflection of the orocline. This pattern decays towards deeper lithospheric layers, where the lateral flow of material is negligible and flow along the shortening direction is dominant. The redistribution of lower crustal and mantle material related to oroclinal buckling is consistent with geophysical (gravity and magnetic) data related to the Tuva-Mongol orocline. The model may explain a formation of giant gravity low situated in the Hangai sector (which corresponds to the hinge zone of the orocline) - that can coincide with vertical flux of hot mantle and hot lower crust. The linear zones of gravity highs, that are associated with the vertical zones parallel to orocline axial plane, may reflect the formation of simulated pop-down structures. Finally, the deformation gradient reported along the southern flank of Mongolian orocline may correspond to the indentation profile expressed by the presented model.

Models of detachment folding

In these models we developed a technique for the quantification of the mass transfer balance between individual model subdomains. The relative material transfer between these model subdomains can be quantified by average divergence evolution in the pre-defined subgrids and compared with the modal volume changes of the low viscosity and highly mobile material representing the molten crust.

The divergence analysis of the displacement field in the detachment folding experiments revealed systematic variations in the height of the folds and their modal melt content that are related to the inflow rate of melt into their cores. The overpressurization of the melt in the locked folds leads to melt expulsion back into the melt source layer, where it can be transferred further laterally into the foreland and facilitate detachment folding of the subsequent folds. The amount of the melt and time-dependent rate of the material transfer between folds and source layers in the crust affects individual evolutionary stages of current fold. The main stages corresponding to: 1. initial amplification of the material undulation; 2. melt inflow and growth of the fold; 3. locking (and necking) of the fold and outflow of the melt from the fold bottom back to the source layer; 4. vertical extrusion of the melt inside the domed region following the axial plane of the fold.

Simulations of Rayleigh-Taylor instability

The modelling of the R-T instability shows how system dynamics change with variation of the initial conditions covering different scenarios of evolving accretionary systems.

The radiogenic heating of the lower felsic crust affects the P-T-t conditions at the individual crustal levels which reflects different paths of the material through the diapiric body. If the density contrast of the crustal layers is low, the higher heating of the FLC can support the growth of the thermal-material perturbation at the layer interface which is followed by vertical transfer. Higher radiogenic heating also decreases the time where the maximum dynamics of the systems occurs. The effect of the heating is also conditioned by the amount of the thermal-productive material which is related to the thickness of the lower felsic crust.

The amplitude and wavelength of the initial material perturbation support the diapiric potential, and partly affects the finite shape and rate of the exhumation. The higher amplitudes decrease the time of the maximum dynamics.

The viscosity contrast between the individual crustal levels affects the incrementally changed geometry and finite shape of the diapir. The density and size of the initial perturbation represent different initial stages (times and distances) of the material transfer in dependence on the indenter distance. In the systems that are characteristized by high convergence rate and low heating, buckling or detachment folding of the lower crust is more typical than diapirism.

The systems with the progressively decreasing convergence rate may be characterized by combination or switching between dipirism and folding. The increasing distance of the Rayleigh-Taylor instabilities from the indenter reflects increasing internal diapiric dynamics while near-oriented instabilities are strongly affected by indentation and buckling of the strong lower crust. If the lower crust is sufficiently weak then the indentation supports diapirism and increases exhumation rate.

7.2 Conclusions of the Part III

Models of mudflows on the cold surface

The modelling results show that both igneous and mud volcanism can produce surface expressions which share certain morphological characteristics. The inflation of decimetre-thick lobes in the frontal part of the mud flows and lava flows is similar for both features. This is the reason for difficulty in recognition between both flow types from currently available remote sensing data

The numerical modelling shows that the morphologies of mud flows at scales larger than those covered by our experiments could be affected by the same processes. Hence Martian mud volcanoes may differ substantially in shape from their terrestrial counterparts.

Sedimentary volcanism has also been proposed for the dwarf planet Ceres which may have a water-muddy ocean beneath a crust made of clays, salts, clathrates and ice. The process of evaporative cooling and associated freezing should also occur there, affecting morphologies of the resulting effusive features; probably even more on Ceres than on Mars as Ceres lacks an atmosphere. This is because once cryomagma, reaches the surface of Ceres, water would be unstable and start to evaporate or freeze or both. The same principles would be applicable for other small bodies and icy moons elsewhere within the Solar system where effusive cryovolcanism has been postulated. The results highlight that it is critical to consider the effects of differing environmental conditions on other planetary surfaces when comparing analogue landforms observed on Earth with apparently similar effusive morphologies on other bodies.

Models of mudflows on the hot surface

The experiments in a vacuum chamber show that a warm and unconsolidated surface has a profound effect on the behaviour of flowing low viscosity mud in a low-pressure environment The resulting boiling occurring during the mass flow, causes transient levitation of the mud above the warm surface as well as the erosion of the unconsolidated sandy substrate. Both mechanisms alter mud propagation in a low pressure environment. Moreover, we expect that these processes would be even more effective on Mars which has a lower gravitational acceleration than on Earth.

On Mars gravity does not change the boiling rate, but the sediments can be more easily entrained. The gas release should levitate mud for a longer period of time than observed in our experiments, as also similarly suggested for wet sand hence allowing the mud to propagate over larger distances than modelled within the low pressure chamber. Additionally, as the process of evaporative cooling would remove the latent heat from the mud and from the surface over which it is propagating, at a certain point, the mud would start to freeze. This would cause the formation of a protective icy-muddy crust affecting the way the mud moves switching from levitation and sliding/creeping to the propagation via mud tubes. The mechanisms of mud propagation on the Earth at different P-T conditions are well studied. Mud propagation, during this relatively simple process, is controlled by mass gravity flow. In contrast, very little is known on the modes controlling the same events on e.g. Mars and other bodies within or absent atmospheres where mud eruptions may be present. The new data from the presented model demonstrates that the behaviour of mud and its propagation in a low-pressure environment, is strongly controlled by the surface temperature since freezing or rapid boiling give rise to different transport mechanisms than simple liquid flow. This suggests that mud eruption activity on other celestial bodies may produce profoundly different morphologies compared to those commonly observed on Earth.

7.3 Afterword

In this thesis we demonstrate the effectivity of both modelling approaches commonly used in geodynamical modelling. In the analogue models we used methods of the image velocimetry and photogrammetry to derive strain components and to describe geometrical and deformation patterns. We extended the PIV analysis by incorporation of the adaptive subgrids to investigate and quantify mass transfer in crucial model subdomains. This methodology represents a bridge between analogue and strictly numerical solution. The applicability of the PIV method to various problems is a subject of recent research in analogue modelling community and has the potential to be extended or modified to combine tracking of a material transfer with other features (e.g. with heat transfer).

Both orocline and detachment folding models represent new and original analogue experiments with promising results that can help to decrypt the problematic formation of large accretionary systems related to large-scale folding and oroclinal buckling. The results were mainly discussed in frame of the CAOB in central Asia. These models were supplemented by numerical model of the R-T instability which represents a native component of large hot orogens where a crustal inversion can be expected. The concept of the model following recent work in the field of the inverted crustal domains and the model results were discussed in the context of modern insight to large-scale accretion systems associated with indentation tectonics.

Another topic of the thesis was related to Martian mud flows with a modelling procedure using a vacuum chamber. These physical models studied the effect of decreased atmospheric pressure to physics of the mud flows and discussed the results in the frame of recent projects that are related to planetology studies. The experimental part was followed by numerical-analytical modelling that interlinked the laboratory experiments and the natural situation at the surface of Mars. Using the large vacuum chamber has a big potential to study not only formation of mud flows but even processes associated directly to transfer of a mud (or other cryo-materials) between an environments with different pressures such as a reservoir and surface. Simulations of a complex cryovolcanic systems including mud extrusion and development of cone structures and individual mud flows will be subject of further research.